Correlating long-term lithium ion battery performance with solid electrolyte interphase (SEI) layer properties

A Dissertation Presented for the
Doctor of Philosophy
Degree
The University of Tennessee, Knoxville

Seong Jin An
August 2017

DEDICATION

To my father
Gil-Sik An (안길식)

my mother
Yeong-Ja Gwon (권영자)

my wife
Sumin Lee (이수민)

and my daughter
Seoyeong An (안서영)

Without the love and understanding of my family, I could not have reached this point.

ACKNOWLEDGEMENTS

I would like to express my deep gratitude to Prof. David L. Wood III for his support and the opportunity he has provided me to work at Oak Ridge National Laboratory. Without his support, it would not be possible to conduct this research. I would like to thank my thesis committee: Dr. Claus Daniel, Dr. Jagjit Nanda, and Prof. Thomas A. Zawodzinski for their encouragement and insightful comments. I would also like to thank Dr. Jianlin Li for the battery expertise and time he shared with me and Dr. Harry M. Meyer for allowing me to use X-ray photoelectron spectroscopy heavily. Thanks also to the Roll-to-Roll Manufacturing team at National Transportation Research Center: Jesse Andrews, Lamuel David, Zhijia Du, Kevin Hays, Chengyu Mao, Nathan Phillip, Rose Ruther, Yangping Sheng, and Marissa Wood for their help and friendship.

I would like to express my appreciation to the U.S. Department of Energy and Vehicle Technologies Office for providing funding for this research and to CAMP (Cell Analysis, Modeling and Prototyping) Facility, Argonne National Laboratory, for providing electrodes used in the electrolyte volume studies. My appreciation is also extended to the Bredesen Center for the Energy Science and Engineering Fellowship. I wish to thank Prof. Lee Riedinger, director of the Bredesen Center, who guided me through my graduate education.

ABSTRACT

This study was conducted to understand effects of some of key factors (i.e., anode surface properties, formation cycling conditions, and electrolyte conditions) on solid electrolyte interphase (SEI) formation in lithium ion batteries (LIBs) and the battery cycle life. The SEI layer passivates electrode surfaces and prevents electron transfer and electrolyte diffusion through it while allowing lithium ion diffusion, which is essential for stable reversible capacities. It also influences initial capacity loss, self-discharge, cycle life, rate capability and safety. Thus, SEI layer formation and electrochemical stability are primary topics in LIB development. This research involves experiments and discussions on key factors (graphite surface properties, electrolyte volume, and formation cycle) affecting SEI formation. For the graphite anode surface property study, ultraviolet (UV) light was applied to battery electrodes for the first time to improve the SEI and cycle life. UV treatment for 40 minutes resulted in the highest capacity retention and the lowest resistance after the cycle life testing. Anode analysis showed changes in surface chemistry and wetting after the UV treatment. It also showed increases in solvent products and decreases in salt products on the SEI surface when UV-treated anodes were used. XPS analysis showed that UV light decomposed polyvinylidene fluoride (binder) but helped to increase the oxygen level on graphite, which, resulted in a thin SEI layer, low resistance, and eventually high capacity retention. For the formation cycling condition study, a fast SEI formation protocol was proposed. The protocol involved more (shallow) charge-discharge cycles between 3.9 V and 4.2 V and fewer (full depth of discharge) cycles below 3.9 V. It improved SEI and capacity retention and shortened formation time by 6 times or more without compromising cell performance. To understand effects of electrolyte conditions, electrolyte volumes were controlled in full cells. A minimum electrolyte volume factor of 1.9 or 3 times the total pore volume of cell components (cathode, anode, and separator) was needed for long-term cyclability and low impedance of cells consisting of graphite anode or 15 weight percent Si-graphite anode, respectively. Less electrolyte resulted in an increase of the measured Ohmic resistances.

TABLE OF CONTENTS

INTRODUCTION 1
Background 1
Understanding the solid electrolyte interphase (SEI) 1
Cost of SEI formation 6
Research problem 8
Research topics 10
References 12
CHAPTER I A review: The State of Understanding of the Lithium-Ion-Battery Graphite Solid Electrolyte Interphase (SEI) and Its Relationship to Formation Cycling 15
Abstract 16
Introduction 16
Understanding nature of solid electrolyte interphase (SEI) 18
Energetics of anode SEI formation 21
SEI features, morphology, and chemical composition 21
Formation mechanism of SEI layer 27
Methods of analyzing and characterizing the SEI layer 33
Effects of carbon/graphite properties on SEI formation 34
Effects of electrolyte composition on SEI formation 36
Relationship between electrolyte decomposition reactions and LIB formation protocol. 39
Prospects for improving SEI properties and reducing formation time 48
Recent progress in SEI layer studies and prospects for future understanding 50
Computational studies 50
SEI on anode metalloid or metal oxide 54
Additives 55
Prospects for future understanding 56
Summary 56
References 58
CHAPTER II Long-Term Lithium-Ion Battery Performance Improvement via Ultraviolet Light Treatment of the Graphite Anode 78
Abstract 79
Introduction 80
Experimental 81
Results and discussion 85
Cycle performance 85
Impedance 89
Solid electrolyte interphase analysis 92
Changes on graphite surfaces after UV treatment 105
Changes in PVDF after UV treatment 109
Conclusions 115
References 118

CHAPTER III Fast Formation Cycling for Lithium Ion Batteries 122
Abstract 123
Introduction 123
Proposed formation method 125
Experimental 126
Results and discussion 130
Formation time reduction and capacity 130
EIS resistances 132
Conclusions 138
References 140
CHAPTER IV Correlation of Electrolyte Volume and Electrochemical Performance in Lithium-ion Pouch Cells with Graphite Anodes and NMC532 Cathodes 142
Abstract 143
Introduction 143
Experimental 145
Results and discussion 150
Correlation of electrolyte volume and capacity fade 150
Hybrid pulse power characterization (HPPC) analysis 152
Impedance analysis - EIS 156
Effect of electrolyte volume 159
Conclusions 161
References 162
CHAPTER V Electrolyte Volume Effects on Electrochemical Performance and Solid Electrolyte Interphase in Si-Graphite/NMC Lithium-Ion Pouch Cells 164
Abstract 165
Introduction 165
Experimental 166
Results and discussion 171
Correlation of electrolyte volume and capacity fade 171
Resistance analysis 178
Anode surface analysis 183
Conclusions 187
References 188
CHAPTER VI Design and Demonstration of Three-Electrode Pouch Cells for Lithium-Ion Batteries 190
Abstract 191
Introduction 191
Experimental 192
Results and discussion 197
Charge and discharge 197
Resistance 201
Solid-state lithium diffusion 208
2D simulation 209

Conclusions....216
References....218
CONCLUSION AND FUTURE WORK....222
VITA....227

LIST OF TABLES

Table 0.1. Reduction and oxidation potential vs. Li/Li+ of solvents and electrolytes, GC and GR are glassy carbon and graphite, respectively 2
Table 0.2. LIB pack cost contributions for baseline electrode processing case (cost per kWh-usable energy assumes a 70% depth of discharge for cycling. (D. L. Wood et al., Journal of Power Sources, 275 (2015) 234-242). 7
Table 1.1. List of known chemical compounds formed on the surface of carbon/graphite SEI layers ("Present" denotes that the compound was identified in the references given, and "Not Present" denotes that the compound was not identified).[48] "Reprinted from Electrochimica Acta, 55, Verma P, Maire P, Novak, A review of the features and analysis of the solid electrolyte interphase in Li-ion batteries, 6332, Copyright (2010), with permission from Elsevier." 28
Table 1.2. SEI formation and electrolyte decomposition reaction categories corresponding to reaction paths in Figures 1.7-1.10.....43
Table 2.1 Cell information 82
Table 2.2 Test group names of pouch cells and their electrode combinations....84
Table 2.3. Representative compounds on an SEI surface and binder and the ratios of their elements to lithium 97
Table 2.4. Binding energy (eV) of SEI components assigned in Figure 2.10 and 2.11.....102
Table 2.5. XPS results on graphite before UV treatment and after the treatment for 40 minutes from narrow scans for O1s and C1s.....108
Table 2.6. Temperature on electrode immediately after UV treatment with different periods of time 111
Table 3.1. Abbreviations used in this study and associated formation conditions 128
Table 3.2. Cell information 129
Table 4.1. Pouch cell information.....146
Table 4.2. Electrolyte volume factor group, F, having five individual factor samples, f, in each group.....148
Table 5.1. Pouch cell information.....168
Table 5.2. Electrolyte volume factor group, F, having five individual factor samples in each group.....169
Table 5.3. Atomic percentages of elements from EDS analysis on cycled anodes of F1.6 and F3.5. The locations of Zone 1 (graphite rich) and Zone 2 (silicon-carbon rich) are indicated at Figure 5.5 175
Table 6.1. Cell information 193
Table 6.2. Abbreviations and definitions 196
Table 6.3. Approximate resistances from the Nyquist plots in Figure 6.6 207
Table 6.4. Parameters and their definitions in Figure 6.9 and for Eq.6 and Eq.7 213

LIST OF FIGURES

Figure 0.1. Voltage profiles of cathode (μC), anode (μA), and cell (VOC) from a three-electrode cell during charge and discharge, area in orange and blue colors indicates unstable voltage window. 3
Figure 0.2. Decomposition reactions of ethylene carbonate (EC), linear carbonate, and salt. (An et al, Carbon 105 (2016) 52-76).....4
Figure 0.3. Schematic of the anode SEI formation process showing (a) graphene layers surrounded by electrolyte salts and solvents above 1.4V vs. Li/Li+, (b) propylene-carbonate (PC) intercalation with lithium ions into graphene layers resulting exfoliations below 0.9V vs. Li/Li+ and (c) stable SEI formation in ethylene-carbonate (EC)-based electrolyte below 0.9V vs. Li/Li+; plane side with thinner SEI and edge side with thicker SEI. (An et al, Carbon 105 (2016) 52-76). 5
Figure 0.4. Key factors affecting SEI formation (surface property, voltage/C-rate, and electrolyte) and relation to work done (fast formation, UV treatment, and electrolyte volume).....11
Figure 1.1. Energetics of the formation of the anode and cathode SEI layers under electro-reduction and electro-oxidation conditions.[21] “Reprinted (adapted) with permission from (Goodenough, J. B.; Kim, Y. Chemistry of Materials 2010, 22, 587). Copyright (2010) American Chemical Society.”...22
Figure 1.2. SEI morphology at various formation potentials reported by Lu et al., (a) 0.7 V, (b) 0.5 V, (c) 0.3 V and (d) 0.0025 V. The right column images are higher magnification (100,000×) of the images in left column (30,000×).[56] “Reprinted (adapted) with permission from (Harris, S. J.; Lu, P. J. Phys. Chem. C 2013, 117, 6481). Copyright (2013) American Chemical Society.” 25
Figure 1.3. TEM images of fresh graphite and SEI on graphite anodes cycled to four cutoff voltages in 1.2M $LiPF_6$/EC during first charge reported by Lie et al., (A) Fresh graphite electrode, (C) 1.3, (E) 0.6, (G) 0.1, and (I) 0.05 V. The insets of (D), (F), (H), and (J) show element composition detected by EDX. The arrows indicate the SEI layer and the edge of graphite, and the red spots indicate locations probed by EDX. .[57] "Reprinted with permission from (Mengyun Nie et al. J. Phys. Chem. C, 2013, 117 (3), 1257). Copyright (2013) American Chemical Society." 26
Figure 1.4. Schematic of the anode SEI formation process showing (a) graphene layers surrounded by electrolyte salts and solvents above 1.4V vs. Li/Li^+, (b) propylene-carbonate (PC) intercalation with lithium ions into graphene layers resulting exfoliations below 0.9V vs. Li/Li^+ and (c) stable SEI formation in ethylene-carbonate (EC)-based electrolyte below 0.9V vs. Li/Li^+; plane side with thinner SEI and edge side with thicker SEI.....30
Figure 1.5. Proposed SEI layer reaction mechanism consisting of a four-step pathway (Yan).[98] “Reprinted from Electrochimica Acta, 55, Jian Yan, Jian Zhang, Yu-Chang Su, Xi-Gui Zhang, Bao-Jia Xia, A Novel Perspective on

the Formation of the Solid Electrolyte Interphase on the Graphite Electrode for Lithium-Ion Batteries, 1788, Copyright (2010), with permission from Elsevier.”.....31
Figure 1.6. Schematic of the lithium-ion intercalation process into and out of graphite [J. Yan et al.] [98] Left: graphite particle showing turbostratic disorder of individual nano-scale regions of high order (crystallinity). Center: graphene layers of an individual crystallite showing edge and basal plane directions. Right: AB stacking of individual graphene layers where lithium ions intercalate between layers A and B. “Reprinted from Electrochimica Acta, 55, Jian Yan, Jian Zhang, Yu-Chang Su, Xi-Gui Zhang, Bao-Jia Xia, A Review of the State of Understanding of the Graphite Solid Electrolyte Interphase (SEI) and Its Relationship to Formation Cycling, 1787, Copyright (2010), with permission from Elsevier.”.....35
Figure 1.7. Ethylene carbonate (EC) reduction process (reference groups in parentheses; details are shown in Table 1.2). 44
Figure 1.8. Propylene carbonate (PC) reduction process (reference groups in parentheses; details are shown in Table 1.2). 45
Figure 1.9. Linear carbonate (LC) reduction process (reference groups in parentheses; details are shown in Table 1.2). 46
Figure 1.10. Electrolyte salt reduction process (reference groups in parentheses; details are shown in Table 1.2). 47
Figure 1.11. Interlayer binding energy of graphite as a function of interlayer separation calculated by LDA, GGA and five different vdW functionals,192 Reproduced from Ref. 192 with permission from The Royal Society of Chemistry.....53
Figure 2.1. Average discharge capacities with 90% confidence intervals (error bars) from preliminary cycle life tests of UV 0min and UV 60 min groups with 1C charge and discharge for 600 cycles (a); from second cycle life tests for verification with 1C charge and discharge rates (b); and from the performance check of the second tests with C/5 charge and discharge rates after every 50 cycles of the cycle life tests (c), from C-rate tests before aging cycles for the second sets (d). Dashed lines in (a) and (b) indicate capacities of UV 0 min and UV 60 min group near 300 cycles. 86
Figure 2.2. Average discharge capacities (a) and irreversible capacity losses (ICL) (b) from formation cycles of different UV groups with C/20 charge and discharge rates. 88
Figure 2.3. Nyquist plots of EIS from UV 0 min before (a) and after cycle lift tests (b); UV 20 min before (c) and after the tests (d); UV 40 min before (e) and after the tests (f); and UV 60 min before (g) and after the tests (h).....90
Figure 2.4. Ohmic, surface film, and charge transfer resistances at different voltages before cycle life tests (a) and after cycle life tests (b); resistance differences before and after the cycle life tests (c); the equivalent circuit model for Nyquist plot fittings is shown on top right. 91

Figure 2.5. Resistances, from a three-electrode pouch cell, after formation cycles at anode and cathode from HPPC tests with respect to different voltages (a), voltages at 0.2C/-0.2C (b). CE-RE, WE-RE, and WE-CE are voltages or resistances from anode, cathode, and cell, respectively. 93
Figure 2.6. Atomic percentages of elements from XPS survey scans on UV-treated and untreated graphite anode electrodes before cell assembly (a) and after 300 cycles of cycle life tests (b). The ratio of each element to lithium after 300 cycles of life tests is shown in (c). 94
Figure 2.7. Contact angles of graphite anode electrodes with different durations of UV treatment in an ambient environment. 96
Figure 2.8. Following 300 cycles, counts per second (CPS) of elements from XPS snapshots during depth profiling of the anode electrodes (a. Estimated thickness of SEI, with elements in white and average thickness compared with the estimated thicknesses in bold red. The numbers on C1s and O1s indicating (1) graphite, (2) surface carbon, (3) carbonate, (4) Li_2O, and (5) surface oxygen (carbonate, carbon, graphite). 99
Figure 2.9. Following 300 cycles, counts per second (CPS) of elements from XPS snapshots during depth profiling of the cathode electrodes. Estimated thickness of SEI, with elements in white and average thickness compared with the estimated thicknesses in bold red. The numbers on O1s indicating (5) surface oxygen (carbonate, carbon, graphite) and and (6) lattice oxygen (O^{2-}). 100
Figure 2.10. Element snapshots from XPS depth profiling and their related compounds at the anode electrodes with different UV treatments. The bold italic numbers denote the thickness close to the SEI or passivation layer, as estimated in Figure 2.8. 103
Figure 2.11. Element snapshots from XPS depth profiling and their related compounds at the cathode electrodes (b) used with the UV treated anodes. The bold italic numbers denote the thickness close to the SEI or passivation layer, as estimated in Figure 2.9. 104
Figure 2.12. XPS survey scan results on A12 graphite powders before UV treatment and after UV treatment for 40 minutes (a), atomic percentages of carbon and oxygen calculated from the survey scans (b), and narrow scan results for O1s (c) and C1s (d). 106
Figure 2.13. XPS narrow scan results of O1s before UV treatment (a) and after UV treatment for 40 minutes (b) and C1s before UV treatment (c) and after UV treatment for 40 minutes (d). 107
Figure 2.14. A proposed pathway for additions of hydroxyl groups on a graphite surface under UV light with humid air. 110
Figure 2.15. Weights and thicknesses of electrodes and PVDF films after UV treatment with different periods of time. 112
Figure 2.16. Backbone, C-H, and C-F scissions of a PVDF polymer chain. 113
Figure 2.17. Schematic diagrams of two different dehydrofluorinations in PVDF (a-b) and a simulation results for atomic distances and angles between

carbons with and without a double bond (c); F: yellow ball, H: white ball, and C: gray. 114
Figure 2.18. XPS survey scans from electrodes before UV treatment (a) and after the treatment for 40 minutes (b) and atomic percentages from the scans (c). 116
Figure 3.1. Typical cathode potential (μC), anode potential (μA), and voltage between anode and cathode (VOC) from a three-electrode pouch cell (graphite anode/Li reference/$Li_{1.02}Ni_{0.50}Mn_{0.29}Co_{0.19}O_2$ cathode) with potential ranges in blue and orange regions where the electrolyte is not stable (a); cell voltage profiles from a baseline and alternative (b) and a modified alternative SEI formation protocol (c). 127
Figure 3.2. Voltage profiles for three baseline formation protocols in blue and alternative protocols (C-rates denoted with “a”) in orange (a) and corresponding formation times (b), voltage profiles for modified alternative protocols in yellow and purple (c) and corresponding formation times (d). 131
Figure 3.3. Average discharge capacities with 90% confidence intervals using different formation protocols during formation cycling (a and c) and post-formation rate capability testing (b and d). Capacities from alternative and modified alternative protocols in (a and c) show only one value at the first cycle for each formation C-rate because the alternative and modified alternative protocols contain only one full discharge. 133
Figure 3.4. Discharge capacities after the baseline and alternative formations (a, c) and after the baseline and modified alternative formations (e-f) and discharge capacity retentions for the baseline and alternative (b, d) during aging for each 1C and -1C cycle (a-b) and each C/5 and -C/5 loop (c-d) where each loop is 50 cycles. 134
Figure 3.5. Equivalent circuit model used in this impedance analysis. 135
Figure 3.6. EIS Nyquist plots from cells with different formation protocols (a, c, and e) near 3.9V ±0.05V during discharge; average areal specific resistances (ASR) of F@C/20 and F@C/5a (b, d, and f) at different voltages before aging cycles (b), after 300 cycles (d), and after 1300 cycles(f). 136
Figure 3.7 Areal resistance of cells with the baseline and modified alternative protocol from HPPC tests (a) and EIS (b) after 500 aging cycles. 139
Figure 4.1. Test protocol and procedure. 149
Figure 4.2. Correlation of electrolyte volume and cell cyclability (a) Discharge capacity fade at 0.33C/-0.33C for different electrolyte volume factor groups, F; (b) individual cell electrolyte volume factors, f, after each “loop”, where each loop corresponds to 20 0.33C/-0.33C aging cycles. Cells with electrolyte volume factors greater than 1.9 demonstrate comparable cyclability. 151
Figure 4.3. Voltage profiles of (a) f 1.29, (b) f 1.94, (c) f 2.50, and (d) f 3.51 on the first cycle of every C/3, aging-cycle test loop, where each loop includes 20 aging cycles. 153

Figure 4.4. Discharge capacities of different electrolyte volume factor groups, F, at (a) C/10 and (b) 1C at the end of each life-cycle test loop, where each loop includes 20 aging cycles. 154
Figure 4.5. Resistances from HPPC tests at different voltages during discharge after every 20 aging cycles for electrolyte volume factor group F 1.3 (a), F 1.9 (b), F 2.5 (c), and F 3.5 (d); resistances of individual electrolyte volume factors, f, at 50% discharge (e) with “0 loop” representing resistance before cycling and each subsequent loop representing 20 additional aging cycles; resistances of individual cells at 50% discharge for electrolyte volume factor groups F 1.3 and F 1.9 (f). 155
Figure 4.6. EIS data of NMC cathode half-cells from harvested pouch-cells before cycling (a-b) with electrolyte volume factors of f 1.25 (a) and f1.89 (b) and after 100 cycles (c-f) with different electrolyte volume factors of f 1.25 (c), f 1.89 (d), f 1.29 (e), and f 1.94 (f).....157
Figure 4.7. Resistances of NMC cathode half-coin cells at 3.6V vs. Li/Li+ (a) calculated using Figure 4.6 data and the equivalent circuit model in Figure 4.6b inset, resistance of half-coin cells at 3.6 V vs. Li/Li+ and full pouch-cells at 3.6 V (vs. LiCx) during discharge after 100 cycles (b). 158
Figure 4.8. Differential voltage curves of harvested half-cells from full pouch cells with f 1.94 (a) and f 1.29 (b) and differential voltage curves of full pouch cells with f 1.94 (c) and f 1.29 (d). (1) and (2) are cathode curves before and after aging cycles, respectively. 160
Figure 5.1. Test protocol and procedure. 170
Figure 5.2. Correlation of electrolyte volume and cell cyclability. Discharge capacities during (a) first three cycles at 0.05C/-0.05C, (c) aging cycles at 0.333C/-0.333C, and (e) last three cycles at 0.05C/-0.05C for different electrolyte volume factor groups, F; corresponding irreversible capacity losses (ICLs) during (b) the first three cycles, (d) aging cycles and (f) the last three cycles. Cut-off voltages were 3 and 4.1 V. Voltage for the aging cycle was held at 4.1 V until current reached 0.05C. Error bars correspond to 95% confidence intervals. 172
Figure 5.3. SEM images of (a) pristine 15 wt.% Si-graphite anode and (b) F1.5 and (c) F3.5 anode cycled 100 times. Magnification of the images on left and right are 200,000 X and 25,000 X, respectively. 174
Figure 5.4. Different EDS analysis areas from cycled anodes of (a) F1.6 and (b) F3.5. Rectangular zone 1 and 2 focus on graphite and Si mixed with carbon, respectively. EDS data are shown in Table 5.3. 176
Figure 5.5. Images of cathodes, anodes and separators from F1.6, F2.6, and F3.5 after 100 cycles. 177
Figure 5.6. Resistances of 15 wt.% Si-graphite/NMC532 cells from HPPC tests at different voltages during discharge at 4^{th} and 97^{th} cycles for electrolyte volume factor group F1.6 (a), F2.1 (b), F2.6 (c), F3.1 (d), and F3.5 (e). 179
Figure 5.7. (a) Impedance spectra of 15 wt.% Si-graphite/NMC532 cells near 3.75 V after 100 cycles with different electrolyte volume factor groups. (b)

Total resistances from EIS at different voltages. Equivalent circuit model for the EIS data fitting is shown in Figure 5.8. 180
Figure 5.8. (a) Equivalent circuit model for EIS data fitting and definitions and four frequency domains of elements. As examples, EIS data of F3.5 at (b) 4.1 V and (c) 3 V after 100 cycles and their data ranges for the fittings. 181
Figure 5.9. Areal specific resistances (ASR) from EIS at different voltages in different electrolyte volume factor groups, (a) ohmic resistance (R_{ohmic}), (b) surface film resistance (R_{sf}), (c) anode charge transfer resistance (R_{ct1}), and (d) cathode charge transfer resistance (R_{ct2}). 182
Figure 5.10. Depth profiles of SEI (LiF and carbonates) and active material (Si-Si and Li_xSiO_y) elements. Black dashed and dotted lines are possible ranges of SEI/Si interface and averages of the ranges, respectively. The depth on x-axis was based on the assumption that the film has the same etching rate as SiO_2. CPS of each element was normalized by its own maximum value. .. 184
Figure 5.11. (a) XPS peaks from depth profiles of F1.6, F2.6, and F3.5 and (b) atomic percentages from the top surface (before sputtering) from XPS survey scans. Depth was calculated based on the sputter rate for SiO_2. 186
Figure 6.1. Cross-sectional (a) and planar (b) view of a schematic three-electrode assembly showing baseline (case 1) and aligned (case 2) electrodes, a schematic view of five leads connections between a cell and measurement instrument (c), images of three-electrode assemblies facing a cathode current collector side up (d), an anode current collector side up (e), an image of a three-electrode pouch cell before (f) and after (g) electrolyte filling and vacuum-sealing, and a lithium foil with a tab (h); WE, CE, and RE denote working electrode, counter electrode, and reference electrode, respectively; P1 and P2 denote power for the control and measurement of current flowing through the electrode; S1, S2, and S3 denote sense for the control and measurement of the electrode potential. The green films are battery-grade acrylic adhesive tapes. 195
Figure 6.2. Capacities during formation cycles at C/10 and -C/10 with cut-off voltages of 4.3 V_{WE-RE} to 3 V_{WE-RE} (a) and discharge capacities at C/5, C/3, 1C, and 3C with cut-off voltages of 4.6 V_{WE-RE} to 3 V_{WE-RE} (b); voltage profiles of baseline (c, d) and aligned electrodes (e, f) with C/10 and –C/10 at first formation cycle (c, e), at second formation cycle (d, f). (+) and (-) denote charge and discharge, respectively. 198
Figure 6.3. Voltage profiles on x-axis of capacity at C/5 and –C/5 with cut-off voltages of 3 V_{WE-RE} and 4.6 V_{WE-RE}. (+) and (-) denote charge and discharge, respectively. 200
Figure 6.4. Differential capacities at different C-rates (a-c) between WE and RE (a), between CE and RE (b), and between WE and CE (c); differential capacities of anode (CE-RE) and cathode (WE-RE) at C/5 (d); (+) and (-) denote charge and discharge, respectively. 202
Figure 6.5. Resistances from HPPC at baseline (a, c) and aligned cells (b, d) before (a, b) and after 15 cycles of C-rate tests (c, d). R_{WE-CE}, R_{WE-RE}, and

R_{CE-RE} denote resistances of a cell, cathode (working electrode), and anode (count electrode), respectively. 203
Figure 6.6. Nyquist plots of baseline and aligned-cell EIS from anodes (a), cathodes (b), and cells (c) at 50% DOD before, data at the 3rd cycle, and after 15 cycles of the C-rate tests, data at the 19th cycle. Frequency values with brackets indicate centers of semicircles and ones without brackets are high and low frequency ranges used for EIS data fits in Figure 6.7. 204
Figure 6.7. Resistances from baseline (a-b) and aligned cell EIS (c-d) for cells (WE-CE) at different voltages before, data at the 3rd cycle, and after 15 cycles of the C-rate tests, data at the 19th cycle. R_{ct}, R_{sf}, and R_{ohmic} denote charge transfer, surface film (SEI), and ohmic resistances, respectively. Equivalent circuit model to fit Nyquist plots is shown on top right. 205
Figure 6.8. Lithium solid-state diffusion coefficients of cathodes from baseline and aligned cells before, data at the 3rd cycle, and after C-rate test, data at the 19th cycle..... 210
Figure 6.9. Cross-section geometries of baseline and aligned cells for 2D-simulations considering only electrolyte sections. All bulk areas of anode, cathode and current collectors were not included in the simulations while their edges facing the electrolyte were used for boundary conditions. Initial condition (IC) and each boundary condition (BC) are shown in Table 6.4. Scales of X- and Y-axes are different. 211
Figure 6.10. Contour plots of electrolyte concentrations at 2D cross-section geometries of the baseline cell at 0.1 sec. (a) and 10 sec. (b) and aligned cell at 0.1 sec. (c) and 10 sec. (c). 214
Figure 6.11. Resistance ratio of anode and cathode to total resistance from unsteady-state simulations and experiments near 3.8 V (Figure 6a and 6b). 215
Figure 7.1. TEM sample preparation for SEI analysis. 224
Figure 7.2. SEM images of TEM grids with graphite particles having SEI on them and EDS analysis results from a graphite particle. 225

INTRODUCTION

Background

Understanding the solid electrolyte interphase (SEI)

Formation cycling is a process of the first few successive and slow charge-discharge cycles of a cell after electrolyte wetting to electrodes, which forms SEI layers on the electrodes. The anode (or cathode) SEI layer is composed of precipitates from reduced (or oxidized) decomposition of solvents, salts, lithium ions, and impurities in the electrolyte due to their instability at the electrode potential operating window.[1-2] Some of the unstable voltage windows and electrolyte decomposition reactions are shown in Figures 0.1 and 0.2, respectively. Reduction and oxidation potentials of common solvents and electrolytes are also listed in Table 0.1. SEI forms mostly during the first charge, but the formation continues slowly after first cycle until the SEI layer is fully developed. A proper SEI layer is expected to have negligible electrical conductivity and high electrolyte diffusion resistance while having high lithium ion selectivity and permeability.

Once it is properly formed, further decomposition reactions with Li ions, salts, and solvents are prevented since electrons cannot transfer through the layer. However, the SEI layer gradually thickens during repeated charge-discharge cycles because, in reality, the layer is not a perfect barrier for electrolyte diffusion and electron transfer, although the layer thickness growth after a few charge-discharge cycles is not as significant as the amount during the first cycle. The gradual thickening of the layer further consumes Li ions, solvents, and salts and increases cell resistance.[2-3] This continuous SEI layer growth during the formation cycling process lowers cell capacity and Coulombic efficiency.

Despite the importance of understanding the formation, composition, morphology, and long-term structural and chemical evolution of the SEI layer, these properties are not yet fully understood because of analysis and measurement difficulties. In fact, the SEI layer formation mechanism is much less understood than the resultant chemical and physical properties themselves. The current understanding of the SEI formation process is briefly shown in Figure 0.3. The SEI is extremely thin, between a few tens and hundreds of angstroms, and sensitive to moisture in the air that may convert SEI components into different forms before or during the analysis.[4-7] Because of the environmental sensitivity, SEI analysis requires inert and well-controlled conditions.

Table 0.1. Reduction and oxidation potential vs. Li/Li+ of solvents and electrolytes, GC and GR are glassy carbon and graphite, respectively

Solvent/Additive/Salt	Reduction (oxidation) potential / V (vs. Li^+/Li)	LUMO / eV
EC	0.9 on GC, 0.8 on GR	0.97-1.175
PC	1.0 on GC, 0.78 on GR	1.02-1.235
DMC	1.35 on GC	1.054
DEC	1.32 on GC	1.21-1.288
VC	1.4 on GC	
FEC	1.63 (7.16) from DFT	
1M $LiPF_6$/EC:DMC (2:1)	(5.1) on $LiMn_2O_4$	
1M $LiPF_6$/EC:DEC(3:7)	(4.3) on Li-rich NMC	

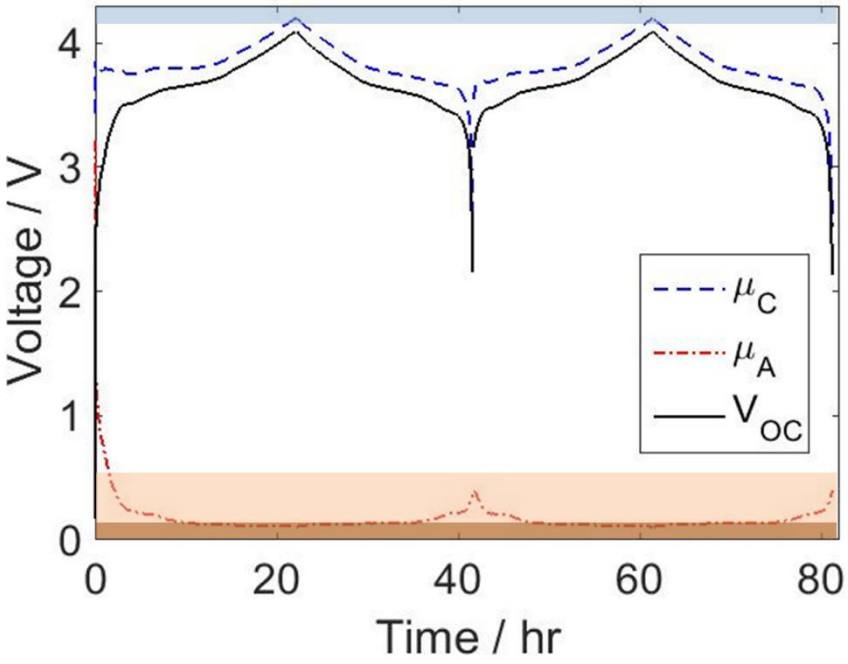


Figure 0.1. Voltage profiles of cathode (μC), anode (μA), and cell (VOC) from a three-electrode cell during charge and discharge, area in orange and blue colors indicates unstable voltage window.

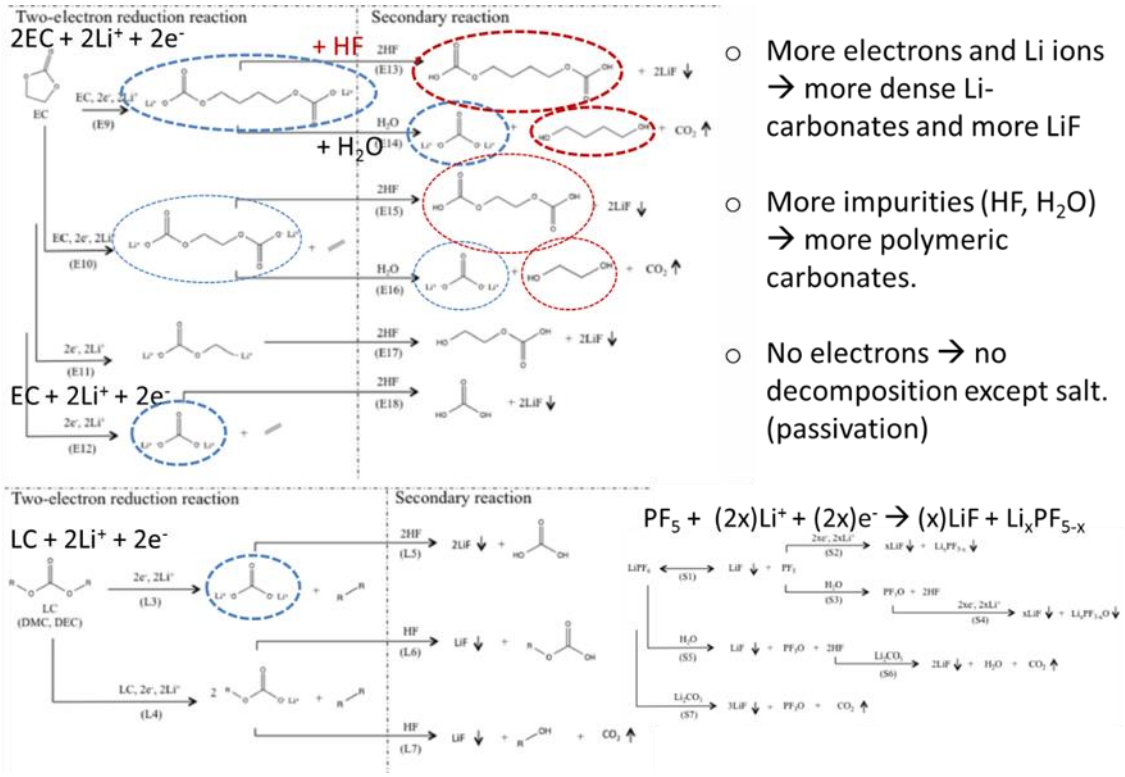


Figure 0.2. Decomposition reactions of ethylene carbonate (EC), linear carbonate, and salt. (An et al, Carbon 105 (2016) 52-76).

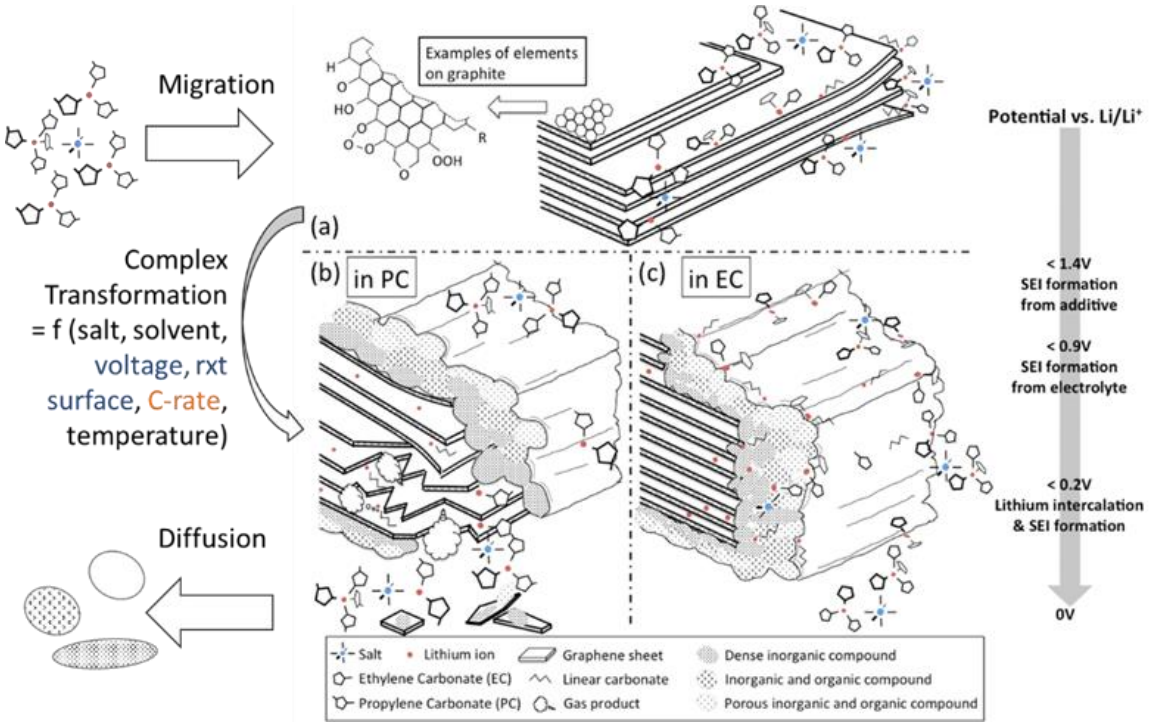


Figure 0.3. Schematic of the anode SEI formation process showing (a) graphene layers surrounded by electrolyte salts and solvents above 1.4V vs. Li/Li+, (b) propylene-carbonate (PC) intercalation with lithium ions into graphene layers resulting exfoliations below 0.9V vs. Li/Li+ and (c) stable SEI formation in ethylene-carbonate (EC)-based electrolyte below 0.9V vs. Li/Li+; plane side with thinner SEI and edge side with thicker SEI. (An et al, Carbon 105 (2016) 52-76).

Functional properties for an ideal SEI layer would be high electrical resistance and high lithium selectivity and permeability. Physical characteristics would be a thickness close to a few Å, high strength, tolerance against expansion and contraction stresses, insolubility in the electrolyte, and stability at a wide range of operating temperatures and potentials. Actual SEI layers seem to not yet have enough of these properties as evidenced by the continued growth over repeated charge-discharge cycles. This growth is closely related to lithium loss from both the electrolyte salt and cathode lithium inventory, as well as lithium diffusion resistance at the liquid interfacial zone adjacent to the SEI layer and within the SEI itself. The lithium consumption and diffusion resistance cause an increase not only in the overall cell resistance but also in anode potential. The increase in the anode potential is attributed to a low number of lithium charges in the electrode after consumption at the SEI. This increased anode potential also induces a similar increase in cathode potential to keep a charge cutoff potential of the cell. When the cathode potential increases and reaches a certain point, the cathode crystal structure rearranges and distorts due to oxygen loss and transition metal shifting. The electrolyte also becomes less stable at higher cathode potentials, which leads to solvent oxidation on the cathode surface (for example $LiPF_6$ in EC:DMC is oxidized around 4.5V vs Li/Li^+ during charging). This gradual SEI growth on the anode negatively affects cathode potential and stability. Therefore, forming a stable and robust SEI layer on the anode carbon/graphite is essential for long LIB lifetime and high capacity retention.

Cost of SEI formation

During the manufacturing process for lithium ion batteries, wetting electrodes with electrolyte and forming SEI layers require 1.5-3 weeks for the entire process.[8-9] Wood et al. at ORNL reported costs for a general wetting and formation process (Table 0.2), which showed the SEI formation can contribute up to $32-33/kWh of usable energy for the battery pack cost (out of a total cost of ~$500/kWh).[9] SEI formation generally takes many days because scan rates are slow, from C/20 down to C/5. After the first charge-discharge cycle, formation cycles generally repeat at different scan rates and/or different temperature to build quality SEI layers. The longer the times and greater the number of charge-discharge cycles, the more expensive the process becomes, which also either lowers cell production rate or increases capital expense.

Before the formation cycles, electrodes need to be fully wetted with electrolyte. The initial wetting process is slow because the electrolyte has to permeate into all pores of the separator and electrodes in a near fully assembled cell. Evacuating gases out of the pores under high vacuum can accelerate infusion of the electrolyte and enable uniform distribution, although it requires more equipment and processing expense.

Table 0.2. LIB pack cost contributions for baseline electrode processing case (cost per kWh-usable energy assumes a 70% depth of discharge for cycling. (D. L. Wood et al., Journal of Power Sources, 275 (2015) 234-242).

Cost component	Cost per kWh-total ($/kWh)	Cost per kWh-usable ($/kWh)
Composite electrode materials	101.7	145.3
Current collectors & separator	80.2	114.6
Electrode processing	36.1	51.6
Electrolyte	24.6	35.1
Wetting and formation cycling	22.6	32.3
Pouch and tab materials	6.7	9.6
Module hardware, power electronics & pack cooling	46.0	65.7
Labor (electrode processing and cell/pack construction)	34.0	48.6
Total	351.9	502.8

Even under an evacuated condition, the smallest pores of the electrodes and separator may not fully wet unless they have a higher surface energy than the electrolyte. This situation is due to the competition between hydrodynamic forces at low pressure and non-wetting surface forces (the smaller the pore size, the lower the vacuum pressure needed to make a non-wetting liquid enter a pore). To avoid costly and time-consuming vacuum pumping, both electrodes (and the separator) should have high wettability of the electrolyte for full active material utilization during the formation cycling process.

Reducing the time for SEI formation would provide higher production rates without needing extra space, equipment, and energy, eventually reducing battery pack and plant costs. Simply increasing the charging rate for faster SEI formation results in incomplete, non-uniform, or compositionally undesirable SEI layers,[10] thereby lowering cell efficiency, durability and safety. In order to reduce formation time without losing cell performance, it is pertinent to understand the SEI formation process, composition, morphology, structure, and their combined effects on both short-term (irreversible capacity loss) and long-term performance (capacity fade).

Research problem

The anode SEI layer is formed from lithium of the cathode, which is the total amount of lithium available for building the SEI and initial charging of the cell, and there is a delicate balance between the ideal surface area the anode should have and the energy and power density of an LIB. The entirety of the anode surface must have the SEI layer present to prevent further undesired decomposition of the electrolyte. The amount of Li ion loss from cathode directly affects the first-cycle irreversible capacity (energy density), while losing Li ions from electrolyte lowers liquid-phase mass transport and decreases power density.[2-3] During the first cycle, 10% of original capacity is generally consumed in irreversible SEI formation.[11] Therefore, the total surface of the anode should be minimized from an energy density or cell cost standpoint. However, the minimization comes with a performance tradeoff – low anode surface area means lower power density (capacity at high C rates) with solid-state diffusion limitations. In contrast, high anode surface area is beneficial to power density, but much greater lithium inventory is consumed when passivating the surface to form the SEI layer, thereby decreasing energy density.

There is also a secondary connection of the SEI layer to LIB safety, and it comes into play once the anode is fully passivated. To avoid lithium plating or dendrite formation at the anode during charging over the life of the cell, capacity is often kept about 10% more than that at cathode[11] (N/P capacity ratio of 1.1 where “N” is the negative electrode, or anode during cell discharging, and “P” is the positive

electrode, or cathode during cell discharging) to prevent internal electrical shorts. Therefore, this extra anode material must also undergo SEI layer passivation adding to the cell cost and detracting the total cell energy. Optimizing the N/P ratio is important to minimize initial lithium inventory loss and decrease initial irreversible capacity. Besides, for long-term capacity retention and Coulombic efficiency, optimizing only the capacity ratio would be insufficient because SEI continuously grows and consumes electrolytes and lithium ions when it is not well formed.[12-13]

It is worth mentioning briefly that a “SEI-like” layer forms on cathodes, as well, by oxidation reactions of electrolytes at high potentials[14-16]. Its impact on cell performance is also significant. Recent studies involving lithium-manganese-rich (LMR) NMC materials ($Li_{1+x}Ni_yMn_zCo_{1-x-y-z}O_2$) for electrical vehicle applications show high capacities when operated at high voltage.[17-23] This cathode material has an operating window of 2~4.8V vs Li/Li^+ and capacities of 200~250 mAh/g [18], but only 150 mAh/g within the typical operating voltage window (3~4.2V).[9] As the voltage approaches 4.7V vs Li/Li^+ or even below, decomposition takes place on cathode surface during charge or storage by oxidation of electrolyte solvent organic carbonates (ethylene carbonate, dimethyl carbonate ethyl methyl carbonate, propylene carbonate, etc.).[1, 14, 24-25] Since these carbonates have oxidation and reduction potentials around 4.7V and 1V vs Li/Li^+, respectively[1, 3], they are decomposed by electro-reduction at the anode below 1V and by electro-oxidation at the cathode above 4.7V during charging or storage. The oxidation potentials of these carbonates are further reduced at elevated temperature where batteries in vehicles or portable devices experience locally, below 4V at 40^{o}C and 3.8V at 60^{o}C.[14, 25-30] Ethers and esters are not stable typically above 4V.[7, 31] Other species in the electrolyte, such as lithium compounds that are partially reduced at the anode and diffuse to the cathode, have even lower oxidation potentials. Wursig et al. reported SEI formed at 4.3V vs Li/Li+ and even at 25^{o}C on various cathode materials.[32] Hence, at high potentials, cathodes suffer from increases in resistance of SEI-like passivation layers as well as from loss or migration of active materials such as Mn and Co. When charge and discharge cycles and storage time are extended, the resistance at the cathode increases more than that of the anode.[33]

The lithium consumption and diffusion resistance cause an increase not only in the overall cell resistance but also in anode potential, inducing an increase in cathode potential to keep a charge cutoff potential of a cell. When the cathode potential increases and reaches a certain point, the cathode crystal structure rearranges and distorts due to oxygen loss and transition metal shifting.[17-20] The electrolyte also becomes less stable at higher cathode potentials, which leads to solvent oxidation on the cathode surface (for example $LiPF_6$ in EC:DMC is oxidized around 4.5V vs Li/Li+ during charging).[34] This gradual SEI growth on the anode negatively affects cathode potential and stability. Therefore, forming an

ideal SEI layer on the anode carbon/graphite is essential for long LIB lifetime and high capacity retention.

SEI formation generally takes many days because scan rates are slow, ~±C/20 down to ~±C/5,[9, 35] to form a denser SEI structure rather than a highly porous one. After the first charge-discharge cycle, formation cycles generally repeat at different scan rates and/or different temperature to build quality SEI layers. The longer the times and greater the number of charge-discharge cycles, the more expensive the process becomes, which also either lowers cell production rate or increases capital expense (i.e. more cycling stations required). If the electrical energy is not “recycled” (i.e. using the energy of one cell after charging it from the primary electricity source to charge another adjacent cell), the cost further increases.

Research topics

The chemical composition, morphology, and stability depend on several factors such as graphite surface properties, electrochemical conditions, and electrolytes. In this study, current understandings of SEI were reviewed to improve SEI formation. Then, three factors (surface properties, electrochemical condition, and electrolyte concentration) were studied. First, as a surface property improvement, anodes were treated under ultraviolet (UV) light to change graphite surface properties and to improve SEI. Second, as an electrochemical condition control, a new formation protocol having potential/C-rate controls in a high voltage region was proposed to shorten SEI formation time and to improve the SEI. Third, electrolyte volume was controlled to study the effects of electrolyte concentration on the SEI and optimize (minimize) the volume. All three controlled factors dealt with in this study showed improvement in battery cycle life because of enhanced SEI quality. The key factors to SEI formation and their relationships to work done in this study are shown in Figure 0.4 as a brief snapshot. Each work is elaborated in following chapters.

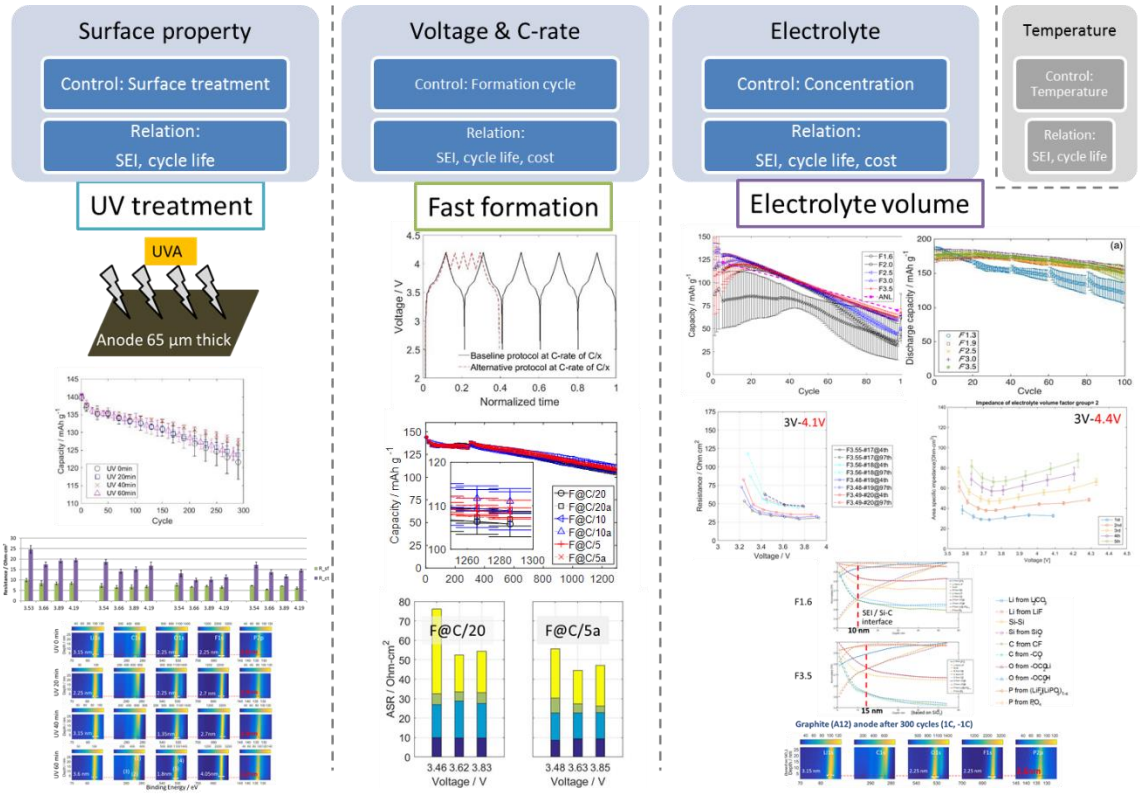


Figure 0.4. Key factors affecting SEI formation (surface property, voltage/C-rate, and electrolyte) and relation to work done (fast formation, UV treatment, and electrolyte volume).

References

1. Goodenough, J. B.; Kim, Y., Challenges for Rechargeable Li Batteries. *Chemistry of Materials* **2010,** *22*, 587–603.
2. Goodenough, J. B.; Park, K.-S., The Li-ion rechargeable battery: a perspective. *Journal of the American Chemical Society* **2013,** *135*, 1167-76.
3. Xu, K., Nonaqueous Liquid Electrolytes for Lithium-Based Rechargeable Batteries. *Chem. Rev.* **2004,** *104*, 4303−4417.
4. Williard, N.; Sood, B.; Osterman, M.; Pecht, M., Disassembly methodology for conducting failure analysis on lithium–ion batteries. *Journal of Materials Science: Materials in Electronics* **2011,** *22*, 1616-1630.
5. Orsini, F.; Du Pasquier, A.; Beaudoin, B.; Tarascon, J. M.; Trentin, M.; Langenhuizen, N.; De Beer, E.; Notten, P., In situ Scanning Electron Microscopy (SEM) observation of interfaces within plastic lithium batteries. *Journal of Power Sources* **1998,** *76*, 19-29.
6. Chusid, O. Y.; Ein Ely, Y.; Aurbach, D.; Babai, M.; Carmeli, Y., Electrochemical and spectroscopic studies of carbon electrodes in lithium battery electrolyte systems. *Journal of Power Sources* **1993,** *43-44*, 47-64.
7. Aurbach, D.; Gojxjeb, H., The electrochemical behavior of selected polar aprotic systems. *Electrochemica Acta* **1989,** *34*, 141-156.
8. Daniel, C., Materials and Processing for Lithium-Ion Batteries. *JOM* **2008,** *60*, 43-48.
9. Wood, D. L.; Li, J.; Daniel, C., Prospects for reducing the processing cost of lithium ion batteries. *Journal of Power Sources* **2015,** *275*, 234-242.
10. Bhattacharya, S.; Alpas, A. T., Micromechanisms of solid electrolyte interphase formation on electrochemically cycled graphite electrodes in lithium-ion cells. *CARBON* **2012,** *50*, 5359–5371.
11. Patil, A.; Patil, V.; Shin, D. W.; Choi, J.-W.; Paik, D.-S.; Yoon, S.-J., Issue and challenges facing rechargeable thin film lithium batteries. *Materials Research Bulletin* **2008,** *43*, 1913–1942.
12. Yazami, R.; Reynier, Y. F., Mechanism of self-discharge in graphite–lithium anode. *Electrochimica Acta* **2002,** *47*, 1217–1223.
13. Yazami, R., Surface chemistry and lithium storage capability of the graphite±lithium electrode. *Electrochimica Acta* **1999,** *45*, 87-97.
14. Wohlfahrt-Mehrens, M.; Vogler, C.; Garche, J., Aging mechanisms of lithium cathode materials. *Journal of Power Sources* **2004,** *127*, 58-64.
15. Vetter, J.; Novák, P.; Wagner, M. R.; Veit, C.; Möller, K. C.; Besenhard, J. O.; Winter, M.; Wohlfahrt-Mehrens, M.; Vogler, C.; Hammouche, A., Ageing mechanisms in lithium-ion batteries. *J. Power Sources* **2005,** *147*, 269-281.
16. Eriksson, T.; Andersson, A. M.; Bishop, A. G.; Gejke, C.; Gustafsson, T. r.; Thomas, J. O., Surface Analysis of LiMn[sub 2]O[sub 4] Electrodes in Carbonate-Based Electrolytes. *Journal of The Electrochemical Society* **2002,** *149*, A69.
17. Mohanty, D.; Huq, A.; Payzant, E. A.; Sefat, A. S.; Li, J.; Abraham, D. P.; Wood, D. L.; Daniel, C., Neutron Diffraction and Magnetic Susceptibility Studies

on a High-Voltage Li1.2Mn0.55Ni0.15Co0.10O2Lithium Ion Battery Cathode: Insight into the Crystal Structure. *Chemistry of Materials* **2013,** *25*, 4064-4070.
18. Mohanty, D.; Kalnaus, S.; Meisner, R. A.; Rhodes, K. J.; Li, J.; Payzant, E. A.; Wood, D. L.; Daniel, C., Structural transformation of a lithium-rich Li1.2Co0.1Mn0.55Ni0.15O2 cathode during high voltage cycling resolved by in situ X-ray diffraction. *Journal of Power Sources* **2013,** *229*, 239-248.
19. Mohanty, D.; Sefat, A. S.; Kalnaus, S.; Li, J.; Meisner, R. A.; Payzant, E. A.; Abraham, D. P.; Wood, D. L.; Daniel, C., Investigating phase transformation in the Li1.2Co0.1Mn0.55Ni0.15O2 lithium-ion battery cathode during high-voltage hold (4.5 V) via magnetic, X-ray diffraction and electron microscopy studies. *Journal of Materials Chemistry A* **2013,** *1*, 6249.
20. Mohanty, D.; Sefat, A. S.; Li, J.; Meisner, R. A.; Rondinone, A. J.; Payzant, E. A.; Abraham, D. P.; Wood, D. L. r.; Daniel, C., Correlating cation ordering and voltage fade in a lithium-manganese-rich lithium-ion battery cathode oxide: a joint magnetic susceptibility and TEM study. *Physical chemistry chemical physics : PCCP* **2013,** *15*, 19496-509.
21. Lu, Z. H.; MacNeil, D. D.; Dahn, J. R., *Electrochemical and Solid-State Letters* **2001,** *4*.
22. Thackeray, M. M.; Johnson, C. S.; Vaughey, J. T.; Li, N.; Hackney, S. A., *Journal of Materials Chemistry* **2006,** *15*.
23. Yabuuchi, N.; Yoshii, K.; Myung, S.-T.; Nakai, I.; Komaba, S., *Journal of American Chemical Society* **2011,** *133*.
24. Krueger, S.; Kloepsch, R.; Li, J.; Nowak, S.; Passerini, S.; Winter, M., How Do Reactions at the Anode/Electrolyte Interface Determine the Cathode Performance in Lithium-Ion Batteries? *Journal of The Electrochemical Society* **2013,** *160*, A542-A548.
25. Amine, K.; Chen, C. H.; Liu, J.; Hammond, M.; Jansen, A.; Dees, D.; Bloom, I.; Vissers, D.; Henriksen, G., Factors responsible for impedance rise in high power lithium ion batteries. *Journal of Power Sources* **2001,** *97-98*, 684-687.
26. Sarre, G.; Blanchard, P.; Broussely, M., Aging of lithium-ion batteries. *Journal of Power Sources* **2004,** *127*, 65-71.
27. Broussely, M.; Biensan, P.; Bonhomme, F.; Blanchard, P.; Herreyre, S.; Nechev, K.; Staniewicz, R. J., Main aging mechanisms in Li ion batteries. *Journal of Power Sources* **2005,** *146*, 90-96.
28. Kostecki, R.; McLarnon, F., Degradation of LiNi[sub 0.8]Co[sub 0.2]O[sub 2] Cathode Surfaces in High-Power Lithium-Ion Batteries. *Electrochemical and Solid-State Letters* **2002,** *5*, A164.
29. Shikano, M.; Kobayashi, H.; Koike, S.; Sakaebe, H.; Ikenaga, E.; Kobayashi, K.; Tatsumi, K., Investigation of positive electrodes after cycle testing of high-power Li-ion battery cells II. *Journal of Power Sources* **2007,** *174*, 795-799.
30. Rahman, M. K.; Saito, Y., Investigation of positive electrodes after cycle testing of high-power Li-ion battery cells. *Journal of Power Sources* **2007,** *174*, 889-894.

31. Etacheri, V.; Marom, R.; Elazari, R.; Salitra, G.; Aurbach, D., Challenges in the development of advanced Li-ion batteries: a review. *Energy Environ. Sci.* **2011,** *4*, 3243–3262
32. Wursig, A.; Buqa, H.; Holzapfel, M.; Krumeich, F.; Novák, P., Film Formation at Positive Electrodes in Lithium-Ion Batteries. *Electrochemical and Solid-State Letters* **2005,** *8*, A34-A37
33. Song, J. Y.; Lee, H. H.; Wang, Y. Y.; Wan, C. C., Two- and three-electrode impedance spectroscopy of lithium-ion batteries. *Journal of Power Sources* **2002,** *111*, 255–267.
34. Scrosati, B.; Garche, J. r., Lithium batteries: Status, prospects and future. *Journal of Power Sources* **2010,** *195*, 2419–2430.
35. Wood, D. L.; Li, J.; Mohanty, D.; Daniel, C.; Armstrong, B.; Dinwiddie, R.; Safa-Sefat, A.; Wang, H.; Trejo, R.; Gallego, N.; Contescu, C.; Howe, J.; Meisner, R.; Kiggans, J.; Brown, B., Advanced Materials Processing and Novel Characterization Methods for Low-Cost, High Energy-Density Lithium-Ion Batteries. *Advanced Automotive Battery Conference* **2013**.

CHAPTER I
A REVIEW: THE STATE OF UNDERSTANDING OF THE LITHIUM-ION-BATTERY GRAPHITE SOLID ELECTROLYTE INTERPHASE (SEI) AND ITS RELATIONSHIP TO FORMATION CYCLING

A version of this chapter was originally published by Seong Jin An, Jianlin Li, Claus Daniel, Debasish Mohanty, Shrikant Nagpure, and David L. Wood III:

Seong Jin An, Jianlin Li, Claus Daniel, Debasish Mohanty, Shrikant Nagpure, and David L. Wood III "The state of understanding of the lithium-ion-battery graphite solid electrolyte interphase (SEI) and its relationship to formation cycling" *Carbon* 105 (2016): 52-76.

The initial draft of this article was created mainly by Seong Jin An and partially by Shrikant Nagpure. Most contests were improved and finalized by Seong Jin An, Jianlin Li, and David L. Wood III. All other co-authors provided comments on contents.

Abstract

An in-depth historical and current review is presented on the science of lithium-ion battery (LIB) solid electrolyte interphase (SEI) formation on the graphite anode, including structure, morphology, composition, electrochemistry, and formation mechanism. During initial LIB operation, the SEI layer forms on the graphite surfaces, the most common anode material. The SEI is essential to the long-term performance of LIBs, and it also has an impact on its initial capacity loss, self-discharge characteristics, rate capability, and safety. While the presence of the anode SEI is vital, it is difficult to control its formation and growth, as they depend on several factors. These factors include the type of graphite, electrolyte composition, electrochemical conditions, and temperature. Thus, SEI formation and electrochemical stability over long-term operation should be a primary topic of future investigation in the LIB development. This article covers the progression of knowledge regarding the SEI, from its discovery in 1979 to the current state of understanding, and covers differences in the chemical and structural makeup when cell materials and components are varied. It also discusses the relationship of the SEI layer to the LIB formation step, involving both electrolyte wetting and subsequent slow charge-discharge cycles to grow the SEI.

Introduction

Much effort has been put into lithium-ion battery (LIB) development for electric vehicles (EVs), plug-in hybrid electrical vehicles (PHEVs), and other electrical system applications.[1-11] Some of the key studies have involved reducing cost, increasing capacity retention, and improving efficiency. [2, 4-7, 12-16] During the operation of LIBs, a solid electrolyte interphase (SEI) layer (also called "solid electrolyte interface" in some literature) forms on the graphite surface, the most commonly used anode material, due to side reactions with the electrolyte solvent and salt. It is accepted that the SEI layer is essential to the performance of LIBs, and it has an impact on its initial capacity loss, self-discharge characteristics,

cycle life, rate capability and safety. While the presence of the anode SEI layer is vital, it is difficult to control its formation and growth, as the chemical composition, morphology, and stability depend on several factors. These factors include the type of graphite, graphite morphology, electrolyte composition, electrochemical conditions, and cell temperature. Thus, SEI layer formation and electrochemical stability over long-term operation should be a primary topic of investigation in further development of LIB technology. This article reviews the state of knowledge on the formation process of the graphite/carbon SEI layer, its chemical composition, morphology, and associated reactions with the liquid electrolyte phase, and will address several important questions:

1.) Why is it important to understand the SEI layer composition and morphology, and how does it impact LIB performance? (Sections 2-3)
2.) What is the solid/liquid surface chemistry behavior at the nanoscale of the SEI layer? (Sections 3-4)
3.) What methods have been used to form the SEI layer during initial charging and discharging? (Section 5)
4.) What methods have been used to characterize the SEI layer properties such as composition, thickness, and morphology? (Section 6)
5.) What are the effects of different types of graphites and carbons on SEI layer properties? (Section 7)
6.) What are the electrolyte, binder, and conductive additive effects on SEI layer properties? (Sections 8)
7.) How is the SEI layer formation tied to the electrolyte wetting of the electrode (during cell manufacturing) and formation protocol, capacity fade, and cell lifetime? (Section 9)
8.) Why is it important to reduce the SEI formation protocol time during cell manufacturing? (Sections 9-10)
9.) How is the most recent understanding of the anode SEI layer impacting cell design and SEI durability? (Section 11)

This paper is a comprehensive review of the science of the LIB anode SEI layer and its relationship to electrolyte wetting, formation cycling, and cell lifetime. It spans from the basic science of the SEI formation interfacial physics and reaction mechanisms to the applied science of reducing formation cycle time and increasing LIB lifetime. The time period covered is from the discovery of lithium-ion intercalation in graphite (1979) up to the present day, and it offers insights into the SEI formation mechanism, chemical and morphological properties of the SEI, and relationship to formation cycling and cell lifetime. This paper will appeal to the entire LIB research community and the broader energy storage community as a whole. Given that it deals with an intricate combination of surface chemistry, electrochemistry, and reaction mechanisms, it will also appeal to chemists and chemical scientists in other fields.

Understanding nature of solid electrolyte interphase (SEI)

The anode SEI layer is formed from the so-called “lithium inventory” of the cathode and electrolyte salt, which is the total amount of lithium available for building the SEI and initial charging of the cell, and there is a delicate balance between the ideal surface area the anode should have and the energy and power density of an LIB. The entirety of the anode surface must have the SEI layer present to prevent further undesired decomposition of the electrolyte, which consumes Li ions. The amount of Li ion loss from the cathode directly affects the first-cycle irreversible capacity (energy density), while losing Li ions from the electrolyte lowers liquid-phase mass transport and increases electrolyte resistance thereby decreasing power density.[1, 17] During the first full cycle, 10% of the original capacity is generally consumed in irreversible SEI formation.[18] Therefore, the total surface of the anode should be minimized from an energy density or cell cost standpoint. However, the minimization comes with a performance tradeoff – low anode surface area means lower power density (capacity at high C rates) with solid-state diffusion limitations. In contrast, high anode surface area is beneficial to power density, but much greater lithium inventory is consumed when passivating the surface to form the SEI layer, thereby decreasing energy density. Section 7 includes an overview and understanding of carbon/graphite properties and related SEI formation.

There is also a secondary connection of the SEI layer to LIB safety, and it comes into play once the anode is fully passivated. To avoid lithium plating or dendrite formation at the anode during charging over the life of the cell, capacity is often kept about 10% more than that at cathode[18] (N/P ratio of 1.1 where “N” is the negative electrode, or anode during cell discharging, and “P” is the positive electrode, or cathode during cell discharging) to prevent internal electrical shorts. Therefore, this extra anode material must also undergo SEI layer passivation adding to the cell cost and diminishing the total cell energy. Optimizing the N/P ratio is important for minimizing initial lithium inventory loss and decreasing initial irreversible capacity. For long-term capacity retention and Coulombic efficiency, optimizing only the capacity ratio would be insufficient because SEI continuously grows and consumes electrolytes and lithium ions when it is not well formed.[19-20]

Better understanding of the state-of-the-art graphite SEI layer composition and morphology is an important step towards growing improved SEI layers that prevent continuous decomposition of electrolyte on the graphite surfaces. The anode SEI layer is composed of precipitates from reduced decomposition of solvents, salts, lithium ions, and impurities in the electrolyte due to their instability at the anode potential operating window.[1, 21] It forms mostly during the first charge, but the formation continues slowly and gradually after first cycle until the SEI layer is fully developed, adding to the complexity of modern LIB formation protocols. An optimized SEI layer is expected to have negligible electrical

conductivity and high electrolyte diffusion resistance while having high lithium ion selectivity and permeability. Once it is properly formed, further decomposition reactions with salts and solvents are prevented since electrons cannot transfer to or through the layer (the increased electronic resistance increases the potential on the graphite surface and shifts the surface potential to within the stability window of the electrolyte). However, in reality, the SEI layer gradually thickens during repeated charge-discharge cycles due to electron exposure to electrolyte or electrolyte diffusion to the graphite surface, although the layer thickness growth after a few charge-discharge cycles is not nearly as great as the amount during the first cycle. The gradual thickening of the layer further consumes Li ions, solvents, and salts and increases cell resistance. This continuous SEI layer growth during the formation cycling process lowers cell capacity and Coulombic efficiency.

It is worth mentioning briefly that a “SEI-like” layer forms on cathodes, as well, by oxidation reactions of electrolytes at high potentials[22-23], but its impact on cell performance is generally less. Recent studies involving lithium-manganese-rich (LMR) NMC materials ($Li_{1+x}Ni_yMn_zCo_{1-x-y-z}O_2$) for EV applications, show high capacities when operated at high voltage.[3, 14, 24-28] This cathode material has an operating window of 2~4.8V vs Li/Li^+ and capacities of 200~250 mAh/g [24], but only 150 mAh/g within the typical operating voltage window (3~4.2V).[15] As the voltage approaches 4.7V vs Li/Li^+ (or even less), decomposition takes place on cathode surface during charge or storage by oxidation of electrolyte solvent organic carbonates (ethylene carbonate, dimethyl carbonate ethyl methyl carbonate, propylene carbonate, etc.).[21-22, 29-30] Since these carbonates have oxidation (highest occupied molecular orbital (HOMO)) and reduction potentials (lowest unoccupied molecular orbital (LUMO)) around 4.7V and 1V vs Li/Li^+, respectively[21], they are decomposed by electro-reduction at the anode below 1V and by electro-oxidation at the cathode above 4.7V during charging or storage. The oxidation potentials of these carbonates are further reduced at elevated temperature (LIBs in vehicles or portable devices experience locally increased temperatures) to 4V at 40^{o}C and 3.8V at 60^{o}C.[22, 30-35] Ethers and esters are not typically stable above 4V.[36-37] Other species in the electrolyte, such as lithium compounds that are partially reduced at the anode and diffuse to the cathode, have even lower oxidation potentials. Wursig et al. reported SEI formation at 4.3V vs Li/Li^+ and even at 25^{o}C on various cathode materials.[38] Hence, at high potentials, cathodes suffer from increases in resistance from SEI-like passivation layers as well as from loss or migration of active materials such as Mn and Co. When initial charge-discharge cycles and storage time are extended, the resistance at the cathode increases even more than that of the anode.[39]

Despite the importance of understanding the formation, composition, morphology, and long-term structural and chemical evolution of the anode SEI layer, these topics are not yet fully understood because of analysis and

measurement difficulties. In fact, the SEI layer formation mechanism is much less understood than the resultant chemical and physical properties themselves. The SEI is quite thin, a few hundreds of angstroms, and sensitive to moisture and oxygen in the air that may convert SEI components into different forms before or during analysis.[40-42] Because of the environmental sensitivity, SEI analysis requires inert and well-controlled conditions.

Functional properties for an ideal SEI layer are high electrical resistance and high lithium selectivity and permeability. Physical ones are a thickness close to a few Å, high strength, tolerance to expansion and contraction stresses (the SEI layer must accommodate expanding and contracting sub-surfaces during charging and discharging, respectively), insolubility in the electrolyte, and stability at a wide range of operating temperatures and potentials. Actual SEI layers seem to not yet have enough of these properties because it has been found that they keep growing over repeated charge-discharge cycles. This growth is closely related to lithium loss from both the electrolyte salt and cathode lithium inventory, as well as lithium diffusion resistance at the liquid interfacial zone adjacent to the SEI layer and within the SEI itself. The lithium consumption and diffusion resistance cause an increase not only in the overall cell resistance but also in anode potential. The increase in the anode potential is attributed to a lower number of Li ions in the electrode after consumption at the SEI. This increased anode potential also induces a similar increase in cathode potential to maintain a charge cutoff potential. When the cathode potential increases and reaches a certain point, the cathode crystal structure rearranges and distorts due to oxygen loss and transition metal shifting.[3, 14, 24-25] The electrolyte also becomes less stable at higher cathode potentials, which leads to solvent oxidation on the cathode surface (for example $LiPF_6$ in ethylene carbonate (EC): dimethyl carbonate (DMC)) is oxidized around 4.5V vs Li/Li^+ during charging).[43-47] This gradual SEI growth on the anode negatively affects cathode potential and stability. Therefore, forming a robust and stable SEI layer on the anode carbon/graphite is essential for long LIB lifetime and high capacity retention.

SEI formation generally takes days because scan rates are slow, ~±C/5 down to ~±C/20,[13, 15] to form a denser SEI structure rather than a highly porous one. After the first charge-discharge cycle, formation cycles generally repeat at different scan rates and/or different temperatures to build quality SEI layers. The longer the times and greater the number of charge-discharge cycles, the more expensive the process becomes, which also either lowers cell production rate or increases capital expense (i.e. more cycling stations required). If the electrical energy is not “recycled” (i.e. using the energy of one cell after charging it from the primary electricity source to charge another adjacent cell), the cost further increases. Reducing the time for SEI formation would provide higher production rates without needing extra space, equipment, and energy, eventually reducing battery pack and plant costs.

Energetics of anode SEI formation

In LIBs an aprotic salt solution with low-molecular-weight organic solvents are the most widely used electrolytes. These electrolytes undergo decomposition at the graphite anode, and the SEI layer is formed from these decomposition products, which then dictates initial performance of the cell and long-term capacity fade characteristics. Therefore, the question is can the electrolyte decomposition be minimized or controlled to provide predictable performance of the cell.

Figure 1.1 shows the relative electron energies of the anode, electrolyte, and cathode of a thermodynamically stable redox pair in a LIB. In the figure, μ_A and μ_C are the electrochemical potentials of the anode and cathode respectively. The stability window of the electrolyte is the difference between the energy of the LUMO and HOMO. This window is shown as E_g. If μ_A is above the LUMO energy, then it will reduce the electrolyte, and, likewise, if μ_C is below the HOMO energy, it will oxidize the electrolyte. The energy separation between the anode and cathode needs to be as high as possible to increase the energy density of the redox pair. The organic electrolytes used in LIBs have oxidation potentials around 4.7 V vs. Li^+/Li and reduction potentials close to 1.0 V vs. Li^+/Li. The intercalation potential of Li into graphite is between 0 V and 0.25 V vs. Li^+/Li, which is below the reduction potential of the electrolyte. Thus, the potential of the graphite electrodes falls below the stability window of the electrolyte during charging, and it decomposes at the graphite surface forming the SEI.

SEI features, morphology, and chemical composition

If all of the decomposition reaction potentials for the SEI formation are more positive than the anode Li ion intercalation potential, the SEI would form more completely under fast kinetics before the onset of the intercalation reaction. Once it is well formed, the SEI should have high Li-ion conductivity and negligible electronic conductivity. The electronically insulating property of the SEI prevents further reduction of the electrolyte on the graphite surface, while the ion conductive nature allows permeation of lithium ions to the graphite surface and provides pathways for the desired ion intercalation. To avoid cracking of SEI layers due to stress from a volume change of graphite during intercalation and de-intercalation and to avoid further passivation reactions, the molecular force between the SEI layer and graphite surface should be strong. Physically, the SEI layer should be strong or flexible enough to accommodate the volume change (expansion during charging and contraction during discharging) of the anode during the cycling process. Ideally, the SEI layer should be uniformly distributed over the graphite surfaces.

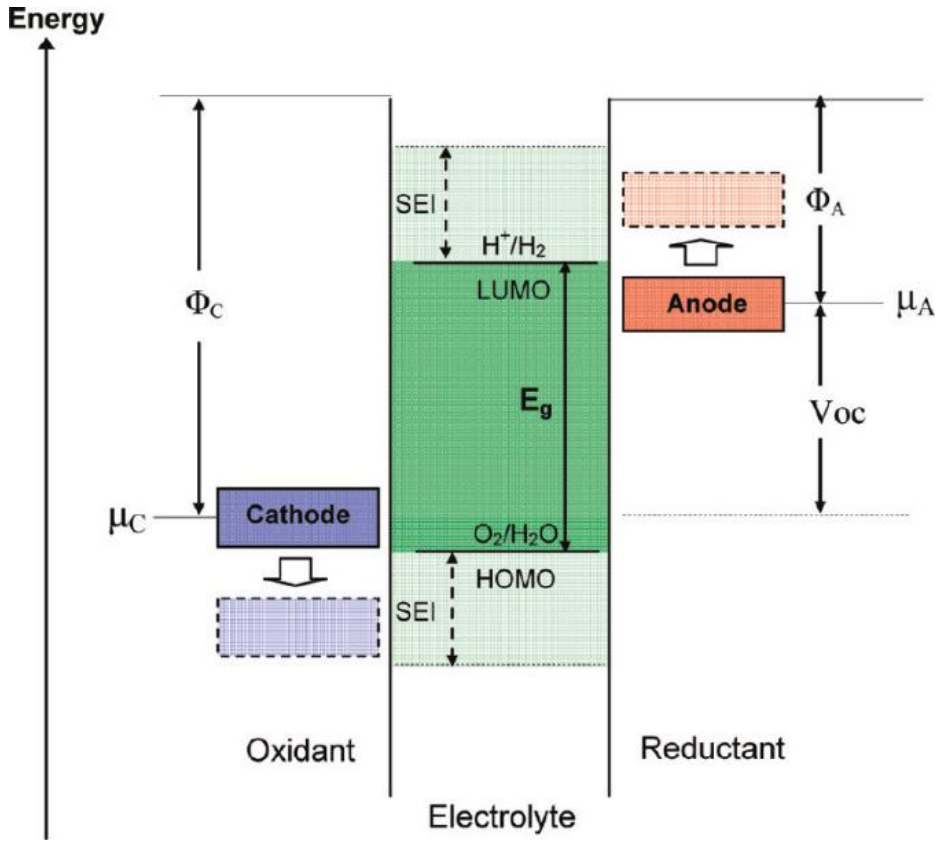


Figure 1.1. Energetics of the formation of the anode and cathode SEI layers under electro-reduction and electro-oxidation conditions.[21] "Reprinted (adapted) with permission from (Goodenough, J. B.; Kim, Y. *Chemistry of Materials* 2010, 22, 587). Copyright (2010) American Chemical Society."

The chemical composition of the SEI should contain stable and insoluble compact inorganic compounds such as Li_2CO_3 rather than metastable organic compounds such as ROLi and $ROCO_2Li$ (where R is an low-molecular-weight alkyl group),[48-49] which is important for confining the loss of lithium inventory to the first few cycles and minimizing irreversible capacity loss. Insolubility of decomposed SEI components to an electrolyte is important for high capacity retention because loosing the components may induce new SEI formation where they dissolved out. According to MD simulations from Tasaki et al., the heat of salt dissolution in ED/DMC is in the order of $[CH_2OCO_2Li]_2$ (LiEDC, -22kcal mol^{-1}) < $LiOCO_2CH_3$ (-4 kcal mol^{-1}) < LiOH < $LiOCO_2C_2H_5$ < $LiOCH_3$ < LiF < $[LiCO_2]_2$ < Li_2CO_3 (32 kcal mol^{-1}) < Li_2O (43 kcal mol^{-1}), indicating that inorganic Li_2O and Li_2CO_3 are endothermic and hard to dissolve in normal operation temperature while organic $[CH_2OCO_2Li]_2$ and $LiOCO_2CH_3$ are exothermic and the most soluble among the listed SEI components.[50] Inorganic products are hard to dissolve but can also diffuse into an electrolyte when surrounded by soluble organic products. Li_2CO_3 is generally abundant on a graphite anode than LiO_2 because of low concentration of lithium on surface of the graphite anode.[51] The concentration of LiO_2 can be increased on lithium metal anode.

From a historical standpoint, the SEI has been thought of as having a bilayer type structure. The layer near the interface of the electrolyte is assumed to be porous and less dense, composed of a large portion of organic components, and filled with electrolyte. This outer, organic layer may undergo further reduction, so its morphology may change in subsequent cycling. The inner layer adjacent to the graphite is presumed to consist mostly of inorganic compounds that protect the anode surface and prevent reduction. Thus, it is assumed to have a denser morphology with lower porosity. In recent studies, the SEI structure shows a bilayer structure in general, but in reality is more complicated.[51-54] For example, according to the results of Takenaka's hybrid Monte Carlo (MC)/molecular dynamics (MD) reaction simulation, inorganic salts such as Li_2CO_3 are abundant near the anode surface and distributed within the whole SEI film, becoming Li_2CO_3 junctions for the organic lithium carbonates and stabilizing the SEI film.[54] Other recent computational studies have also shown detailed and complicated structures, even though they were based on many simplifying assumptions. Considering real-world LIB systems involving side reactions, impurities, and uneven current distribution, it is likely that SEI structures are even more complicated than those depicted by fundamental simulations.

Recently Lu et al. studied the morphological evolution of the SEI during the formation process.[55-56] Figure 1.2 shows SEM micrographs at two different magnifications of the graphite anode surface from their study at different degrees of polarization during the first charge. The SEI thickness increased as the formation cycle proceeded (i.e. as the potential of the anode moved towards the intercalation potential). According to their model, the SEI at the beginning of the

formation process contained mainly loosely held organic polymer compounds. As the potential was lowered, the SEI layer transformed into a more compact structure of inorganic salts. Figure 1.2 and Figure 1.3 captures this morphological evolution.[55, 57]

The SEI layer formed at the graphite basal plane differs in morphology and chemical composition from that formed at the edge plane. The SEI formed at the basal plane does not need to have ionic conductivity, but it does need to be electronically insulating and impermeable to other electrolyte components. Since lithium ions cannot intercalate into graphene layers across the basal planes, these planes are ionic insulators and do not contribute to reversible capacity. Hence, SEI formation at these locations should be minimized to avoid unnecessary loss of lithium inventory. Due to the different behavior of the SEI layer formed at basal and edge planes, the true SEI formation potentials are not captured by conventional electrochemical measurements.

The chemical composition and morphology of the SEI are affected not only by the electrolyte, but also by the chemical compositions and morphologies of carbon/graphite surfaces. In the case of the 1M $LiPF_6$ in EC:DMC electrolyte and highly ordered graphite, the SEI at the edge plane is thought to be several times thicker (several nm) than that at basal plane. A thicker layer on the edge plane is consistent with the observation of higher reaction current at the edge plane than the basal plane.[58] On the edge sites for this particular case, the SEI is mainly composed of loosely packed inorganic lithium carbonates, organic lithium alkali carbonates and polymeric compounds on the electrolyte side. On the graphite side of the edge sites, the SEI is mainly composed of densely packed LiF, Li_2O, and Li_2CO_3. In between these two phases, there is an intermixed zone forming a trilayer structure. Overall, LiF and Li_2CO_3 make up more than half of the SEI layer.[59-60] On the basal sites, the SEI is composed of lithium carbonates more than LiF on the electrolyte side.

On the graphite side of the basal sites, the SEI is composed of similar portions of Li_2O, LiF, and lithium carbonates with small portions of polymeric compounds. LiF in the SEI is typically found in fluorine system electrolytes such as $LiAsF_6$, $LiPF_6$, and $LiBF_4$. Depending on LIB operating, anode sampling, and analysis conditions, the compositions of the SEI may vary even with the same electrolytes and electrodes used in a cell. $LiPF_6$ salts are unstable in elevated temperature and may precipitate into LiF during storage or operation. Lithium carbonates can be also decompose and form LiF after reacting with HF. Hence, LiF may be found in the SEI more frequently when there are other reactions before or during the surface analysis. HF formation, particularly observed in the case of $LiPF_6$ based electrolytes, is considered to dramatically affect the performance of LIBs by attacking the SEI layer.

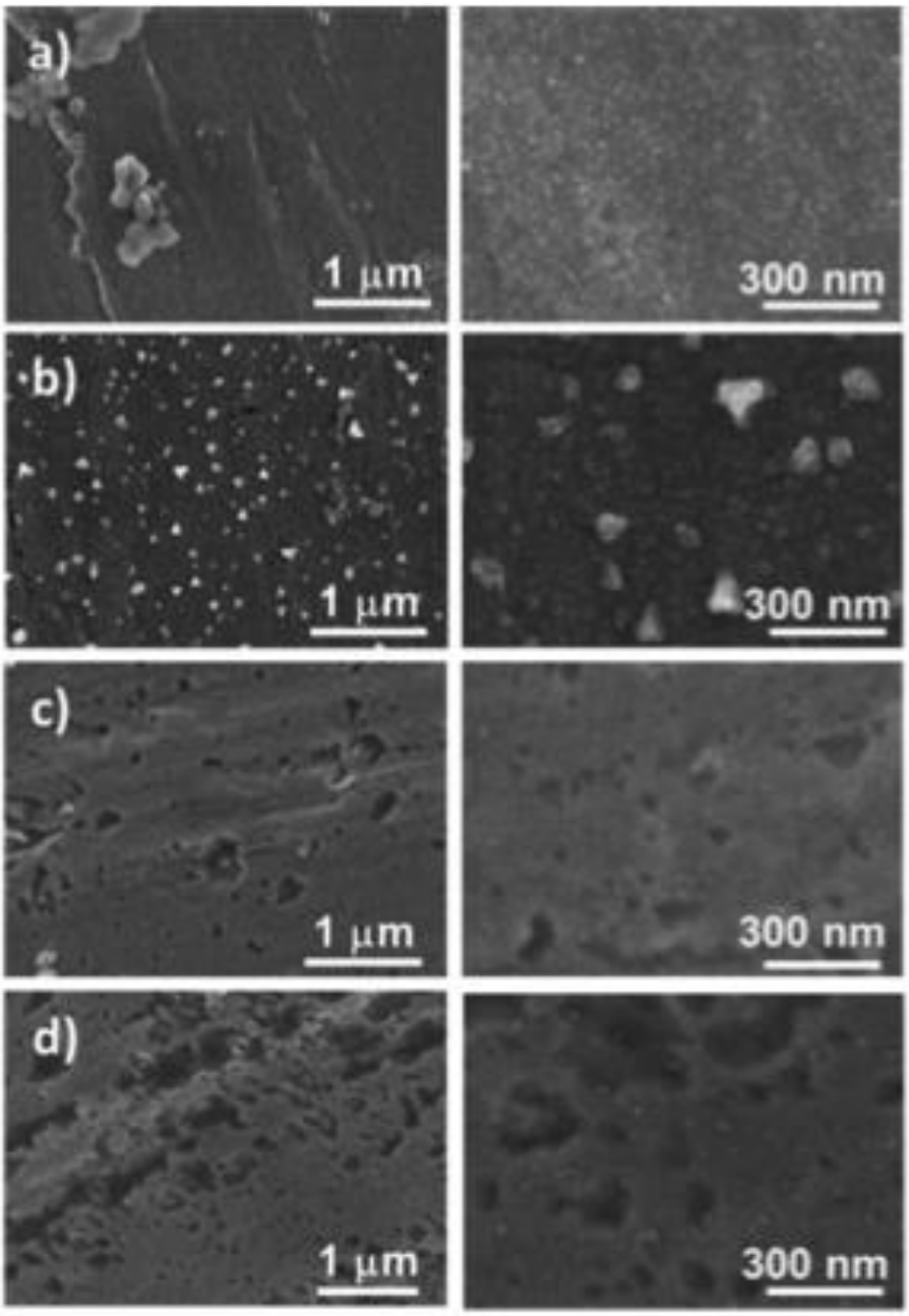
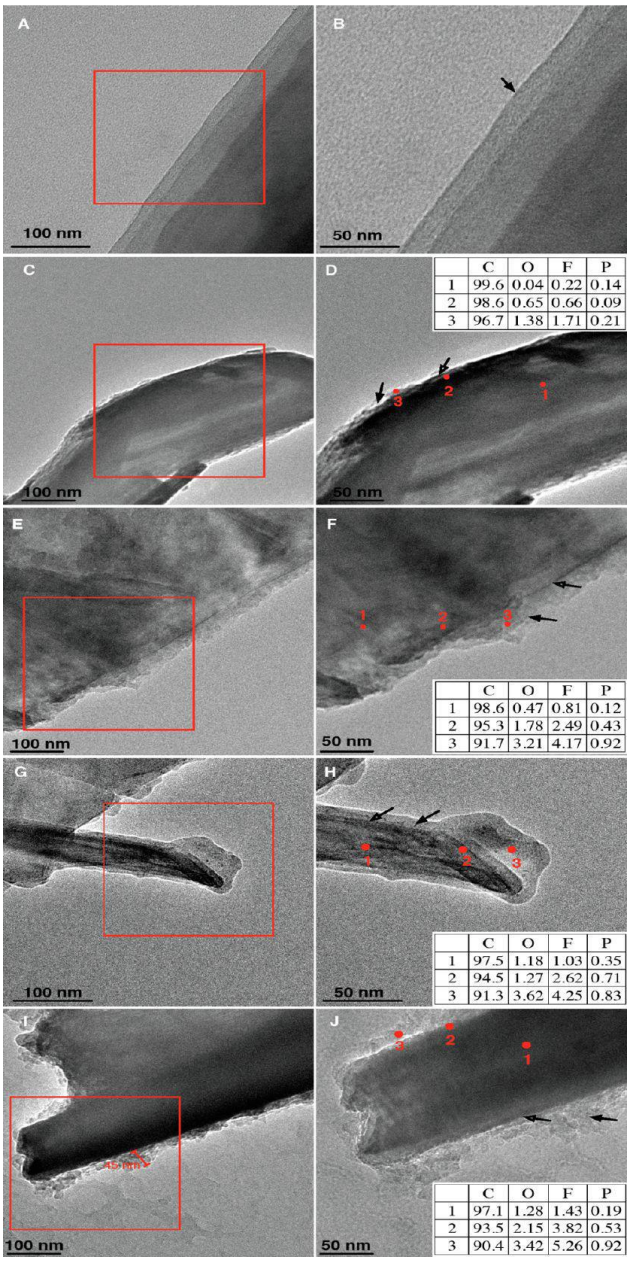


Figure 1.2. SEI morphology at various formation potentials reported by Lu et al., (a) 0.7 V, (b) 0.5 V, (c) 0.3 V and (d) 0.0025 V. The right column images are higher magnification (100,000×) of the images in left column (30,000×).[56] "Reprinted (adapted) with permission from (Harris, S. J.; Lu, P. *J. Phys. Chem. C* 2013, 117, 6481). Copyright (2013) American Chemical Society."



	C	O	F	P
1	99.6	0.04	0.22	0.14
2	98.6	0.65	0.66	0.09
3	96.7	1.38	1.71	0.21

	C	O	F	P
1	98.6	0.47	0.81	0.12
2	95.3	1.78	2.49	0.43
3	91.7	3.21	4.17	0.92

	C	O	F	P
1	97.5	1.18	1.03	0.35
2	94.5	1.27	2.62	0.71
3	91.3	3.62	4.25	0.83

	C	O	F	P
1	97.1	1.28	1.43	0.19
2	93.5	2.15	3.82	0.53
3	90.4	3.42	5.26	0.92

Figure 1.3. TEM images of fresh graphite and SEI on graphite anodes cycled to four cutoff voltages in 1.2M $LiPF_6$/EC during first charge reported by Lie et al., (A) Fresh graphite electrode, (C) 1.3, (E) 0.6, (G) 0.1, and (I) 0.05 V. The insets of (D), (F), (H), and (J) show element composition detected by EDX. The arrows indicate the SEI layer and the edge of graphite, and the red spots indicate locations probed by EDX. .[57] "Reprinted with permission from (Mengyun Nie et al. *J. Phys. Chem. C*, 2013, *117* (3), 1257). Copyright (2013) American Chemical Society."

HF production during the SEI formation process is due to the reaction between decomposition products of the $LiPF_6$ salt and traces of water in the liquid electrolyte phase and/or adsorbed on the graphite surfaces. In recent studies, the amount of LiF found in the SEI still varies considerably from one study to the next. In particular, computational simulations rarely show LiF formation because they generally do not consider impurities like water causing HF production or self-decomposition from a salt, a poor assumption.

For the case of soft carbon in the same electrolyte, polymer and solvent reduction products are more prevalent than salt reduction products.[61] For other salts such as $LiBF_4$, LiTFSI, or LiBETI, the percentage of LiF is small and other carbonated species comprise most of the SEI layer.[62] In general, SEI layers are composed of densely packed inorganic compounds such as Li_2O, Li_2CO_3 and LiF on the graphite side and loosely packed inorganic and organic species like Li_2CO_3, lithium alkyl carbonate ($ROCO_2Li$) and polymer on the electrolyte side.[63] There are also other studies that argue large portions of inorganic Li compounds such as LiF are also found on electrolyte side [64-66]. These components, formed by solvent, lithium salt, and electrolyte additive decomposition, are neither uniformly distributed nor well-ordered within the SEI layer. These semi-quantitative concepts about SEI compositions are much less debated than those hypotheses with respect to exact composition, morphology, structure, and formation. The reasons for the uncertainty and inconsistency among different studies arise from analysis difficulty, different electrolyte compositions, different types of carbon/graphite, various SEI formation processes, and other physical and environmental conditions (i.e. temperature). Table 1.1 from Verma et al. provides a thorough list of the most agreed upon compounds found in the SEI on graphite anodes.[48]

Formation mechanism of SEI layer

There are various reduction processes that compete with each other on the carbon/graphite surface during charging. The reactants are solvents, salts, additives, and trace air impurities (such as water). Electrochemical reaction rates differ depending on their intrinsic properties such as reductive potential, reduction activation energy, and exchange current density. They also depend on reaction sites (basal or edge), pre-decomposed precipitate sites, and many other different anode surface conditions.[58, 93-96] lithium ions and solvent co-intercalate into the graphene planes. If this co-intercalation is excessive, the SEI layer may not fully develop because of continuous exfoliation. Figure 1.4 illustrates these processes graphically.

Table 1.1. List of known chemical compounds formed on the surface of carbon/graphite SEI layers ("Present" denotes that the compound was identified in the references given, and "Not Present" denotes that the compound was not identified).[48] "Reprinted from *Electrochimica Acta*, 55, Verma P, Maire P, Novak, A review of the features and analysis of the solid electrolyte interphase in Li-ion batteries, 6332, Copyright (2010), with permission from Elsevier."

Component	Present	Not present	Notes
$(CH_2OCO_2Li)_2$	66-69		Being a two electron reduction product of EC; it is found mostly in the SEI formed in EC based electrolytes.
$ROCO_2Li$	66-67, 70-71		They are present in the outer layer of the SEI. They occur in most PC containing electrolytes, especially when the concentration of PC in the electrolyte is high.
Li_2CO_3	67-68, 71-72	70, 73-75	It may also appear as a reaction product of semicarbonates with HF, water, or CO_2.
ROLi	73, 75-78		Most commonly found in the SEI formed in ether electrolytes like tetrahydrofuran (THF), but may also appear as DMC or ethyl methyl carbonate (EMC) reduction product.[72] It is soluble and may undergo further reactions.[79]
LiF	72, 74, 80		Mostly found in electrolytes comprising of fluorinated salts like $LiAsF_6$, $LiPF_6$, $LiBF_4$. It is a major salt reduction product. HF contaminant also reacts with semicarbonates to give LiF byproduct. Amount of LiF increases during storage.[74]
Li_2O	74, 81-82	80, 83-85	It may be a degradation product of Li_2CO_3 during Ar+ sputtering in the XPS experiment.
Polycarbonate	80, 86		Present in the outermost layer of the SEI, close to the electrolyte phase. This part imparts flexibility to the SEI.
LiOH	69, 87-88	80-81	It is mainly formed due to water contamination.[89-90] It may also result from reaction of Li2O with water or with ageing.[75]
$Li_2C_2O_4$	75, 78		It is found to be present in 18650 cells assembled in Argonne National Laboratory containing 1.2 M $LiPF_6$ in EC:EMC (3:7) electrolyte. Li carboxylate and Li methoxide were also found in their SEI.[75]
HF	91-92		It is formed from decomposition $LiPF_6$ and the water in the solvents. It is highly toxic and can attack components of the cell.

In general it has been accepted that the SEI formation is a two-step process. During the first step when the graphite electrode is polarized, the components in the organic electrolyte undergo reductive decomposition to form new chemical species. In the second step, these decomposition products undergo a precipitation process and begin forming the SEI layer until all the sites on the graphite surface are covered. Even though several studies have been conducted to understand the formation mechanism of the SEI, it has been a major topic of debate, which centers on the reduction pathways, especially of the solvent molecules. There are typically four different reactions possible during the first cathodic polarization of the graphite electrode. The pathways of the four reactions are shown schematically in Figure 1.5.

The ionic radius of a Li ion (0.59 Å)[99] is much smaller than the corresponding anionic counter ion in the salt. Due to this size difference, Li ions are strongly solvated in the electrolyte solution, which also contains weakly solvated anions (such as PF_6^-) and isolated solvent molecules.[100] The solvated Li ions diffuse towards the surface of the graphite electrode due to the concentration polarization in the liquid phase. At the graphite surface, these solvated ions can undertake different pathways leading to different reductive decomposition products.

i. Intercalation of Li ion without the solvation shell into the graphene layers.
ii. Heterogeneous transfer of electrons from the solid phase graphite electrode to the solvent molecules.
iii. Co-intercalation of the solvent molecules with the solvated Li ions into the graphene layers.
iv. Heterogeneous transfer of electrons from the solid phase graphite electrode to the salt anions.

These possible pathways are based on electron transfer to salts/solvents in electrolyte solutions caused by the cathodic polarization of the electrode, thermodynamic simulations using molecular orbital calculations, and ionic sizes. Among these possibilities, reaction (i) is the desired reaction and leads to the faradaic current within the cell. This reaction occurs at a potential more negative than the potential of the other reactions, so during cathodic polarization, other reactions are preferred until the potential drops close to the intercalation potential.

Reactions (ii) and (iii), which address the reduction of the solvent molecules, are the major source of debate in the literature. According to Dahn and Aurbach, the reduction of a solvent molecule (for example [EC]-) is a one-electron reaction occurring at the surface of the graphite.

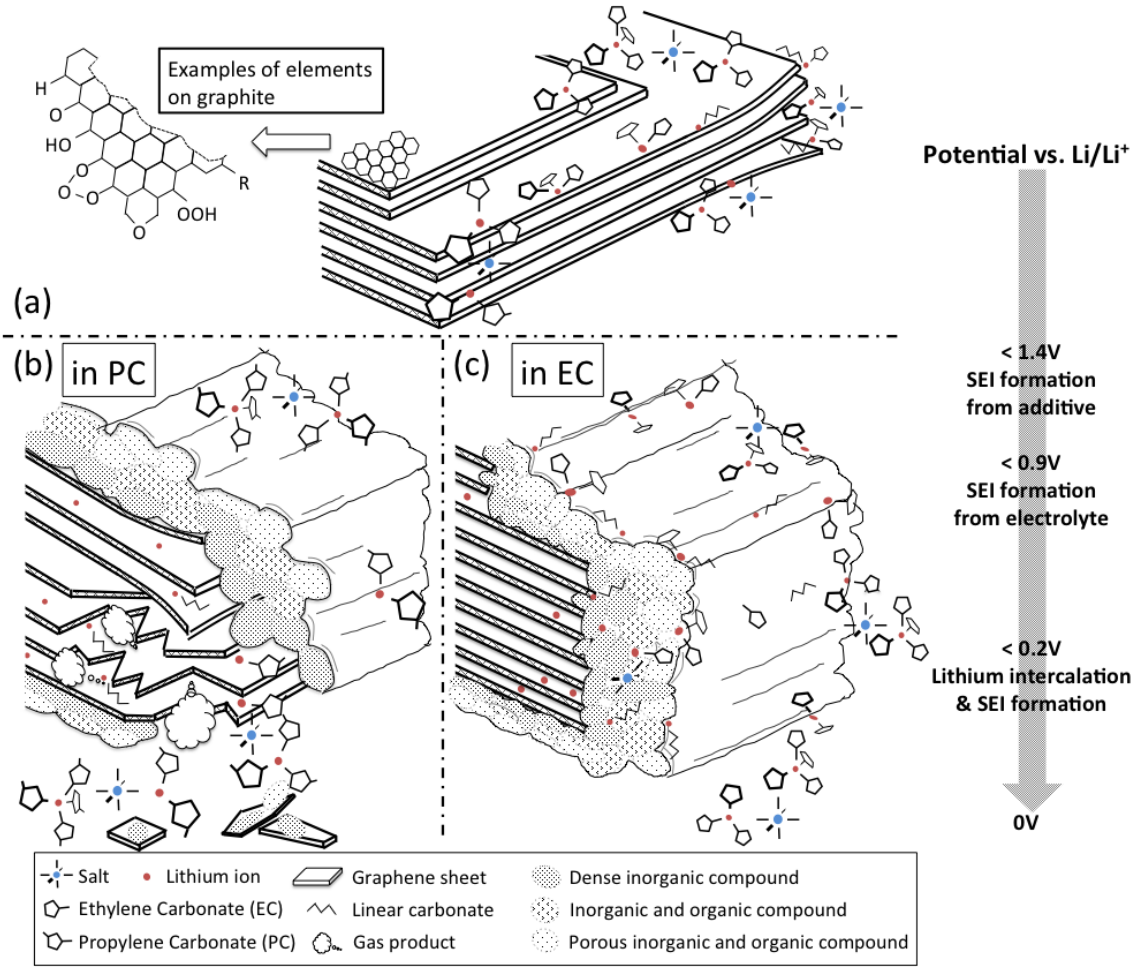


Figure 1.4. Schematic of the anode SEI formation process showing (a) graphene layers surrounded by electrolyte salts and solvents above 1.4V vs. Li/Li$^+$, (b) propylene-carbonate (PC) intercalation with lithium ions into graphene layers resulting exfoliations below 0.9V vs. Li/Li$^+$ and (c) stable SEI formation in ethylene-carbonate (EC)-based electrolyte below 0.9V vs. Li/Li$^+$; plane side with thinner SEI and edge side with thicker SEI.

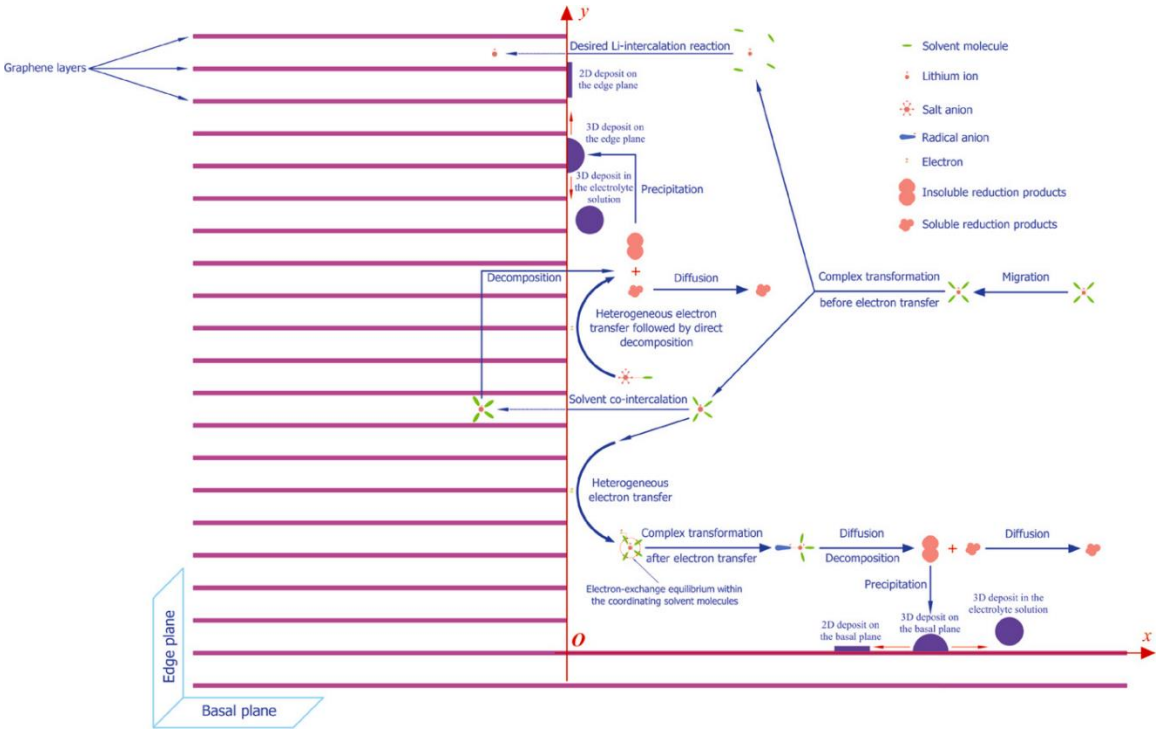
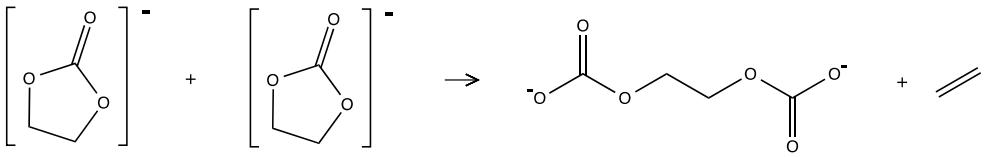


Figure 1.5. Proposed SEI layer reaction mechanism consisting of a four-step pathway (Yan).[98] "Reprinted from Electrochimica Acta, 55, Jian Yan, Jian Zhang, Yu-Chang Su, Xi-Gui Zhang, Bao-Jia Xia, A Novel Perspective on the Formation of the Solid Electrolyte Interphase on the Graphite Electrode for Lithium-Ion Batteries, 1788, Copyright (2010), with permission from Elsevier."

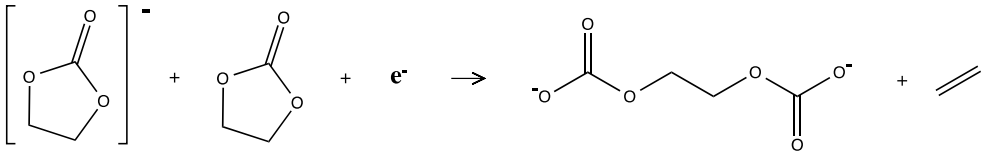
Therefore, according to this hypothesis, reaction (ii) proceeds with the solvent molecule being reduced to form an intermediate radical anion.

This radical anion undergoes further decomposition according to one of the pathways shown below (Path 1 or 2), and finally solid lithium ethylene dicarbonate (LiEDC) precipitates as shown below. Aurbach[49, 79] also argued that LiEDC is extremely reactive with traces of water in the electrolyte and forms Li_2CO_3 upon reacting.

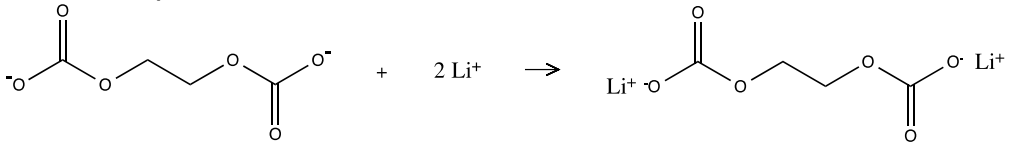
Path 1:



Path 2:



Solid Precipitation:



According to the second theory proposed by Dey et al.[101], Besenhard et al.[102] and Chung et al.[103], reaction (iii) is a more preferred reaction and [EC-] undergoes a two-electron reduction reaction. The solvated Li ions are co-intercalated into the graphene layers held by weak van der Waals forces and form intermediate ternary graphite intercalated compounds (GIC) such as $[Li(Sol)_xC_y]$. The ternary GICs are subsequently reduced to form the SEI. Since the literature supports both hypotheses, the proposed mechanisms are still debated. Reaction (ii) and reaction (iii) may even compete against each other and both might occur in parallel during the SEI formation process. Reaction (iv) is the heterogeneous transfer of electrons directly to the salt anions to form inorganic SEI products.

Methods of analyzing and characterizing the SEI layer

SEI layers easily react with ambient CO_2 and H_2O to form inorganic lithium-containing compounds such as Li_2CO_3 and Li_2O.[42, 89, 104] Hence, washing the electrode in electrolyte solvents for analysis can easily introduce artifacts in the morphology and chemical composition of the SEI layer. For example, $ROCO_2Li$ and ROLi react with CO_2 to form Li_2CO_3.[105] The lithium in the SEI will also react spontaneously with atmospheric oxygen to form various lithium oxides (Li_2O, Li_2O_2 and LiO_2).[36] These oxides are strong nucleophiles and react further with organic solvents and semi-carbonates to form carbonates and alkoxides.[106] Thus, specialized sample chambers are necessary when transferring SEI specimens from the inert atmosphere of a glove box to an analytical instrument to avoid chemical contamination and physical damage.

A variety of tools and techniques have been used to analyze the SEI, including traditional electrochemical methods such as electrochemical impedance spectroscopy (EIS) and Cyclic Voltammetry (CV). EIS is a nondestructive analysis tool, which provides useful information from a complex electrochemical system having a diffusion layer, electrolyte resistance, electrode kinetics, and double-layer capacitance.[55, 64, 107-114] To diagnose EIS spectra properly, a good equivalent circuit model is required. CV, which measures current in the anodic (oxidation) and cathodic (reduction) directions, has also been successfully implemented to understand the SEI. [112, 114-119] Traditional tools of scanning electron microscopy (SEM) [38, 55, 64, 112, 116, 120-123], transmission electron microscopy (TEM) [65, 118, 121, 124-125], scanning tunneling microscopy (STM) [119, 126], atomic force microscopy (AFM) [64, 85, 126], and Ellipsometry [115] have been implemented to image the surface features and morphology of the SEI. TEM can also show surface crystallinity, in-situ interface formation, and lithiation/delithiation in operando.[127-129] AFM is a useful tool for studying SEI morphology and thickness because it can measure differences in depth at Angstrom resolution. Ellipsometry is a non-destructive optical tool that measures thickness and roughness of thin films by using reflectance ratios, but its weakness is that the measured signal depends not only on thickness, but also material properties.

Because the anode SEI is a thin layer on graphite, surface analysis tools such as X-ray photoelectron spectroscopy (XPS) [16, 55, 62, 64-65, 91, 110, 112, 116, 118, 121, 123-124] and Fourier transform infrared spectroscopy (FTIR) [64, 118, 125-126] have been used for characterization because of their surface sensitivity and chemical identification ability. Raman spectroscopy [16, 64, 121], X-ray diffraction (XRD) [16, 121], Secondary Ion Mass Spectrometry (SIMS) [55, 65] , nuclear magnetic resonance (NMR) [92, 109-110, 118], neutron reflectometry (NR) [130], small-angle neutron scattering (SANS) [131], and temperature-programed desorption mass spectrometry (TPD-MS) [120] have also been successfully applied to identify SEI surface species.

Effects of carbon/graphite properties on SEI formation

Carbons are widely used as LIB anodes because of their stability and low working potential. Graphite is a crystallite and the most stable allotrope of carbon. It has perfect stacking of graphene layers in AB form and in some cases ABC form. In general, aggregates of perfectly stacked graphite crystallites exist with different orientations in an electrode. Graphite has a redox potential very close to Li/Li^+, is safe, is the most stable form of carbon, is environmentally benign, and has low (pre-processed) cost. A lithium atom is intercalated between the graphite layers to form an intercalation compound (i.e. LiC_6) during LIB operation.[19-20] The intercalation reaction prevents the deposition of metallic lithium on the graphite surface and avoids dendritic growth making these types of LIBs safe. The lithium-ion charge is also maintained, essentially eliminating the activation energy associated with the formation of a chemical bond. The carbon is reduced to maintain charge balance.

Figure 1.6 shows an aggregate graphite particle and the graphite layers within that particle. In a crystallite of graphite, the two characteristic surfaces are referred to as basal and edge planes. The surfaces parallel to the graphene layers are called basal planes, and the surfaces normal to the graphene layers are edge planes. Lithium predominantly intercalates into the graphene layers through the edge planes in the direction parallel to the basal plane. The SEI formation process also differs at these two planes. Thus the ratio of basal plane to edge planes determines electrochemical performance of graphite electrodes. Different types of graphite such as highly oriented pyrolytic graphite (HOPG) and natural graphite have been used as anodes. Since the basal plane to edge plane ratios will differ in different forms of graphite, the SEI formation process will be different, as well as the chemical and physical properties of the SEI layer. In turn, these property differences will affect electrode performance during early life and the shape of the long-term capacity fade curve.

The SEI layer forms differently depending on composition and structure of carbon/graphite surface. The key factors for SEI formation are particle size, basal-to-edge-plane ratio, pore size, degree of crystallinity, and surface chemical composition (adsorbed species).[132-133] The surface area of small particles is greater than that of large ones for the same weight. Smaller particle size generally causes more edge sites, as well as more SEI formation surface area. The decomposition on basal planes and edges differs because edge sites provide better reactivity than basal ones. Hence, electrolyte decomposition occurs at edge sites first. The edge sites are also the access points for lithium intercalation to graphene layers. Lithium ions diffuse along with solvent molecules and salts. At a potential lower than 0.2V vs. Li/Li^+, lithium intercalation into the graphene layers via edge sites begins.

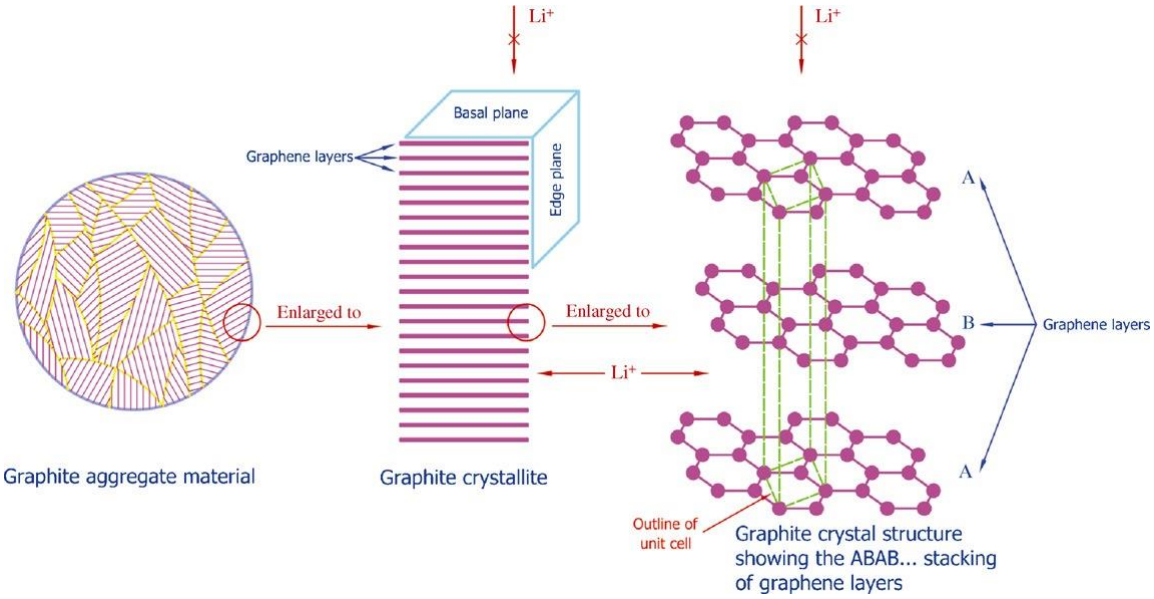


Figure 1.6. Schematic of the lithium-ion intercalation process into and out of graphite [J. Yan et al.] [98] Left: graphite particle showing turbostratic disorder of individual nano-scale regions of high order (crystallinity). Center: graphene layers of an individual crystallite showing edge and basal plane directions. Right: AB stacking of individual graphene layers where lithium ions intercalate between layers A and B. "Reprinted from Electrochimica Acta, 55, Jian Yan, Jian Zhang, Yu-Chang Su, Xi-Gui Zhang, Bao-Jia Xia, A Review of the State of Understanding of the Graphite Solid Electrolyte Interphase (SEI) and Its Relationship to Formation Cycling, 1787, Copyright (2010), with permission from Elsevier."

This intercalation generates concentration differences inducing solvent and salt reactants to move towards the edge sites and decompose there if the edge sites are not fully occupied by the SEI layer. This process also results in a thicker SEI on edge sites than on basal planes.

Few studies have been reported on the effect of the graphite particle size distribution, porosity, surface roughness, surface chemistry and crystallinity.[120, 132, 134-137] Graphite with low specific surface area tends to exfoliate more. As the surface area is decreased by heat treatment, the number of surface defects increases and the exfoliation tendency of the graphite further increases. Above a critical specific surface area of 0.2 m^2/g, the exfoliation tendency is suppressed in the absence of surface defects.[120] Graphite particle sizes with surface areas of 1-5 m^2/g may mitigate exfoliation without introducing excessive irreversible capacity loss. The degree of graphite crystallinity is also an important factor in SEI formation, and highly ordered graphite is preferred for high-energy LIB anodes. When the particle size is small, irreversible capacity loss increases due to larger surface area for lithium inventory loss during SEI formation (a side benefit, though, is that the power density increases with smaller anode particle size). Increasing graphite size is one way for lower irreversible capacity loss and higher energy density, but large particle sizes increase the probability of exfoliation.

Chemical composition on carbon/graphite surfaces may also affect the exchange current density and potential for SEI formation, as well as wettability of electrolyte, chemical adhesion between carbon and the SEI layer after decomposition, and between carbon and electrolyte before decomposition.[64, 93, 138-144] The presence of oxygen species on graphite surfaces increases the reduction potential vs Li/Li^+ and helps early SEI formation before lithium intercalation. The presence of these species has been shown to be vital in SEI formation by serving as nucleation sites for electrolyte decomposition, and a lack of them can hinder the decomposition reactions and increase the exfoliation of the graphene layers.[145] Oxygen species on graphite surfaces can be attached by heat treatment in various environments. Natural graphite usually has oxygen-containing species on its surface, although the degree of crystallinity may not be that high. To increase it, calcination in air produces more crystallites and increases the adsorbed oxygen-containing species.

Effects of electrolyte composition on SEI formation

LIB liquid electrolytes are commonly composed of a combination of low-molecular-weight organic solvents like ethylene carbonate (EC), dimethyl carbonate (DMC), diethyl carbonate (DEC), ethyl methyl carbonate (EMC), or propylene carbonate (PC) and lithium salts like $LiPF_6$ or $LiBF_4$. Because of the high oxidation potential (4.7V vs. Li/Li^+) of these organic carbonates, SEI

formation is prevented on the cathode surface during charging. PC had historically been a widely used solvent because it is a liquid at cell operating temperatures and has a high dielectric constant (ε=64).[146] The dielectric constant is an important indicator that predicts degree of salt dissolution. The drawback of using PC is severe solvent co-intercalation with lithium ions into graphite that exfoliates the graphene sheets, forming decomposition products within the sheets and releasing gases like propylene. Instead, EC is widely used because of its high dielectric constant (ε=89) and stable SEI formation, although its high viscosity and melting point of 36°C require thinning solvents such as DMC, DEC, and EMC. For example, 1-1.2M $LiPF_6$ in 1:1 wt ratio of EC/DEC is a common electrolyte composition. In mixtures of EC/DEC or EC/DMC, $LiPF_6$ dissolves well and yields ionic conductivities of up to ~10^{-2} S/cm^{-1}, a high reduction potential of 1.3V vs Li/Li^+, and an oxidation potential of above 4.5V vs Li/Li^+. This combination results in excellent electrolyte properties, but it is highly flammable.

$LiClO_4$ has high ionic conductivity (5.6mS/cm in PC, 8.4 mS/cm in EC/DMC) and may form less resistive SEI layers than $LiPF_6$ and $LiBF_4$ due to no LiF decomposition. The drawback is thermal instability that the salt reacts with solvents at elevated temperature and it is explosive. $LiBF_4$ shows better thermal stability and less sensitivity to moisture than $LiPF_6$. But it was not commonly adopted in industry because of low ion conductivity (3.4 mS/cm in PC, 4.9 mS/cm in EC/DMC): about 40% lower than $LiPF_6$ (5.8 mS/cm in PC, 10.7 mS/cm in EC/DMC) and high resistance of SEI from $LiBF_4$ electrolyte.[147] Lithium Bis(trifluoromethanesulfonyl) imide(Li Imide) is highly ion-conductive (5.1mS/cm in PC, 9.0 mS/cm in EC/DMC) and thermally stable: no decomposition until 360^{o}C. But it has a serious Al corrosion issue. $LiAsF_6$ is not adopted in industries because of concerns about the toxicity of As(V) although it has high ion conductivity. $LiPF_6$ is a well-known salt that is currently used in industries. It may not be the best in all requirements for an electrolyte but well balanced. In terms of safety, an inorganic electrolyte of $LiBF_4$ in 1-ethyl-3-methylimidazolium tetrafluoroborate (EMI-BF_4) is one alternative due to its higher boiling point than $LiPF_6$ in EC/DEC and non-flammability. EMI-BF_4 also has a higher oxidation potential, but its ionic conductivity is lower due to the high solvent viscosity. Lithium bis(oxalato)borate (LiBOB) also has less thermal reactivity. It is used as a salt by itself or an additive in an electrolyte. LiBOB stabilizes the graphite structure effectively even in pure propylene carbonate (PC) and facilitates SEI formation on the surface of electrode materials. On the other hand, its solubility and conductivity in other common solvents such as EC and PC are inferior. However, these limitations are improved by using a more appropriate solvent such as dimethyl sulfite (DMS) with γ-butyrolactone (γBL).[148-149]

In order to enhance early and stable SEI formation on the graphite anode surface and to prevent exfoliation during the lithium intercalation, liquid additives are often used in organic electrolytes. The most commonly used additive is vinylene

carbonate (VC), and it has lower reductive activation energy (13 kcal/mol) and higher reduction potential (1.05~1.4V Li/Li^+) than EC (24.9 kcal/mol and 0.65~0.9V Li/Li^+, respectively) and PC (26.4 kcal/mol and 0.5~0.75V Li/Li^+).[36, 150-151] VC added to PC promotes reductive decomposition at potentials around 1.3V. About 3 wt% of VC is usually incorporated and improves cycle life and Coulombic efficiency by creating a more stable SEI layer. During the first charging step, VC in EC or PC increases the reduction potential by around 0.2V, so the solvent mixture decomposes earlier in the formation process than without VC, which starts building an enhanced SEI layer before lithium intercalation begins. When VC is used in EC, it is possible to have large portions of polymer species in SEI.[152]

Tasaki et al. investigated the reduction activation energy of various additives in the presence of a lithium anode.[150] This study showed that reduction activation energy (energy difference between the reactant and its transition state) of VC is 13 kcal/mol, which is lower than that of EC (24.9 kcal/mol) and PC (26.4 kcal/mol) and indicates the tendency of VC to reduce easier than EC or PC. Regarding reduction potential, Yoon et al.[153] reported reduction potentials of various additives including VC and N-substituted caprolactam (CL) derivatives. The reductions of CL, VC, and EC take place at 1.10V, 1.05V, and 0.65V vs. Li/Li^+, respectively. Jung et al.[154] also obtained similar results via DFT calculations and experiment and showed that EC (0.6V vs. Li/Li^+, -55.9 kJ/mol Gibbs free energy of reduction) has lower reduction potential than VC (0.75V vs. Li/Li^+, -160.0 kJ/mol Gibbs free energy of reduction), which agrees with the calculations of Tasaki et al. On the other hand, Wang et al.[155-156] found different results from a polarized continuum model in calculating reduction activation energy of $(EC)_nLi^+(VC)$, n=1-3. Ring-opening barriers of EC (8.8~11.1 kcal/mol) were found to be lower than that of VC (20.1~21.1 kcal/mol) for reduction reactions, and a major conclusion was that EC decomposes more readily than VC because VC acts as a stable anion intermediate and assists nearby EC reduction. Although the calculations from Wang et al.[156] yielded slightly different results, agreement was found that VC increases solvent reduction reaction rates. Considering reduction potential, reaction enthalpy and activation energy, VC is reduced before EC and PC do during a reduction cycle (charge) although the reduction products of VC may not be as stable as those of EC and PC.[153] In industry, many different proprietary additives are used in even more combinations together with variations on the formation protocol, and the resulting SEI structures are closely guarded.

Relationship between electrolyte decomposition reactions and LIB formation protocol.

In 1979, Peled first used the term solid electrolyte interphase (SEI) for the LIB anode passivation layer [140], and, in 1990, Dahn et al. discovered the advantage of using EC in the electrolyte for forming the SEI.[157] Before the use of EC was commonplace, PC was the most widely used LIB electrolyte solvent, which was highly compatible with lithium metal anodes. Early LIBs implemented lithium anodes, but dendrite growth was a problem in terms of safety and long-term performance.[158-161] Once the discovery of graphite as a safe, high-performing anode intercalation material was made, its major drawback was also quickly discovered. PC easily co-intercalates with lithium ions and exfoliates the graphene layers during electrolyte decomposition, while also releasing propylene gas. Attention shifted to using amorphous carbons having little crystallinity because they tended to exfoliate much less in PC based electrolyte solutions and showed good reversible capacity. The problem with these materials, though, was high initial capacity loss due to thick SEI layer formation. When Dahn et al. found that EC reduced the first-cycle capacity loss (due to a much thinner SEI layer formation) and increased the stability of the SEI by mitigating exfoliation of graphite, solvent mixtures high in EC concentration were mainly used. As the appreciation of having a stable, durable SEI has grown since the early 1990s, much effort has been dedicated to: 1) improving its formation by using additives that result in better SEI-layer architectures; 2) modifying the anode surface for improving exchange current density and charge-discharge reaction kinetics; 3) implementing charge-discharge cycles that enhance layer formation; and 4) developing alternative electrolytes that result in less lithium inventory loss during formation.

Current densities, cut-off voltages, and temperatures used during formation cycling have all been shown to have a profound effect on the chemical and microstructural properties of the SEI layer. It starts to form around 0.8 V vs Li/Li^+, and the thickness gradually increases until around 0.3V vs Li/Li^+. At higher charging anode potentials vs Li/Li^+, the SEI is composed of loosely aggregated organic components with lower ionic conductivity. As the anode potential drops, the SEI becomes more compact and begins to contain inorganic components with higher conductivity. The kinetics of the different SEI forming reactions can be exploited by varying the current densities and temperature. At higher current densities, the formed SEI has a more porous nature with high electronic and ionic conductivity. At lower current densities, the formed SEI is denser with lower electronic conductivity and higher ionic conductivity, which is the main reason formation protocols have historically required extremely low first-charge (and even low second and third charge) rates.[121, 162-163] Elevated temperature also enables formation of a stable SEI.

Few studies have been reported on electrolyte wetting of electrodes, although it is an important factor for reducing SEI formation time and manufacturing resources that directly affect LIB pack cost. In fact, wetting takes the majority of cell production time and involves many of the latter manufacturing steps such as addition of insulators, seals, and safety devices[7]. It takes many hours for electrolyte to completely wet the separator and reach the smallest pores of the electrodes[15], and studying wetting transport phenomena without a complete cell assembly facility is difficult.

Wetting electrodes (at low vacuum pressures during electrolyte filling and subsequently at elevated temperature after cell sealing) with electrolyte and forming SEI layers requires ~0.5-2 weeks for the entire process.[7, 15] Wood et al. reported costs for a general wetting and formation process, which showed the SEI formation can contribute up to $32-33/kWh of usable energy for the battery pack cost (out of a total cost of ~$500/kWh).[15] Anode and cathode electrodes need to be fully wetted with electrolyte during the initial portion of formation cycling, which is the process of the first 1-2 successive, slow and shallow charge-discharge cycles of a cell's life where the anode SEI layer is first formed. The initial wetting process is slow because the electrolyte has to permeate into all pores of the separator and electrodes in a near fully assembled cell. Evacuating gases out of the pores under high vacuum during cell assembly can accelerate infusion of the electrolyte and enable uniform distribution, although it requires more equipment and processing expense. Even under an evacuated condition, the smallest pores of the electrodes and separator may not fully wet unless they have a higher surface energy than the electrolyte. This situation is due to the competition between hydrodynamic forces at low pressure and non-wetting surface forces (the smaller the pore size, the lower the vacuum pressure needed to make a non-wetting liquid enter a pore). To avoid costly and time-consuming vacuum pumping, both electrodes (and the separator) should have high wettability of the electrolyte for full active material utilization during the formation cycling process. The formation process cannot commence until full wetting of all component porous volume is achieved. Wettability of the electrolyte into the electrode pores can be enhanced by lowering surface tension of electrolyte with an additive(s) or by increasing the composite surface energy of the electrode. Stable SEI formation also requires proper charge-discharge protocols that involve significant time due to slow charge rates between C/5 and C/20.[15] Simply increasing charge rates for fast SEI formation results in incomplete, non-uniform, electrochemically unstable layers or deposits,[121, 171-173] thereby lowering cell efficiency, durability and safety. Similarly, insufficient electrolyte wetting leads to a low-quality SEI layer, inactive surface area, and/or premature cell performance degradation.

Electrolyte wetting and charge rate, particularly first-charge rate, are highly interlinked by a symbiotic electrochemical and mass transport relationship. In

order to reduce formation time without losing cell performance, it is pertinent to fully review the current understanding of the SEI formation process, composition, morphology, structure, and their combined effects on both short-term (irreversible capacity loss) and long-term performance (capacity fade). During SEI formation, lithium ions react at extremely electro-reducing potentials (close to 0 V vs. Li/Li^+) with electrolyte solvents and salts and anode electrons via electro-reduction reactions during charging. The reduced reactants precipitate and form the passive anode SEI layers, and reported reactions are enumerated in Table 1.2. SEI formation takes place mainly during first charging due to abundant electron availability to the electrolyte constituents because of negligible electrical resistance on the anode active material surface. The reduction processes for EC and PC on a charging graphite anode are very similar, yielding similar SEI chemical compositions, but the layers behave differently during subsequent charge-discharge cycles (i.e. irreversible capacity loss and capacity fade) due to different bulk properties (i.e. thickness, porosity, tortuosity, etc.) of the reduction species.[140, 174-175]

An electrolyte system with $LiPF_6$ dissolved in an EC:DMC mixture is mostly stable above 1V vs. Li/Li^+[55, 65, 154], and no significant decomposition occurs. At potentials below 1V vs. Li/Li^+, minor decomposition of the electrolyte species may occur, depending on the surface chemistry and morphology of graphite and the nature of electrolyte additives. Temperature and charge rate below this potential threshold also affect the decomposition reaction rates and products [113-114, 125]. Disordered carbonaceous structures have a broader range of decomposition potentials than highly oriented ones because of differing reaction site energetics.[64] Graphite surface coatings or modifications can also alter the decomposition potential range. In some cases, minor amounts of highly resistive LiF precipitates can form in the SEI above 1V vs. Li/Li^+ due to the stability of PF_5 in a compact polar solvent such as EC. [92] This LiF is sometimes detected during the early stages of electrolyte decomposition in nanometer-sized crystallites.[55] PF_5 is known as a strong Lewis acid that can also react with traces of water to produce HF, eliminate alkyl carbonate from lithium alkyl carbonate, and react with solvent carbonyl groups to produce insoluble ether-containing species.[17, 92, 145] At higher anode potentials, decomposition products like LiF are usually generated on graphite edge plane sites, which are preferable for nucleation due to a lower energy requirement than on basal plane sites. Fortunately LiF generation is kinetically slow and the amount of decomposition is small above 1 V vs. Li/Li^+.

It is well accepted that most of the SEI layer formation takes place within the potential range of 0.2-1.0 V vs. Li/Li^+. However, the formation mechanism(s) is highly debated. There have been two different concepts on the SEI formation process hypothesized, although their final structures are mostly alike. One

concept follows a one-electron transfer to the electrolyte at high potential and a multi-electron transfer at low potential.[55, 145]

In other words, “bulk” lithium compounds (precipitates) are first partially reduced at high potential by a one-electron process due to insufficient electrons with low electron transfer resistance from electrode to electrolyte for complete reduction. At low potential, “compact” lithium compounds are generated from further reduction of preexisting bulk lithium-containing precipitates on the anode surface, or directly by complete reduction of lithium compounds in electrolyte driven by high energy at low potential. The second concept supposes little or no precipitates preoccupying the anode graphite surface at high potential. Hence, electrons can transfer to electrolyte constituents without interference from resistive interfacial compounds. This high electron transfer rate induces compact lithium compound formation at higher potentials, and, as the potential is lowered and the decomposition layer thickens, electrolyte solvent molecules are gradually reduced. Subsequently, partially reduced bulk lithium compounds precipitate on top of the resistive compact layer to a greater extent as the potential reaches ~0.2 V vs. Li/Li^+.

Proponents of both hypotheses agree that major SEI formation begins around 0.8V vs. Li/Li^+, but it can be higher for certain highly porous carbonaceous active materials [131]. In an ideal situation, the SEI formation will occur prior to lithium intercalation, which prevents co-intercalation of electrolyte constituents. For highly oriented graphite, lithium intercalation occurs at 0.2V vs. Li/Li^+ or less, but it can start at slightly higher potentials in disordered or porous carbons [64, 116, 131]. Within the potential range of 0.6-0.8V vs. Li/Li^+, electrons at the graphite surface transfer to the liquid electrolyte containing solvated lithium ions. These cations diffuse towards the graphite particles with an average of four strongly coordinated solvent molecules and an uncoordinated PF_6^- anion.[118] Uncoordinated solvent molecules are less likely to accept an electron because they are more stable than those associated with lithium ions. Most decomposition products from electro-reduction precipitate on the anode surfaces, while minor amounts diffuse back into the liquid phase and eventually re-precipitate elsewhere.

Decomposition reactions prefer graphite edges because these sites usually include defects that are unstable and tend to be highly reactive. As the reaction rate on edge sites slows due to an increase in the coverage of precipitates, decomposition takes place on basal planes as well. These electrolyte decomposition reactions are irreversible and result in loss of lithium ions (cathode lithium inventory), solvent molecules, and salt anions (see Table 1.2 and Figures 1.7-1.10).[145]

Table 1.2. SEI formation and electrolyte decomposition reaction categories corresponding to reaction paths in Figures 1.7-1.10

	Reaction group	Reaction index
Ethylene carbonate (EC)	One-electron reduction	E1[58, 79, 109, 113, 164], E2[145, 155], E3[145, 155], E4[145, 155], E5[155], E6[58, 79, 109, 113], E7[109], E8[109]
	Two-electron reduction	E9[155, 165-166], E10[58, 62, 66, 79, 109, 150, 155, 165-167], E11[55, 145, 155], E12[55, 60, 62, 79, 91, 125, 155]
	Secondary reaction	E13[145, 168], E14[145], E15[145, 167-168], E16[145, 167], E17[145], E18[145, 167-168], E19[165-166, 168], E20[125, 166, 169], E21[62, 166, 170], E22[17, 145]
Propylene carbonate (PC)	One-electron reduction	P1[37, 58, 126, 164], P2[109, 126], P3[37, 126], P4[37, 42], P5[58, 109, 126], P6[109], P7[109]
	Two-electron reduction	P8[17, 58], P9[58, 79, 126], P10[17, 168]
	Secondary reaction	P11[165, 168], P12[104, 168], P13[165, 168], P14[37, 104, 168], P15[17, 165, 168], P16[125, 165-166], P17[37], P18[37], P19[37]
Linear carbonate (LC)	One-electron reduction	L1[166-167], L2[164]
	Two-electron reduction	L3[62, 91], L4[62, 91]
	Secondary reaction	L5[165, 167-168], L6[165, 167-168], L7[17], L8[17, 104, 165-166, 168-169], L9[17, 145]
Salt		S1[17, 91-92, 145, 165-170], S2[17, 55, 165-167], S3[17, 60, 145, 165-169], S4[165-168], S5[17, 91-92], S6[91], S7[91], S8[17, 42, 60, 104, 165, 168], S9[17, 42, 104, 165, 168], S10[17, 42, 104], S11[165-166]

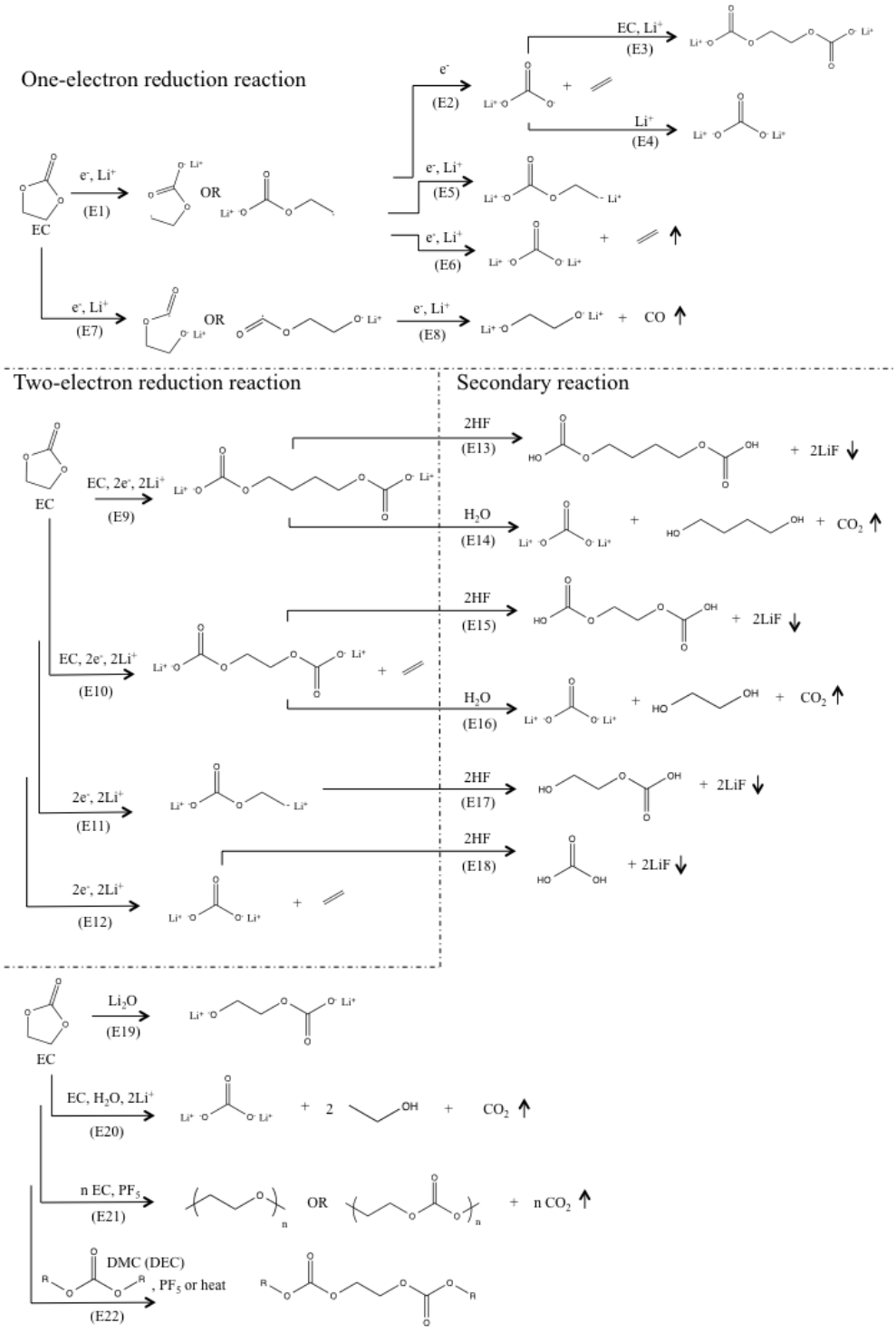


Figure 1.7. Ethylene carbonate (EC) reduction process (reference groups in parentheses; details are shown in Table 1.2).

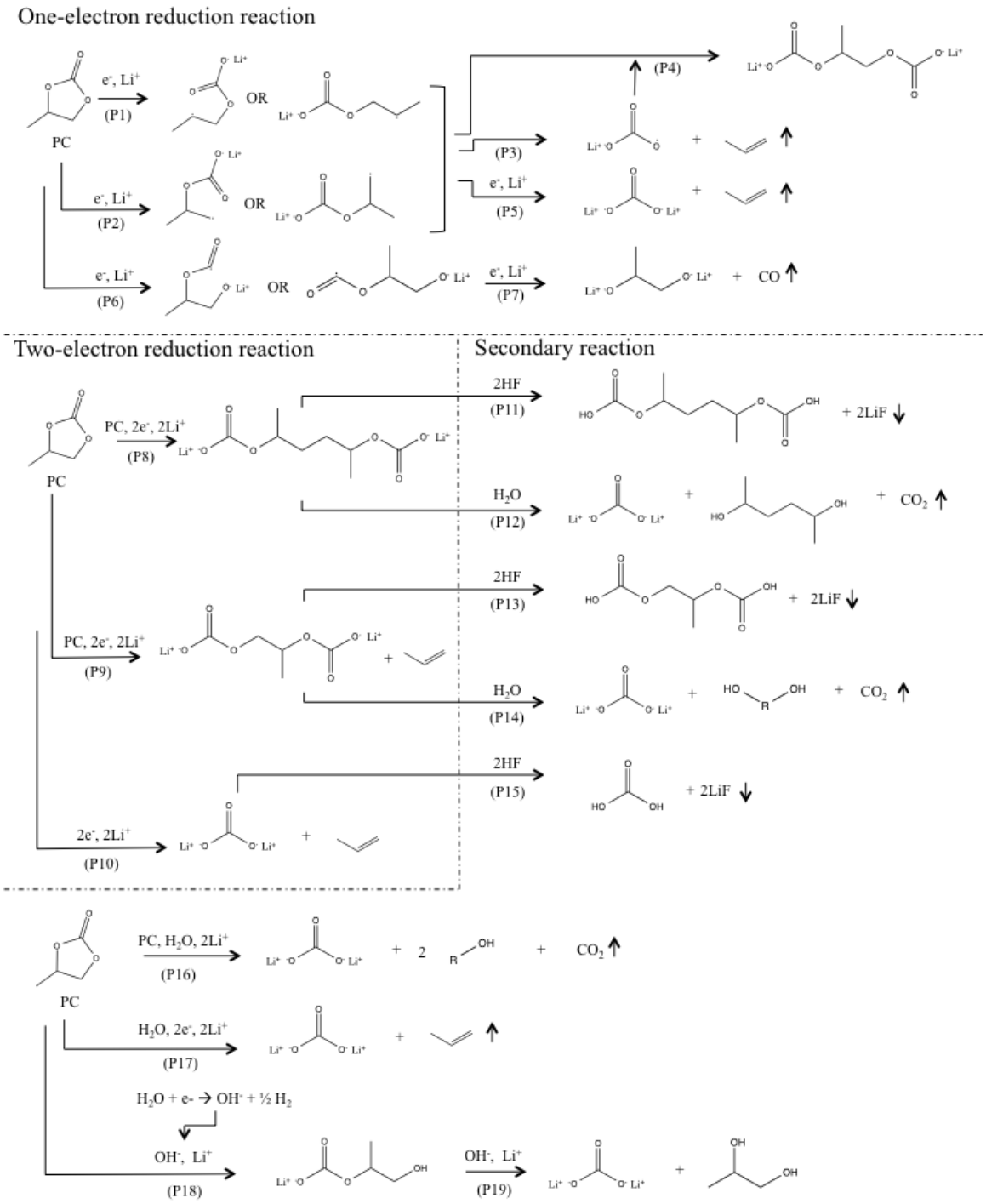


Figure 1.8. Propylene carbonate (PC) reduction process (reference groups in parentheses; details are shown in Table 1.2).

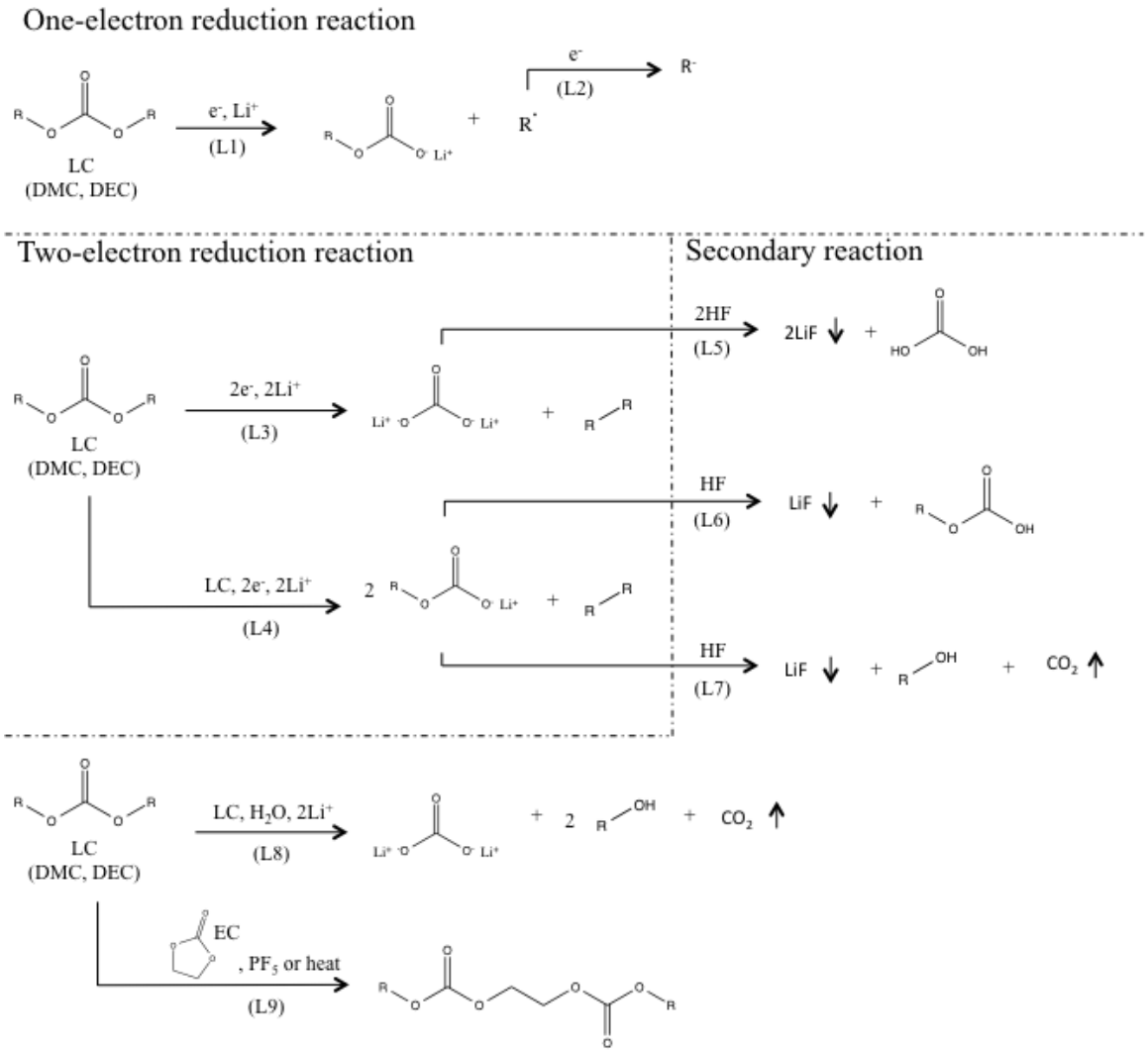


Figure 1.9. Linear carbonate (LC) reduction process (reference groups in parentheses; details are shown in Table 1.2).

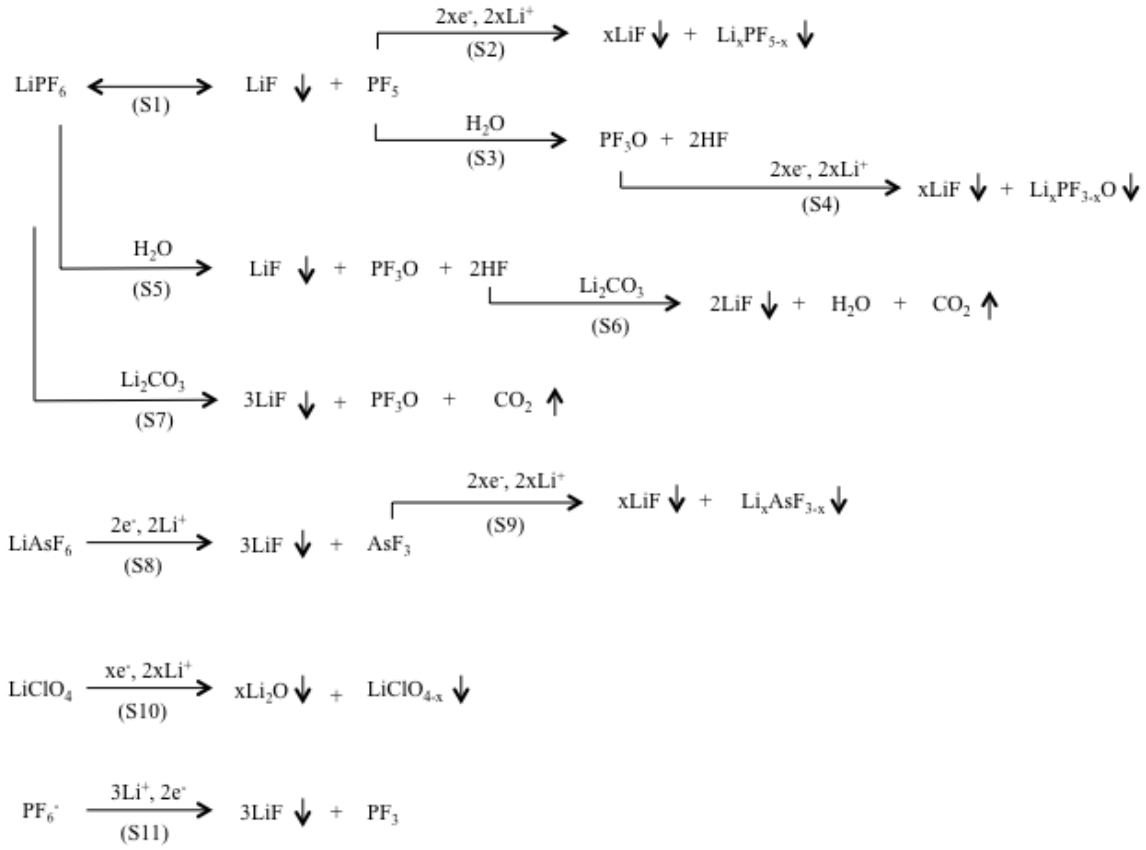


Figure 1.10. Electrolyte salt reduction process (reference groups in parentheses; details are shown in Table 1.2).

Below 0.6V vs. Li/Li^+, a much greater extent of electrolyte decomposition takes place[55]. Dense inorganic lithium compound formation (i.e. LiO_2, Li_2CO_3 and LiF) is highly favorable at edge sites because of low electronic resistance to reducing solvent-coordinated lithium ions. Some less dense inorganic species such as lithium alkali carbonates and other organic species generally decompose on basal planes where reactions are less favorable. Since electronic resistance increases when a dense inorganic film is present on the graphite surfaces, subsequent decomposition onto the inorganic compounds will involve only partial reduction resulting in precipitation of loosely aggregated compounds such as lithium alkyl carbonates, or polymers. A portion of the lithium alkyl carbonate can be further reduced to form LiO_2 or Li_2CO_3 and release ethylene (from EC), propylene (from PC), or CO_2 gases.[131] The release of these gases may cause cracks in the existing SEI layer or even expose new anode graphite surface to electrolyte for further SEI decomposition reactions (further consuming lithium inventory).

A second or even third formation charging is usually needed to completely form a stable SEI layer for long LIB lifetimes. These subsequent charging half-cycles are often at progressively faster C rates.

Prospects for improving SEI properties and reducing formation time

Reducing LIB formation protocol time is necessary to lower production cost of cells (and ultimately packs) and manufacturing capital costs. The process currently lasts from about 4-5 days up to ~2 weeks depending on the cell chemistry, and it consumes a great deal of process energy (low-grade heat and electricity). In addition, it is also a substantial process bottleneck unless an inordinate amount of formation cyclers is used. SEI formation time can be reduced four ways: 1) by mixing additives into the electrolyte to form the SEI compounds more quickly and/or alter the overall composition of the SEI layer; 2) by modifying the anode graphite surface chemistry or substitution of the inactive binder and conductive additive materials with those having better wettability; 3) by charging and discharging the cells at higher rates within certain portions of the operating voltage window; and 4) by increasing the cell temperature during wetting and SEI formation.

Besides the popular vinyl carbonate (VC) additive, fluoroethylene carbonate, diphenyloctyl phosphate, acetyl caprolactam, 3-fluoro-1,3-propane sultone, prop-1-ene-1,3-sultone, and others have been proposed recently [112, 123, 153-154] These chemicals show different advantages over VC with respect to SEI composition and stability and cell lifetime, yet they have not been shown to save time during the formation cycling process. Developing or discovering an additive with an

even higher reduction potential and high reactivity could result in reduced SEI formation time.

Anode active material surface coatings and chemical modifications can also improve SEI layer properties.[144, 176] The volume change of carbonaceous materials during lithium intercalation is much lower when compared to other anode materials such as Al, Si, Sn, and Sb.[43] It has been found that an increase in disordered carbon anode surface oxygen resulted in low graphite exfoliation and stable SEI formation.[135, 143, 177-178] Using this property, a thin carbon coating on graphite can be implemented for improving capacity retention. Non-graphitic carbons do not undergo exfoliation to a great extent, but their first-cycle irreversible capacity loss is much higher due to greater surface area. When graphite is used without a carbon coating, reversible capacity is lower; however, once coated by a high-surface-area disordered carbon, reversible capacity increases because the majority of the SEI layer forms within the thin coating. This surface modification tends to prevent extensive graphite exfoliation.[96, 136, 179]

It is plausible that SEI compounds differ not only depending on the reaction sites, such as edges vs. basal planes, but also depending on the initial surface elemental composition.
Initial precipitates on the non-oxidized graphite surfaces are likely different from those on oxidized surfaces, which could affect subsequent precipitation. Other surface modifications of various types of anode graphite have shown significant effects on SEI formation.[93-94, 136-138, 179-181]

Generally, a high charging rate during the first cycle results in a porous and highly resistive SEI layer, while a low charging rate results in the opposite SEI characteristics. It has been found that for a 0.5C charging rate during SEI formation, capacity retention at room temperature operation was negatively affected.[113] Also, when the cell temperature was held above 40°C, capacity retention was even more negatively affected for a 0.5C SEI formation charging rate.[114] Hence, a first charging rate between 0.05C and 0.2C is preferred for stable SEI formation. In some cases, though, high charging rate can be beneficial to SEI formation. For example, when TIMREX® SFG44 graphite was heat-treated in an inert gas at 3000°C, a high charge current of 320mA/g (~1C), showed better reversible capacity in 1M $LiPF_6$ EC/DMC than a much lower charge current of 10mA/g (~0.03C).[122] In this case, high current decomposed the electrolyte faster than solvents could intercalate into graphene sheets and cause exfoliation. Low charging rates may be beneficial for SEI formation, but they slow cell production rates and increase production cost and plant capital expense. Building a stable SEI with a charging rate greater than 0.5C may require a great deal of further effort on developing proper additives, optimizing cell temperature, and modifying the anode surface chemistry.

At higher temperatures, SEI formation may also be accelerated. SEI layers formed at temperatures around 40°C tend to have more compact lithium precipitates, such as Li_2CO_3 and Li_2O, rather than softer, organic precipitates like $ROCO_2Li$. However, high temperature may induce LiF precipitation from fluorine containing salts.

Recent progress in SEI layer studies and prospects for future understanding

Computational studies

Overview of molecular dynamics (MD) and density functional theory (DFT) studies

Molecular dynamics (MD) and density functional theory (DFT) simulation methods have been used to understand the intricate relationship between the SEI layer and electrolyte. The MD approach uses atomic force calculations through solving Newton's equations of motion and investigates dynamic movements and equilibrium of atoms and molecules primarily with potentials from semi-empirical relationships. While MD has provided detailed information on classical many-body problems, ab-initio molecular dynamics (AIMD) has extended MD capability by combining the Schrödinger wave equation with Newton's equations. Certain interfacial reduction and oxidation reactions have been described in the literature using AIMD.[182-188] APPLE&P (Atomistic Polarizable Potential for Liquids, Electrolytes, & Polymers) is another many-body polarizable force field for MD simulations that can capture electrostatic interactions in polarizable environments. Binding energies between lithium ions and solvent molecules may vary with different theory levels of APPLE&P force fields. For example, M05-2X and B3LYP are common levels, which are thought to have overestimated lithium-ion/$MECO_3^-$ binding energy in lithium alkyl carbonate electrolytes. The M06-L, MP2, and G4MP2 levels, on the other hand, have shown similar, and more reasonable, binding energies.[189-191]

Density functional theory (DFT) is more rigorous than MD, and the former is another computational approach in quantum mechanics that solves Schrödinger equation. It estimates the electronic structures in atomic and molecular systems, but it is limited to smaller simulation sizes than MD because of the associated computational intensity. One of the issues in using DFT is weak van-der-Waals-like forces of graphene layers, which can affect calculations for lithium-ion/solvent-molecule co-intercalation into graphite. Computed graphene interlayer binding energy significantly varies depending on DFT functionals.[192] Local-density approximation (LDA), a well-known and simple functional,

underestimates the binding energy of graphite interlayer as shown in Figure 1.11. The binding energies from experiments were 31-52meV/atom.[193-195] Another issue in using quantum simulations is that the simulations are typically not suitable for estimating competing reactions.

DFT and MD mainly deal with Angstrom and nanometer length scales, respectively. Because of the small length scales and heavy calculation load, it is extremely difficult to fully combine electrode, SEI layer, electrolyte, and all of their interactions together into a single model. Hence, the computational literature on SEI formation and physical chemistry is comprised of reactions and molecular coordination of lithium ions with one or two types of molecules. In this section, some of the SEI-related calculations are discussed.

Correlation of SEI with graphite

Jorn et al. performed ab initio molecular dynamics simulations with graphite in $LiPF_6$/EC electrolytes, while considering graphite basal and edge planes.[196] In this study, the SEI layer was composed of Li_2EDC (lithium ethylene dicarbonate) only or Li_2EDC with different amounts of LiF. They found that edge planes could accommodate more Li ions than basal planes due to the broad range of EC orientations, which might cause different SEI formation processes and structures at the two types of reaction sites. Thicker SEI layers or higher HF contents in the electrolyte resulted in a higher lithium ion concentration in the vicinity of the SEI surface, promoting higher probability of lithium ion transport from solvent to SEI. DFT calculations also showed that irreversible capacity loss (ICL) on graphite surfaces, generally on edges, having dangling bonds is higher than that on graphite surfaces having H-terminated edges.[197] This finding perhaps implies greater SEI formation thickness due to unstable graphite edges. Surface properties of graphite may also affect adhesion of the SEI to the graphite surfaces. DFT-MD simulations were carried out with probable SEI film components from EC-based electrolyte (Li_2EDC) to see their adhesion to graphite having H-terminations.[198] It was found that the adhesion to the H-terminated graphite was unstable in EC. Dissolution energies of Li_2EDC in EC were +12.2 kcal/mol.

There have been other computational approaches to understanding SEI formation and lithium-ion/solvent co-intercalation into graphene layers. DFT and MD simulations showed that half-distances between C-C (graphene) interlayers were 0.59 nm for $Li^+(EC)C_{72}$, 0.69 nm for $Li^+(EC)_4C_{72}$, 0.70 nm for $Li^+(PC)C_{72}$, and 0.85 nm for $Li^+(PC)_4C_{72}$ when no ring openings of EC or PC were assumed.[199] Half-distances between C-C interlayers were 0.325-0.335 nm with no lithium ions or solvent molecules and 0.356-0.376 nm for LiC_6.[199-202] If there were ring openings of EC or PC, the difference between the associated EC and PC C-C distances would be little because the PC methyl group would have free

rotation after the ring opening. For the case where the PC and EC molecules would not undergo ring opening during co-intercalation, $Li^+(PC)_n$ and $Li^+(EC)_n$ could cause graphite disintegration by widening the C-C layers (which experience only weak van der Waals forces), and since $Li^+(PC)_n$ is more massive than $Li^+(EC)_n$, the probability of this disintegration process could be higher for $Li^+(PC)_n$ than $Li^+(EC)_n$.

Reduction reactions

Most reduction processes take place between 0.9V and 0.2V vs Li/Li^+ on highly ordered graphite, but salt products may decompose at higher voltages according to one DFT study. LiF formation, deposition, and radical recombination were found to occur near 2V vs Li/Li^+ before the main solvent reduction reactions below 0.9V vs. Li/Li^+ for FEC or below 0.6V vs. Li/Li^+ for EC.[203] In the case of EC and PC based electrolytes, reduction energies of $Li^+(EC)_4$ were 8 kcal/mol lower than $Li^+(PC)_4$,[199] which implies that $Li^+(EC)_n$ is more prone to reduction than $Li^+(EC)_n$. Statistical and surface analyses also showed that smaller molecular-weight compounds and salt decomposed on the anode surfaces in the presence of electrolyte, followed by long-chain oligomer compounds.[204-206]

For the case of 1M $LiPF_6$ with different binary solvents such as EC:EMC, EC:DMC, or EC:DEC (1:2 volume ratio), in-situ experiments showed the released gases were in the following order of amount: $C_2H_4>CO>CH_4>C_2H_6>CO_2$.[207] Contrary to these experimental findings of greater CO than CO_2, a particular DFT study showed different results.[208] Calculations using the hybrid-level functionals B3LYP with basis set 6-311++G(d,p) showed that EC strongly coordinated with the PF_6^- anion and was prone to oxidation to the EC radical cation on cathode via 1-electron transfer. The EC radical cation was subsequently reduced on the anode and produced CO_2, aldehyde, and oligomers of alkyl carbonates. CO_2 was generated to a greater extent than CO due to the high activation energy for CO.

Regarding the common VC additive, DFT based MD simulations from Ushirogata et al. showed that VC reacted with an EC anion radical causing a one-electron reduction of EC, [182] which implies that VC assists the EC reduction process. Although exactly how VC decomposes is not yet clear, experimental and computational agreement has been found that VC increases solvent reduction reaction rates.

SEI layer composition and ion diffusion

A molecular dynamics study from Kim et al. showed that Li_2CO_3 and Li_2O were the main SEI components on anodes when EC and DMC were used as the electrolyte solvents.[51]

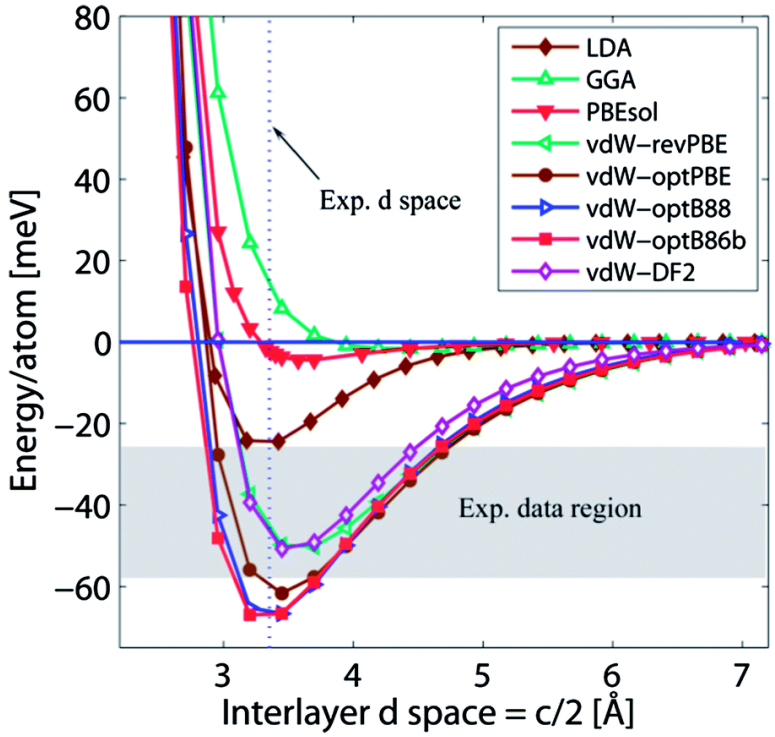


Figure 1.11. Interlayer binding energy of graphite as a function of interlayer separation calculated by LDA, GGA and five different vdW functionals,192 Reproduced from Ref. 192 with permission from The Royal Society of Chemistry.

SEI layers were found to form at about 1 V vs. Li/Li^+, and they were composed primarily of inorganic components close to the anode surface and primarily of organic ones close to the liquid electrolyte. In these simulations, however, lithium metal was considered as the anode instead of graphite. It should also be noted that the presence of electrolyte salts were not considered, and reaction gas products from the inner portion of the SEI were not allowed to diffuse outward into the liquid phase (these gases would be removed under real-world formation conditions). Hence, actual SEI layers are composed of somewhat different compounds than these particular calculated ones.

Lithium ion transport in Li_2EDC, a common component of SEI layers, was studied by EIS experiments and MD simulations with APPLE&P force field and G4MP2 and MP2 levels.[189] The conductivity of Li_2EDC at room temperature was found to be 10^{-9} S/cm from EIS analysis and 2×10^{-10} – 10^{-8} S/cm from MD simulation. The calculated activation energy ranged from 64-84 kJ/mol at 393K, indicating that lithium ion transport exhibited a hopping mechanism at high temperature.

SEI on anode metalloid or metal oxide

Metalloid or metal oxides, especially SiO_x and SnO_x, are regarded as prime candidate materials for high-energy batteries due to high theoretical capacity and earth abundance, [209-211] despite Si and Sn having higher operating potentials than graphite (around 0.4V and 0.6V vs. Li/Li^+, respectively). One of main problems, however, is that these two materials suffer from extreme volume changes during lithium intercalation and deintercalation, leading to: 1) extensive, unstable, and thick SEI formation; 2) poor long-term mechanical properties; and 3) severe capacity fade.

In order to build stable SEI layers on these materials, research has concentrated on a combined materials approach such as Si alloys [52, 209-210, 212], Sn alloys [213-216], Si-C or Sn-C composites [213, 217-230], Sn or Si composited with carbon nanomaterials [231-239], Mo-C or Ni-C [240-244], or mixing with graphene [245-247]. For these solutions, volumetric capacities drop to half of those of pure Si or Sn, but the reductions in capacity still result in anodes with much higher specific capacities than graphite. Volume changes on these composited and blended materials also become smaller, making the formed SEI layers more chemically stable and longer lasting. Coating Al_2O_3 on these materials also mitigates volume changes.[248-249]

Lithium metal is also being reconsidered as a possible anode candidate because it has the highest specific capacity, but it suffers from significant safety concerns related to lithium dendrite growth into and through the separator (electrical shorting). One reason this degradation and potential failure mechanism occurs is

because the SEI layer is not uniform and tough enough to prevent dendrite growth. Some of the proposed ways to prevent lithium dendrite growth are hollow carbon nanospheres covering surface of lithium anode, adopting an alternative salt, and electrolyte additives.[250-252]

Additives

Some additives having fluorine can also improve SEI formation on metal anode materials. For example, FEC has moved to the forefront as an attractive additive since it improves SEI layer properties and cell cycle life of metal anode systems.[253-254] It is especially effective when the when the metal particles are nanoscale.[255] Studies on understanding FEC's effect on metal anode formation mechanisms are currently ongoing.[183, 256-257]

In general, most additive research focuses on forming stable and robust SEI layers. Zhu et al., on the other hand, used polyfluoroalkyl compounds as an additive to build a micelle-like SEI layer on an anode electrode. The heads of the additive decompose on the electrode surfaces and solvophobic tails point outwards towards the electrolyte.[258] They found 4-(perfluorooctyl)-1,3-dioxolan-2-one improved capacity retention and lowered impedance in high voltage lithium ion batteries. These pre-formed SEI layers were found to protect the cathode from electrolyte decomposition as well as the anode. They also tested lithium difluorooxalatoborate, triphenylamine, and 1,4-benzodiozane-6,7-diol as a combined additive and obtained improved capacity retention and lowered impedance for a $Li_{1.2}Ni_{0.15}Mn_{0.55}Co_{0.1}O_2$ (TODA HE5050)/graphite cell.[259]

PC as an electrolyte solvent has excellent properties with the exception of exfoliating the graphite during unstable SEI formation. Wagner et al. improved anode SEI formation by using methyl vinyl sulfone (MVS) and ethyl vinyl sulfone (EVS) additives in PC.[260] These additives decomposed on graphite and built protective SEI layers before PC could intercalate and react because MVS and EVS have 1.3 eV and 1.2 eV lower LUMO energies, respectively, than PC. Unlike these "active" additives that decompose on the anode, there are other additives that prevent decomposition during cycling. For example, Chrétien et al. mixed both LiF and glyme additives ($CH_3O[CH_2CH_2O]_nCH_3$) in the electrolyte to inhibit side reactions.[261] Glymes and lithium salt compounds are more electrochemically stable than ethers and have high oxidation potentials close to 4.7 V, allowing high-voltage operation with NMC.

Prospects for future understanding

LIBs for high energy or high power demands like vehicle application require high capacity, high capacity retention, high voltage operation, low cost, low weight and volume, etc. All of these requirements are deeply related to SEI layers. Regarding capacity and capacity retention during the first few charge cycles, batteries lose approximately 10 to 15% of their capacity due to initial anode SEI formation. Afterword, irreversible capacity loss continues due to gradual SEI deposition during long-term cycling, although it is far less than the loss during initial SEI formation. The capacity loss percentage and initial SEI properties vary depending on formation conditions such as anode material surface area, surface properties of the material, anode-to-cathode capacity ratio, temperature, charge rate, charge depth, surface properties of the anode materials, salt/solvent properties, additives, and impurities. Detailed information about the effects of these properties and conditions can be found in previous sections of this paper.

High-voltage operation of LIBs does not significantly affect anode SEI formation directly, but it does have indirect effects. Cathode materials designed for operation at high cell potential (i.e. overcharged NMC or LMR-NMC) release cathode constituents (mostly Mn, some Ni, and a minor amount of Co) into the electrolyte that diffuse through the separator to the anode side, and in turn, induce more SEI formation by increasing the electron conductivity of SEI layer. High-voltage operation of cells also causes electrolyte instability (oxidation) on the cathode surfaces, and a SEI-like layer forms at the cathode that is chemically less stable than its anode counterpart. Hence, under these cell operating conditions, cell impedance increases due to both changes in the anode SEI layer and excessive growth of the cathode SEI layer.

Summary

This paper comprehensively reviews the science of SEI layer formation on carbon/graphite anode surfaces in the LIBs, including structure, morphology, chemical composition, electrochemistry, formation mechanism, and formation cycling. In order to develop shorter, more robust LIB formation protocols, which are needed to reduce cell manufacturing cost and battery plant capital investment, a thorough understanding of the relationship between state-of-the-art SEI layer compositions and capacity fade are still needed. Furthermore, new formation protocols which develop ideal SEI layers (those that consume minimal lithium inventory during formation and reduce capacity fade during long-term cell operation) in shorter time periods will require an understanding of SEI layer evolution over the LIB life, a subject which is currently not well understood. It is understood and accepted, however, that the SEI is formed by the decomposition products of the electrolyte solvent molecules and lithium salt, and

it critically affects the short-term and long-term performance of the cell. The importance of the SEI layer was given in terms of first-cycle efficiency, capacity retention, and cell cost, as well as the state of understanding of the SEI formation mechanism and methods of analysis and characterization. Various factors that affect SEI formation were also discussed such as anode materials, surface properties, formation current density, electrolyte additives, and cell temperature.

The anode SEI layer covers the graphite surfaces and shields lithium ions from the electrolyte solution, which prevents further electrolyte decomposition. This shielding property enables reversible capacity during extended charge-discharge cycling. However, the SEI formation process consumes lithium ions and electrolyte when generated, resulting in first-cycle irreversible capacity and lithium inventory losses. This irreversible capacity loss may continue if the SEI is not well formed by hindering electrolyte diffusion or allowing unwanted electron transfer from the graphite to the liquid phase.

SEI compositions and morphologies are complicated and differ depending on graphite surface properties, electrolyte, and formation conditions. Several modeling and experimental efforts are underway to address the correct pathways of these electro-reduction reactions and elucidate the debate within the LIB research community. SEI analysis is a challenging task due to its thickness being only ~3-100 nanometers and its delicate nature. A variety of traditional experimental techniques have been used for the electrochemical, morphological, and chemical analysis of the SEI layer.

The morphology and chemical makeup of an SEI is unique to the specific graphite surface and electrolyte solution pair, but it can generally be thought of as consisting of three layers: an outer porous, less-compact layer formed from the organic compounds near the liquid electrolyte zone; an inner more-compact inorganic structure adjacent to the graphite surface; and an intermixed layer with intermediate properties between the inner and outer layers.

References

1. Goodenough, J. B.; Park, K.-S., The Li-ion rechargeable battery: a perspective. *Journal of the American Chemical Society* **2013,** *135* (4), 1167-76.
2. Mohanty, D.; Li, J.; Born, R.; Maxey, L. C.; Dinwiddie, R. B.; Daniel, C.; Wood, I. I. I. D. L., Non-destructive evaluation of slot-die-coated lithium secondary battery electrodes by in-line laser caliper and IR thermography methods. *Analytical Methods* **2014,** *6* (3), 674.
3. Mohanty, D.; Huq, A.; Payzant, E. A.; Sefat, A. S.; Li, J.; Abraham, D. P.; Wood, D. L.; Daniel, C., Neutron Diffraction and Magnetic Susceptibility Studies on a High-Voltage Li1.2Mn0.55Ni0.15Co0.10O2Lithium Ion Battery Cathode: Insight into the Crystal Structure. *Chemistry of Materials* **2013,** *25* (20), 4064-4070.
4. Li, J.; Armstrong, B. L.; Daniel, C.; Kiggans, J.; Wood, D. L. r., Optimization of multicomponent aqueous suspensions of lithium iron phosphate (LiFePO4) nanoparticles and carbon black for lithium-ion battery cathodes. *Journal of colloid and interface science* **2013,** *405*, 118-24.
5. Li, J.; Armstrong, B. L.; Kiggans, J.; Daniel, C.; Wood, D. L. r., Lithium Ion Cell Performance Enhancement Using Aqueous LiFePO4 Cathode Dispersions and Polyethyleneimine Dispersant. *Journal of the Electrochemical Society* **2012,** *160* (2), A201-A206.
6. Li, J.; Daniel, C.; Wood, D. L., Materials processing for lithium-ion batteries. *Journal of Power Sources* **2011,** *196*, 2452–2460.
7. Daniel, C., Materials and Processing for Lithium-Ion Batteries. *The Journal of The Minerals, Metals & Materials Society* **2008,** *60*, 43-48.
8. Croy, J. R.; Abouimrane, A.; Zhang, Z., Next-generation lithium-ion batteries: The promise of near term advancements. *MRS Bulletin* **2014,** *39* (05), 407-415.
9. Zhang, S. S., Status, opportunities, and challenges of electrochemical energy storage. *Frontiers in Energy Research* **2013,** *1*, 1-6.
10. Tarascon, J.-M.; Armand, M., Building better batteries. *Nature* **2008,** *451*, 652-657.
11. Whittingham, M. S., Lithium Batteries and Cathode Materials. *Chemical Reviews* **2004,** *104*, 4271-4301.
12. Li, J.; Rulison, C.; Kiggans, J.; Daniel, C.; Wood, D. L. r., Superior Performance of LiFePO4 Aqueous Dispersions via Corona Treatment and Surface Energy Optimization. *Journal of the Electrochemical Society* **2012,** *159* (8), A1152-A1157.
13. Wood, D. L.; Li, J.; Mohanty, D.; Daniel, C.; Armstrong, B.; Dinwiddie, R.; Safa-Sefat, A.; Wang, H.; Trejo, R.; Gallego, N.; Contescu, C.; Howe, J.; Meisner, R.; Kiggans, J.; Brown, B., Advanced Materials Processing and Novel Characterization Methods for Low-Cost, High Energy-Density Lithium-Ion Batteries. *Advanced Automotive Battery Conference* **2013**.

14. Mohanty, D.; Sefat, A. S.; Li, J.; Meisner, R. A.; Rondinone, A. J.; Payzant, E. A.; Abraham, D. P.; Wood, D. L. r.; Daniel, C., Correlating cation ordering and voltage fade in a lithium-manganese-rich lithium-ion battery cathode oxide: a joint magnetic susceptibility and TEM study. *Physical chemistry chemical physics : PCCP* **2013,** *15* (44), 19496-509.
15. Wood, D. L.; Li, J.; Daniel, C., Prospects for reducing the processing cost of lithium ion batteries. *Journal of Power Sources* **2015,** *275*, 234-242.
16. Gallego, N. C.; Contescu, C. I.; Meyer, H. M.; Howe, J. Y.; Meisner, R. A.; Payzant, E. A.; Lance, M. J.; Yoon, S. Y.; Denlinger, M.; Wood, D. L., Advanced surface and microstructural characterization of natural graphite anodes for lithium ion batteries. *Carbon* **2014,** *72*, 393-401.
17. Xu, K., Nonaqueous Liquid Electrolytes for Lithium-Based Rechargeable Batteries. *Chem. Rev.* **2004,** *104*, 4303−4417.
18. Patil, A.; Patil, V.; Shin, D. W.; Choi, J.-W.; Paik, D.-S.; Yoon, S.-J., Issue and challenges facing rechargeable thin film lithium batteries. *Materials Research Bulletin* **2008,** *43*, 1913–1942.
19. Yazami, R.; Reynier, Y. F., Mechanism of self-discharge in graphite–lithium anode. *Electrochimica Acta* **2002,** *47*, 1217–1223.
20. Yazami, R., Surface chemistry and lithium storage capability of the graphite-lithium electrode. *Electrochimica Acta* **1999,** *45*, 87-97.
21. Goodenough, J. B.; Kim, Y., Challenges for Rechargeable Li Batteries. *Chemistry of Materials* **2010,** *22*, 587–603.
22. Wohlfahrt-Mehrens, M.; Vogler, C.; Garche, J., Aging mechanisms of lithium cathode materials. *Journal of Power Sources* **2004,** *127* (1-2), 58-64.
23. Vetter, J.; Novák, P.; Wagner, M. R.; Veit, C.; Möller, K. C.; Besenhard, J. O.; Winter, M.; Wohlfahrt-Mehrens, M.; Vogler, C.; Hammouche, A., Ageing mechanisms in lithium-ion batteries. *J. Power Sources* **2005,** *147* (1-2), 269-281.
24. Mohanty, D.; Kalnaus, S.; Meisner, R. A.; Rhodes, K. J.; Li, J.; Payzant, E. A.; Wood, D. L.; Daniel, C., Structural transformation of a lithium-rich Li1.2Co0.1Mn0.55Ni0.15O2 cathode during high voltage cycling resolved by in situ X-ray diffraction. *Journal of Power Sources* **2013,** *229*, 239-248.
25. Mohanty, D.; Sefat, A. S.; Kalnaus, S.; Li, J.; Meisner, R. A.; Payzant, E. A.; Abraham, D. P.; Wood, D. L.; Daniel, C., Investigating phase transformation in the Li1.2Co0.1Mn0.55Ni0.15O2 lithium-ion battery cathode during high-voltage hold (4.5 V) via magnetic, X-ray diffraction and electron microscopy studies. *Journal of Materials Chemistry A* **2013,** *1* (20), 6249.
26. Lu, Z.; MacNeilb, D. D.; Dahn, J. R., Layered Cathode Materials $Li[Ni_xLi_{(1/3-2x/3)}Mn_{(2/3-x/3)}]O_2$ for Lithium-Ion Batteries. *Electrochemical and Solid-State Letters* **2001,** *4* (11), A191-A194.
27. Thackeray, M. M.; Johnson, C. S.; Vaughey, J. T.; Li, N.; Hackney, S. A., Advances in manganese-oxide 'composite' electrodes for lithium-ion batteries. *Journal of Materials Chemistry* **2005,** *15*, 2257–2267.
28. Yabuuchi, N.; Yoshii, K.; Myung, S.-T.; Nakai, I.; Komaba, S., Detailed Studies of a High-Capacity Electrode Material for Rechargeable Batteries,

Li2MnO3−LiCo1/3Ni1/3Mn1/3O2. *Journal of American Chemical Society* **2011,** *133*, 4404–4419.
29. Krueger, S.; Kloepsch, R.; Li, J.; Nowak, S.; Passerini, S.; Winter, M., How Do Reactions at the Anode/Electrolyte Interface Determine the Cathode Performance in Lithium-Ion Batteries? *Journal of The Electrochemical Society* **2013,** *160*, A542-A548.
30. Amine, K.; Chen, C. H.; Liu, J.; Hammond, M.; Jansen, A.; Dees, D.; Bloom, I.; Vissers, D.; Henriksen, G., Factors responsible for impedance rise in high power lithium ion batteries. *Journal of Power Sources* **2001,** *97-98*, 684-687.
31. Sarre, G.; Blanchard, P.; Broussely, M., Aging of lithium-ion batteries. *Journal of Power Sources* **2004,** *127* (1-2), 65-71.
32. Broussely, M.; Biensan, P.; Bonhomme, F.; Blanchard, P.; Herreyre, S.; Nechev, K.; Staniewicz, R. J., Main aging mechanisms in Li ion batteries. *Journal of Power Sources* **2005,** *146* (1-2), 90-96.
33. Kostecki, R.; McLarnon, F., Degradation of LiNi[sub 0.8]Co[sub 0.2]O[sub 2] Cathode Surfaces in High-Power Lithium-Ion Batteries. *Electrochemical and Solid-State Letters* **2002,** *5* (7), A164-A166.
34. Shikano, M.; Kobayashi, H.; Koike, S.; Sakaebe, H.; Ikenaga, E.; Kobayashi, K.; Tatsumi, K., Investigation of positive electrodes after cycle testing of high-power Li-ion battery cells II. *Journal of Power Sources* **2007,** *174* (2), 795-799.
35. Rahman, M. K.; Saito, Y., Investigation of positive electrodes after cycle testing of high-power Li-ion battery cells. *Journal of Power Sources* **2007,** *174* (2), 889-894.
36. Etacheri, V.; Marom, R.; Elazari, R.; Salitra, G.; Aurbach, D., Challenges in the development of advanced Li-ion batteries: a review. *Energy Environ. Sci.* **2011,** *4*, 3243–3262
37. Aurbach, D.; Gojxjeb, H., The electrochemical behavior of selected polar aprotic systems. *Electrochemica Acta* **1989,** *34*, 141-156.
38. Wursig, A.; Buqa, H.; Holzapfel, M.; Krumeich, F.; Novák, P., Film Formation at Positive Electrodes in Lithium-Ion Batteries. *Electrochemical and Solid-State Letters* **2005,** *8*, A34-A37
39. Song, J. Y.; Lee, H. H.; Wang, Y. Y.; Wan, C. C., Two- and three-electrode impedance spectroscopy of lithium-ion batteries. *Journal of Power Sources* **2002,** *111*, 255–267.
40. Williard, N.; Sood, B.; Osterman, M.; Pecht, M., Disassembly methodology for conducting failure analysis on lithium–ion batteries. *Journal of Materials Science: Materials in Electronics* **2011,** *22* (10), 1616-1630.
41. Orsini, F.; Du Pasquier, A.; Beaudoin, B.; Tarascon, J. M.; Trentin, M.; Langenhuizen, N.; De Beer, E.; Notten, P., In situ Scanning Electron Microscopy (SEM) observation of interfaces within plastic lithium batteries. *Journal of Power Sources* **1998,** *76*, 19-29.

42. Chusid, O. Y.; Ein Ely, Y.; Aurbach, D.; Babai, M.; Carmeli, Y., Electrochemical and spectroscopic studies of carbon electrodes in lithium battery electrolyte systems. *Journal of Power Sources* **1993,** *43-44*, 47-64.
43. Scrosati, B.; Garche, J. r., Lithium batteries: Status, prospects and future. *Journal of Power Sources* **2010,** *195*, 2419–2430.
44. Markevich, E.; Salitra, G.; Fridman, K.; Sharabi, R.; Gershinsky, G.; Garsuch, A.; Semrau, G.; Schmidt, M. A.; Aurbach, D., Fluoroethylene carbonate as an important component in electrolyte solutions for high-voltage lithium batteries: role of surface chemistry on the cathode. *Langmuir : the ACS journal of surfaces and colloids* **2014,** *30* (25), 7414-24.
45. Xu, M.; Tsiouvaras, N.; Garsuch, A.; Gasteiger, H. A.; Lucht, B. L., Generation of Cathode Passivation Films via Oxidation of Lithium Bis(oxalato) Borate on High Voltage Spinel (LiNi0.5Mn1.5O4). *The Journal of Physical Chemistry C* **2014,** *118* (14), 7363-7368.
46. Bouayad, H.; Wang, Z.; Dupré, N.; Dedryvère, R.; Foix, D.; Franger, S.; Martin, J. F.; Boutafa, L.; Patoux, S.; Gonbeau, D.; Guyomard, D., Improvement of Electrode/Electrolyte Interfaces in High-Voltage Spinel Lithium-Ion Batteries by Using Glutaric Anhydride as Electrolyte Additive. *The Journal of Physical Chemistry C* **2014,** *118* (9), 4634-4648.
47. Li, X.; Chen, Y.; Nguyen, C. C.; Nie, M.; Lucht, B. L., Stability of Inactive Components of Cathode Laminates for Lithium Ion Batteries at High Potential. *Journal of the Electrochemical Society* **2014,** *161* (4), A576-A582.
48. Verma, P.; Maire, P.; Novák, P., A review of the features and analyses of the solid electrolyte interphase in Li-ion batteries. *Electrochimica Acta* **2010,** *55*, 6332–6341.
49. Aurbach, D.; Levi, M. D.; Levi, E.; Schechter, A., Failure and Stabilization Mechanisms of Graphite Electrodes. *J. Phys. Chem. B* **1997,** *101*, 2195–2206.
50. Tasaki, K.; Harris, S. J., Computational Study on the Solubility of Lithium Salts Formed on Lithium Ion Battery Negative Electrode in Organic Solvents. *J. Phys. Chem. C* **2010,** *114*, 8076-8083.
51. Kim, S.-P.; Duin, A. C. T. v.; Shenoy, V. B., Effect of electrolytes on the structure and evolution of the solid electrolyte interphase (SEI) in Li-ion batteries: A molecular dynamics study. *Journal of Power Sources* **2011,** *196* (20), 8590-8597.
52. Zheng, J.; Zheng, H.; Wang, R.; Ben, L.; Lu, W.; Chen, L.; Chen, L.; Li, H., 3D visualization of inhomogeneous multi-layered structure and Young's modulus of the solid electrolyte interphase (SEI) on silicon anodes for lithium ion batteries. *Physical chemistry chemical physics : PCCP* **2014,** *16* (26), 13229-13238.
53. Nie, M.; Lucht, B. L., Role of Lithium Salt on Solid Electrolyte Interface (SEI) Formation and Structure in Lithium Ion Batteries. *Journal of the Electrochemical Society* **2014,** *161* (6), A1001-A1006.
54. Takenaka, N.; Suzuki, Y.; Sakai, H.; Nagaoka, M., On Electrolyte-Dependent Formation of Solid Electrolyte Interphase Film in Lithium-Ion

Batteries: Strong Sensitivity to Small Structural Difference of Electrolyte Molecules. *The Journal of Physical Chemistry C* **2014,** *118* (20), 10874-10882.
55. Lu, P.; Li, C.; Schneider, E. W.; Harris, S. J., Chemistry, Impedance, and Morphology Evolution in Solid Electrolyte Interphase Films during Formation in Lithium Ion Batteries. *J. Phys. Chem. C* **2014,** *118*, 896−903.
56. Harris, S. J.; Lu, P., Effects of Inhomogeneities—Nanoscale to Mesoscale—on the Durability of Li-Ion Batteries. *J. Phys. Chem. C* **2013,** *117*, 6481-6492.
57. Nie, M.; Chalasani, D.; Abraham, D. P.; Chen, Y.; Bose, A.; Lucht, B. L., Lithium Ion Battery Graphite Solid Electrolyte Interphase Revealed by Microscopy and Spectroscopy. *The Journal of Physical Chemistry C* **2013,** *117* (3), 1257-1267.
58. Tsubouchi, S.; Domi, Y.; Doi, T.; Ochida, M.; Nakagawa, H.; Yamanaka, T.; Abe, T.; Ogumi, Z., Spectroscopic Characterization of Surface Films Formed on Edge Plane Graphite in Ethylene Carbonate-Based Electrolytes Containing Film-Forming Additives. *Journal of The Electrochemical Society* **2012,** *159*, A1786-A1790.
59. Peled, E.; Golodnitsky, D.; Menachem, C.; BarTow, D., An advanced tool for the selection of electrolyte components for rechargeable lithium batteries. *j. Electrochem. Soc.* **1998,** *145*, 3482-3486.
60. Eshkenazi, V.; Peled, E.; Burstein, L.; Golodnitsky, D., XPS analysis of the SEI formed on carbonaceous materials. *Solid State Ionics* **2004,** *170* (1-2), 83-91.
61. Peled, E.; Golodnitsky, D.; Ulus, A.; Yufit, V., Effect of carbon substrate on SEI composition and morphology. *Electrochimica Acta* **2004,** *50* (2-3), 391-395.
62. Leroy, S.; Martinez, H.; Dedryve`re, R.; Lemordant, D.; Gonbeau, D., Influence of the lithium salt nature over the surface film formation on a graphite electrode in Li-ion batteries: An XPS study. *Applied Surface Science* **2007,** *253*, 4895–4905.
63. Peled, E.; Golodnitsky, D.; Ardel, G., Advanced Model for Solid Electrolyte Interphase Electrodes in Liquid and Polymer Electrolyte. *J. Electrochem. Soc.* **1997,** *144*, L208-L210.
64. Naoi, K.; Ogihara, N.; Igarashi, Y.; Kamakura, A.; Kusachi, Y.; Utsugi, K., Disordered Carbon Anode for Lithium-Ion Battery - I. An Interfacial Reversible Redox Action and Anomalous Topology Changes. *Journal of The Electrochemical Society* **2005,** *152*, A1047-A1053.
65. Tokranov, A.; Sheldon, B. W.; Lu, P.; Xiao, X.; Mukhopadhyay, A., The Origin of Stress in the Solid Electrolyte Interphase on Carbon Electrodes for Li Ion Batteries. *Journal of The Electrochemical Society* **2014,** *161*, A58-A65.
66. Zhang, H.-L.; Li, F.; Liu, C.; Tan, J.; Cheng, H.-M., New Insight into the Solid Electrolyte Interphase with Use of a Focused Ion Beam. *J. Phys. Chem. B* **2005,** *109*, 22205-22211.

67. Aurbach, D., Review of selected electrode–solution interactions which determine the performance of Li and Li ion batteries. *J. Power Sources* **2000,** *89* 206-218.
68. Mori, S.; Asahina, H.; Suzuki, H.; Yonei, A.; Yokoto, K., Chemical properties of various organic electrolytes for lithium rechargeable batteries: 1. Characterization of passivating layer formed on graphite in alkyl carbonate solutions. *J. Power Sources* **1997,** *68*, 59-64.
69. Aurbach, D.; Moshkovich, M., A Study of Lithium Deposition-Dissolution Processes in a Few Selected Electrolyte Solutions by Electrochemical Quartz Crystal Microbalance. *J. Electrochem. Soc.* **1998,** *145*, 2629-2639.
70. Peled, E.; Bar Tow, D.; Merson, A.; Gladkich, A.; Burstein, L.; Golodnitsky, D., Composition, Depth Profiles and Lateral Distribution of Materials in the SEI Built on HOPG-TOF SIMS and XPS Studies. *J. Power Sources* **2001,** *97–98*, 52-57.
71. Augustsson, A.; Herstedt, M.; Guo, J. H.; Edstrom, K.; Zhuang, G. V.; Ross, P. N.; Rubensson, J. E.; Nordgren, J., Solid electrolyte interphase on graphite Li-ion battery anodes studied by soft X-ray spectroscopy. *Phys. Chem. Chem. Phys.* **2004,** *6*, 4185-4189.
72. Aurbach, D., Electrode–solution interactions in Li-ion batteries: a short summary and new insights. *J. Power Sources* **2003,** *119–121* 497-503.
73. Peled, E.; Golodnitsky, D.; Menachem, C.; BarTow, D., An advanced tool for the selection of electrolyte components for rechargeable lithium batteries. *J. Electrochem .Soc.* **1998,** *145*, 3482-3486.
74. Aurbach, D.; Einely, Y.; Zaban, A., The surface chemistry of lithium electrodes in alkyl carbonate solutions. *J. Electrochem. Soc.* **1994,** *141*, L1-L3.
75. Morigaki, K.-I.; Ohta, A., Analysis of the surface of lithium in organic electrolyte by atomic force microscopy, Fourier transform infrared spectroscopy and scanning auger electron microscopy. *J. Power Sources* **1998,** *76*, 159-166.
76. Bar-Tow, D.; Peled, E.; Burstein, L., A Study of Highly Oriented Pyrolytic Graphite as a Model for the Graphite Anode in Li-Ion Batteries. *J. Electrochem. Soc.* **1999,** *146*, 824-832.
77. Kanamura, K.; Tamura, H.; Takehara, Z., In-situ electrogeneration of [2,2′-ethylenebis(nitrilomethylidyne)diphenolato]nickelate(I) — nickel(I) salen — as a catalyst for reductive intramolecular cyclizations of 6-iodo- and 6-bromo-1-phenyl-1-hexyne. *J. Electroanal. Chem.* **1992,** *333* 127-134.
78. Odziemkowski, M.; Irish, D. E., An Electrochemical Study of the Reactivity at the Lithium Electrolyte/Bare Lithium Metal Interface: II . Unpurified Solvents. *J. Electrochem. Soc.* **1993,** *140*, 1546-1555.
79. Aurbach, D.; Markovsky, B.; Weissman, I.; Levi, E.; Ein-Eli, Y., On the correlation between surface chemistry and performance of graphite negative electrodes for Li ion batteries. *Electrochim. Acta* **1999,** *45*, 67–86.
80. Kominato, A.; Yasukawa, E.; Sato, N.; Ijuuin, T.; Asahina, H.; Mori, S., Analysis of surface films on lithium in various organic electrolytes. *J. Power Sources* **1997,** *68*, 471-475.

81. Pasquier, A. D.; Disma, F.; Bowmer, T.; Gozdz, A. S.; Amatucci, G.; Tarascon, J. M., Differential Scanning Calorimetry Study of the Reactivity of Carbon Anodes in Plastic Li-Ion Batteries. *J. Electrochem. Soc.* **1998,** *145*, 472-477.
82. Lee, H. H.; Wan, C. C.; Wang, Y. Y., Thermal Stability of the Solid Electrolyte Interface on Carbon Electrodes of Lithium Batteries. *J. Electrochem. Soc.* **2004,** *151*, A542-A547.
83. Aurbach, D.; Gofer, Y.; Benzion, M.; Aped, P., The behaviour of lithium electrodes in propylene and ethylene carbonate: Te major factors that influence Li cycling efficiency. *J. Electroanal. Chem.* **1992,** *339* 451-471.
84. Zhuang, G. R.; Chen, Y. F.; Ross, P. N., The Reaction of Lithium with Dimethyl Carbonate and Diethyl Carbonate in Ultrahigh Vacuum Studied by X-ray Photoemission Spectroscopy. *Langmuir : the ACS journal of surfaces and colloids* **1999,** *15*, 1470–1479.
85. Alliata, D.; Kotz, R.; Novák, P.; Siegenthaler, H., Electrochemical SPM investigation of the solid electrolyte interphase film formed on HOPG electrodes. *Electrochemistry Communications* **2000,** *2*, 436–440.
86. Richard, M. N.; Dahn, J. R., Accelerating Rate Calorimetry Study on the Thermal Stability of Lithium Intercalated Graphite in Electrolyte. I. Experimental. *J. Electrochem. Soc.* **1999,** *146* 2068-2077.
87. MacNeil, D. D.; Larcher, D.; Dahn, J. R., Comparison of the Reactivity of Various Carbon Electrode Materials with Electrolyte at Elevated Temperature. *J. Electrochem. Soc.* **1999,** *146*, 3596-3602.
88. Joho, F.; Novák, P.; Spahr, M. E., Safety Aspects of Graphite Negative Electrode Materials for Lithium-Ion Batteries. *J. Electrochem. Soc.* **2002,** *149* A1020-A1024.
89. Aurbach, D.; Cohen, Y., The application of Atomic Force Microscopy for the Study of Li Deposition Porcesses. *J. Electrochem. Soc.* **1996,** *143*, 3525-3532.
90. Aurbach, D.; Daroux, M. L.; Faguy, P. W.; Yeager, E., Identification of Surface Films Formed on Lithium in Propylene Carbonate Solutions. *J. Electrochem .Soc.* **1987,** *134*, 1611-1620.
91. Leroy, S.; Blanchard, F.; Dedryvere, R.; Martinez, H.; Carre, B.; Lemordant, D.; Gonbeau, D., Surface film formation on a graphite electrode in Li-ion batteries: AFM and XPS study. *Surface and Interface Analysis* **2005,** *37* (10), 773-781.
92. Tasaki, K.; Kanda, K.; Nakamura, S.; Ue, M., Decomposition of LiPF6 and Stability of PF5 in Li-Ion Battery Electrolytes. *Journal of The Electrochemical Society* **2003,** *150*, A1628-A1636
93. Peled, E.; Menachem, C.; Bar-Tow, D.; Melman, A., Improved Graphite Anode for Lithium-Ion Batteries, Chemicaly Bonded Solid Electrolyte Interface and Nanochanel Formation. *J. Electrochem. Soc.* **1995,** *143*, L4-L7.
94. Loebl, A. J.; Oldham, C. J.; Devine, C. K.; Gong, B.; Atanasov, S. E.; Parsons, G. N.; Fedkiw, P. S., Solid Electrolyte Interphase on Lithium-Ion Carbon

Nanofiber Electrodes by Atomic and Molecular Layer Deposition. *Journal of The Electrochemical Society* **2013,** *160*, A1971-A1978
95. Jeong, S.-K.; Inaba, M.; Abe, T.; Ogumi, Z., Surface Film Formation on Graphite Negative Electrode in Lithium-Ion Batteries: AFM Study in an Ethylene Carbonate-Based Solution. *Journal of The Electrochemical Society* **2001,** *148*, A989-A993.
96. Bernardo, P.; Le Meins, J. M.; Vidal, L.; Dentzer, J.; Gadiou, R.; Märkle, W.; Novák, P.; Spahr, M. E.; Vix-Guterl, C., Influence of graphite edge crystallographic orientation on the first lithium intercalation in Li-ion battery. *Carbon* **2015,** *91*, 458-467.
97. Bhattacharya, S.; Riahi, A. R.; Alpas, A. T., Thermal cycling induced capacity enhancement of graphite anodes in lithium-ion cells. *Carbon* **2014,** *67*, 592-606.
98. Yan, J.; Zhang, J.; Su, Y.-C.; Zhang, X.-G.; Xia, B.-J., A novel perspective on the formation of the solid electrolyte interphase on the graphite electrode for lithium-ion batteries. *Electrochimica Acta* **2010,** *55*, 1785-1794.
99. Park, M.; Zhang, X.; Chung, M.; Less, G. B.; Sastry, A. M., A review of conduction phenomena in Li-ion batteries. *Journal of Power Sources* **2010,** *195*, 7904–7929.
100. Endo, E.; Ata, M.; Tanaka, K.; Sekai, K., Electron Spin Resonance Study of the Electrochemical Reduction of Electrolyte Solutions for Lithium Secondary Batteries. *J. Electrochem .Soc.* **1998,** *145*, 3757-3764.
101. Dey, A. N.; Sullivan, B. P., The Electrochemical Decomposition of Propylene Carbonate on Graphite. *J. Electrochem .Soc.* **1970,** *117*, 222.
102. Besenhard, J. O.; Winter, M.; Yang, J.; Biberacher, W., Filming mechanism of lithium-carbon anodes in organic and inorganic electrolytes. *Journal of Power Sources* **1995,** *54*, 228-231.
103. Chung, G.-C.; Kim, H.-J.; Yu, S.-I.; Jun, S.-H.; Choi, J.-W.; Kim, M.-H., Origin of Graphite Exfoliation An Investigation of the Important Role of Solvent Cointercalation. *J. Electrochem .Soc.* **2000,** *147*, 4391-4398.
104. Aurbach, D.; Zaban, A., Impedance spectroscopy of lithium electrodes-Part 1- General behavior in propylene carbonate solutions and the correlation to surface chemistry and cycling efficiency. *J. Electroanal. Chem.* **1993,** *348*, 155-179.
105. Aurbach, D.; Gamolsky, K.; Markovsky, B.; Gofer, Y.; Schmidt, M.; Heider, U., On the use of vinylene carbonate (VC) as an additive to electrolyte solutions for Li-ion batteries. *Electrochimica Acta* **2002,** *47*, 1423–1439.
106. Aurbach, D.; Gofer, Y.; Langzam, J., The Correlation Between Surface Chemistry, Surface Morphology, and Cycling Efficiency of Lithium Electrodes in a Few Polar Aprotic Systems. *J. Electrochem .Soc.* **1989,** *136*, 3198-3205.
107. Reeves, S. D.; Morris, R. S., Improved MCMB Anodes by Surface Modification with Self-Assembling Nonionic Surfactants. *Electrochemical and Solid-State Letters* **2004,** *7*, B29-B30.

108. Wang, C.; Appleby, A. J.; Little, F. E., Irreversible capacities of graphite anode for lithium-ion batteries. *Journal of Electroanalytical Chemistry* **2002,** *519*, 9–17.
109. Xu, K., Whether EC and PC Differ in Interphasial Chemistry on Graphitic Anode and How. *Journal of The Electrochemical Society* **2009,** *156*, A751-A755.
110. Marino, C.; Darwiche, A.; Dupre, N.; Wilhelm, H. A.; Lestriez, B.; Martinez, H.; Dedryveѐre, R.; Zhang, W.; Ghamouss, F.; Lemordant, D.; Monconduit, L., Study of the Electrode/Electrolyte Interface on Cycling of a Conversion Type Electrode Material in Li Batteries. *J. Phys. Chem. C* **2013,** *117*, 19302−19313.
111. Lee, H.-H.; Wang, Y.-Y.; Wan, C.-C.; Yang, M.-H.; Wu, H.-C.; Shieh, D.-T., A fast formation process for lithium batteries. *Journal of Power Sources* **2004,** *134*, 118–123.
112. Park, I.-J.; Nam, T.-H.; Kim, J.-G., Diphenyloctyl phosphate as a solid electrolyte interphase forming additive for Li-ion batteries. *Journal of Power Sources* **2013,** *244*, 122-128.
113. Huang, C.; Huang, K.; Wang, H.; Liu, S.; Zeng, Y., The effect of solid electrolyte interface formation conditions on the aging performance of Li-ion cells. *J Solid State Electrochem* **2011,** *15*, 1987–1995.
114. He, Y.-B.; Li, B.; Yang, Q.-H.; Du, H.; Kang, F.; Ling, G.-W.; Tang, Z.-Y., Effects of current densities on the formation of LiCoO2/graphite lithium ion battery. *J Solid State Electrochem* **2011,** *15*, 1977–1985.
115. Lei, J.; Li, L.; Kostecki, R.; Muller, R.; McLarnon, F., Characterization of SEI Layers on LiMn2O4 Cathodes with In Situ Spectroscopic Ellipsometry. *Journal of The Electrochemical Society* **2005,** *152*, A774-A777
116. Zheng, M.-S.; Dong, Q.-F.; Cai, H.-Q.; Jin, M.-G.; Lin, Z.-G.; Sun, S.-G., Formation and Influence Factors of Solid Electrolyte Interphase Film on the Negative Electrode Surface in Lithium-Ion Batteries. *Journal of The Electrochemical Society* **2005,** *152*, A2207-A2210.
117. Tavassol, H.; Buthker, J. W.; Ferguson, G. A.; Curtiss, L. A.; Gewirth, A. A., Solvent Oligomerization during SEI Formation on Model Systems for Li-Ion Battery Anodes. *Journal of The Electrochemical Society* **2012,** *159*, A730-A738.
118. Nie, M.; Abraham, D. P.; Seo, D. M.; Chen, Y.; Bose, A.; Lucht, B. L., Role of Solution Structure in Solid Electrolyte Interphase Formation on Graphite with LiPF6 in Propylene Carbonate. *J. Phys. Chem. C* **2013,** *117*, 25381−25389.
119. Wang, L.; Deng, X.; Dai, P.-X.; Guo, Y.-G.; Wang, D.; Wan, L.-J., Initial solid electrolyte interphase formation process of graphite anode in LiPF6 electrolyte: an in situ ECSTM investigation. *Phys. Chem. Chem. Phys.* **2012,** *14*, 7330–7336.
120. Ng, S. H.; Vix-Guterl, C.; Bernardo, P.; Tran, N.; Ufheil, J.; Buqa, H.; Dentzer, J.; Gadiou, R.; Spahr, M. E.; Goers, D.; Novák, P., Correlations between surface properties of graphite and the first cycle specific charge loss in lithium-ion batteries. *CARBON* **2009,** *47*, 705–712.

121. Bhattacharya, S.; Alpas, A. T., Micromechanisms of solid electrolyte interphase formation on electrochemically cycled graphite electrodes in lithium-ion cells. *CARBON* **2012,** *50*, 5359–5371.
122. Markle, W.; Lu, C.-Y.; Novák, P., Morphology of the Solid Electrolyte Interphase on Graphite in Dependency on the Formation Current. *Journal of The Electrochemical Society* **2011,** *158*, A1478-A1482.
123. Li, B.; Wang, Y.; Rong, H.; Wang, Y.; Liu, J.; Xing, L.; Xu, M.; Li, W., A novel electrolyte with the ability to form a solid electrolyte interface on the anode and cathode of a LiMn2O4/graphite battery. *Journal of Materials Chemistry A* **2013,** *1*, 12954-12961.
124. Herstedt, M.; Andersson, A. M.; Rensmo, H.; Siegbahn, H.; Edstro¨m, K., Characterisation of the SEI formed on natural graphite in PC-based electrolytes. *Electrochimica Acta* **2004,** *49*, 4939–4947.
125. Lee, S.-B.; Pyun, S.-I., The effect of electrolyte temperature on the passivity of solid electrolyte interphase formed on a graphite electrode. *Carbon* **2002,** *40*, 2333–2339.
126. Zhu, L.; Hommet, F.; Salace, G.; Claude-Montigny, B.; Metrot, A., STM observation of the electro-adsorption of lithium ions onto graphite and of the ensuing solid electrolyte interphase formation. *Surface Science* **2002,** *512*, 84–96.
127. Zeng, Z.; Liang, W.-I.; Liao, H.-G.; Xin, H. L.; Chu, Y.-H.; Zheng, H., Visualization of Electrode−Electrolyte Interfaces in LiPF6/EC/DEC Electrolyte for Lithium Ion Batteries via in Situ TEM. *Nano Lett.* **2014,** *14*, 1745−1750.
128. Gu, M.; Parent, L. R.; Mehdi, B. L.; Unocic, R. R.; McDowell, M. T.; Sacci, R. L.; Xu, W.; Connell, J. G.; Xu, P.; Abellan, P.; Chen, X.; Zhang, Y.; Perea, D. E.; Evans, J. E.; Lauhon, L. J.; Zhang, J.-G.; Liu, J.; Browning, N. D.; Cui, Y.; Arslan, I.; Wang, C.-M., Demonstration of an Electrochemical Liquid Cell for Operando Transmission Electron Microscopy Observation of the Lithiation/ Delithiation Behavior of Si Nanowire Battery Anodes. *Nano Lett.* **2013,** *13*, 6106−6112.
129. Mehdi, B. L.; Gu, M.; Parent, L. R.; Xu, W.; Nasybulin, E. N.; Chen, X.; Unocic, R. R.; Xu, P.; Welch, D. A.; Abellan, P.; Zhang, J.-G.; Liu, J.; Wang, C.-M.; Arslan, I.; Evans, J.; Browning, N. D., In-Situ Electrochemical Transmission Electron Microscopy for Battery Research. *Microscopy and Microanalysis* **2014,** *20*, 484-492.
130. Owejan, J. E.; Owejan, J. P.; DeCaluwe, S. C.; Dura, J. A., Solid Electrolyte Interphase in Li-Ion Batteries: Evolving Structures Measured In situ by Neutron Reflectometry. *Chem. Mater.* **2012,** *24*, 2133−2140.
131. Bridges, C. A.; Sun, X.-G.; Zhao, J.; Paranthaman, M. P.; Dai, S., In Situ Observation of Solid Electrolyte Interphase Formation in Ordered Mesoporous Hard Carbon by Small-Angle Neutron Scattering. *J. Phys. Chem. C* **2012,** *116*, 7701−7711.

132. Joho, F.; Rykart, B.; Blome, A.; Novák, P., Relation between surface properties, pore structure and first-cycle charge loss of graphite as negative electrode in lithium-ion batteries. *Journal of Power Sources* **2001,** *97*, 78-82.
133. Li, M.; Wu, Y.; Zhao, F.; Wei, Y.; Wang, J.; Jiang, K.; Fan, S., Cycle and rate performance of chemically modified super-aligned carbon nanotube electrodes for lithium ion batteries. *Carbon* **2014,** *69*, 444-451.
134. Novák, P.; Ufheil, J.; Buqa, H.; Krumeich, F.; Spahr, M. E.; Goers, D.; Wilhelm, H.; Dentzer, J.; Gadiou, R.; Vix-Guterl, C., The importance of the active surface area of graphite materials in the first lithium intercalation. *Journal of Power Sources* **2007,** *174*, 1082–1085.
135. Spahr, M. E.; Wilhelm, H.; Palladino, T.; Dupont-Pavlovsky, N.; Goers, D.; Joho, F.; Novák, P., The role of graphite surface group chemistry on graphite exfoliation during electrochemical lithium insertion. *Journal of Power Sources* **2003,** *119-121*, 543-549.
136. Yoshio, M.; Wang, H.; Fukuda, K.; Hara, Y.; Adachi, Y., Effect of Carbon Coating on Electrochemical Performance of Treated Natural Graphite as Lithium-Ion Battery Anode Material. *Journal of The Electrochemical Society* **2000,** *147*, 1245-1250.
137. Wu, Y.; Jiang, C.; Wan, C.; Tsuchida, E., Effects of catalytic oxidation on the electrochemical performance of common natural graphite as an anode material for lithium ion batteries. *Electrochemistry Communications* **2000,** *2*, 272–275.
138. Wu, Y. P.; Jiang, C.; Wan, C.; Holze, R., Anode materials for lithium ion batteries by oxidative treatment of common natural graphite. *Solid State Ionics* **2003,** *156*, 283–290.
139. Rafiee, J.; Mi, X.; Gullapalli, H.; Thomas, A. V.; Yavari, F.; Shi, Y.; Ajayan, P. M.; Koratkar, N. A., Wetting transparency of graphene. *Nature materials* **2012,** *11*, 217–222.
140. Peled, E., The Electrochemical Behavior of Alkali and Alkaline Earth Metals in Nonaqueous Battery Systems-The Solid Electrolyte Interphase Model. *Journal of the electrochemical society* **1979,** *126*, 2047-2051.
141. Christensen, J.; Newman, J., A Mathematical Model for the Lithium-Ion Negative Electrode Solid Electrolyte Interphase. *Journal of The Electrochemical Society* **2004,** *151*, A1977-A1988.
142. Colclasure, A. M.; Smith, K. A.; Kee, R. J., Modeling detailed chemistry and transport for solid-electrolyte-interface (SEI) films in Li–ion batteries. *Electrochimica Acta* **2011,** *58*, 33–43.
143. Ein-Eli, Y.; Koch, V. R., Chemical Oxidation: A Route to Enhanced Capacity in Li-Ion Graphite Anodes. *J. Electrochem. Soc.* **1997,** *144*, 2968-2973.
144. Collins, J.; Gourdin, G.; Foster, M.; Qu, D., Carbon surface functionalities and SEI formation during Li intercalation. *Carbon* **2015,** *92*, 193-244.
145. Yan, J.; Xia, B.-J.; Su, Y.-C.; Zhou, X.-Z.; Zhang, J.; Zhang, X.-G., Phenomenologically modeling the formation and evolution of the solid electrolyte

interface on the graphite electrode for lithium-ion batteries. *Electrochimica Acta* **2008,** *53*, 7069–7078.
146. Abraham, K. M., Directions in secondary lithium battery research and development. *electrochemica Acta* **1993,** *38*, 1233-1248.
147. Zhang, S. S.; Xu, K.; Jow, T. R., EIS study on the formation of solid electrolyte interface in Li-ion battery. *Electrochimica Acta* **2006,** *51* (8-9), 1636-1640.
148. Ping, P.; Wang, Q.; Sun, J.; Feng, X.; Chen, C., Effect of sulfites on the performance of LiBOB/γ-butyrolactone electrolytes. *Journal of Power Sources* **2011,** *196* (2), 776-783.
149. Cui, X.; Zhang, H.; Li, S.; Li, X.; Feng, H., Electrochemical performances of a novel lithium bis(oxalate)borate-based electrolyte for lithium-ion batteries with LiFePO4 cathodes. *Ionics* **2014,** *20* (6), 789-794.
150. Tasaki, K.; Kanda, K.; Kobayashi, T.; Nakamura, S.; Ue, M., Theoretical Studies on the Reductive Decompositions of Solvents and Additives for Lithium-Ion Batteries near Lithium Anodes. *Journal of The Electrochemical Society* **2006,** *153*, A2192-A2197
151. Flandroisa, S.; Simon, B., Carbon materials for lithium-ion rechargeable batteries. *Carbon* **1999,** *37*, 165–180.
152. Lee, S.-H.; You, H.-G.; Han, K.-S.; Kim, J.; Jung, I.-H.; Song, J.-H., A new approach to surface properties of solid electrolyte interphase on a graphite negative electrode. *Journal of Power Sources* **2014,** *247*, 307-313.
153. Yoon, S.; Kim, H.; Cho, J.-J.; Han, Y.-K.; Lee, H., Lactam derivatives as solid electrolyte interphase forming additives for a graphite anode of lithium-ion batteries. *Journal of Power Sources* **2013,** *244*, 711-715.
154. Jung, H. M.; Park, S.-H.; Jeon, J.; Choi, Y.; Yoon, S.; Cho, J.-J.; Oh, S.; Kang, S.; Han, Y.-K.; Lee, H., Fluoropropane sultone as an SEI-forming additive that outperforms vinylene carbonate. *Journal of Materials Chemistry A* **2013,** *1*, 11975–11981
155. Wang, Y.; Nakamura, S.; Ue, M.; Balbuena, P. B., Theoretical Studies To Understand Surface Chemistry on Carbon Anodes for Lithium-Ion Batteries: Reduction Mechanisms of Ethylene Carbonate. *J. Am. Chem. Soc.* **2001,** *123*, 11708-11718.
156. Wang, Y.; Nakamura, S.; Tasaki, K.; Balbuena, P. B., Theoretical Studies To Understand Surface Chemistry on Carbon Anodes for Lithium-Ion Batteries: How Does Vinylene Carbonate Play Its Role as an Electrolyte Additive? *J. AM. CHEM. SOC.* **2002,** *124*, 4408-4421.
157. Fong, R.; Sacken, U. y.; Dahn, J. R., Studies of Lithium Intercalation into Carbons Using Nonaqueous Electrochemical Cells. *Journal of The Electrochemical Society* **1990,** *137*, 2009-2013.
158. Epelboin, I.; Froment, M.; Garreau, M.; Thevenin, J.; Warin, D., Behavior of Secondary Lithium and Aluminum-Lithium Electrode in Propylene Carbonate. *J. Electrochem. Soc.* **1980,** *127*, 2100-2104.

159. Crowther, O.; West, A. C., Effect of Electrolyte Composition on Lithium Dendrite Growth. *Journal of The Electrochemical Society* **2008,** *155*, A806-A811
160. Arakawa, M.; Tobishima, S.-i.; Nemoto, Y.; Ichimura, M.; Yamaki, J.-I., Lithium electrode cycleability and morphology dependence on current density. *Journal of Power Sources* **1993,** *43-44*, 27-35.
161. Brandt, K., Historical development of secondary lithium batteries. *Solid State Ionics* **1994,** *69*, 173-183.
162. TRAN, T. D.; FEIKERT, J. H.; PEKALA, R. W., Rate effect on lithium-ion graphite electrode performance. *Journal of Applied Electrochemistry* **1996,** *26*, 1161-1167.
163. Bhattacharya, S.; Riahi, A. R.; Alpas, A. T., Role of Voltage Scan Rate on Degradation of Graphite Electrodes Electrochemically Cycled vs. Li/Li+. *MRS Proceedings* **2012,** *1388*, 1-6.
164. Zhang, X.; Kostecki, R.; Richardson, T. J.; Pugh, J. K.; Ross, P. N., Electrochemical and Infrared Studies of the Reduction of Organic Carbonates. *Journal of The Electrochemical Society* **2001,** *148* (12), A1341-A1345.
165. Aurbach, D.; Markovsky, B.; Shechter, A.; Ein-Eli, Y.; Cohen, H., A comparative sutdy of synthetic graphite and Li ectrodes in Electrolyte Solutions Based on Ethylene Carbonate-Dimethyl Carbonate Mixtures. *J. Electrochem. Soc.* **1996,** *143*, 3809-3820.
166. Eriksson, T.; Andersson, A. M.; Bishop, A. G.; Gejke, C.; Gustafsson, T. r.; Thomas, J. O., Surface Analysis of LiMn[sub 2]O[sub 4] Electrodes in Carbonate-Based Electrolytes. *Journal of The Electrochemical Society* **2002,** *149* (1), A69-A78.
167. Aurbach, D., Review of selected electrode–solution interactions which determine the performance of Li and Li ion batteries. *Journal of Power Sources* **2000,** *89*, 206–218.
168. Aurbach, D.; Zaban, A.; Ein-Eli, Y.; Weissman, I.; Chusid, O.; Markovsky, B.; Levi, M.; Levi, E.; Schechter, A.; Granot, E., Recent studies on the correlation between surface chemistry, morphology, three-dimensional structures and performance of Li and Li-C intercalation anodes in several important electrolyte systems. *Journal of Power Sources* **1997,** *68*, 91-98.
169. Kawamura, T.; Kimura, A.; Egashira, M.; Okada, S.; Yamaki, J.-I., Thermal stability of alkyl carbonate mixed-solvent electrolytes for lithium ion cells. *Journal of Power Sources* **2002,** *104*, 260-264.
170. Sloop, S. E.; Pugh, J. K.; Wang, S.; Kerr, J. B.; Kinoshita, K., Chemical Reactivity of PF[sub 5] and LiPF[sub 6] in Ethylene Carbonate/Dimethyl Carbonate Solutions. *Electrochemical and Solid-State Letters* **2001,** *4* (4), A42-A44.
171. Agubra, V. A.; Fergus, J. W., The formation and stability of the solid electrolyte interface on the graphite anode. *Journal of Power Sources* **2014,** *268*, 153-162.
172. Agubra, V. A.; Fergus, J. W.; Fu, R.; Choe, S.-y., Analysis of the Deposit Layer from Electrolyte Side Reaction on the Anode of the Pouch Type Lithium

Ion Polymer Batteries: The Effect of State of Charge and Charge Rate. *Electrochimica Acta* **2014,** *149*, 1-10.
173. Agubra, V. A.; Fergus, J. W.; Fu, R.; Choe, S.-Y., Analysis of effects of the state of charge on the formation and growth of the deposit layer on graphite electrode of pouch type lithium ion polymer batteries. *Journal of Power Sources* **2014,** *270*, 213-220.
174. Thackeray, M. M.; Dekock, A.; Rossouw, M. H.; Liles, D.; Bittihn, R.; Hoge, D., Spinel Electrodes from the Li-Mn-O System for Rechargeable Lithium Battery Applications. *J. Electrochem .Soc.* **1992,** *139*, 363-366.
175. Padhi, A. K.; Nanjundaswamy, K. S.; Goodenough, J. B., Phospho-olivines as Positive-Electrode Materials for Rechargeable Lithium Batteries. *J. Electrochem .Soc.* **1997,** *144*, 1188-1194.
176. Bhattacharya, S.; Riahi, A. R.; Alpas, A. T., Electrochemical cycling behaviour of lithium carbonate (Li2CO3) pre-treated graphite anodes – SEI formation and graphite damage mechanisms. *Carbon* **2014,** *77*, 99-112.
177. Spahr, M. E.; Wilhelm, H.; Joho, F.; Panitz, J.-C.; Wambach, J. r.; Novák, P.; Dupont-Pavlovsky, N., Purely Hexagonal Graphite and the Influence of Surface Modifications on Its Electrochemical Lithium Insertion Properties. *Journal of The Electrochemical Society* **2002,** *149* (8), A960-A966.
178. Han, Y.-J.; Kim, J.; Yeo, J.-S.; An, J. C.; Hong, I.-P.; Nakabayashi, K.; Miyawaki, J.; Jung, J.-D.; Yoon, S.-H., Coating of graphite anode with coal tar pitch as an effective precursor for enhancing the rate performance in Li-ion batteries: Effects of composition and softening points of coal tar pitch. *Carbon* **2015,** *94*, 432-438.
179. Kuribayashi, I.; Yokoyama, M.; Yamashita, M., Battery characteristics with various carbonaceous materials. *Journal of Power Sources* **1995,** *54*, 1-5.
180. Zhan, Y.; Zhang, B.; Cao, L.; Wu, X.; Lin, Z.; Yu, X.; Zhang, X.; Zeng, D.; Xie, F.; Zhang, W.; Chen, J.; Meng, H., Iodine doped graphene as anode material for lithium ion battery. *Carbon* **2015,** *94*, 1-8.
181. Ye, J. C.; Charnvanichborikarn, S.; Worsley, M. A.; Kucheyev, S. O.; Wood, B. C.; Wang, Y. M., Enhanced electrochemical performance of ion-beam-treated 3D graphene aerogels for lithium ion batteries. *Carbon* **2015,** *85*, 269-278.
182. Ushirogata, K.; Sodeyama, K.; Okuno, Y.; Tateyama, Y., Additive effect on reductive decomposition and binding of carbonate-based solvent toward solid electrolyte interphase formation in lithium-ion battery. *Journal of the American Chemical Society* **2013,** *135* (32), 11967-74.
183. Leung, K.; Rempe, S. B.; Foster, M. E.; Ma, Y.; Martinez del la Hoz, J. M.; Sai, N.; Balbuena, P. B., Modeling Electrochemical Decomposition of Fluoroethylene Carbonate on Silicon Anode Surfaces in Lithium Ion Batteries. *Journal of the Electrochemical Society* **2013,** *161* (3), A213-A221.
184. Leung, K., Two-electron reduction of ethylene carbonate: A quantum chemistry re-examination of mechanisms. *Chemical Physics Letters* **2013,** *568-569*, 1-8.

185. Leung, K., First-Principles Modeling of the Initial Stages of Organic Solvent Decomposition on LixMn2O4(100) Surfaces. *The Journal of Physical Chemistry C* **2012,** *116* (18), 9852-9861.
186. Leung, K.; Budzien, J., Ab initio Molecular Dynamics Simulations of the Initial Stages of Solid-electrolyte Interphase Formation on Lithium Ion Battery Graphitic Anodes. *Physical Chemistry Chemical Physics* **2010,** *12*, 6583-6586.
187. Blint, R. J., Binding of Ether and Carbonyl Oxygens to Lithium Ion. *J. Electrochem. Soc.* **1995,** *142*, 696-702.
188. Bhatt, M. D.; Cho, M.; Cho, K., Density functional theory calculations andab initiomolecular dynamics simulations for diffusion of Li+within liquid ethylene carbonate. *Modelling and Simulation in Materials Science and Engineering* **2012,** *20* (6), 065004.
189. Borodin, O.; Zhuang, G. V.; Ross, P. N.; Xu, K., Molecular Dynamics Simulations and Experimental Study of Lithium Ion Transport in Dilithium Ethylene Dicarbonate. *The Journal of Physical Chemistry C* **2013,** *117* (15), 7433-7444.
190. von Wald Cresce, A.; Borodin, O.; Xu, K., Correlating Li+Solvation Sheath Structure with Interphasial Chemistry on Graphite. *The Journal of Physical Chemistry C* **2012,** *116* (50), 26111-26117.
191. Borodin, O.; Smith, G. D., Quantum Chemistry and Molecular Dynamics Simulation Study of Dimethyl Carbonate: Ethylene Carbonate Electrolytes Doped with LiPF6. *J. Phys. Chem. B* **2009,** *113*, 1763–1776.
192. Wang, Z.; Selbach, S. M.; Grande, T., Van der Waals density functional study of the energetics of alkali metal intercalation in graphite. *RSC Adv.* **2014,** *4* (8), 3973-3983.
193. Liu, Z.; Liu, J. Z.; Cheng, Y.; Li, Z.; Wang, L.; Zheng, Q., Interlayer binding energy of graphite: A mesoscopic determination from deformation. *Physical Review B* **2012,** *85* (20).
194. Zacharia, R.; Ulbricht, H.; Hertel, T., Interlayer cohesive energy of graphite from thermal desorption of polyaromatic hydrocarbons. *Physical Review B* **2004,** *69* (15).
195. Benedict, L. X.; Chopra, N. G.; Cohen, M. L.; Zettl, A.; Louie, S. G.; Crespi, V. H., Microscopic determination of the interlayer binding energy in graphite. *Chemical Physics Letters* **1998,** *286*, 490-496.
196. Jorn, R.; Kumar, R.; Abraham, D. P.; Voth, G. A., Atomistic Modeling of the Electrode–Electrolyte Interface in Li-Ion Energy Storage Systems: Electrolyte Structuring. *The Journal of Physical Chemistry C* **2013,** *117* (8), 3747-3761.
197. Omichi, K.; Ramos-Sanchez, G.; Rao, R.; Pierce, N.; Chen, G.; Balbuena, P. B.; Harutyunyan, A. R., Origin of Excess Irreversible Capacity in Lithium-Ion Batteries Based on Carbon Nanostructures. *Journal of The Electrochemical Society* **2015,** *162* (10), A2106-A2115.
198. Ushirogata, K.; Sodeyama, K.; Futera, Z.; Tateyama, Y.; Okuno, Y., Near-Shore Aggregation Mechanism of Electrolyte Decomposition Products to Explain

Solid Electrolyte Interphase Formation. *Journal of The Electrochemical Society* **2015,** *162* (14), A2670-A2678.
199. Tasaki, K.; Goldberg, A.; Winter, M., On the difference in cycling behaviors of lithium-ion battery cell between the ethylene carbonate- and propylene carbonate-based electrolytes. *Electrochimica Acta* **2011,** *56* (28), 10424-10435.
200. Persson, K.; Hinuma, Y.; Meng, Y. S.; Van der Ven, A.; Ceder, G., Thermodynamic and kinetic properties of the Li-graphite system from first-principles calculations. *Physical Review B* **2010,** *82* (12).
201. Qi, Y.; Guo, H.; Hector, L. G.; Timmons, A., Threefold Increase in the Young's Modulus of Graphite Negative Electrode during Lithium Intercalation. *Journal of The Electrochemical Society* **2010,** *157* (5), A558.
202. Kganyago, K. R.; Ngoepe, P. E., Structural and electronic properties of lithium intercalated graphiteLiC6. *Physical Review B* **2003,** *68* (20).
203. Borodin, O.; Olguin, M.; Spear, C.; Leiter, K.; Knap, J.; Yushin, G.; Childs, A.; Xu, K., Challenges with Quantum Chemistry-Based Screening of Electrochemical Stability of Lithium Battery Electrolytes. *ECS Transactions* **2015,** *69* (1), 113-123.
204. Gourdin, G.; Zheng, D.; Qu, D., Adaption of kinetics to solid electrolyte interphase layer formation and application to electrolyte-soluble reaction products. *Journal of Power Sources* **2015,** *299*, 451-459.
205. Gourdin, G.; Collins, J.; Zheng, D.; Foster, M.; Qu, D., Spectroscopic Compositional Analysis of Electrolyte during Initial SEI Layer Formation. *The Journal of Physical Chemistry C* **2014,** *118* (31), 17383-17394.
206. Aurbach, D.; Markovsky, B.; Levi, M. D.; Levi, E.; Schechter, A.; Moshkovich, M.; Cohen, Y., New insights into the interactions between electrode materials and electrolyte solutions for advanced nonaqueous batteries. *Journal of Power Sources* **1999,** *81–82*, 95–111.
207. Teng, X.; Zhan, C.; Bai, Y.; Ma, L.; Liu, Q.; Wu, C.; Wu, F.; Yang, Y.; Lu, J.; Amine, K., In Situ Analysis of Gas Generation in Lithium-Ion Batteries with Different Carbonate-Based Electrolytes. *ACS applied materials & interfaces* **2015,** *7* (41), 22751-5.
208. Xing, L.; Li, W.; Wang, C.; Gu, F.; Xu, M.; Tan, C.; Yi, J., Theoretical Investigations on Oxidative Stability of Solvents and Oxidative Decomposition Mechanism of Ethylene Carbonate for Lithium Ion Battery Use. *J. Phys. Chem. B* **2009,** *113*, 16596–16602.
209. Liang, B.; Liu, Y.; Xu, Y., Silicon-Based Materials as High Capacity Anodes for Next Generation Lithium Ion Batteries. *J. Power Sources* **2014,** *267*, 469-490.
210. Su, X.; Wu, Q.; Li, J.; Xiao, X.; Lott, A.; Lu, W.; Sheldon, B. W.; Wu, J., Silicon-Based Nanomaterials for Lithium-Ion Batteries: A Review. *Advanced Energy Materials* **2014,** *4* (1), 1-23.
211. Goriparti, S.; Miele, E.; De Angelis, F.; Di Fabrizio, E.; Proietti Zaccaria, R.; Capiglia, C., Review on Recent Progress of Nanostructured Anode Materials for Li-ion Batteries. *J. Power Sources* **2014,** *257*, 421-443.

212. Li, M.; Gu, J.; Feng, X.; He, H.; Zeng, C., Amorphous-silicon@silicon oxide/chromium/carbon as an anode for lithium-ion batteries with excellent cyclic stability. *Electrochimica Acta* **2015,** *164*, 163-170.
213. Xu, Y.; Zhu, Y.; Liu, Y.; Wang, C., Electrochemical Performance of Porous Carbon/Tin Composite Anodes for Sodium-Ion and Lithium-Ion Batteries. *Advanced Energy Materials* **2013,** *3* (1), 128-133.
214. Ehinon, K. K. D.; Naille, S.; Dedryve`re, R.; Lippens, P.-E.; Jumas, J.-C.; Gonbeau, D., Ni3Sn4 Electrodes for Li-Ion Batteries- Li−Sn Alloying Process and Electrode Electrolyte Interface Phenomena. *Chem. Mater.* **2008,** *20*, 5388–5398.
215. Zhu, X. J.; Guo, Z. P.; Zhang, P.; Du, G. D.; Zeng, R.; Chen, Z. X.; Li, S.; Liu, H. K., Highly porous reticular tin–cobalt oxide composite thin film anodes for lithium ion batteries. *Journal of Materials Chemistry* **2009,** *19* (44), 8360-8365.
216. Mouyane, M.; Aldon, L.; Womes, M.; Ducourant, B.; Jumas, J. C.; Olivier-Fourcade, J., Tin dispersed in an oxide matrix as negative electrode material for Li-ion batteries. *Journal of Power Sources* **2009,** *189* (1), 818-822.
217. Ji, L.; Tan, Z.; Kuykendall, T.; An, E. J.; Fu, Y.; Battaglia, V.; Zhang, Y., Multilayer nanoassembly of Sn-nanopillar arrays sandwiched between graphene layers for high-capacity lithium storage. *Energy & Environmental Science* **2011,** *4* (9), 3611-3616.
218. Wang, G.; Wang, B.; Wang, X.; Park, J.; Dou, S.; Ahn, H.; Kim, K., Sn/graphene nanocomposite with 3D architecture for enhanced reversible lithium storage in lithium ion batteries. *Journal of Materials Chemistry* **2009,** *19* (44), 8378-8384.
219. Hu, R.; Liu, H.; Zeng, M.; Wang, H.; Zhu, M., Core/shell and multi-scale structures enhance the anode performance of a Sn–C–Ni composite thin film in a lithium ion battery. *Journal of Materials Chemistry* **2011,** *21* (12), 4629-4635.
220. Mouyane, M.; Ruiz, J. M.; Artus, M.; Cassaignon, S.; Jolivet, J. P.; Caillon, G.; Jordy, C.; Driesen, K.; Scoyer, J.; Stievano, L.; Olivier-Fourcade, J.; Jumas, J. C., Carbothermal synthesis of Sn-based composites as negative electrode for lithium-ion batteries. *Journal of Power Sources* **2011,** *196* (16), 6863-6869.
221. Li, N.; Song, H.; Cui, H.; Wang, C., Sn@graphene grown on vertically aligned graphene for high-capacity, high-rate, and long-life lithium storage. *Nano Energy* **2014,** *3*, 102-112.
222. Li, W.; Yang, R.; Zheng, J.; Li, X., Tandem plasma reactions for Sn/C composites with tunable structure and high reversible lithium storage capacity. *Nano Energy* **2013,** *2* (6), 1314-1321.
223. Xu, Y.; Liu, Q.; Zhu, Y.; Liu, Y.; Langrock, A.; Zachariah, M. R.; Wang, C., Uniform nano-Sn/C composite anodes for lithium ion batteries. *Nano letters* **2013,** *13* (2), 470-474.
224. Yun, Q.; Qin, X.; Lv, W.; He, Y.-B.; Li, B.; Kang, F.; Yang, Q.-H., “Concrete” inspired construction of a silicon/carbon hybrid electrode for high performance lithium ion battery. *Carbon* **2015,** *93*, 59-67.

225. Wu, J.; Qin, X.; Zhang, H.; He, Y.-B.; Li, B.; Ke, L.; Lv, W.; Du, H.; Yang, Q.-H.; Kang, F., Multilayered silicon embedded porous carbon/graphene hybrid film as a high performance anode. *Carbon* **2015,** *84*, 434-443.
226. Li, X.-H.; He, Y.-B.; Miao, C.; Qin, X.; Lv, W.; Du, H.; Li, B.; Yang, Q.-H.; Kang, F., Carbon coated porous tin peroxide/carbon composite electrode for lithium-ion batteries with excellent electrochemical properties. *Carbon* **2015,** *81*, 739-747.
227. Zhang, F.; Yang, X.; Xie, Y.; Yi, N.; Huang, Y.; Chen, Y., Pyrolytic carbon-coated Si nanoparticles on elastic graphene framework as anode materials for high-performance lithium-ion batteries. *Carbon* **2015,** *82*, 161-167.
228. Joe, M.; Han, Y.-K.; Lee, K.-R.; Mizuseki, H.; Kim, S., An ideal polymeric C60 coating on a Si electrode for durable Li-ion batteries. *Carbon* **2014,** *77*, 1140-1147.
229. Kim, A. Y.; Kim, J. S.; Hudaya, C.; Xiao, D.; Byun, D.; Gu, L.; Wei, X.; Yao, Y.; Yu, R.; Lee, J. K., An elastic carbon layer on echeveria-inspired SnO2 anode for long-cycle and high-rate lithium ion batteries. *Carbon* **2015,** *94*, 539-547.
230. Ma, C.; Ma, C.; Wang, J.; Wang, H.; Shi, J.; Song, Y.; Guo, Q.; Liu, L., Exfoliated graphite as a flexible and conductive support for Si-based Li-ion battery anodes. *Carbon* **2014,** *72*, 38-46.
231. Yu, Y.; Gu, L.; Lang, X.; Zhu, C.; Fujita, T.; Chen, M.; Maier, J., Li storage in 3D nanoporous Au-supported nanocrystalline tin. *Advanced materials* **2011,** *23* (21), 2443-2447.
232. Luo, B.; Wang, B.; Li, X.; Jia, Y.; Liang, M.; Zhi, L., Graphene-confined Sn nanosheets with enhanced lithium storage capability. *Advanced materials* **2012,** *24* (26), 3538-3543.
233. Zhou, X.; Wan, L. J.; Guo, Y. G., Binding SnO2 nanocrystals in nitrogen-doped graphene sheets as anode materials for lithium-ion batteries. *Advanced materials* **2013,** *25* (15), 2152-2157.
234. Wang, Y.; Wu, M.; Jiao, Z.; Lee, J. Y., Sn@CNT and Sn@C@CNT nanostructures for superior reversible lithium ion storage. *Chemistry of Materials* **2009,** *21* (14), 3210-3215.
235. Nobili, F.; Meschini, I.; Mancini, M.; Tossici, R.; Marassi, R.; Croce, F., High-performance Sn@carbon nanocomposite anode for lithium-ion batteries: Lithium storage processes characterization and low-temperature behavior. *Electrochimica Acta* **2013,** *107*, 85-92.
236. Zhang, L.; Wu, H. B.; Liu, B.; Lou, X. W., Formation of porous SnO2 microboxes via selective leaching for highly reversible lithium storage. *Energy & Environmental Science* **2014,** *7* (3), 1013-1017.
237. Tian, Q.; Zhang, Z.; Yang, L.; Hirano, S.-i., Three-dimensional wire-in-tube hybrids of tin dioxide and nitrogen-doped carbon for lithium ion battery applications. *Carbon* **2015,** *93*, 887-895.
238. Sun, L.; Wang, X.; Susantyoko, R. A.; Zhang, Q., High performance binder-free Sn coated carbon nanotube array anode. *Carbon* **2015,** *82*, 282-287.

239. Yao, F.; Li, B.; So, K.; Chang, J.; Ly, T. H.; Vu, A. Q.; Mun, H.; Cojocaru, C. S.; Yue, H.; Xie, S.; Lee, Y. H., A strategy to overcome the limits of carbon-based materials as lithium-ion battery anodes. *Carbon* **2014,** *79*, 563-571.
240. Ihsan, M.; Wang, H.; Majid, S. R.; Yang, J.; Kennedy, S. J.; Guo, Z.; Liu, H. K., MoO2/Mo2C/C spheres as anode materials for lithium ion batteries. *Carbon* **2016,** *96*, 1200-1207.
241. Xu, X.; Tan, H.; Xi, K.; Ding, S.; Yu, D.; Cheng, S.; Yang, G.; Peng, X.; Fakeeh, A.; Kumar, R. V., Bamboo-like amorphous carbon nanotubes clad in ultrathin nickel oxide nanosheets for lithium-ion battery electrodes with long cycle life. *Carbon* **2015,** *84*, 491-499.
242. Liu, H.; Li, Z.; Liang, Y.; Fu, R.; Wu, D., Facile synthesis of MnO multi-core@nitrogen-doped carbon shell nanoparticles for high performance lithium-ion battery anodes. *Carbon* **2015,** *84*, 419-425.
243. Susantyoko, R. A.; Wang, X.; Fan, Y.; Xiao, Q.; Fitzgerald, E.; Pey, K. L.; Zhang, Q., Stable cyclic performance of nickel oxide–carbon composite anode for lithium-ion batteries. *Thin Solid Films* **2014,** *558*, 356-364.
244. Susantyoko, R. A.; Wang, X.; Xiao, Q.; Fitzgerald, E.; Zhang, Q., Sputtered nickel oxide on vertically-aligned multiwall carbon nanotube arrays for lithium-ion batteries. *Carbon* **2014,** *68*, 619-627.
245. Kang, C.; Baskaran, R.; Hwang, J.; Ku, B.-C.; Choi, W., Large scale patternable 3-dimensional carbon nanotube–graphene structure for flexible Li-ion battery. *Carbon* **2014,** *68*, 493-500.
246. Rangasamy, B.; Hwang, J. Y.; Choi, W., Multi layered Si–CuO quantum dots wrapped by graphene for high-performance anode material in lithium-ion battery. *Carbon* **2014,** *77*, 1065-1072.
247. Zhang, J.; Xie, Z.; Li, W.; Dong, S.; Qu, M., High-capacity graphene oxide/graphite/carbon nanotube composites for use in Li-ion battery anodes. *Carbon* **2014,** *74*, 153-162.
248. Wang, D.; Yang, J.; Liu, J.; Li, X.; Li, R.; Cai, M.; Sham, T.-K.; Sun, X., Atomic layer deposited coatings to significantly stabilize anodes for Li ion batteries: effects of coating thickness and the size of anode particles. *Journal of Materials Chemistry A* **2014,** *2* (7), 2306-2312.
249. Yu, M.; Wang, A.; Wang, Y.; Li, C.; Shi, G., An alumina stabilized ZnO-graphene anode for lithium ion batteries via atomic layer deposition. *Nanoscale* **2014,** *6* (19), 11419-24.
250. Zheng, G.; Lee, S. W.; Liang, Z.; Lee, H. W.; Yan, K.; Yao, H.; Wang, H.; Li, W.; Chu, S.; Cui, Y., Interconnected hollow carbon nanospheres for stable lithium metal anodes. *Nature nanotechnology* **2014,** *9* (8), 618-23.
251. Bouchet, R., A stable lithium metal interface. *Nature nanotechnology* **2014,** *9*, 572-573.
252. Shkrob, I. A.; Marin, T. W.; Zhu, Y.; Abraham, D. P., Why Bis(fluorosulfonyl)imide Is a “Magic Anion” for Electrochemistry. *The Journal of Physical Chemistry C* **2014,** *118* (34), 19661-19671.

253. Etacheri, V.; Haik, O.; Goffer, Y.; Roberts, G. A.; Stefan, I. C.; Fasching, R.; Aurbach, D., Effect of fluoroethylene carbonate (FEC) on the performance and surface chemistry of Si-nanowire Li-ion battery anodes. *Langmuir* **2012,** *28* (1), 965-976.
254. Choi, N.-S.; Yew, K. H.; Lee, K. Y.; Sung, M.; Kim, H.; Kim, S.-S., Effect of fluoroethylene carbonate additive on interfacial properties of silicon thin-film electrode. *J. Power Sources* **2006,** *161* (2), 1254-1259.
255. Eom, K.; Jung, J.; Lee, J. T.; Lair, V.; Joshi, T.; Lee, S. W.; Lin, Z.; Fuller, T. F., Improved stability of nano-Sn electrode with high-quality nano-SEI formation for lithium ion battery. *Nano Energy* **2015,** *12*, 314-321.
256. Shkrob, I. A.; Wishart, J. F.; Abraham, D. P., What Makes Fluoroethylene Carbonate Different? *The Journal of Physical Chemistry C* **2015,** *119* (27), 14954-14964.
257. Martinez de la Hoz, J. M.; Soto, F. A.; Balbuena, P. B., Effect of the Electrolyte Composition on SEI Reactions at Si Anodes of Li-Ion Batteries. *The Journal of Physical Chemistry C* **2015,** *119* (13), 7060-7068.
258. Zhu, Y.; Casselman, M. D.; Li, Y.; Wei, A.; Abraham, D. P., Perfluoroalkyl-substituted ethylene carbonates: Novel electrolyte additives for high-voltage lithium-ion batteries. *Journal of Power Sources* **2014,** *246*, 184-191.
259. Zhu, Y.; Li, Y.; Bettge, M.; Abraham, D. P., Electrolyte additive combinations that enhance performance of high-capacity Li1.2Ni0.15Mn0.55Co0.1O2–graphite cells. *Electrochimica Acta* **2013,** *110*, 191-199.
260. Wagner, R.; Brox, S.; Kasnatscheew, J.; Gallus, D. R.; Amereller, M.; Cekic-Laskovic, I.; Winter, M., Vinyl sulfones as SEI-forming additives in propylene carbonate based electrolytes for lithium-ion batteries. *Electrochemistry Communications* **2014,** *40*, 80-83.
261. Chrétien, F.; Jones, J.; Damas, C.; Lemordant, D.; Willmann, P.; Anouti, M., Impact of Solid Electrolyte Interphase lithium salts on cycling ability of Li-ion battery: Beneficial effect of glymes additives. *Journal of Power Sources* **2014,** *248*, 969-977.

CHAPTER II
LONG-TERM LITHIUM-ION BATTERY PERFORMANCE IMPROVEMENT VIA ULTRAVIOLET LIGHT TREATMENT OF THE GRAPHITE ANODE

A version of this chapter was originally published by Seong Jin An, Jianlin Li, Yangping Sheng, Claus Daniel and David L.Wood III:

Seong Jin An, Jianlin Li, Yangping Sheng, Claus Daniel and David L.Wood III "Long-Term Lithium-Ion Battery Performance Improvement via Ultraviolet Light Treatment of the Graphite Anode" *Journal of The Electrochemical Society*, 163 (2016): A2866-A2875.

This chapter includes additional results and discussions besides the published contents. The sections for the additions are "Changes on graphite surfaces after UV treatment" and "Changes in PVDF after UV treatment". Abstract, Introduction, and Conclusion are also updated to take account of the added results. All experiments, data analysis, and initial draft for this article were done by Seong Jin An. The draft was improved and finalized by Seong Jin An, Jianlin Li, and David L. Wood III. All other co-authors provided comments on contents.

Abstract

Effects of ultraviolet (UV) light on dried graphite anodes were investigated in terms of the cycle life of lithium ion batteries. The time variations for the UV treatment were 0 (no treatment), 20, 40, and 60 minutes. UV-light-treated graphite anodes were assembled for cycle life tests in pouch cells with pristine $Li_{1.02}Ni_{0.50}Mn_{0.29}Co_{0.19}O_2$ (NMC 532) cathodes. UV treatment for 40 minutes resulted in the highest capacity retention and the lowest resistance after the cycle life testing. X-ray photoelectron spectroscopy (XPS) and contact angle measurements on the graphite anodes showed changes in surface chemistry and wetting after the UV treatment. XPS also showed increases in solvent products and decreases in salt products on the SEI surface when UV-treated anodes were used. The thickness of the surface films and their compositions on the anodes and cathodes were also estimated using survey scans and snapshots from XPS depth profiles. To understand chemistry changes on pristine anode right after UV treatment (before cell assemblies for any testing), pristine graphite powders and polyvinylidene fluoride (PVDF) films (components of anode) with and without UV treatment were individually analyzed. XPS analysis showed a 300% increase in atomic percentage of oxygen on graphite powder surfaces after the UV treatment; however, fluorine level decreased at the PVDF film by more than 10%. The PVDF film also expanded in thickness by 3.7% after the 40 min-UV treatment, indicating scissions at polymer backbones. The changes in PVDF weight, thickness, and fluorine atomic percentage from XPS peaks also indicated the release of fluorine compound gas (e.g., hydrogen fluoride and tetrafluoroethylene gas) after crosslink and scission at the PVDF polymer. Although UV light decomposed PVDF, it helped to increase the oxygen level on graphite, which, resulted in a thin SEI layer, low resistance, and eventually high

capacity retention. Hence, this chapter proved that UV treatment delivered more advantages than disadvantages.

Introduction

Lithium ion batteries (LIBs) are commonly used as power sources for portable devices. They are also a key to improving the economic and environmental sustainability of vehicles. Many automotive companies and research institutions worldwide are trying to produce affordable plug-in electric vehicles by reducing the cost, volume, and weight of LIBs while concurrently improving the batteries' power, energy, and durability. [1-4] Improving the performance of LIBs would aid the transition to a light-duty fleet of hybrid electric vehicles and plug-in electric vehicles, which could reduce oil dependence and greenhouse gas emissions. [5-7]

During LIB production processes, the wetting and formation cycles are the most important processes affecting the quality of solid electrolyte interphase (SEI) formation, utilization of electrochemical redox reactions, and even cycle life. [8-9] Particularly, because graphite is hydrophobic, [10] the electrolyte wetting process takes from a few hours to a few tens of hours, depending on the size and number of battery cells. Because of the hydrophobic nature of graphite, electrodes, especially their pores, do not wet quickly with electrolyte. Thus, the use of a vacuum environment is preferred to accelerate electrolyte wetting into graphite electrode pores [11]; this requires additional equipment and energy.

The surface of the graphite plays an important role in electrolyte wettability, reduction potential, and SEI formation.[8, 10, 12-13] For example, heat or acid treatment of graphite surfaces changes oxygen levels and affects SEI formation and reversible capacity.[14] Effects of other surface treatments on SEI formation have also been reported.[15-18] Increasing hydrophilicity of hydrophobic graphite improves electrolyte wetting, especially in small pores.[19] In the polymer industry, carbon nanotubes have been used as strength-enhancing materials in polymer structures,[20] but the carbon nanotubes do not disperse well in the polymer matrix because their surfaces are hydrophobic like graphite. Collins et al. found that carbon nanotube surfaces exhibit extreme oxygen sensitivity,[21] but Savage et al. and M. Lebron-Colon et al. showed that UV and acid treatment can control oxygen levels on these surfaces to improve hydrophilicity, resulting in better wettability.[22-23] Naoi et al. study also showed that oxygen atoms on carbon surfaces interacted with lithium ion electrolyte more because they induce high electron density around oxygen atoms and polarities.[24] This interaction may affect electrolyte wetting on the graphite surfaces. Oxygen atoms on graphite surfaces also seem to play an important role in stable SEI formation. According to heat treatment studies, heat-treated graphite particles under inert gas atmosphere resulted in low oxygen contents on the graphite surfaces and

exfoliations during formation cycles while the exfoliations were mitigated after they were oxidized again.[25-26] Treatments with chemicals such as HNO_3 and $(NH_2)_2S_2O_8$ also increased oxygen levels on carbon particles and caused an increase in the reversible capacity.[27] On the other hand, a recent study showed that natural graphite having high oxygen contents had less capacity retention than the graphite having lower oxygen contents. But, when the graphite further lost oxygen, the capacity retention slightly decreased, which, however, was still higher than the natural graphite.[28] Hence, optimum oxygen content levels (or types of oxygen contents) on graphite surfaces seem to exist for the SEI formation and cycle life although types of oxygen functional groups on a graphite surface and their functionality are still not fully understood.

Since acid can destroy graphite structures, ultraviolet (UV) light in air atmosphere was chosen in this study to control oxygen levels on anode graphite surfaces. Furthermore, it is believed that the UV process can be inserted immediately following an electrode coating process so that the electrode can be continuously produced without a significant modification of other existing processes. To the best of our knowledge, UV treatment has not been used in battery applications although this technique is commonly used in carbon fiber reinforced polymer industries. UV light was applied to common graphite anodes to improve their wettability by the electrolyte and enable uniform and stable SEI formation and extended cycle life. Full cells in pouch form were prepared for preliminary testing with 600 aging cycles and detailed testing with 300 aging cycles. The graphite anodes were exposed to UV light for varying periods of time prior to the full cell assembly. $Li_{1.02}Ni_{0.50}Mn_{0.29}Co_{0.19}O_2$ (NMC 532, also called NCM 523) cathodes without UV treatment were used as cathodes for all of the full cells. C-rate and cycle life tests were conducted for electrochemical performance evaluation. Electrochemical impedance spectroscopy (EIS) and x-ray photoelectron spectroscopy (XPS) were adopted to investigate resistance and analyze the surface elements, respectively. XPS depth profiles were used to estimate SEI thicknesses and compositions. Graphite particles and PVDF polymer were individually treated under UV light so that the effect of UV on each of them could be separated. XPS was used to analyze element changes on surfaces of graphite powders and PVDF polymer films. A high precision balance and caliper were used to measure weight and thickness changes of the materials.

Experimental

Anode and cathode electrodes were coated on one side of copper and aluminum foils, respectively, using a slot-die coater (Frontier Industrial Tech.). To avoid bending the single-side electrodes during cell assembly, a calendering process was not applied. The cell chemistry and construction are given in Table 2.1. To treat the graphite anodes, 5000-EC UV curing lamps (Dymax Corp.) were used.

Table 2.1 Cell information

	Composition	Electrode size (loading)
Anode	Electrode: 92 wt % A12 graphite (ConocoPhillips), 2 wt % C-65 carbon black (Timcal), 6 wt % polyvinylidene fluoride (PVDF, Kureha 9300) Current collector: Copper foil Tab: nickel Calendering: No	84.4 mm×56 mm×65 μm (6.18 mg/cm^2)
Cathode	Electrode: 90 wt % $Li_{1.02}Ni_{0.50}Mn_{0.29}Co_{0.19}O_2$ (TODA America Inc.), 5 wt % powder grade carbon black (Denka), 5 wt % PVDF (Solvay Solef® 5130) Current collector: Aluminum foil Tab: Aluminum Calendering: No	84.4 mm×56 mm×64 μm (12.27 mg/cm^2)
Separator	Polypropylene–polyethylene–polypropylene (Celgard® 2325)	89 mm × 61 mm × 25 μm
Electrolyte	1.2 M $LiPF_6$ in EC:DEC (3:7 by weight, BASF)	–

The UV lamps had 400 W of output power (225 mW cm^{-2}) and delivered concentrated light primarily in the UVA range, 320–390 nm wavelength, to achieve maximum UV penetration depths. In case of carbonate sand, UVB penetrates 100 µm depth with 90% of the incident intensity.[29] Since UVA penetrates into a substrate more than UVB, UVA used in this study can penetrate through the 65 µm thick anodes with more than 90% of the incident. A12 graphite anodes were exposed to the UV light for different periods of time, 0 (no UV treatment), 20, 40, and 60 minutes. Contact angles of the anodes were measured using a goniometer (Model 260-F4, Ramé-Hart Instrument Co.). The electrode processing from powders to wet-coating-and-drying did not change since UV was applied to fully dried electrodes on current collectors.

All UV-treated anodes and pristine cathodes were kept in an evacuated oven in a dry room (RH 0.2% at 21°C) to minimize the moisture content in the electrodes until immediately before they were used for the cell assemblies. Each UV-treated anode was inserted into a pouch cell with a pristine NMC 532 cathode, an electrolyte consisting of 1.2 M $LiPF_6$ in ethylene carbonate (EC):diethyl carbonate (DEC) (3:7 by weight), and a trilayer separator (Table 2.1). The cell assemblies were carried out in a dry room to avoid negative effects of moisture on the battery performance.[30] The different electrode combinations of the pouch cells and their group names are listed in Table 2.2. Three UV-treated (60 minutes) and three untreated pouch cells were prepared for preliminary testing. After the preliminary testing, twelve additional pouch cells were prepared for four different combination groups with three cells in each group.

The pouch cells were tested using a battery tester (Series 4600, Maccor Inc.) connected with a temperature chamber (ESPEC Corp.) at 30 °C. The cells went through three formation cycles, C-rate performance tests, EIS to test initial resistance, cycle life testing (300 cycles), and EIS to test the resistance increase after cycle life testing. All charging and discharging were performed between 2.5 V and 4.2 V at different C-rates. Charge and discharge rates of C/20 were applied for formation cycles in which 1C was based on 160 mA g^{-1}. For the C-rate tests, C/5 was applied until the voltage reached 4.2 V, followed by a constant voltage charge until the current dropped to C/20. Then the cells were discharged at various C-rates (e.g., C/5, C/2, 1C, 3C). After the C-rate tests, 1C charge and discharge rates were applied for 300 cycles for cycle life tests.

Impedance measurements were taken before and after the cycle life tests using VSP potentiostat systems (Bio-Logic Science Instruments SAS). The measurements were performed at discharge capacity increments of 25%. The EIS frequencies ranged from 400 kHz to 10 mHz with 5 mV oscillation amplitudes. EC-Lab software was used to analyze the ohmic resistance (R_{ohmic}), surface film resistance ($R_{sf,}$ or passivation layer resistance), and charge transfer resistance (R_{ct}).

Table 2.2 Test group names of pouch cells and their electrode combinations

Group name	A12 graphite anode electrode	NMC 532 cathode electrode
UV 0 min	No UV treatment	No UV treatment
UV 20 min	UV treatment for 20 minutes	
UV 40 min	UV treatment for 40 minutes	
UV 60 min	UV treatment for 60 minutes	

After the cycle life tests, the anodes and cathodes were analyzed by XPS (K-Alpha, Thermo Scientific). All cells were discharged until the cell voltage reached 2.5V before disassembly. Specimens for XPS were harvested from the tested pouch cells and washed using a DEC solvent in an argon-filled glove box. The washed specimens were dried in the glove box for at least 24 hours and transferred to the XPS using a vacuum transfer module (VTM, Thermo Fisher Scientific). The VTM was evacuated again in the ultra-high vacuum ($< 10^{-9}$ millibar) chamber of the XPS. Thus, specimens were never exposed to air. A 400 μm x-ray beam was used for survey scans and depth profile snapshots to obtain average percentages of the elements in a large area of an electrode. A flood gun was turned on to avoid a charge buildup at the specimens, which were placed on a glass plate. Depth profile analysis was carried out after every 10 second etching cycle for 60 levels. The Ar ion gun for etching was set at 1 keV.

To understand UV effects on graphite, A12 graphite powder (Conco Phillips) was carefully placed on double-sided tape attached to a glass plate and the top layer of the powder was compressed using another clean glass plate such that the powder stuck together on the double-sided tape. The layer of powder was thick and fully covered the tape, and this coverage prevented the UV light and XPS beam from reaching directly to the tape or glass plate. One A12 graphite sample on the glass plate was treated with UV light for 40 minutes. Another sample was not treated with UV to serve as a baseline for comparisons. These two samples were then dried overnight at 700 mbar and 80 °C in a vacuum chamber located in a dry room. Next, they were transferred to the XPS chamber using a vacuum transfer module. Surface chemistry information was obtained using the XPS.

To understand UV effects on PVDF, a doctor blade (20 cm width, Pacific scientific®, Gardner Neo Tec.) was used to create a PVDF film of 8% PVDF solution (9300 Kureha) on a Cu foil. The PVDF film was dried and cut into one large sheet and several small sheets. The large sheet was used for measurements of weight and thickness before and after 40-minute UV treatment. A 0.01mg precision balance (HR-202i, A&D) and 0.001mm precision micrometer (IP65, Mitutoyo) were used for the weight and thickness measurements, respectively. One small sheet was treated with UV for 40 minutes and another one was not treated for a baseline. The surface chemistry of each was analyzed via the XPS.

Results and discussion

Cycle performance

First sets of experiments included UV 0 min group and UV 60 min group for preliminary cycle life testing. They were tested for 600 aging cycles and showed positive effects of UV treatment on the cycle life (Figure 2.1a).

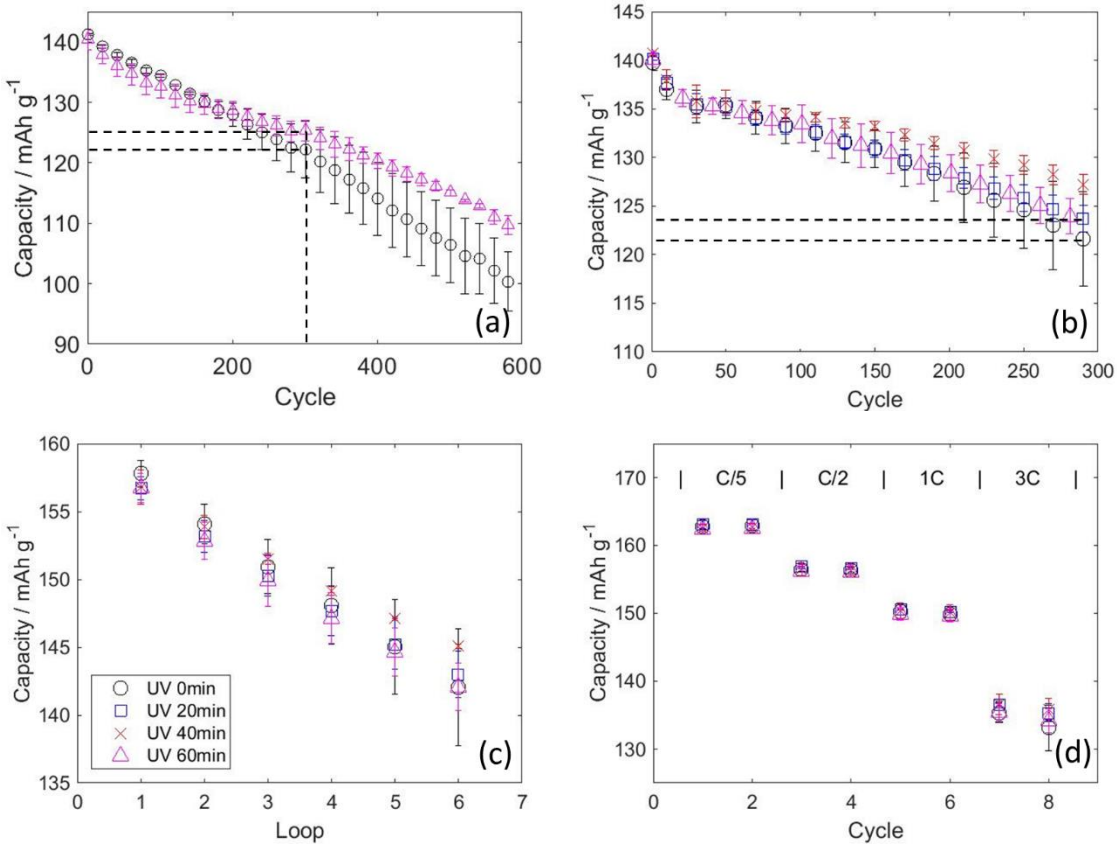


Figure 2.1. Average discharge capacities with 90% confidence intervals (error bars) from preliminary cycle life tests of UV 0min and UV 60 min groups with 1C charge and discharge for 600 cycles (a); from second cycle life tests for verification with 1C charge and discharge rates (b); and from the performance check of the second tests with C/5 charge and discharge rates after every 50 cycles of the cycle life tests (c), from C-rate tests before aging cycles for the second sets (d). Dashed lines in (a) and (b) indicate capacities of UV 0 min and UV 60 min group near 300 cycles.

Since the first sets showed promising results for extending the cycle life, new sets of experiments were designed for detailed analysis with four different UV groups (UV 0 min, UV 20 min, UV 40 min, and UV 60 min). Initial discharge capacities were measured at various discharge rates (C/5, C/2, 1C, and 3C) after charging at a C/5 rate.

The average capacities with 90% confidence intervals (error bars) at each C-rate are shown in Figure 2.1d. Before the aging cycles, all test groups showed almost the same capacities at the same discharge C-rate up to 1C: 162 mAh g^{-1} at C/5, 156 mAh g^{-1} at C/2, and 150 mAh g^{-1} at 1C. But from a 3C discharge rate, the capacity from the UV 0 min group (133 mAh g^{-1}) began to deviate from the other groups with about 3 mAh g^{-1} lower capacity than the UV-treated groups (136 mAh g^{-1}). We note that the effect is small before aging testing, with all groups within the error range.

Figure 2.1a and 2.1b show average capacities of preliminary tests and verification tests with 90% confidence intervals, respectively, during cycle life tests at 1C charge and discharge rates. All groups started at similar capacities, near 140 mAh g^{-1}. After 300 cycles of cycle life tests, the capacity fade of the UV 40 min group, 0.0433 mAh g^{-1} $cycle^{-1}$, was the slowest among all groups. The capacity fades of the UV 20 min and the UV 60 min groups were the second slowest and were almost identical, 0.0560 mAh g^{-1} $cycle^{-1}$. The UV 0 min group showed the fastest capacity fade, 0.0623 mAh g^{-1} $cycle^{-1}$ (44% faster than UV 40 min group).
All of these capacity fade rates were slightly high because no calendaring process was used on the electrodes and because of the high C-rates.

Figure 2.1a (preliminary test) and 1b (verification test) show good agreements of UV 0 min and UV 60 min group not only in average capacities but also in error ranges, implying that the UV treatment also affected reproducibility. Cell-to-cell variations at the 300th cycle were the smallest for the UV 40 min group, 1.5% (2 mAh g^{-1}), and the largest for the UV 0 min group, 8.2% (10 mAh g^{-1}). The variations for the UV 20 min group and 60 min group were 2.1% (2.6 mAh g^{-1}) and 2.9% (3.6 mAh g^{-1}), respectively. Figure 2.1c shows capacities at C/5 measured at every 50 cycles of the cycle life tests. Each loop on the x-axis includes 50 cycles from previous measurements. After 300 cycles (at the sixth loop), the capacities at C/5 from the UV 40 min group were again the best, 145 mAh g^{-1}, followed by the UV 20 min group, 143 mAh g^{-1}. The capacities of the UV 0 min and the UV 60 min groups were almost the same, 142 mAh g^{-1}.

Unlike the results of the cycle life testing, UV 40 min group had lower discharge capacities than other groups during formation cycles (Figure 2.2). At the first formation cycle, the discharge capacity and irreversible capacity losses (ICL) from UV 40 min group were 137 mAh g^{-1} and 14 μAh g^{-1} (17% loss from the

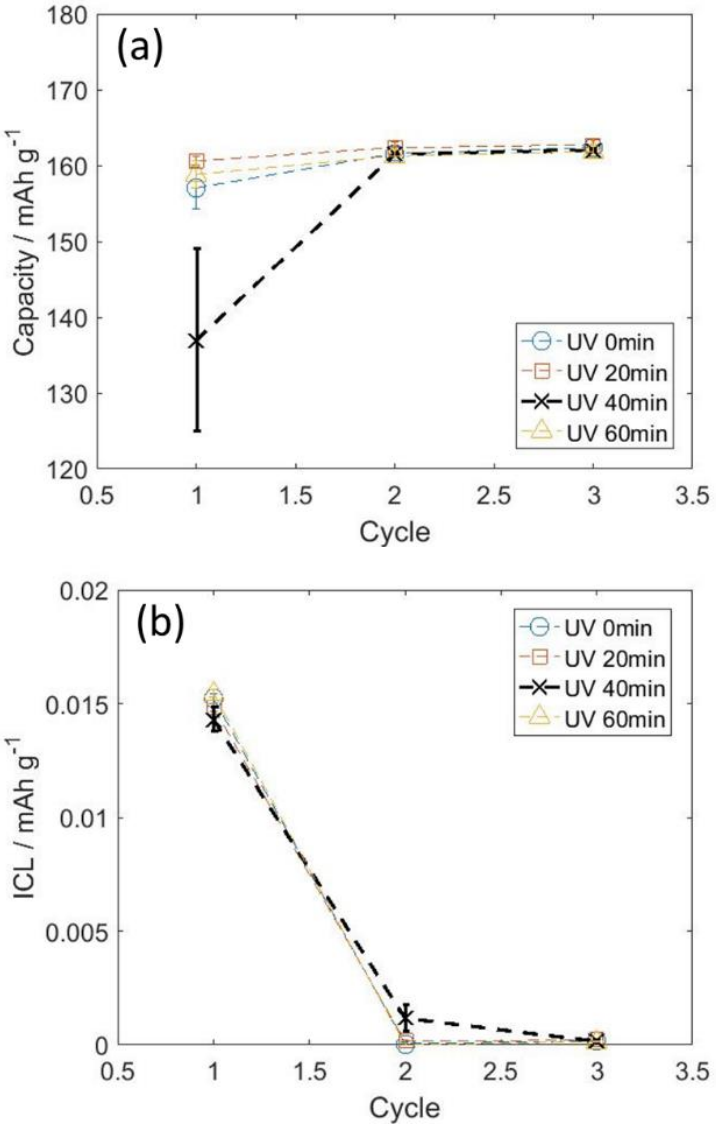


Figure 2.2. Average discharge capacities (a) and irreversible capacity losses (ICL) (b) from formation cycles of different UV groups with C/20 charge and discharge rates.

charge capacity), respectively, while those from other groups were close to 160 mAh g^{-1} and 15 µAh g^{-1} (15% loss from the charge capacity), respectively. Then, at the third cycle, these from all groups converged to 162 mAh g^{-1} and 0.14 µAh g^{-1} (0.02% loss from the charge capacity).

The summations of ICL for three formation cycles were 0.0154 µAh g^{-1} in UV 0min group, 0.0152 µAh g^{-1} in UV 20min group, 0.0156 µAh g^{-1} in UV 40min group, and 0.0156 µAh g^{-1} in UV 60min group. Since it is believed that ICL is related to SEI formation, it is possible that the SEI layer was formed during the formation cycles more in UV 40 min and 60 min groups than the other groups, which, later, might contribute to the increase in the cycle life of UV 40 min and 60 min groups.

Impedance

Resistances were analyzed using EIS. Nyquist plots from a representative pouch cell in each test group are shown in Figure 2.3. Average resistances from all EIS measurements are summarized with 90% confidence intervals at each group in Figure 2.4. The equivalent circuit model used for the impedance analysis is shown next to Figure 2.4a. Instead of capacitor elements in the model, constant phase elements were adopted to accommodate the imperfect capacitor behavior in a large porous electrode. Warburg elements at low-frequency domains were not included in the EIS data fitting because they were related to solid-state diffusion rather than resistance. The ohmic resistance (R_{ohmic}) had large error bars for every group because 12 different channels of a VSP potentiostat system were used for the EIS measurements in this study. Unlike surface film (R_{sf}) and charge transfer (R_{ct}) resistance, R_{ohmic} involves resistance not only from a battery cell but also from the cables between a cell and a potentiostat system and from the electrical connections at every socket and clip. Hence, R_{ohmic} varies when different potentiostat systems are used.

Although the R_{ohmic} in this study had large error bars because of the different potentiostat systems, it was found that overall R_{ohmic} slightly decreased by 2–5 Ohm-cm^2 after 300 cycles. This decrease might have occurred as the separators and electrodes were rearranged and became more compact as a result of the pressure on the pouch cells from the metal guide plates holding the cells and electrode swelling. When the separators become compact and thinner, the electrolyte resistance decreases because the distance between the anodes and cathodes reduces. In addition, when electrodes are pressed under the metal holder for a long time, particles in the electrodes move closer, lowering the contact resistance between particles. Thus, a slight decrease in R_{ohmic} is likely caused by better particle-to-particle contacts in electrodes and the closer distances between electrodes as cells are held under pressure.

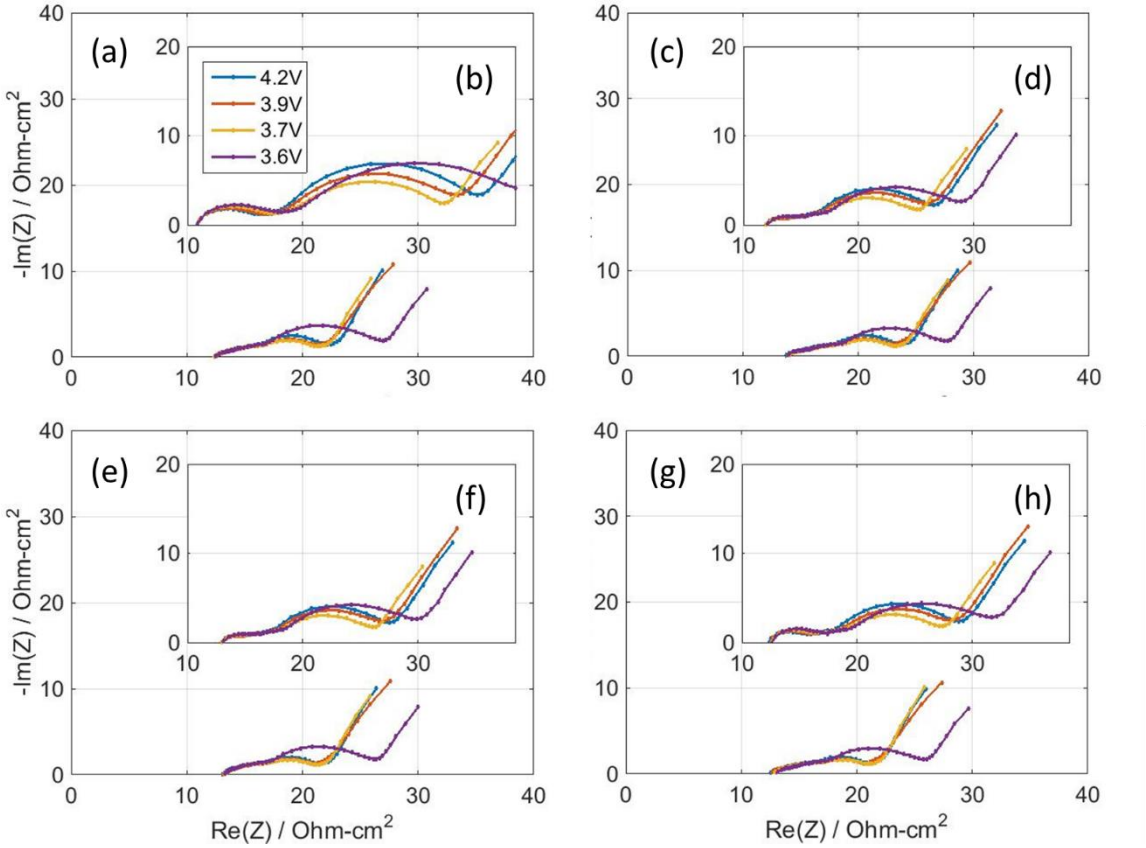


Figure 2.3. Nyquist plots of EIS from UV 0 min before (a) and after cycle lift tests (b); UV 20 min before (c) and after the tests (d); UV 40 min before (e) and after the tests (f); and UV 60 min before (g) and after the tests (h).

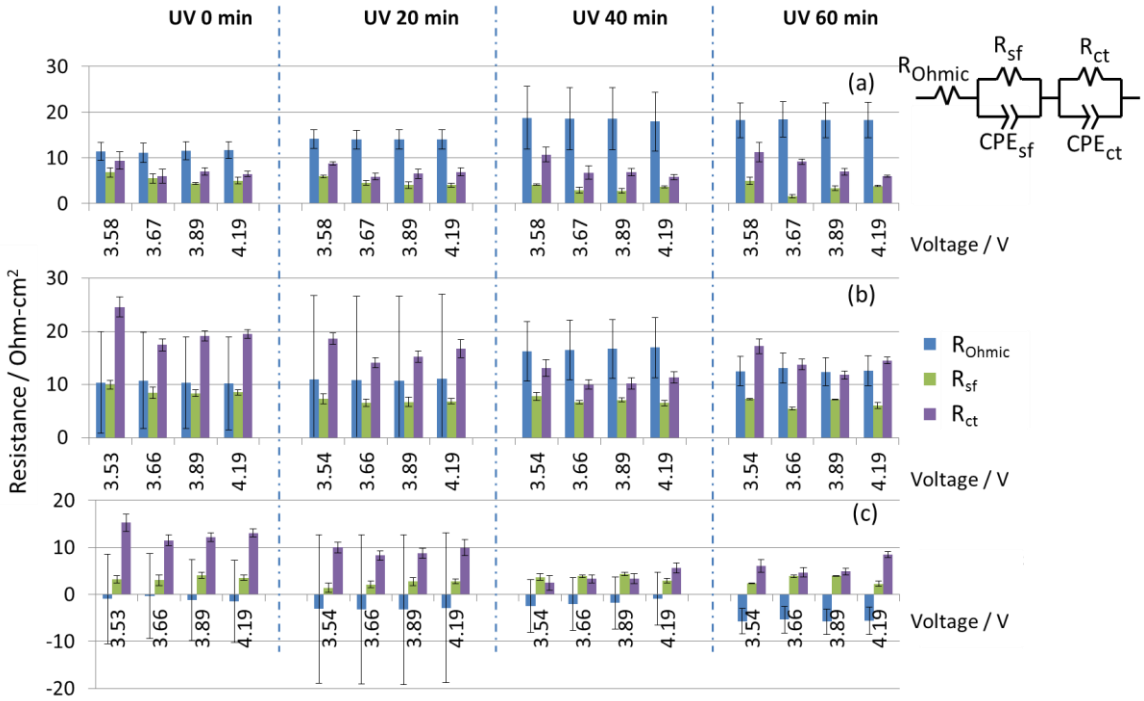


Figure 2.4. Ohmic, surface film, and charge transfer resistances at different voltages before cycle life tests (a) and after cycle life tests (b); resistance differences before and after the cycle life tests (c); the equivalent circuit model for Nyquist plot fittings is shown on top right.

Before the cycle life tests (Figure 2.4a), R_{sf} decreased as the time period of the UV treatment increased. After 300 cycles of the cycle life tests (Figure 2.4b and 2.4c), the R_{ct} increased significantly for the UV 0 min group, by 10–15 Ohm-cm^2, while the R_{ct} for the UV 40 min group showed the smallest increase (2–5 Ohm-cm^2).

The general relationship between current density (i) and overpotential (η) is expressed by Butler-Volmer equation.[31] When the concentration on the electrode surface is similar to the bulk concentration, the redox reaction is dominated by charge transfer. Then, the R_{ct} can be obtained by solving the Butler–Volmer equation for η/i and is a function of exchange current density (i_0) and transfer coefficient (α or reaction order) when cells are tested under the same conditions. Since large differences in R_{ct} were observed between the UV-treated and untreated groups, UV treatment might affect exchange current density, the transfer coefficient, or both at the electrodes.

The R_{ct} and R_{sf} shown in Figure 2.4 involve both the anode and cathode. Thus, the resistance of each electrode is not clear. In three-electrode pouch cell study with electrodes that were not UV-treated, the resistance at the cathode was about 1.5 times above 3.7 V and 10 times near 3.5 V higher than that at the anode. Figure 2.5a shows the anode resistance and cathode resistance measured by a hybrid pulse power characterization (HPPC) technique with the three-electrode cell. Since resistance near 3.5 V from the cathode side is much higher than that at the anode, it is assumed that most of the R_{ct} and R_{sf} near 3.5 V in Figure 2.4 were from the cathode side. In the contrast, the resistance above 3.7 V from anode accounts for a significant portion (ca. 40%) of the total resistance, implying changes on anodes can affect total resistance significantly. The cathode voltage at the fully charged state can reach 4.3 V (Figure 2.5b). 4.3 V is the threshold voltage where transition metals start dissolving out from NMC particles to electrolytes.[32] As the three-electrode cells were cycled, the anode voltage gradually increased due to loss of lithium to passivation layers. The increase in voltage at the anode does not significantly change anode surface properties. However, the cathode voltage steadily increased above 4.3 V to maintain a net cell voltage of 4.2 V. Pushing the cathode voltage about 4.3 V likely resulted in the release of transition metals.[32-33] Losing transition metals from the particles will change the surface properties of the NMC, affecting both charge transfer and passivation layer formation on the cathode. Hence, it is reasonable to expect that small changes on the anode could cause significant changes not only on the total resistance but also on the cathode.

Solid electrolyte interphase analysis

Surface films at both the anode (SEI layers) and cathode (passivation layers) were analyzed using XPS. Figure 2.6 shows the surface elements on the anodes

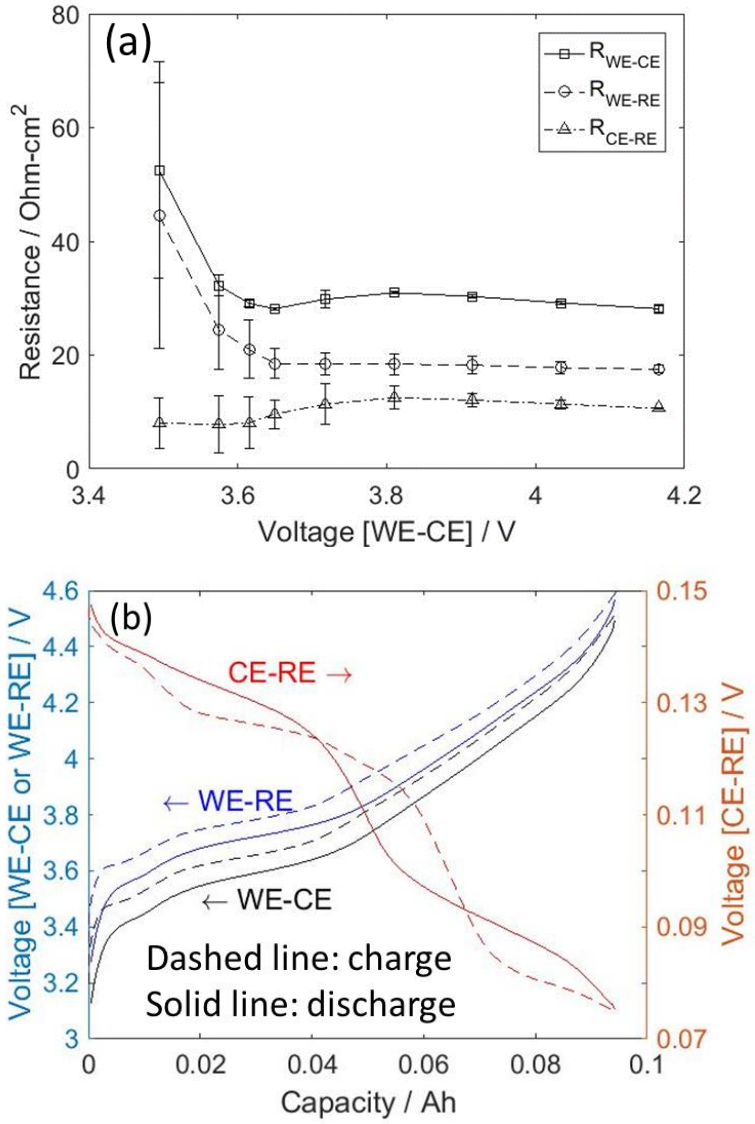


Figure 2.5. Resistances, from a three-electrode pouch cell, after formation cycles at anode and cathode from HPPC tests with respect to different voltages (a), voltages at 0.2C/-0.2C (b). CE-RE, WE-RE, and WE-CE are voltages or resistances from anode, cathode, and cell, respectively.

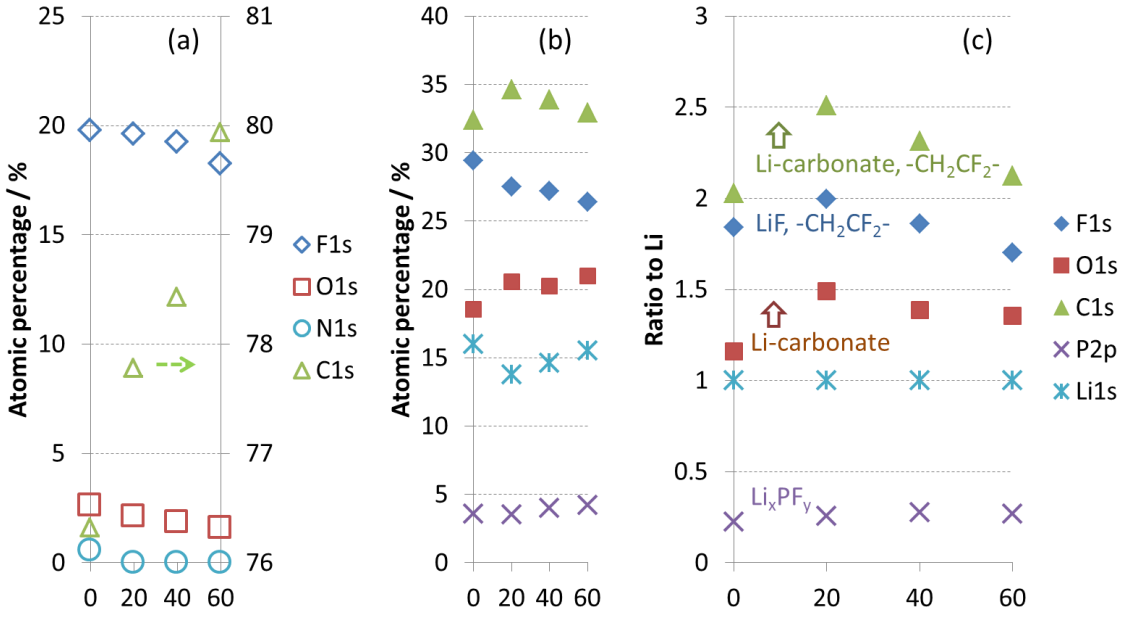


Figure 2.6. Atomic percentages of elements from XPS survey scans on UV-treated and untreated graphite anode electrodes before cell assembly (a) and after 300 cycles of cycle life tests (b). The ratio of each element to lithium after 300 cycles of life tests is shown in (c).

with and without UV treatment. Before cell assembly and any testing (Figure 2.6a), the amount of carbon on the anode increased as UV treatment was applied, whereas the amounts of all other elements decreased. The oxygen and nitrogen existing on the surfaces of the A12 graphite and carbon black decreased after the UV treatment.

The amount of nitrogen after UV treatment was below the detection limit of the XPS instrument. The contact angles of the graphite anodes were measured using water instead of DEC because water showed much clearer contact angle: It's challenging to measure contact angles of DEC on graphite anodes with a sessile drop due to high DEC wettability to the surfaces, resulting in very small contact angles.

The contact angles and images of the measurements are illustrated with respect to different durations of UV treatment in Figure 2.7. The contact angles decreased from 115° at the UV 0 min to 102° at the UV 40min. Then, the angle increased again to 111° at the UV 60 min. According to a water splitting study using graphene from Xu et al., the hydrophobic surfaces of graphene became hydrophilic as the graphene was irradiated by UV light,[34] which could be the reason why the graphite electrodes became more hydrophilic as the durations of UV treatment increased. However, it was not clear why the contact angles increased from the UV 40 min to the UV 60 min. UV treatment might affect not only graphite but also other inactive components (binder, conductive material, or both) after the long UV light exposure. These results of the contact angle measurements and the XPS analysis show that the UV light changed the surface chemistry of the anodes and might affect electrolyte wetting after cell assembly. Because the hydrophilic property highly enhances the affinity of graphite electrodes for the electrolyte, the electrolyte can wet the electrodes fast and distribute widely, resulting in uniform SEI formation during the formation cycles.

After 300 cycles of life tests, UV-treated groups showed different element percentages on the surfaces of the SEI layers (Figure 2.6b). Compared with the non-UV-treated group, the UV-treated groups showed higher carbon and oxygen content, which are components of solvent decomposition products (e.g., lithium carbonate, Li_2CO_3, and Li_2O); whereas the fluorine, which is a component of salt products (e.g., LiF), decreased. It was assumed that the amount of fluorine from the binders did not change, since the same amount of the binder was used at all anodes. Since the SEI is composed mainly of lithium-associated compounds,[35-36] normalizing the element percentages by the lithium percentages provides a better understanding of its composition. Figure 2.6c and Table 2.3 show the ratios of other elements to lithium at the anode and their theoretical element ratios to lithium. As Table 2.3 shows, all lithium-associated oxygen compounds were solvent products and increased when the electrodes were treated with UV light (Figure 2.6c).

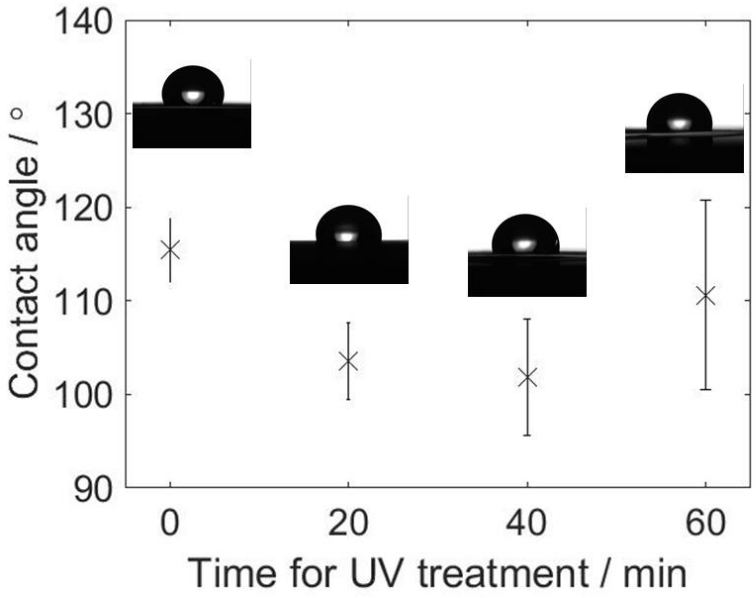


Figure 2.7. Contact angles of graphite anode electrodes with different durations of UV treatment in an ambient environment.

Table 2.3. Representative compounds on an SEI surface and binder and the ratios of their elements to lithium

Compounds		Ratio to lithium		
		O	C	F
Solvent (EC, DEC) products	$C_2H_5OCO_2Li$	3	3	0
	$(-C_2H_4OCO_2Li)_2$	3	3	0
	$C_4H_9OCO_2Li$	3	5	0
	$(-C_4H_8OCO_2Li)_2$	3	5	0
	Li_2CO_3	1.5	0.5	0
	Li_2O	0.5	0	0
	LiF (due to HF)	0	0	1
Salt ($LiPF_6$) products	LiF	0	0	1
	Li_xPF_y (x < y)	0	0	> 1
Non-SEI (binder)	$-CH_2CF_2-$	0	infinite	infinite

On the other hand, phosphorus, existing as the salt product Li_xPF_y, is the only element whose ratio to lithium did not change after UV treatment. One molecule of $LiPF_6$ can decompose and precipitate as multiple LiF molecules in combination with lithium ions from the cathode.

Changes in the amount of fluorine could result from the LiF from salt products or LiF from the side reaction of lithium carbonates (solvent products) with HF, as in Reactions (1) and (2).[8]

$Li_2CO_3 \downarrow + 2\ HF \rightarrow 2\ LiF \downarrow + H_2CO_3$, Reaction (1)

$ROCO_2Li \downarrow + HF \rightarrow LiF \downarrow + ROCO_2H$, Reaction (2)

where *R* represents hydrocarbon groups. HF is generated by a side reaction of decomposed $LiPF_6$ salt products with water impurities in the electrolyte or traces of water adsorbed on the graphite or NMC 532.

The surface film thicknesses of both the anode and cathode were estimated using XPS depth profiles. The depth values on the y-axis shown in Figure 2.8 and 2.9 are the distances from the outer surfaces of the anode and cathode, respectively. Since direct correlation of SEI film thickness with etching rates has not been reported, the distance is calculated based on the assumption that the surface film had a similar etching rate to silicon oxides.

This technique is used to compare relative changes in thickness within the sample groups although the accuracy using this technique can significantly vary depending on target properties such as uniformity, density, element distribution, etc. The thickness of the surface film was estimated using element distributions across the depth from the surface. A 400 μm x-ray beam was used for survey scans and depth profile snapshots to determine the average element distribution in a large area covering multiple 5–15 μm–diameter particles of the active materials. Hence, after the surfaces of the active or conductive materials were reached by etching, surface film elements were continuously detected from the newly exposed surface films of the particles beneath the top particles. To estimate the thickness of the surface film, reasonable hypotheses were made based on the literature [8, 37-39]:

1) Bulk SEI compounds such as $ROCO_2Li$ and polycarbonates are distributed in greater amounts on the outer surface of the SEI layer because fewer electrons are accessible from the anode for reduction into more compact SEI compounds, such as Li_2O and Li_2CO_3.
2) Dense SEI compounds such as LiF, Li_2O, and Li_2CO_3 are distributed in greater amounts on the graphite/SEI interface side because abundant electrons and lithium are available for reduction reactions.

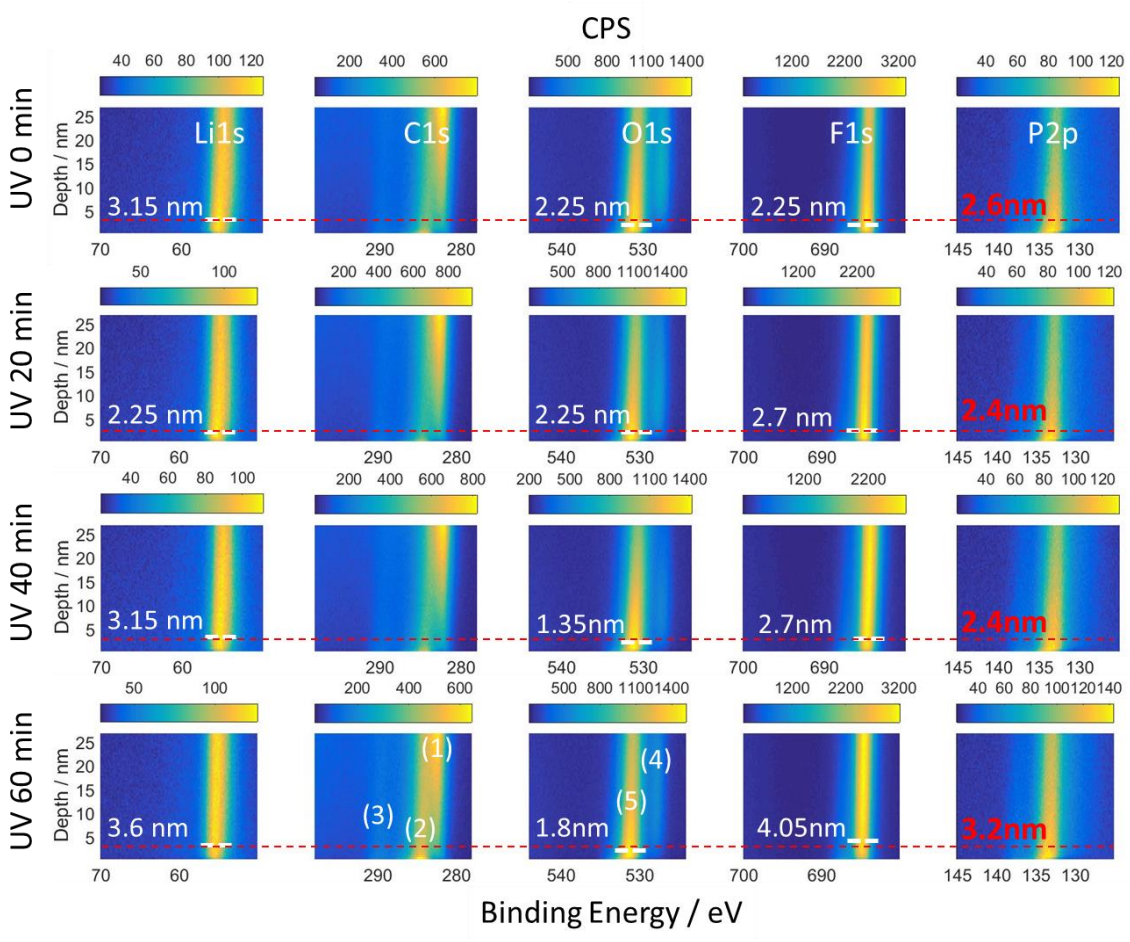


Figure 2.8. Following 300 cycles, counts per second (CPS) of elements from XPS snapshots during depth profiling of the anode electrodes (a. Estimated thickness of SEI, with elements in white and average thickness compared with the estimated thicknesses in bold red. The numbers on C1s and O1s indicating (1) graphite, (2) surface carbon, (3) carbonate, (4) Li_2O, and (5) surface oxygen (carbonate, carbon, graphite).

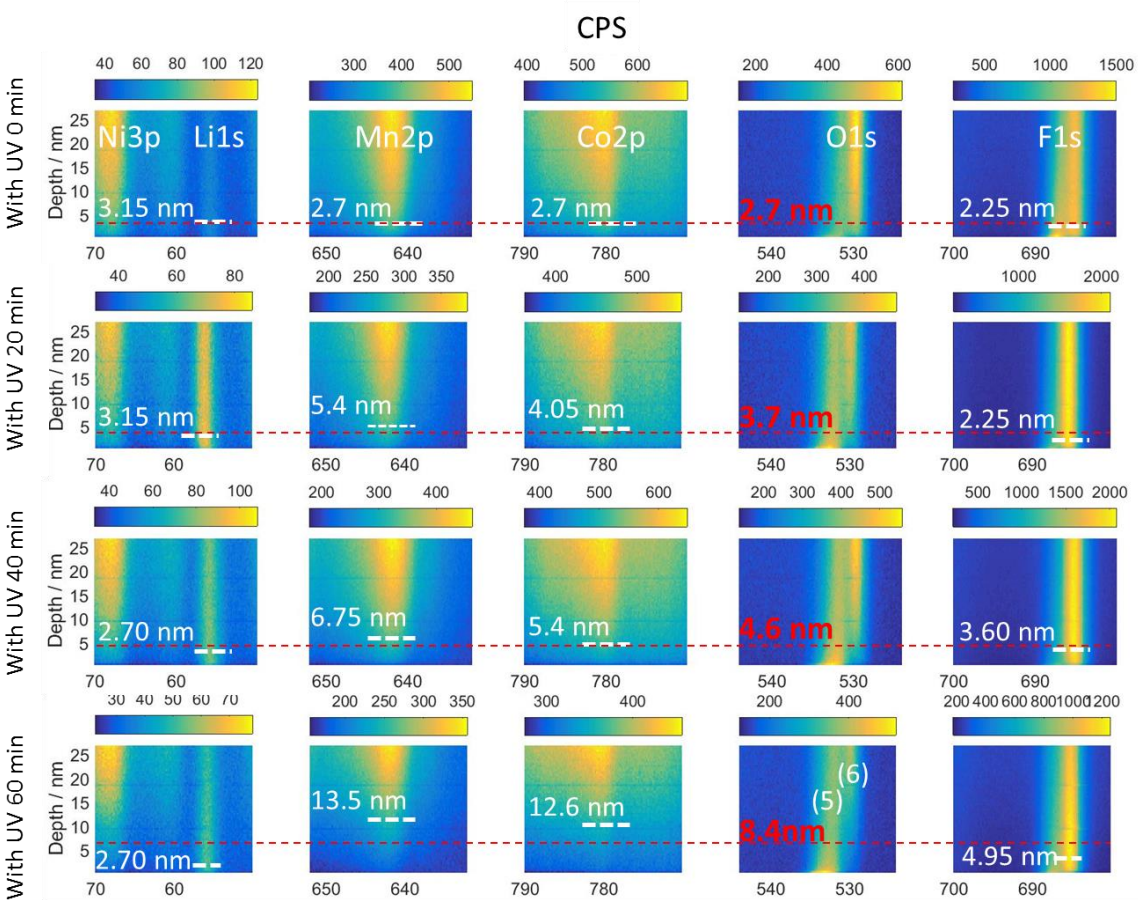


Figure 2.9. Following 300 cycles, counts per second (CPS) of elements from XPS snapshots during depth profiling of the cathode electrodes. Estimated thickness of SEI, with elements in white and average thickness compared with the estimated thicknesses in bold red. The numbers on O1s indicating (5) surface oxygen (carbonate, carbon, graphite) and and (6) lattice oxygen (O^{2-}).

3) C-C peaks from graphite should appear at C 1s XPS spectra when the etching level reaches the surfaces of the graphite.
4) Transition metal (TM) peaks at each TM spectrum from NMC and TM-O peaks at O 1s XPS spectra should appear when the etching level reaches the NMC surfaces.

Based on hypothesis 1 and 2, the percentages of Li, F, and O in the XPS spectra should increase in the SEI layer on the anode (or the passivation layer on the cathode) as the SEI (or the passivation layer) is etched; and they should be highest when the etching reaches the graphite/SEI interface of the anode and the NMC/SEI interface of the cathode. Hence, for the anode in Figure 2.8, the thickness of the SEI layer should be the distance between the top surface of the SEI, 0 nm, and the depth (numbers and dashed lines in white) at which the counts per second (CPS) of the elements are highest in the Li 1s, O 1s, and F 1s spectra. The average thicknesses of the SEI layer based on the elements are shown in red on the P 2p figures. These average thicknesses corresponded well with the depth at which the graphite C-C peaks appeared at C 1s, which agrees well with hypothesis 3. For the cathode, the thicknesses of the passivation layer shown in Figure 2.9 were based on hypotheses 1, 2, and 4.

The average thicknesses of the layer at the cathode are shown on the O 1s figures. The smallest average thickness of the SEI layer at the anode, 2.4 nm, was from UV 20 min and UV 40 min, followed by UV 0 min (2.6 nm) and UV 60 min (3.2 nm). The smallest average thicknesses of the passivation layer at the cathode were from UV 0 min (2.7 nm), followed by UV 20 min (3.7 nm), UV 40 min (4.6 nm), and UV 60 min (8.4 nm). The calculated thickness showed that surface films at the cathode were thicker than the ones at the anode. The actual thickness might differ from the calculation because the etching rate varies depending on the chemistry and density. Overall, XPS analysis agrees well with the resistance analysis and three-electrode voltage analysis showing that changes on the anode caused larger changes on the cathode.

The average thicknesses of the SEI (or passivation layer) from all of the UV treatment groups were used as depth levels for the SEI layer (or passivation layer) analysis. XPS element snapshots were taken at the outer surface and at every level of the etched surface from the surface to the near-average SEI (or passivation layer) thickness. Table 2.4 and Figure 2.10 and 2.11 show the XPS spectra of Li 1s, C 1s, O 1s, F 1s, and P 2p with possible SEI (or passivation) layer compounds at indicated binding energies. The bold italic numbers in Figure 2.10 denote the thicknesses close to the SEI (or passivation layer) thickness estimated in Figure 2.8 and 2.9. Unlike the thickness analysis illustrated in Figure 2.8 and 2.9, the composition analysis within the SEI layer (from 0 nm to the indicated thickness at each group) does not show clear differences among all UV groups on the anode side (Figure 2.10).

Table 2.4. Binding energy (eV) of SEI components assigned in Figure 2.10 and 2.11

Element	Compound	Binding energy / eV
Li 1s	Li_2CO_3 Li_2O, LiF $LiPO_4$ $LiPF_6$ (Salt)	55.1–55.2 55.6–55.7 55.4 56
C 1s	C-C (Graphite) -***C***H_2CF_2- (PVDF) $CO_3$2-, Li_2CO_3 Poly carbonate -CH_2***C***F_2-	284.8 286.8 289.5–290 290.4 292.6
O 1s	Li_2O TM(transition metal)-O -CO_3, Li_2CO_3 R–CH_2OCO_2Li R–CH_2OCO_2H	528.7 529.2–529.4 531.5–532 532.9 533.5
F 1s	TM(transition metal)-F_2 LiF $LiFP_6$ -CH_2CF_2-	684.8–684.9 685–685.3 687–687.4 688.1
P 2p	$(LiF)_{0.4}(LiPO_3)_{0.6}$ $(LiF)_{0.1}(LiPO_3)_{0.9}$ P_2O_5	134 134.5 135.5

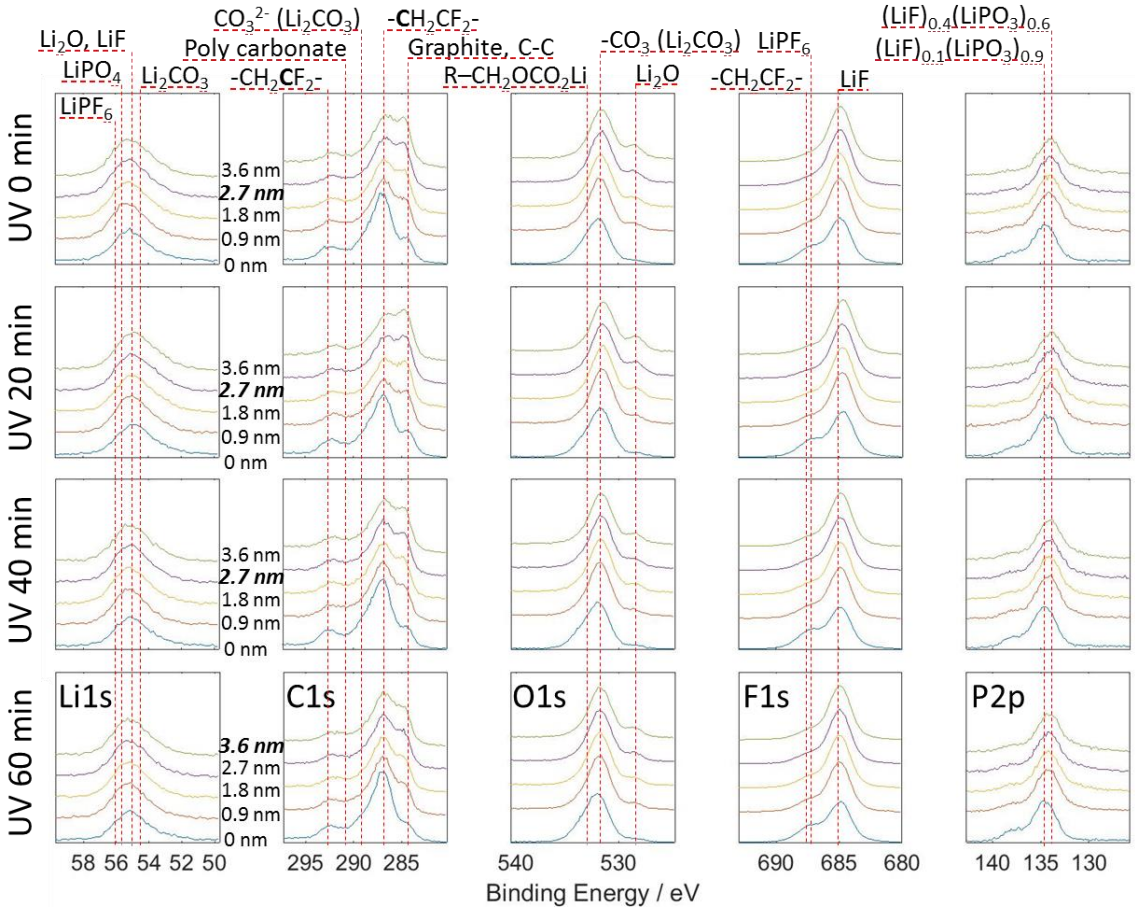


Figure 2.10. Element snapshots from XPS depth profiling and their related compounds at the anode electrodes with different UV treatments. The bold italic numbers denote the thickness close to the SEI or passivation layer, as estimated in Figure 2.8.

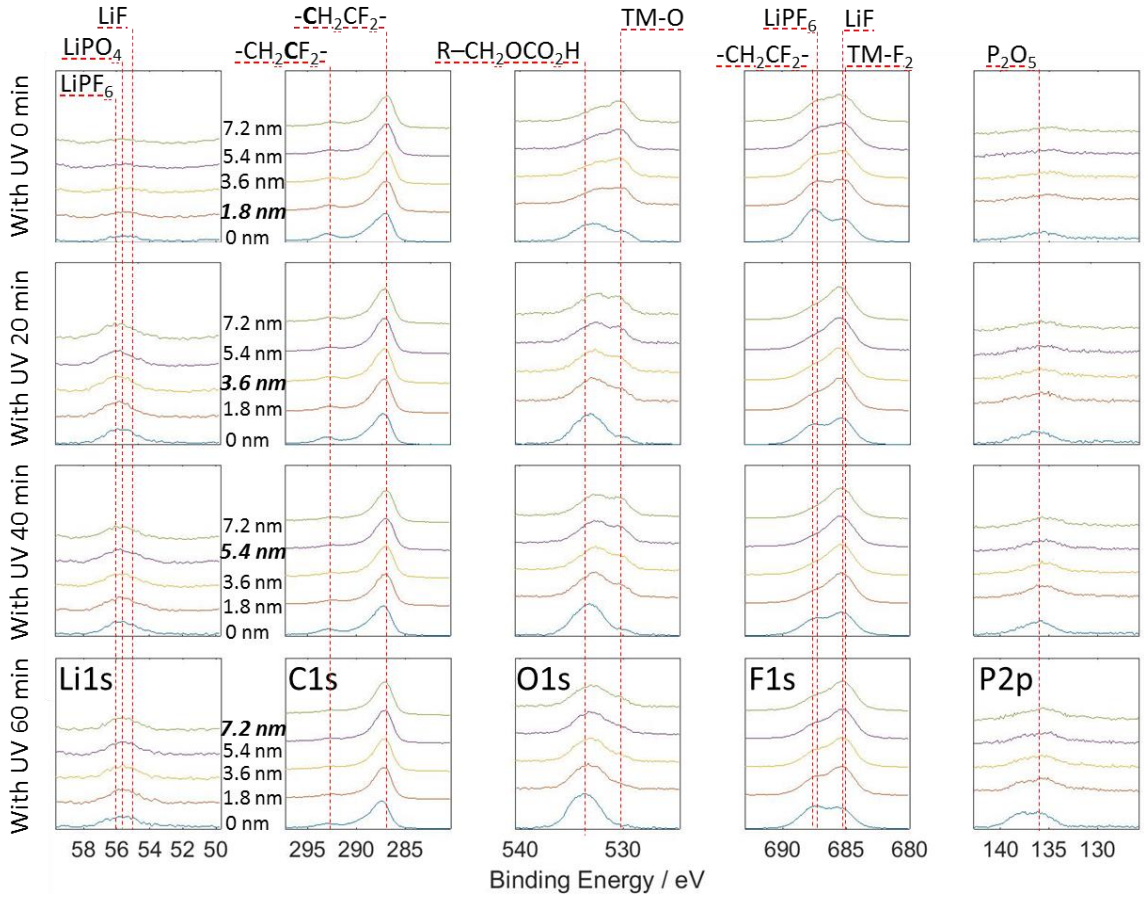


Figure 2.11. Element snapshots from XPS depth profiling and their related compounds at the cathode electrodes (b) used with the UV treated anodes. The bold italic numbers denote the thickness close to the SEI or passivation layer, as estimated in Figure 2.9.

They all have compact lithium compounds near the SEI/graphite interface (e.g., LiF in F 1s and P 2p spectra, Li_2O in O 1s spectra) and bulk lithium compounds near the outer surface of the SEI (e.g., R–CH_2OCO_2Li in O 1s).

The cathode shown in Figure 2.11, on the other hand, does not show clear evidence of Li_2O or lithium carbonates. Instead, significant amounts of salt and polymerized EC products were detected (Figure 2.11 O1s). Polymerized EC is generated when the cathode voltage is higher than 4.3 V.[33] This indicates cathode voltages reached above 4.3 V when the cells were charged to 4.2 V. On the F 1s figures, it is not clear whether the peaks near 684.8–685.3 eV are from LiF or TM-F_2. The salt ($LiPF_6$) peaks and binder (-CH_2CF_2-) peaks are also too close to each other to differentiate them. Similarly, it is hard to differentiate the compositions of the passivation layer (from 0 nm to the indicated thickness at each group) among the cathodes in the different UV groups. However, it was clear in Figure 2.11 that the passivation layers at cathodes with UV-treated anode groups had less transition metal (TM-O at O 1s), less salt products ($LiPF_6$ at F 1s) and more solvent products (carbonate at O 1S) than those at the cathodes with the untreated group. Especially, high transition metal (TM-O at O 1s) on surfaces of the passivation layers (0 nm) with untreated group is the evidence that transition metals dissolved out from the NMC particles. This result supports the resistance and three-electrode analysis showing changes at anodes significantly affected cathodes.

Changes on graphite surfaces after UV treatment

Elemental analysis was conducted on graphite powder where no other electrode components, such as binder and conductive carbon, were present. XPS survey scans showed that the percentage of oxygen on the graphite surfaces increased by a factor of 3.4 after 40-minute UV treatment (Figure 2.12). In Figure 2.13, for peak analysis, 531.8 eV and 532.5 eV were assigned to the peak centers of C=O and C-O-H in O1s narrow scans, respectively (Figure 2.13a and b). For peak centers in C1s narrow scans (Figure 2.13c and d), 284.6 ev, 285.5 eV, 286.3 eV, 287.1 eV, 288.6 eV, 291.3 eV were assigned to C-C sp2, C-C sp3, C-OH, C-O-C, C=O, and O=C-OH, respectively. XPS narrow scans for O1s indicated that hydroxyl group prevalence increased from 23% to 55% within the oxygen content after 40-minute UV treatment while carbonyl group decreased from 77% to 45% (Figure 2.13 and Table 2.5). The scan for C1s also showed that hydroxyl groups on carbon increased from 5.9% to 7.6% of the carbon content. Carbonyl groups from C1s increased from 3.1% to 8.6% but carboxyl groups having C=O decreased from 8.8% to 2.3%. Hence, net carbon percentage from C=O decreased after the UV treatment, which is in agreement with the decrease in oxygen percentage from C=O in O1s peaks.

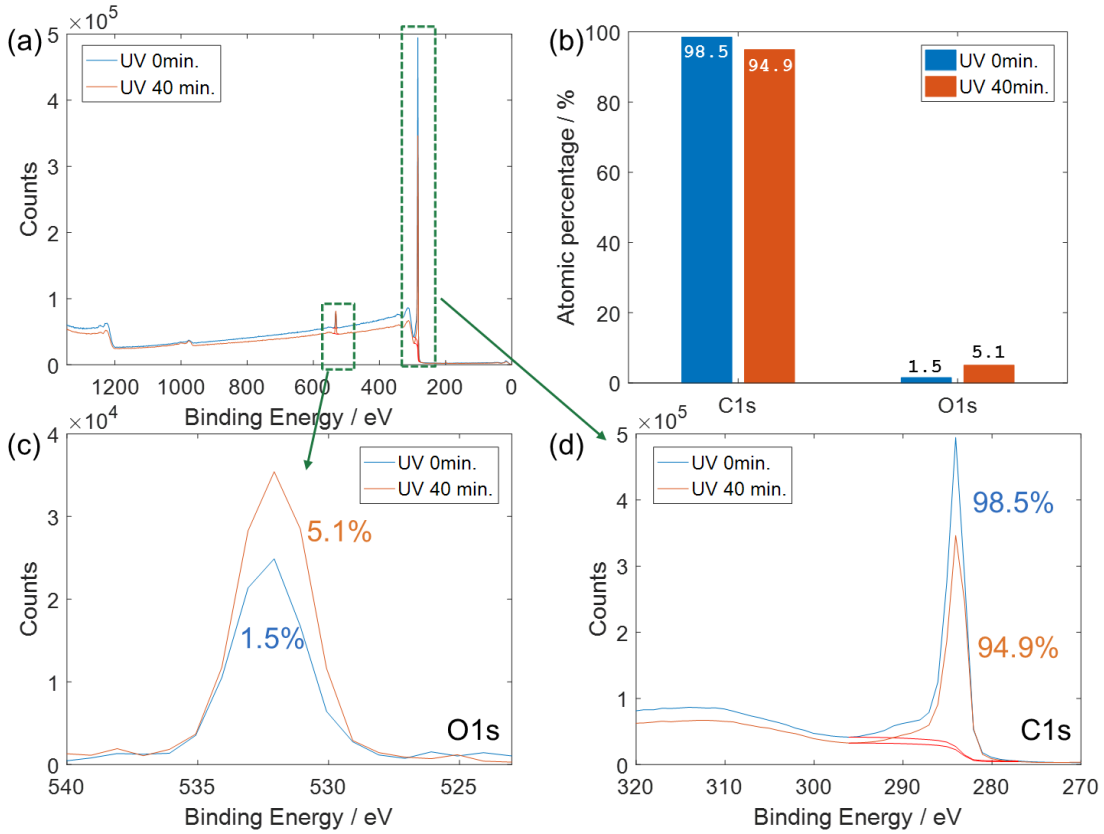


Figure 2.12. XPS survey scan results on A12 graphite powders before UV treatment and after UV treatment for 40 minutes (a), atomic percentages of carbon and oxygen calculated from the survey scans (b), and narrow scan results for O1s (c) and C1s (d).

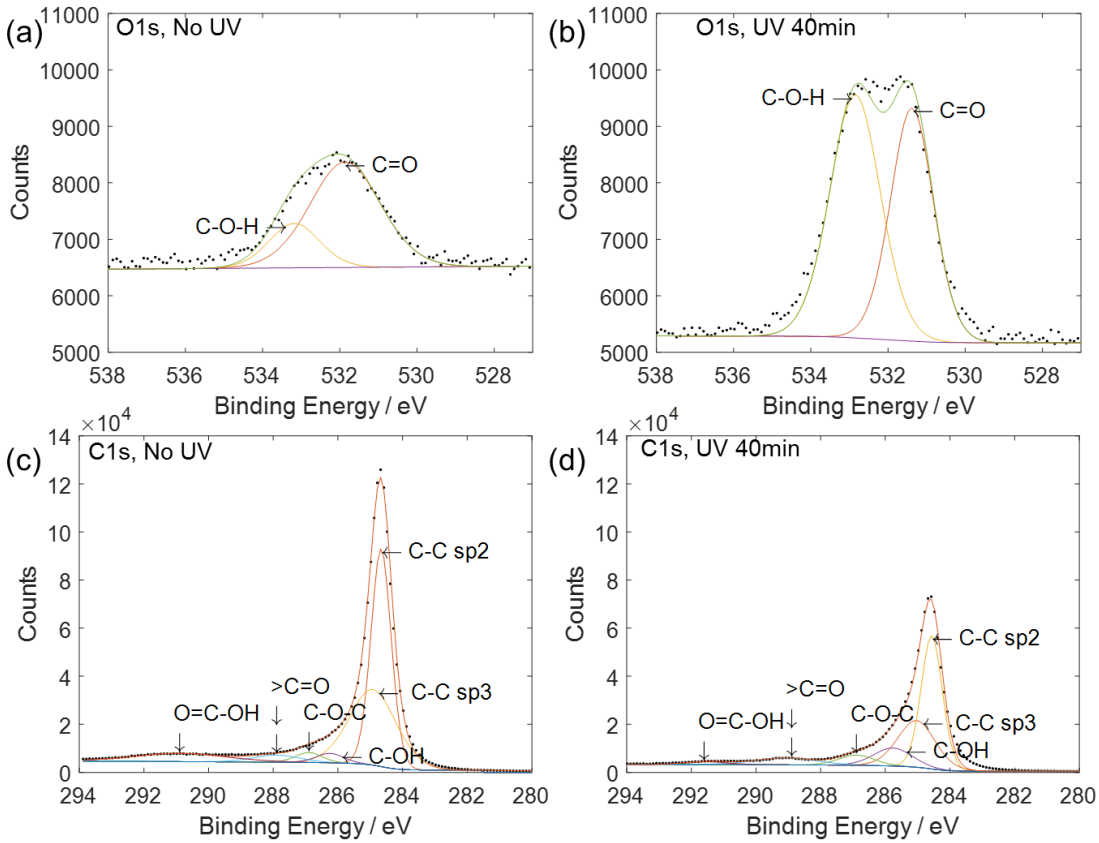


Figure 2.13. XPS narrow scan results of O1s before UV treatment (a) and after UV treatment for 40 minutes (b) and C1s before UV treatment (c) and after UV treatment for 40 minutes (d).

Table 2.5. XPS results on graphite before UV treatment and after the treatment for 40 minutes from narrow scans for O1s and C1s

Peak	Element	No UV	UV 40 min
O1s	C-O-H	23.24	55.15
	C=O	76.76	44.85
C1s	C-C (Gr)	79.4	77.8
	C-OH	5.92	7.59
	C-O-C	2.86	3.81
	>C=O	3.06	8.55
	O=C-OH	8.8	2.28

Like the O1s peaks and peaks from survey scans, the C1s peaks showed that the percentage of carbon with oxygen groups increased after the UV treatment.

Figure 2.14 shows a mechanism proposed in this study for increasing hydroxyl group concentration on a graphite surface. Graphite has defects and edges where oxygen groups can attach. Typical oxygen groups found on a graphite surface are carbonyl, epoxide, hydroxyl, and carboxyl groups. Since the UV treatment was carried out under atmospheric conditions where moisture is present, the source of additional hydroxyl groups on the graphite surfaces probably came from the air and moisture in the air. Possible water reactions under UV light are proposed as Reaction 1 and 2.[40]

$$H_2O \xrightarrow{h\nu} HO\cdot + H\cdot \qquad \text{Reaction (1)}$$

$$H_2O \xrightarrow{h\nu} HO\cdot + H^+ + e^- \qquad \text{Reaction (2)}$$

These splits may not occur with water alone in the UVA range due to low absorption in that range. However, those reactions can happen when graphite surfaces and heat induced by UV are taken into account. Surface temperatures of the electrodes were close to 100 ºC (Table 2.6). The temperatures were measured on electrodes using a portable infrared thermometer immediately after UV treatments for different periods of time. Hence, temperature during the UV treatment must be higher than the results shown in Table 2.6.

Changes in PVDF after UV treatment

A PVDF film was made with 8% PVDF solution using a doctor blade. The dried thicknesses of the film were 4-5 µm at six different measurement points. The average thickness was 4.5 µm from the measurement points. Figure 2.15 shows the thickness changes after the 40-minute UV treatment. The average thickness increased by 0.167 µm, which corresponds to a 3.7% increase from the 4.5 µm average thickness of the original film. This measurement probably contained a large error because the micrometer has 1 µm precision, a value that is much larger than the thickness change of 0.167 µm. However, it was determined that the thickness increased slightly after UV treatment. In general, thickness of a PVDF film can increase when the film experiences backbone scissions, resulting in polymer change disconnections (Figure 2.16). This backbone scission explains the thickness increase until 40-minute UV treatment. Similar thickness changes were obtained at the anode containing both graphite and PVDF binders until 40 minutes of the treatment, but the thickness decreased from 40 minutes to 60 minutes. The thickness can decrease when C-H and C-F scissions occur, resulting in cross-linking between polymer chains or creation of double bonds in the polymer backbones (Figure 2.17).[41]

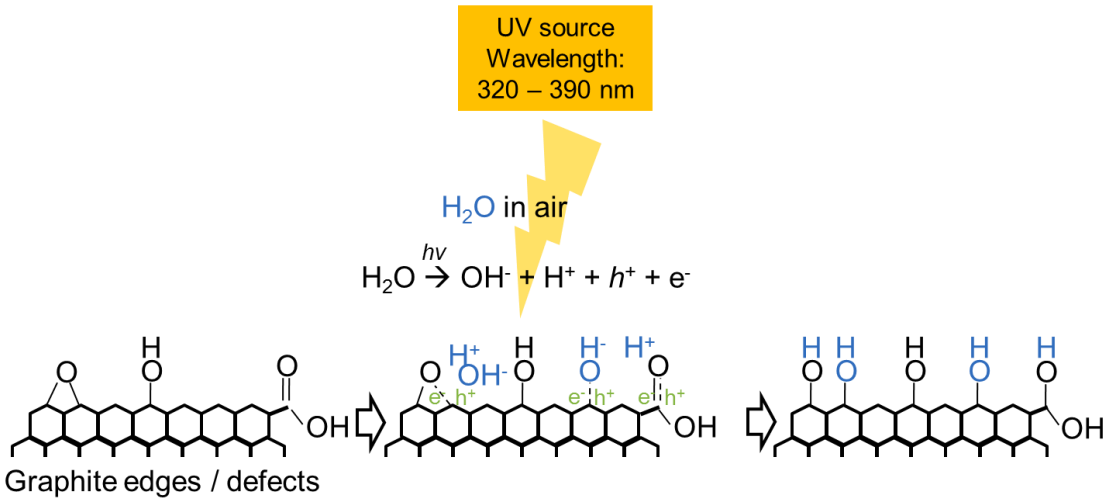


Figure 2.14. A proposed pathway for additions of hydroxyl groups on a graphite surface under UV light with humid air.

Table 2.6. Temperature on electrode immediately after UV treatment with different periods of time

Time for UV treatment / min	Temperature on electrode side / ºC
0	23
20	93.5
40	93
60	97.5

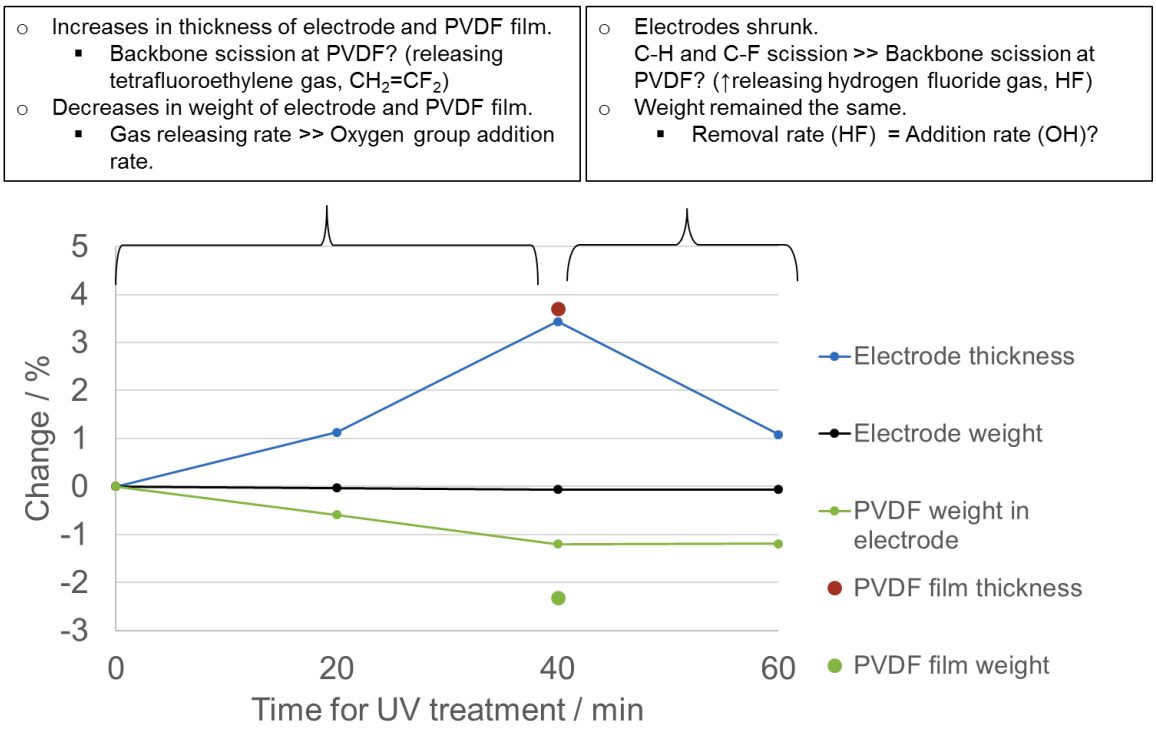


Figure 2.15. Weights and thicknesses of electrodes and PVDF films after UV treatment with different periods of time.

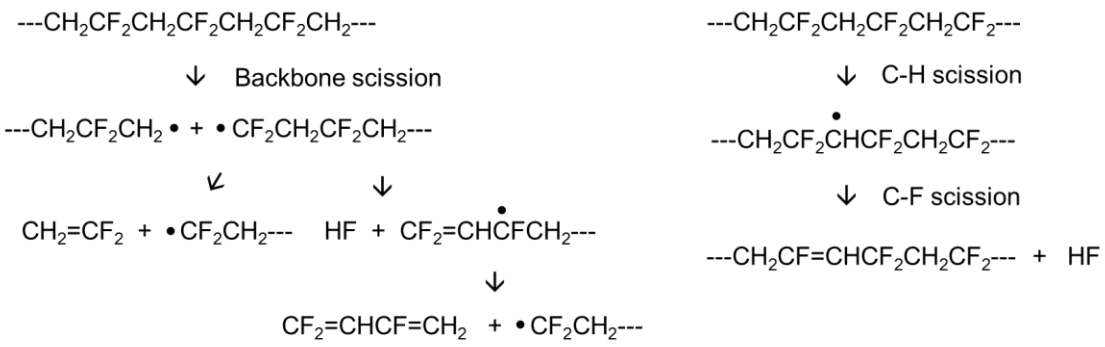


Figure 2.16. Backbone, C-H, and C-F scissions of a PVDF polymer chain.

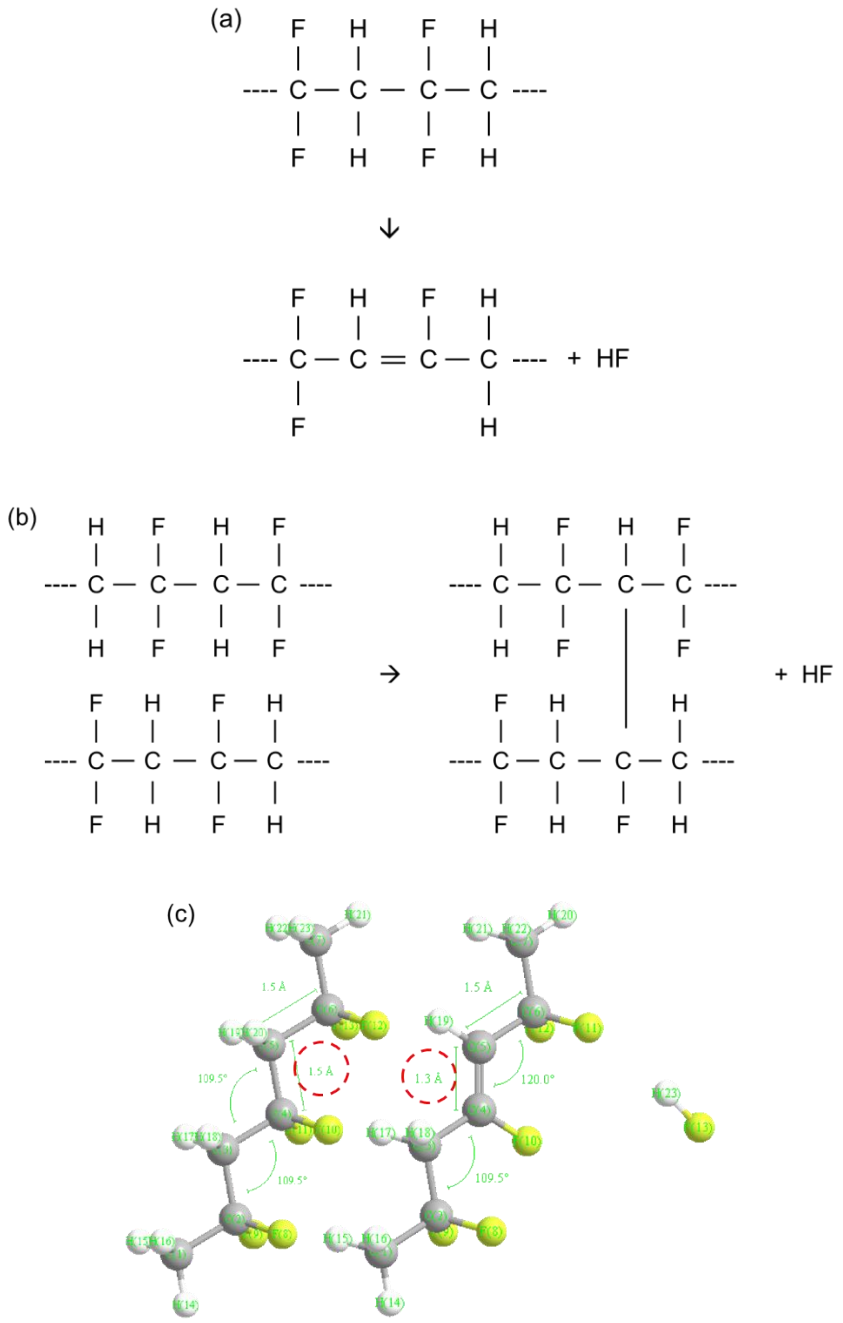


Figure 2.17. Schematic diagrams of two different dehydrofluorinations in PVDF (a-b) and a simulation results for atomic distances and angles between carbons with and without a double bond (c); F: yellow ball, H: white ball, and C: gray.

The carbon to carbon distances and angles at PVDF polymer with/without a double bond were calculated in Figure 2.17 using Chem3D (CambridgeSoft Co.). The crosslinking in polymer chains may negatively affect the volume expansion of graphite during lithiation.

It is reasonable that backbone scissions happen under UV treatment before C-H and C-F scissions since C-H and C-F bonds are stronger than C-C backbones. This scissoring sequence explains the thickness changes in Figure 2.15. Although the micrometer did not have enough precision for measurements involving submicron thickness changes, the results from the thickness changes were reasonable and could be explained by the different scission processes.

These scissions involve release of tetrafluoroethylene gas and hydrogen fluoride gas and cause a loss of weight in the PVDF film, a result that was also observed in this study (Figure 2.15). The results from XPS survey scans showed that the weight losses after the 40-minute UV treatment were from loss of fluorine (Figure 2.18), which agreed well with the weight changes in Figure 2.15. However, from 40 minutes to 60 minutes in the treatment, the weight of the electrode did not change much. The weight might not change much after 40 minutes when the removal rate of the fluorine atoms to the graphite surfaces is competing with the addition rate of oxygen and other elements. A large increase in the oxygen percentage after the UV treatment in Figure 2.18 indicates the addition of oxygen did occur.

Conclusions

In this UV treatment study, UV light was applied to lithium ion battery electrodes for the first time to control oxygen levels on the anode and improve battery cycle life. Dried graphite anodes were treated with UV light for different periods of time to improve the cycle life of graphite/NMC 532 LIBs. The anodes were more hydrophilic with UV treatment and were most hydrophilic when treated for 40 min.

Similarly, when treated by UV for 40 min, the electrodes demonstrated the highest capacity retentions during 300 cycles of life tests with 1C charging and discharging rates between 2.5 V and 4.2 V while the electrodes without UV treatment showed the fastest capacity fade. Charge transfer resistance increased after 300 cycles of life tests whereas maximum and minimum increase were observed from electrodes without and with 40 min UV treatment, respectively.

According to XPS analysis, UV treatment lowered the amounts of fluorine and oxygen on the surfaces of pristine anodes. The SEI was composed of more solvent products and fewer salt products on UV-treated anodes than on the untreated one. The average thicknesses of the SEI layers at the anode were the

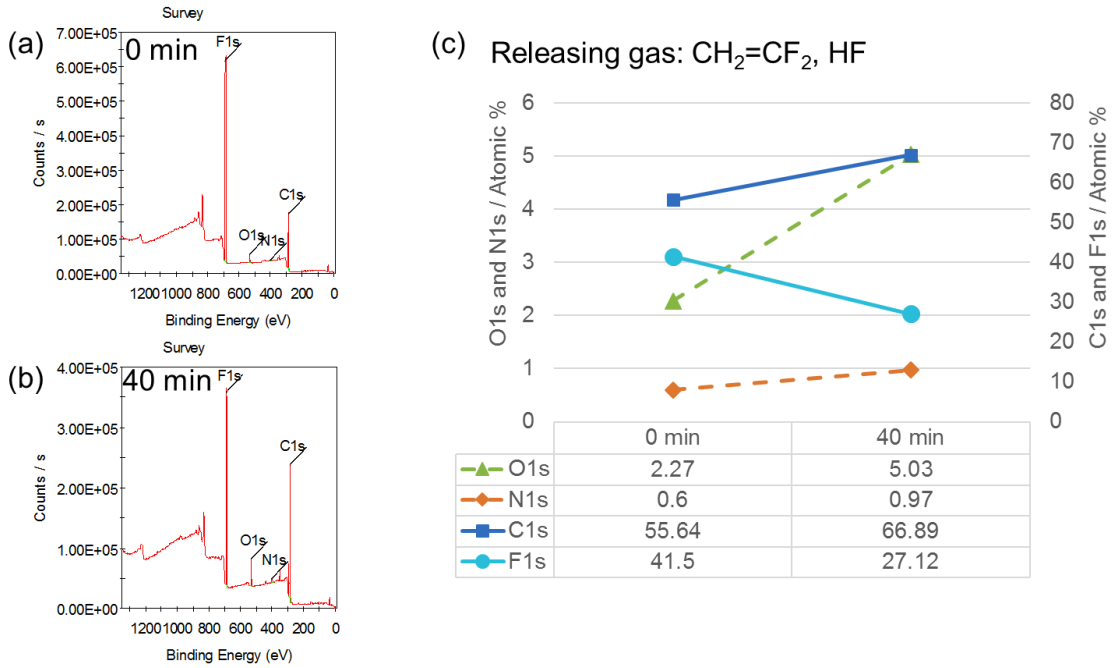


Figure 2.18. XPS survey scans from electrodes before UV treatment (a) and after the treatment for 40 minutes (b) and atomic percentages from the scans (c).

smallest at UV 20 min and UV 40 min, followed by UV 0 min and UV 60 min. The average thicknesses of the passivation layer at the cathode were smallest at UV 0 min followed by UV 20 min, UV 40 min, and UV 60 min. The average thickness of the surface film was lower at the anode than at the cathode. Transition metal oxides detected on the top surfaces of the passivation layers with the untreated group provided evidence that transition metals dissolved out from the NMC particles.

The XPS results of the A12 powder and PVDF film showed that UV light with humid air increased oxygen levels, particularly in hydroxyl form, on graphite surfaces while reducing fluorine levels in the PVDF binders. This increase in oxygen levels is believed to improve SEI formation and cycle life.

References

1. Sierzchula, W.; Bakker, S.; Maat, K.; van Wee, B., The competitive environment of electric vehicles: An analysis of prototype and production models. *Environmental Innovation and Societal Transitions* **2012,** *2*, 49-65.
2. Wood, D. L.; Li, J.; Daniel, C., Prospects for reducing the processing cost of lithium ion batteries. *Journal of Power Sources* **2015,** *275*, 234-242.
3. Daniel, C., Materials and Processing for Lithium-Ion Batteries. *The Journal of The Minerals, Metals & Materials Society* **2008,** *60*, 43-48.
4. Wood, D. L.; Li, J.; Mohanty, D.; Daniel, C.; Armstrong, B.; Dinwiddie, R.; Safa-Sefat, A.; Wang, H.; Trejo, R.; Gallego, N.; Contescu, C.; Howe, J.; Meisner, R.; Kiggans, J.; Brown, B., Advanced Materials Processing and Novel Characterization Methods for Low-Cost, High Energy-Density Lithium-Ion Batteries. *Advanced Automotive Battery Conference* **2013**.
5. SAMARAS, C.; MEISTERLING, K., Life Cycle Assessment of Greenhouse Gas Emissions from Plug-in Hybrid Vehicles: Implications for Policy. *Environ. Sci. Technol.* **2008,** *42*, 3170–3176.
6. Thomas, C. E., Fuel cell and battery electric vehicles compared. *International Journal of Hydrogen Energy* **2009,** *34*, 6005-6020.
7. Michalek, J. J.; Chester, M.; Jaramillo, P.; Samaras, C.; Shiau, C. S.; Lave, L. B., Valuation of plug-in vehicle life-cycle air emissions and oil displacement benefits. *Proceedings of the National Academy of Sciences of the United States of America* **2011,** *108*, 16554-8.
8. An, S. J.; Li, J.; Daniel, C.; Mohanty, D.; Nagpure, S.; Wood, D. L., The State of Understanding of the Lithium-ion-Battery Graphite Solid Electrolyte Interphase (SEI) and its Relationship to Formation Cycling. *Carbon* **2016,** *105*, 52-76.
9. Goodenough, J. B.; Park, K.-S., The Li-ion rechargeable battery: a perspective. *Journal of the American Chemical Society* **2013,** *135*, 1167-76.
10. Rafiee, J.; Mi, X.; Gullapalli, H.; Thomas, A. V.; Yavari, F.; Shi, Y.; Ajayan, P. M.; Koratkar, N. A., Wetting transparency of graphene. *Nature materials* **2012,** *11*, 217–222.
11. Austin, R. A.; Fauteux, D., BATTERY IN A VACUUM SEALED ENVELOPING MATERIAL AND A PROCESS FOR MAKING THE SAME. *United States Patent* **1991,** *US 4,997,732*, 1-9.
12. Colclasure, A. M.; Smith, K. A.; Kee, R. J., Modeling detailed chemistry and transport for solid-electrolyte-interface (SEI) films in Li–ion batteries. *Electrochimica Acta* **2011,** *58*, 33–43.
13. Collins, J.; Gourdin, G.; Foster, M.; Qu, D., Carbon surface functionalities and SEI formation during Li intercalation. *Carbon* **2015,** *92*, 193-244.
14. Wu, Y. P.; Jiang, C.; Wan, C.; Holze, R., Anode materials for lithium ion batteries by oxidative treatment of common natural graphite. *Solid State Ionics* **2003,** *156*, 283–290.

15. Ye, J. C.; Charnvanichborikarn, S.; Worsley, M. A.; Kucheyev, S. O.; Wood, B. C.; Wang, Y. M., Enhanced electrochemical performance of ion-beam-treated 3D graphene aerogels for lithium ion batteries. *Carbon* **2015,** *85*, 269-278.
16. Zhan, Y.; Zhang, B.; Cao, L.; Wu, X.; Lin, Z.; Yu, X.; Zhang, X.; Zeng, D.; Xie, F.; Zhang, W.; Chen, J.; Meng, H., Iodine doped graphene as anode material for lithium ion battery. *Carbon* **2015,** *94*, 1-8.
17. Wu, Y.; Jiang, C.; Wan, C.; Tsuchida, E., Effects of catalytic oxidation on the electrochemical performance of common natural graphite as an anode material for lithium ion batteries. *Electrochemistry Communications* **2000,** *2*, 272–275.
18. Loebl, A. J.; Oldham, C. J.; Devine, C. K.; Gong, B.; Atanasov, S. E.; Parsons, G. N.; Fedkiw, P. S., Solid Electrolyte Interphase on Lithium-Ion Carbon Nanofiber Electrodes by Atomic and Molecular Layer Deposition. *Journal of The Electrochemical Society* **2013,** *160*, A1971-A1978
19. Leese, H.; Bhurtun, V.; Lee, K. P.; Mattia, D., Wetting behaviour of hydrophilic and hydrophobic nanostructured porous anodic alumina. *Colloids and Surfaces A: Physicochemical and Engineering Aspects* **2013,** *420*, 53-58.
20. Volder, M. F. L. D.; Tawfick, S. H.; Baughman, R. H.; Hart, A. J., Carbon nanotubes: present and future commercial applications. *Science* **2013,** *339*, 535-539.
21. Collins, P. G., Extreme Oxygen Sensitivity of Electronic Properties of Carbon Nanotubes. *Science* **2000,** *287*, 1801-1804.
22. Savage, T.; Bhattacharya S; Sadanadan, B.; Gaillard, J.; Tritt, T. M.; Sun, Y.-P.; Wu, Y.; Nayak, S.; Car, R.; Marzari, N.; Ajayan, P. M.; Rao, A. M., Photoinduced oxidation of carbon nanotubes. *J. Phys.: Condens. Matter* **2003,** *15*, 5915–5921.
23. Lebro´n-Colo´n, M.; Meador, M. A.; Lukco, D.; Sola´, F.; Santos-Pe´rez, J.; McCorkle, L. S., Surface oxidation study of single wall carbon nanotubes. *Nanotechnology* **2011,** *22*, 455707.
24. Naoi, K.; Ogihara, N.; Igarashi, Y.; Kamakura, A.; Kusachi, Y.; Utsugi, K., Disordered Carbon Anode for Lithium-Ion Battery - I. An Interfacial Reversible Redox Action and Anomalous Topology Changes. *Journal of The Electrochemical Society* **2005,** *152*, A1047-A1053.
25. Spahr, M. E.; Wilhelm, H.; Joho, F.; Panitz, J.-C.; Wambach, J. r.; Novák, P.; Dupont-Pavlovsky, N., Purely Hexagonal Graphite and the Influence of Surface Modifications on Its Electrochemical Lithium Insertion Properties. *Journal of The Electrochemical Society* **2002,** *149*, A960-A966.
26. P. Nova´k, J. U., H. Buqa, F. Krumeich, M.E. Spahr, D. Goers, H. Wilhelm, J. Dentzer, R. Gadiou, C. Vix-Guterl, The importance of the active surface area of graphite materials in the first lithium intercalation. *Journal of Power Sources* **2007,** *174*, 1082–1085.
27. Ein-Eli, Y.; Koch, V. R., Chemical Oxidation: A Route to Enhanced Capacity in Li-Ion Graphite Anodes. *J. Electrochem. Soc.* **1997,** *144*, 2968-2973.

28. Gallego, N. C.; Contescu, C. I.; Meyer, H. M.; Howe, J. Y.; Meisner, R. A.; Payzant, E. A.; Lance, M. J.; Yoon, S. Y.; Denlinger, M.; Wood, D. L., Advanced surface and microstructural characterization of natural graphite anodes for lithium ion batteries. *Carbon* **2014,** *72*, 393-401.
29. Garcia-Pichel, F.; Bebout, B. M., Penetration of ultraviolet radiation into shallow water sediments:high exposure for photosynthetic communities. *Mar Ecol Prog Ser* **1996,** *131*, 257-262.
30. Li, J.; Daniel, C.; An, S. J.; Wood, D., Evaluation Residual Moisture in Lithium-Ion Battery Electrodes and Its Effect on Electrode Performance. *MRS Advances* **2016,** *1*, 1029-1035.
31. Paunovic, M.; Schlesinger, M., Fundamentals of Electrochemical Deposition, Second Edition: Chapter 6. Kinetics and Mechanism of Electrodeposition. *John Wiley & Sons, Inc.* **2005,** *Chapter 6*.
32. Zheng, H.; Sun, Q.; Liu, G.; Song, X.; Battaglia, V. S., Correlation between dissolution behavior and electrochemical cycling performance for LiNi1/3Co1/3Mn1/3O2-based cells. *Journal of Power Sources* **2012,** *207*, 134-140.
33. Yang, L.; Ravdel, B.; Lucht, B. L., Electrolyte Reactions with the Surface of High Voltage LiNi[sub 0.5]Mn[sub 1.5]O[sub 4] Cathodes for Lithium-Ion Batteries. *Electrochemical and Solid-State Letters* **2010,** *13*, A95.
34. Xu, Z.; Ao, Z.; Chu, D.; Younis, A.; Li, C. M.; Li, S., Reversible Hydrophobic to Hydrophilic Transition in Graphene via Water Splitting Induced by UV Irradiation
SCIENTIFIC REPORTS **2014,** *4*, 1-9.
35. Aurbach, D., Review of selected electrode–solution interactions which determine the performance of Li and Li ion batteries. *J. Power Sources* **2000,** *89* 206-218.
36. Aurbach, D.; Markovsky, B.; Weissman, I.; Levi, E.; Ein-Eli, Y., On the correlation between surface chemistry and performance of graphite negative electrodes for Li ion batteries. *Electrochim. Acta* **1999,** *45*, 67–86.
37. Lu, P.; Li, C.; Schneider, E. W.; Harris, S. J., Chemistry, Impedance, and Morphology Evolution in Solid Electrolyte Interphase Films during Formation in Lithium Ion Batteries. *J. Phys. Chem. C* **2014,** *118*, 896−903.
38. Kim, S.-P.; Duin, A. C. T. v.; Shenoy, V. B., Effect of electrolytes on the structure and evolution of the solid electrolyte interphase (SEI) in Li-ion batteries: A molecular dynamics study. *Journal of Power Sources* **2011,** *196*, 8590-8597.
39. Peled, E.; Golodnitsky, D.; Ulus, A.; Yufit, V., Effect of carbon substrate on SEI composition and morphology. *Electrochimica Acta* **2004,** *50*, 391-395.
40. Heit, G.; Neuner, A.; Saugy, P.-Y.; Braun, A. M., Vacuum-UV (172 nm) Actinometry. The Quantum Yield of the Photolysis of Water. *J. Phys. Chem. A* **1998,** *102*, 5551-5561.
41. Zulfiqar, S.; Zulfiqar, M.; Rizvi, M.; Munir, A., Study of the thermal degradation of polychlorotrifluoroethylene, poly(vinylidene fluoride) and copolymers of

chiorotrifluoroethylene and vinylidene fluoride. *Polym. Degrad. Stab.* **1994,** *43*, 423-430.

CHAPTER III
FAST FORMATION CYCLING FOR LITHIUM ION BATTERIES

A version of this chapter was originally published by Seong Jin An, Jianlin Li, Zhijia Du, Claus Daniel, David L. Wood III:

Seong Jin An, Jianlin Li, Zhijia Du, Claus Daniel, David L. Wood III "Fast Formation Cycling for Lithium Ion Batteries" *Journal of Power Sources*, 342 (2017): 846-852.

This chapter includes additional results and discussions besides the published contents. The additions are modified alternative protocols and their results. Abstract, Introduction, Results, and Conclusion are also updated to take account of the additions. All experiments, data analysis, and initial draft for this article were done by Seong Jin An. The draft was improved and finalized by Seong Jin An, Jianlin Li, and David L. Wood III. All other co-authors provided comments on contents.

Abstract

The formation process for lithium ion batteries typically takes several days or more, and it is necessary for providing a stable solid electrolyte interphase on the anode (at low potentials vs. Li/Li^+) for preventing irreversible consumption of electrolyte and lithium ions. An analogous layer known as the cathode electrolyte interphase layer forms at the cathode at high potentials vs. Li/Li^+. However, several days, or even up to a week, of these processes result in either lower LIB production rates or a prohibitively large size of charging-discharging equipment and space (i.e. excessive capital cost). In this study, a fast and effective electrolyte interphase formation protocol is proposed and compared with an Oak Ridge National Laboratory baseline protocol. Graphite, NMC 532, and 1.2 M $LiPF_6$ in ethylene carbonate : diethyl carbonate were used as anodes, cathodes, and electrolytes, respectively. Results from electrochemical impedance spectroscopy show the new protocol reduced surface film (electrolyte interphase) resistances, and 1300 aging cycles show an improvement in capacity retention.

Introduction

Solid electrolyte interphase (SEI) formation is affected by various conditions such as electrolyte compositions and concentrations, additives, surface properties of active and conductive materials, temperatures, C-rates (also correlated to thickness of electrodes), cut-off voltages, electrolytes wetting on electrodes, impurities in cells, volume changes of active materials during cycling, and many unknown factors. In terms of volume changes of materials, Si (one of the most promising anode materials) experiences large volume changes (about 320% of the original volume) during lithiations and delithiations, which makes the SEI layer unstable. The volume of graphite also changes but it is only a change of

about 10%. If the volume change is minimized during the formation cycles, a SEI layer on the graphite will become more stable.

This volume change of graphite can be estimated using lithiation stages: stage I, II, III, and IV. The stage index number indicates the number of graphite layers between lithium layers. Hence, stage I is more lithiated than stage II while stage IV is the least lithiated. The stage index number can be used to calculate the repeat distance, I_c, of a lithium layer and graphite layers (Eq. 1)[1]

$$I_c = nc_0 + d_i \qquad (1)$$

where n, c_0, and d_i are the stage index number, the distance between adjacent graphite layers (3.35 Å), and the lithium intercalate layer thickness (0.35 Å). As equation 1 shows, the repeating distance changes when there is a transition from one stage to another stage. As such, the distance does not change within each stage during lithiations and delithiations. Approximate voltage ranges of the stages are 210 mV or higher (stage IV), 210 – 120 mV (stage III), 120 – 85 mV (stage II), and 85 mV or below (stage I).[2] The lithium composition, x in Li_xC_6, corresponding to the voltage is 0.08 – 0.17 (stage IV), 0.17 – 0.33 (stage III), 0.33 – 0.50 (stage II), and 0.50 or higher (stage I). If the SEI formation takes place within the same stage, the volume change of the graphite will be minimized, which helps SEI layers stabilize during formation cycles.

The anode SEI and cathode electrolyte interphase (CEI) form when the electrolyte is accessible to electrons at the electrode and, simultaneously the electrolyte experiences an unstable voltage range.[3] During a charging cycle, the electrolyte decomposes and precipitates at low potentials at the anode via reduction reactions and at high potential on cathode via oxidation reactions. Irreversible capacity loss indicating electrolyte interphase formation is the highest after the first charge/discharge cycle (*ca.* 10% in the case of graphite anode), significantly lower after the second cycle, and even lower after the third cycle and so on (less than 0.05%). The irreversible capacity loss varies depending on negative-to-positive capacity ratio, surface area of particles, operation conditions, etc.[4] Most electrolyte interphase forms during the first charge/discharge cycle because the pristine anode and cathode do not have previously formed passivation layers that electronically insulate the electrode from the electrolyte. If after the first cycle, the anode graphite was not significantly exfoliated, further cycling results in significantly lower electrolyte interphase formation because the preformed interphase layer (from the first charging cycle) impedes solvent molecule diffusion towards the electrode surface and electron transfer between the electrode and electrolyte. To form a dense SEI layer, low anode voltage is preferred because the lower the anode voltage (or the higher cell voltage) applied, the more SEI layer is reduced. Hence, cycling cells at a high voltage (low voltage at anode, stage I) would be beneficial to stabilize a SEI layer.

Besides material cost, according to Wood et al.,[5] the electrolyte wetting and SEI formation steps are the second expensive processes ($36.1/kWh for electrode processing and $22.6/kWh for wetting/formation cycling) because of the slow wetting and slow charge/discharge rates (e.g. 3-5 cycles at C-rate of C/20 and 3-5 cycles at higher C-rate at a higher temperature). This process may take up to 1.5-3 weeks, depending on the cell manufacturer and cell chemistry, requiring a tremendous number of charge/discharge cycles for mass production of LIBs, large floor space, and intense energy for the cyclers and environmental chambers. These processes are a major production bottleneck; therefore, it is important to reduce wetting and formation time for cost and production rate benefits.

There have been several electrolyte interphase formation studies that attempted to reduce the required time. For example, skipping the high state-of-charge (SOC) region reduced formation time, but it also resulted in a decrease in capacity retention.[6] Increasing C-rates also reduced formation time. However, it generally caused negative effects on electrolyte interphase formation such as non-uniform thickness and discontinuity of the layer on the anode.[7-8] Formation at high voltage (4.2 V) has rarely been reported, although high-voltage operation is beneficial for high-energy batteries.

In this study, Oak Ridge National Laboratory (ORNL) baseline protocol with different C-rates were evaluated with high-voltage cells (graphite as anodes and layered oxides, NMC 532, as cathodes) and compared with the new protocol, which not only reduced formation time, but also increased cell capacity retention. A simple wetting process was applied in this study. C-rate tests, aging tests, and performance checks during aging were conducted for six different formation protocols (three baseline protocols and three alternative protocols). Electrochemical impedance spectroscopy (EIS) was also measured to investigate total resistance and resistance components.

Proposed formation method

As the electrolyte becomes unstable during cell charging, in this study, it was hypothesized that:

1) Most SEI and CEI form at a high SOC because electrolytes undergo more reduction reactions at anode and more oxidation reactions at cathode.[9]
2) An anode SEI layer at high SOC is more compact and stable than that at low SOC because the potentials at high SOC result in more electrolyte instability and more lithium is available at the anode for reduction with bulk compounds.[10]

3) The SOC should remain high for a longer period of time and low for a shorter period of time in order to have a compact and stable electrolyte interphase layer, but the SOC should not simply be held at a higher cut-off voltage that results in the current (electron-flow) dropping down to nearly zero.

Typical potential profiles (cathode denoted as μ_C, anode denoted as μ_A, and potential difference between anode and cathode denoted as V_{OC}) from a three-electrode pouch cell (graphite/Li/ $Li_{1.02}Ni_{0.50}Mn_{0.29}Co_{0.19}O_2$) are illustrated in Figure 3.1a showing the unstable potential ranges of the cathode[11] (light blue zone) and anode (light orange zone and dark orange zone). The color intensity indicates the relative degree of instability of the electrolyte. Based on the hypothesis of this study, an alternative protocol for electrolyte interphase formation in Figure 3.1b is shown and compared with a baseline protocol, the latter of which consists of a series of charge and discharge cycles at a constant C-rate without any interruption between the lower and upper cut-off voltages. The alternative protocol, however, involves repeated cycling within a high SOC region, anode lithiation stage I (cell voltage 3.9 V and above), after the first charge until the last cycle where a full discharge takes place. The same concept was applied to another alternative protocol with a slight modification above cell voltage 3.9 V (Figure 3.1c). Below 3.9 V at cells, C/3 or 1C were applied in addition to C/5 while C/5 was used above 3.9 V.

In this study, the baseline formation protocol was evaluated with three different equal charge and discharge C-rates: C/20, C/10, and C/5. Rates of C/20 or C/10 are generally used for at least the first formation cycle in standard cell manufacturing. The baseline formation protocols were compared with the alternative protocols using the same three equal charging and discharging C-rates: C/20, C/10, and C/5 and with modified alternative protocols using various C-rates below 3.9 V. Abbreviations used in this study are listed with their respective descriptions in Table 3.1. Prior to beginning all formation cycling, each cell was exposed to a three-hour electrolyte wetting process.

Experimental

Eighteen pouch cells were assembled for testing using the baseline and alternative formation protocols (three pouch cells were used for each protocol). Sixteen pouch cells were additionally assembled for another set of testing using the baseline and modified alternative formation protocols (four pouch cells were used for each protocol). The cell chemistry and dimensions are listed in Table 3.2. Electrodes were coated and dried using a slot-die coater (Frontier Industrial Technology) in the DOE Battery Manufacturing R&D Facility at ORNL, but they were not calendered. Cell assembly was completed in a dry room where the

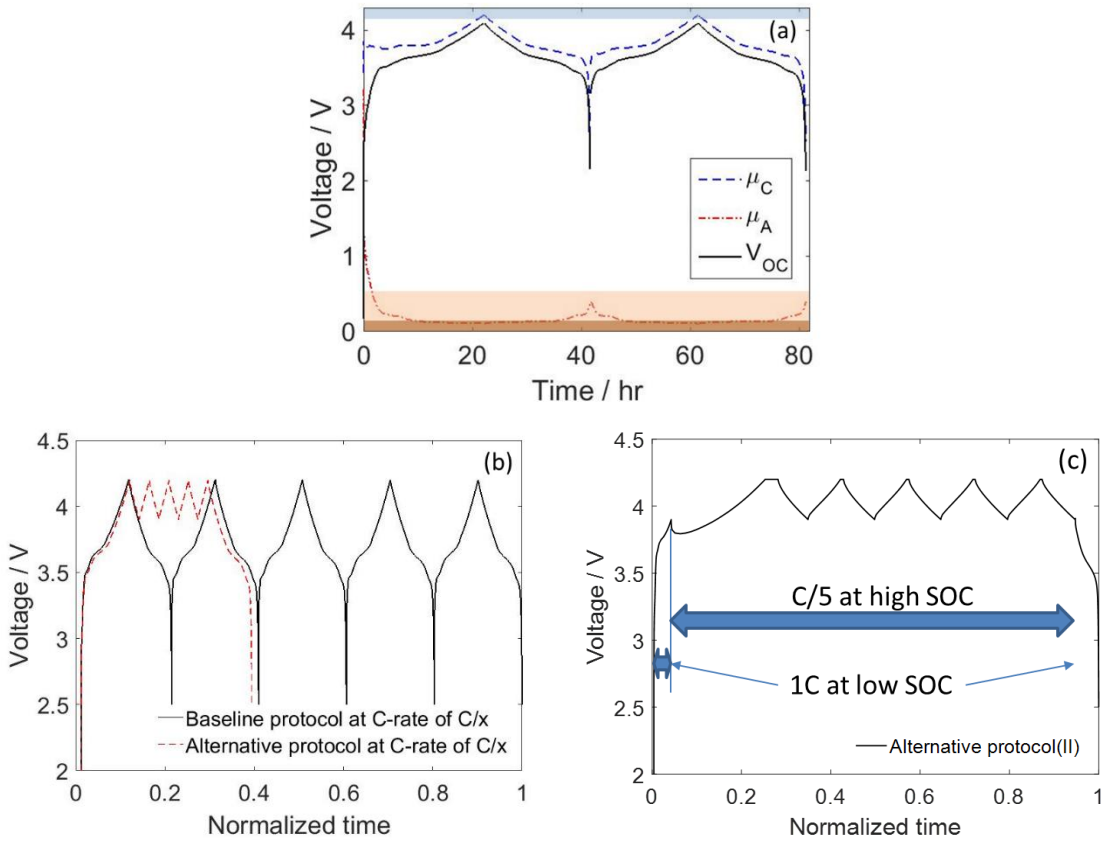


Figure 3.1. Typical cathode potential (μC), anode potential (μA), and voltage between anode and cathode (VOC) from a three-electrode pouch cell (graphite anode/Li reference/$Li_{1.02}Ni_{0.50}Mn_{0.29}Co_{0.19}O_2$ cathode) with potential ranges in blue and orange regions where the electrolyte is not stable (a); cell voltage profiles from a baseline and alternative (b) and a modified alternative SEI formation protocol (c).

Table 3.1. Abbreviations used in this study and associated formation conditions

	Test group abbreviation	SEI formation condition				
		C-rate	Higher cut-off voltage	Intermediate voltage turning to charge mode	Lower cut-off voltage	Number of charge/discharge cycles
Baseline formation	F@C/20	C/20	4.2 V	None	2.5 V	5
	F@C/10	C/10				
	F@C/5	C/5				
Alternative formation	F@C/20a	C/20		4.0 V		
	F@C/10a	C/10		3.9 V		
	F@C/5a	C/5		3.9 V		
Modified alternative formation	F@C/3a	C/3 below 3.9 V, C/5 above 3.9 V		3.9 V		
	F@C/1a	1C below 3.9 V, C/5 above 3.9 V		3.9 V		

Table 3.2. Cell information

	Composition	Size (loading) [porosity]
Anode	Electrode: 92 wt % A12 graphite (ConocoPhillips), 2 wt % C-65 carbon black (Timcal), 6 wt % polyvinylidene fluoride (PVDF, Kureha 9300) Current collector: Copper foil Tab: nickel	Electrode only 84.4 mm×56 mm× 65 μm (6.36 mg/cm^2) [55%]
Cathode	Electrode: 90 wt % $Li_{1.02}Ni_{0.50}Mn_{0.29}Co_{0.19}O_2$ (NMC 532 or NCM 523, TODA America Inc.), 5 wt % powder grade carbon black (Denka), 5 wt % PVDF (Solvay Solef® 5130) Current collector: Aluminum foil Tab: Aluminum	Electrode only 84.4 mm×56 mm× 64 μm (12.02 mg/cm^2) [55%]
Separator	Polypropylene–polyethylene–polypropylene (Celgard® 2325)	89 mm × 61 mm × 25 μm [39%]
Electrolyte	1.2 M $LiPF_6$ in EC:DEC (3:7 by weight, BASF)	–

relative humidity was held between 0.1-0.2% at a room temperature of 21°C. Secondary drying of the electrodes was completed overnight at 80°C under vacuum prior to assembly to minimize moisture content. The electrolyte volume ratio used in each cell was 2.5 (ratio of electrolyte volume to total cell pore volume) to minimize the effect of insufficient electrolyte, and the cells were sealed under vacuum at 700 mm Hg.

After assembly, all cells were rested for 2 hours at 21°C for the first electrolyte wetting, then placed in an environmental chamber (ESPEC Corp.) at 30°C, and connected to a battery tester (Series 4600, Maccor Inc.). Next they were charged at C/3 until the tap voltage reached 1.5 V to avoid corrosion of the copper current collector and rested again for 1 hour for the second electrolyte wetting. The pouch cells went through their respective series of formation cycles using the protocols shown in Table 3.1 and Figure 3.1b and 3.1c, and were subsequently evaluated at C/5, C/2, 1C, and 3C for initial rate performance. Capacity fades after the alternative and modified alternative protocols were measured over 1300 cycles and 500 cycles, respectively, at 1C charge/discharge rates where 1C was based on 160 mAh/g (normalized by the NMC 532 weight). Upper and lower cut-off voltages were 4.2 V and 2.5 V, respectively, for all charge-discharge cycles.

EIS for the alternative protocols was measured before the aging cycles, after 300 cycles, and after 1300 cycles to analyze resistance increases using VSP potentiostat systems (EC-Lab, Bio-Logic Science Instruments SAS). EIS for the modified alternative protocols was measured after 500 cycles. These measurements were performed at 25% discharge intervals and frequencies from 400 kHz to 10 mHz with 5 mV oscillation amplitudes. Nyquist plots were fitted using EC-Lab software (Bio-Logic Science Instruments SAS) to analyze ohmic resistance (R_{ohmic}), surface film resistance (R_{sf}), and charge transfer resistance (R_{ct}). All other data processing and calculations were performed using Matlab R2016 (MathWorks, inc).

Results and discussion

Formation time reduction and capacity

Most formation processes utilize three cycles or more at C/10 or C/20 charge and discharge rates. In this study, five formation cycles were conducted to confirm capacity convergence. Figure 3.2 shows experimental results of voltage profiles vs. time for the baseline, alternative, and modified alternative protocols at different C-rates. Five formation cycles with the baseline C/20, C/10, and C/5 charging and discharging rates resulted in 212-220, 107 and 55 hours, respectively, while those with the proposed alternative C/20 (C/20a), C/10

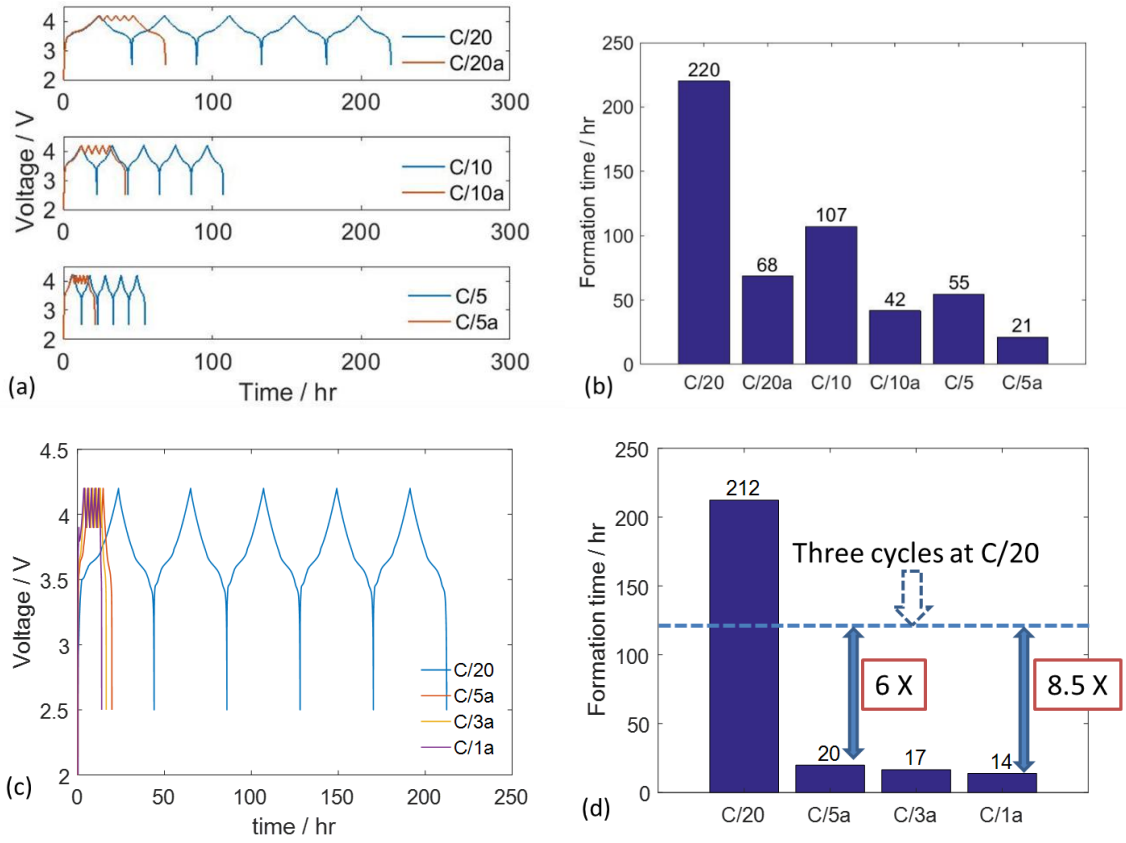


Figure 3.2. Voltage profiles for three baseline formation protocols in blue and alternative protocols (C-rates denoted with "a") in orange (a) and corresponding formation times (b), voltage profiles for modified alternative protocols in yellow and purple (c) and corresponding formation times (d).

(C/10a), and C/5 (C/5a) rates resulted in 68, 42, and 20-21 hours. Compared to the baseline protocol, the alternatives reduced formation time by 60% or more at each C-rate. When the alternative C/5 (C/5a) protocol is compared to the baseline C/20 protocol, a 90% reduction in formation time is realized. For a more realistic case of only three C/20 baseline cycles, the formation time with C/5a is still 6 times faster. The modified alternative at C/1a further reduced formation time by a factor of 8.5.

During formation cycling, discharge capacities with the alternative formation protocol were lower than those with the baseline protocol (Figure 3.3a and 3.3c). (The capacity data sets for the alternative and modified alternative formation protocols are all located on cycle # 1 because the protocols contain only one full discharge step.) However, cells cycled with the baseline, alternative, and modified alternative protocols had similar discharge capacities during rate capability testing as shown in Figure 3.3b and 3.3d (error bars correspond to 90% confidence intervals).

Initial and final capacities of cells cycled with different formation protocols were also similar during aging (Figure 3.4). The three different C-rates (C/20, C/10, and C/5) for baseline, alternative, and modified alternative protocols did not significantly affect capacities at C-rate and aging tests. A capacity increase in Figure 3.4a and 3.4c occurred for each cell after EIS measurements at 300^{th} cycle. Capacity retention after 1000 cycles at 1C charge and discharge rates was about 80% for cells using the baseline protocols and about 82% for cells using the alternative protocol ones. The cyclability at C/5 charge and discharge rates is also similar with 86% capacity retention after 1000 cycles (20^{th} loop). Although these results are similar when considering the error bars of each data, the implication is that the alternative formation protocol had a positive impact on the cell performance rather than any negative one. Discharge capacities of modified protocols were also the same within the error range during C-rate performance tests and aging cycles with 1C/-1C and C/5/-C/5 (Figure 3.4e and 3.4f). Through further careful optimization, it is likely that the formation time can be further reduced below 14 hours without compromising cell performance.

EIS resistances

The equivalent circuit model used for the EIS fitting is shown in Figure 3.5. R_{ohmic}, R_{sf}, and R_{ct} represent the ohmic resistance, surface film (electrolyte interphase) resistance, and charge transfer resistance, respectively. On the left in Figure 3.6, the EIS intercepts with the real axis in the high-frequency region are generally considered as R_{ohmic}, which involves resistances from lithium ion transport through the electrolyte and from electron transport through the electrodes,

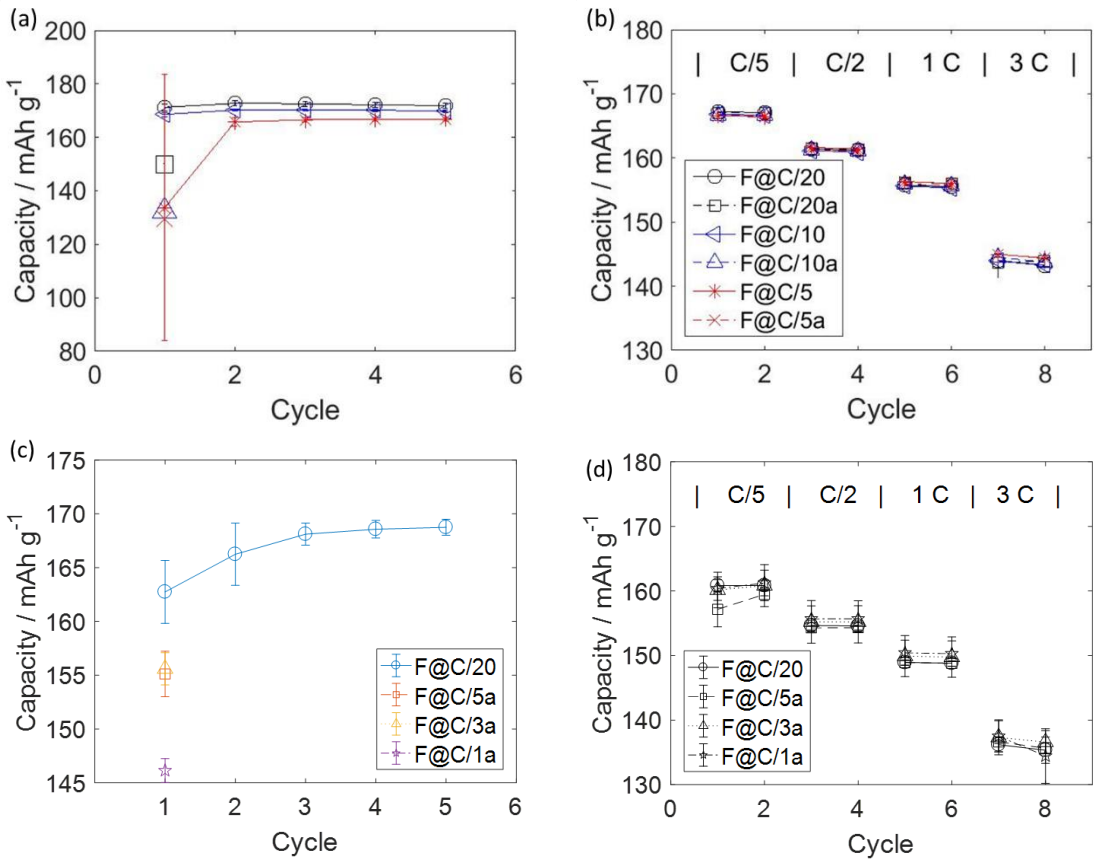


Figure 3.3. Average discharge capacities with 90% confidence intervals using different formation protocols during formation cycling (a and c) and post-formation rate capability testing (b and d). Capacities from alternative and modified alternative protocols in (a and c) show only one value at the first cycle for each formation C-rate because the alternative and modified alternative protocols contain only one full discharge.

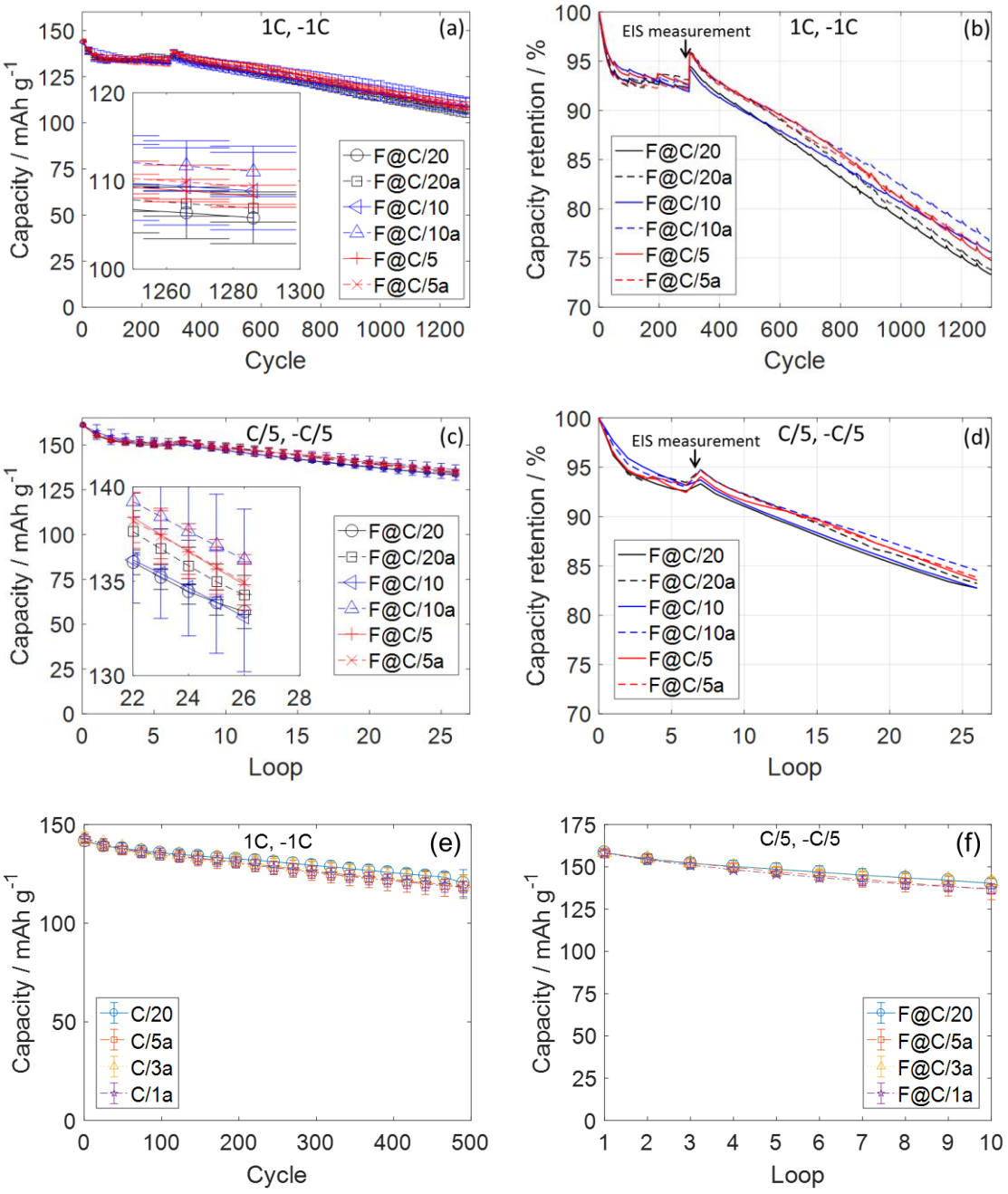


Figure 3.4. Discharge capacities after the baseline and alternative formations (a, c) and after the baseline and modified alternative formations (e-f) and discharge capacity retentions for the baseline and alternative (b, d) during aging for each 1C and -1C cycle (a-b) and each C/5 and -C/5 loop (c-d) where each loop is 50 cycles.

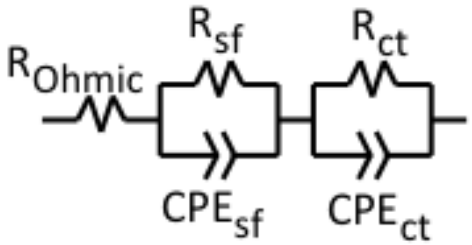


Figure 3.5. Equivalent circuit model used in this impedance analysis.

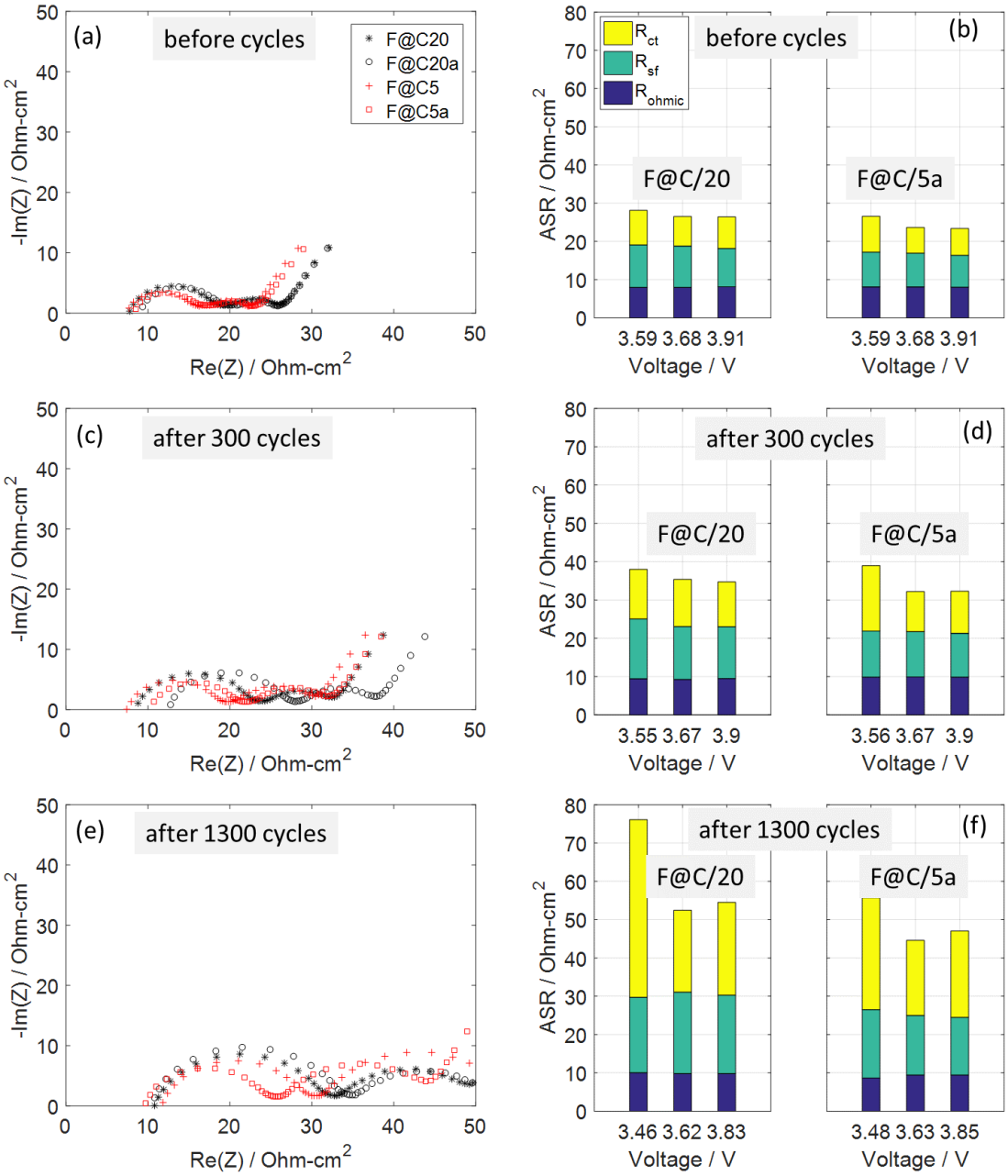


Figure 3.6. EIS Nyquist plots from cells with different formation protocols (a, c, and e) near 3.9V ±0.05V during discharge; average areal specific resistances (ASR) of F@C/20 and F@C/5a (b, d, and f) at different voltages before aging cycles (b), after 300 cycles (d), and after 1300 cycles(f).

current collectors, cables, and lead clips between the cell and potentiostat. The first semicircles at the high-to-medium frequency region (ca. 80k - 200 Hz) are related to R_{sf} and attributed to impedances from lithium ion migration through the surface films.[12-13] The second semicircles at the medium-to-low frequency region (ca. 200 – 0.4 Hz) are related to R_{ct} and are impedances from charge transfer between the liquid electrolyte and solid surface.[14]

The linear Warburg-type elements at the low frequency region (ca. 0.4 – 0.01 Hz) correspond to lithium-ion diffusion in the active material particles, which were not included in the data fitting in this study. In parallel to R_{sf} and R_{ct} in the equivalent circuit model, CPE_{sf} and CPE_{ct} represent the capacitance of the surface film and charge transfer, respectively. A constant phase element (CPE) was applied instead of an ideal capacitor element to take into account imperfect capacitor behavior in a large, porous electrode.

Representative impedances near 3.9 V during discharge from F@C20, F@C/20a, F@C/5 and F@C/5a are shown in Nyquist plots on the left side of Figure 3.6. On the right side of Figure 3.6, average areal specific resistances from the EIS of two extreme cases (F@C/20 and F@C/5a) were compared at different voltages. Resistances from F@C/5a (fastest alternative formation protocol) before aging cycles were slightly lower than those from F@C/20 (slowest baseline formation protocol). As the cells were cycled, the resistances from F@C/5a were significantly smaller than those from F@C/20. In this study, all ohmic resistances increased slightly (by *ca.* 10%) after 1300 cycles while surface film resistances and charge transfer resistances significantly increased (by 80% or more). The increase in charge transfer resistance was larger than that of the surface film resistance for both F@C/20 and F@C/5a. However, F@C/5a showed 25-30% smaller surface film resistance than F@C/20 both before and after aging cycles, implying the cells with alternative formation cycles had more robust electrolyte interphase layers than those with the baseline formation cycles.

Like the alternative protocols, the additional study for the modified formation protocol also showed that resistances of baseline were also similar to those of cells with the modified protocol (Figure 3.7). Figure 3.7a and 3.7b were obtained using hybrid pulse power characterization (HPPC) analysis and AC electrochemical impedance spectroscopy (EIS).

Regarding baseline protocols, SEI analysis using X-ray photoelectron spectroscopy and separation of anode and cathode resistances using three-electrode cells were elaborated elsewhere.[15-16] Further studies are needed to obtain detail cause and effect for the improvement after the alternative formation protocols, including any irreversible change in active materials.

Conclusions

This study demonstrates the effectiveness of a formation protocol having more (shallow) charge-discharge cycles between 3.9 V and 4.2 V and fewer (full depth of discharge) cycles below 3.9 V. The proposed formation protocol shortened formation time by 6 times or more without compromising cell performance; rather, it improved capacity retention, which will have a tremendous impact on the operating and capital cost of manufacturing LIBs. On the other hand, for both protocols, the different C-rates, at least up to C/5 during formation, did not significantly affect capacities and capacity fades. Analysis via EIS showed substantially lower surface film (electrolyte interphase) resistance for the cells that underwent the fastest alternative formation protocol than those that underwent the slowest baseline formation protocol, implying that the alternative protocol provided a more robust and chemically stable electrolyte interphase layer.

A modified fast formation protocol was also proposed and reduced SEI formation time by a factor of 8 or more without compromising cell performance. In the protocol, 1C and C/3 below 3.9 V were used in an attempt to reduce the formation time, while the same C/5 was applied between 3.9 and 4.2 V (shallow cycling region). Discharge capacities during the aging cycles and resistances after the aging cycles were the same with and without the modified protocol within the error range.

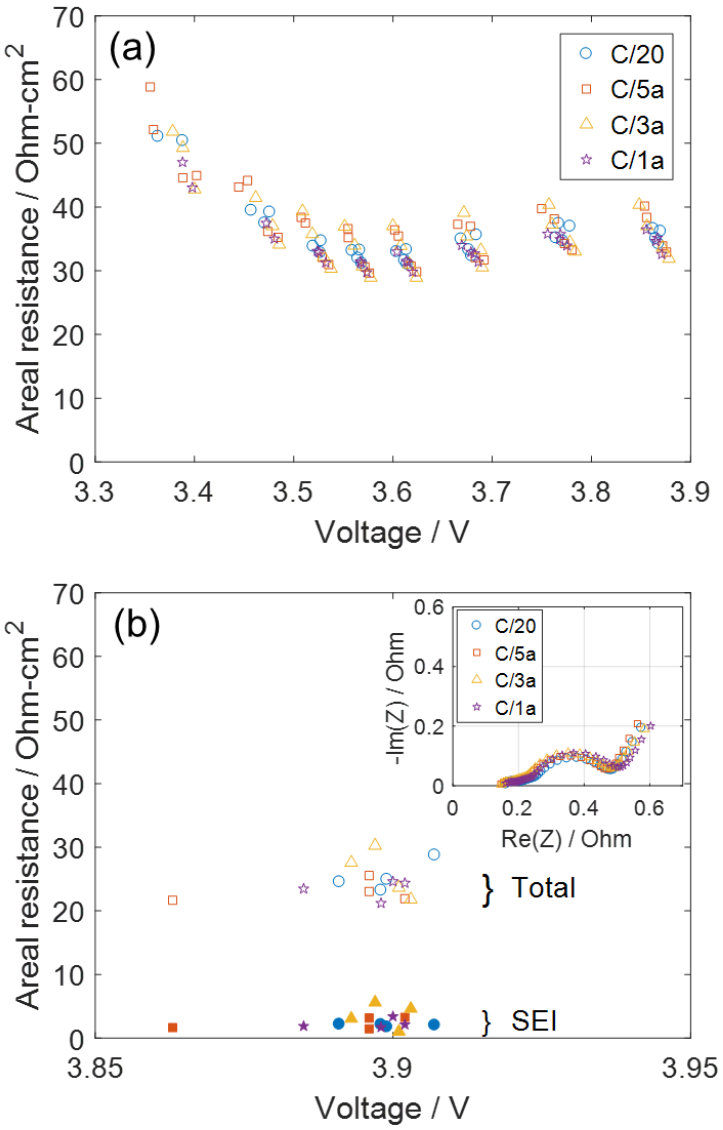


Figure 3.7 Areal resistance of cells with the baseline and modified alternative protocol from HPPC tests (a) and EIS (b) after 500 aging cycles.

References

1. Dresselhaus, M. S.; Dresselhaus, G., Intercalation compounds of graphite. *Advances in Physics* **2002,** *51*, 1-186.
2. Ohzuku, T.; Iwakoshi, Y.; Sawai, K., Formation of Lithium-Graphite Intercalation Compounds in Nonaqueous Electrolytes and Their Application as a Negative Electrode for a Lithium Ion (Shuttlecock) Cell. *J. Electrochem. Soc.* **1993,** *140*, 2490-2498.
3. Goodenough, J. B.; Kim, Y., Challenges for Rechargeable Li Batteries. *Chemistry of Materials* **2010,** *22*, 587–603.
4. An, S. J.; Li, J.; Daniel, C.; Mohanty, D.; Nagpure, S.; Wood, D. L., The State of Understanding of the Lithium-ion-Battery Graphite Solid Electrolyte Interphase (SEI) and its Relationship to Formation Cycling. *Carbon* **2016,** *105*, 52-76.
5. Wood, D. L.; Li, J.; Daniel, C., Prospects for reducing the processing cost of lithium ion batteries. *Journal of Power Sources* **2015,** *275*, 234-242.
6. Lee, H.-H.; Wang, Y.-Y.; Wan, C.-C.; Yang, M.-H.; Wu, H.-C.; Shieh, D.-T., A fast formation process for lithium batteries. *Journal of Power Sources* **2004,** *134*, 118-123.
7. Bhattacharya, S.; Alpas, A. T., Micromechanisms of solid electrolyte interphase formation on electrochemically cycled graphite electrodes in lithium-ion cells. *Carbon* **2012,** *50*, 5359-5371.
8. Bhattacharya, S.; Riahi, A. R.; Alpas, A. T., Role of Voltage Scan Rate on Degradation of Graphite Electrodes Electrochemically Cycled vs. Li/Li+. *MRS Proceedings* **2012,** *1388*, 1-6.
9. Lu, P.; Li, C.; Schneider, E. W.; Harris, S. J., Chemistry, Impedance, and Morphology Evolution in Solid Electrolyte Interphase Films during Formation in Lithium Ion Batteries. *The Journal of Physical Chemistry C* **2014,** *118*, 896-903.
10. Kim, S.-P.; Duin, A. C. T. v.; Shenoy, V. B., Effect of electrolytes on the structure and evolution of the solid electrolyte interphase (SEI) in Li-ion batteries: A molecular dynamics study. *Journal of Power Sources* **2011,** *196*, 8590-8597.
11. Zheng, H.; Sun, Q.; Liu, G.; Song, X.; Battaglia, V. S., Correlation between dissolution behavior and electrochemical cycling performance for LiNi1/3Co1/3Mn1/3O2-based cells. *Journal of Power Sources* **2012,** *207*, 134-140.
12. Aurbach, D.; Markovsky, B.; Weissman, I.; Levi, E.; Ein-Eli, Y., On the correlation between surface chemistry and performance of graphite negative electrodes for Li ion batteries. *Electrochim. Acta* **1999,** *45*, 67–86.
13. Aurbach, D.; Markovsky, B.; Levi, M. D.; Levi, E.; Schechter, A.; Moshkovich, M.; Cohen, Y., New insights into the interactions between electrode materials and electrolyte solutions for advanced nonaqueous batteries. *Journal of Power Sources* **1999,** *81–82*, 95–111.
14. Levi, M. D.; Aurbach, D., Simultaneous Measurements and Modeling of the Electrochemical Impedance and the Cyclic Voltammetric Characteristics of

Graphite Electrodes Doped with Lithium. *J. Phys. Chem. B* **1997,** *101*, 4630-4640.
15. An, S. J.; Li, J.; Daniel, C.; Wood, D. L., Design and Demonstration of Three-Electrode Pouch Cells for Lithium-Ion Battery. *Electrochim. Acta* **2017**, under review.
16. An, S. J.; Li, J.; Sheng, Y.; Daniel, C.; Wood III, D. L., Long-Term Lithium-Ion Battery Performance Improvement via Ultraviolet Light Treatment of the Graphite Anode. *J. Electrochem. Soc.* **2016,** *163*, A2866-A2875

CHAPTER IV
CORRELATION OF ELECTROLYTE VOLUME AND ELECTROCHEMICAL PERFORMANCE IN LITHIUM-ION POUCH CELLS WITH GRAPHITE ANODES AND NMC532 CATHODES

A version of this chapter was originally published by Seong Jin An, Jianlin Li, Debasish Mohanty, Claus Daniel, Bryant J. Polzin, Jason R. Croy, Stephen E. Trask, and David L. Wood III:

Seong Jin An, Jianlin Li, Debasish Mohanty, Claus Daniel, Bryant J. Polzin, Jason R. Croy, Stephen E. Trask, and David L. Wood III "Correlation of Electrolyte Volume and Electrochemical Performance in Lithium-Ion Pouch Cells with Graphite Anodes and NMC532 Cathodes" *Journal of The Electrochemical Society*, 164 (2017): A1195-A1202.

All experiments, data analysis, and initial draft for this article were done by Seong Jin An. The draft was improved and finalized by Seong Jin An, Jianlin Li, and David L. Wood III. The electrodes used in this study were provided by Bryant J. Polzin, Jason R. Croy, Stephen E. Trask. All other co-authors provided comments on contents.

Abstract

The work herein reports on studies aimed at exploring the correlation between electrolyte volume and electrochemical performance of full cell, pouch-cells consisting of graphite/ $Li_{1.02}Ni_{0.50}Mn_{0.29}Co_{0.19}O_2$ (NMC-532) as the electrodes and 1.2 M $LiPF_6$ in ethylene carbonate:ethylmethyl carbonate (EC:EMC) as the electrolyte. It is demonstrated that a minimum electrolyte volume factor of 1.9 times the total pore volume of cell components (cathode, anode, and separator) is needed for long-term cyclability and low impedance. Less electrolyte results in an increase of the measured Ohmic resistances. Increased resistance ratios for charge transfer and passivation layers at cathode, relative to initial values, were 1.5 – 2.0 after 100 cycles. At the cathode, the resistance from charge transfer was 2-3 times higher than for passivation layers. Differential voltage analysis showed that anodes were less delithiated after discharging as the cells were cycled.

Introduction

In general, aging within cells begins during formation cycles with the decomposition of electrolyte constituents on anode surfaces to form the so-called, solid electrolyte interphase (SEI).[1] Decomposition of electrolyte components and subsequent precipitation of reaction products can also take place on cathode surfaces, particularly when the charge cut-off voltage is higher than the voltage stability of the electrolyte. Typical electrolyte formulations are based on constituents such as ethylene carbonate (EC), diethyl carbonate (DEC), ethylmethyl carbonate (EMC), and $LiPF_6$ and are generally stable up to ~4.5 V vs. Li^+/Li (or lower at elevated temperatures). [2-4] These various, unwanted

“side reaction” occurring during operation and storage are the main contributors to decreased cycle-life of cells through the loss of cyclable lithium and surface degradation resulting in untenable increases in cell impedance due to passivation of the electrode surfaces impeding Li transport to the electrodes.

Increases in electrolyte resistances during aging is typically not severe because the ionic conductivity and electrolyte volumes are sufficiently high initially. However, if the electrolyte becomes overly depleted due to side reactions, its resistance can comprise a considerable portion of the overall cell resistance, resulting in gradual performance decline. Furthermore, loss of lithium ions due to persistent SEI formation continuously shifts the anode to higher voltages as it becomes more underlithiated from cycle-to-cycle. Simultaneously, a corresponding voltage shift is seen at the cathode to maintain the net upper-voltage, charge cut-off. This results in over-delithation of the cathode as well as an increased propensity for transition metal (TM) dissolution from cathode particles.[5] TM dissolution can cause crystal structure disordering at particle surfaces[6-7], film formation, and accelerated lithium loss at the anode due to migration of TM ions through the electrolyte and subsequent incorporation at the anode surface [8-10]; all of which may contribute to further impedance rise and a decrease in cycle-life.

Ultimately related to both cycle-life and energy densities, overall cost reduction is an important factor for vehicle applications. According to a cost analysis from Wood et al.,[11-13] conducted in 2015, a materials cost breakdown showed that the electrolyte accounted for 9.9% of the total materials cost, making it the third most expensive material after the Ni-Mn-Co-based (NMC) cathode powder and separator. In addition, volumetric energy considerations (Wh/l) are critical for transportation applications and the total volume and weight of battery systems must be accounted for. Therefore, minimizing electrolyte volumes (i.e., cost and weight) used in lithium ion cells, without sacrificing battery performance, is of interest.

To date, very few electrolyte-volume optimization studies have been reported in the literature creating a knowledge gap with respect to smaller-scale research and development. For example, laboratory studies on battery metrics such as cycle-life, power, safety, additives, etc., should be performed under standardized condition that are, as much as possible, relevant to actual battery applications. The effect of electrolyte volume on coin cell performance has been report by Long et al.,[14] and they found that a factor of 2.7 was identified as a better volume to pore ratio among factors of 1.7, 2.7, 4.7, and 8.7. However, the optimal electrolyte volume strongly depends on cell configuration. For example, there are variables in coin or pouch cell configuration, such as the dead volume from coin cell parts and ratio of electrode area to pouch or can area. Coin cells have large dead volume at spring zone and around spacers in the cans while pouch cells

are tightly sealed in flexible pouches without spacers and springs under vacuum. Hence, pouch cells generally have negligible dead volume, in which the electrolyte volume to pore ratio is less affected by the dead volume.

Herein, we report our efforts on optimizing (minimizing) the volume of electrolyte used in single-layer, 70 mAh pouch-cells for characterization of NMC/graphite full cell systems and evaluate the effect of cell configuration on the optimal electrolyte volume. Pouch cells with one single-sided NMC cathode, 1 layer of separator and one single-sided graphite anode were used since they represent the typical repeating unit in pouch cells. The electrolyte-volume to pore-volume factors for the pouch cells were evaluated between 1.3 and 3.5 with about 0.5 increments, which covers the optimum factor (2.7) found for coin cells in the Long et al. study within a narrow range. The effect of electrolyte volume used in the cell fabrication on cell performance was characterized in terms of rate capability, capacity fade, impedance change, and hybrid pulse power characterization (HPPC).[15] Differential voltage analysis was used to understand the state of discharge of cells before and after aging. Half-cells (Li counter electrodes), coin-cells having graphite or NMC working electrodes were also tested to separate the anode differential voltage from that of the cathode, and to compare these data with those of full cells.

Experimental

70 mAh single-unit-pouch cells were fabricated using single–sided graphite anodes, single-sided $Li_{1.02}Ni_{0.50}Mn_{0.29}Co_{0.19}O_2$ (NMC-532 from Toda Japan) cathodes, and 1.2 M $LiPF_6$ in ethylene carbonate (EC) : ethylmethyl carbonate (EMC) (3:7 wt. ratio) electrolytes, denoted as GEN2. All assembly processes were completed in the DOE Battery Manufacturing R&D Facility (BMF) dry room (dew point ≤ -55°C) at Oak Ridge National Laboratory (ORNL) to mitigate water-vapor-related decomposition effects on the electrolyte.[16] Detailed cell-build information is listed in Table 4.1. The electrodes were fabricated at, and provided by, the Cell Analysis, Modeling, and Prototyping (CAMP) Facility at Argonne National Laboratory (ANL).

The total pore volume of cells was calculated as the sum of individual anode, cathode, and separator pore volumes. The electrolyte volume factor, ***f***, was defined as the supplied electrolyte volume divided by the total cell pore volume, and was tested in the range $1.3 \leq f \leq 3.6$. During vacuum sealing of pouch cells, small amounts of electrolyte solvent can be evaporated, the amount of evaporated solvents were accounted for 11% of the supplied electrolyte by weighing and subtracted from the added amount when calculating ***f***. The average molar concentration of $LiPF_6$ also increased from 1.2 M to ~1.3 M after solvent evaporation.

Table 4.1. Pouch cell information

	Composition	Loading (Electrode size) Porosity
Anode	91.8wt% A12 graphite (ConocoPhillips), 2wt% C-45 carbon (Timcal), 6wt% PVDF (Kureha 9300), 0.17wt% oxalic acid	5.88 mg/cm^2 (86.4 mm, 58 mm, 44 μm) 38.4%
Cathode	90wt% $Li_{1.02}Ni_{0.50}Mn_{0.29}Co_{0.19}O_2$ (NMC-532, Toda Japan), 5wt% C-45 carbon (IMERYS Graphite & Carbon), 5wt% PVDF (Solvay® 5130)	9.17 mg/cm^2 (84.4 mm, 56 mm, 34 μm) 38.4%
Separator	Polypropylene–polyethylene–polypropylene (Celgard® 2325)	- (89 mm, 61 mm, 25 μm) 39%
Electrolyte	1.2 M $LiPF_6$ in EC:EMC (3:7 by weight)	-

The pouch-cells were consistently sealed directly adjacent to the electrode stack to minimize the void between the electrodes and the sealing edges. Electrolyte volume factor groups, ***F*** (from 1.3 to 3.5) were investigated with five pouch-cells in each group. Table 4.2 shows the five factor groups, ***F***, along with individual factors, ***f***, for each cell in the group. Each cell was placed for testing between two metal plates and held by four bolts at the plate corners under 0.1 kg/cm^2 pressure. The 25 pouch-cells in Table 4.2 were tested using a MACCOR Series 4600 cycler in conjunction with a temperature chamber held at 30°C. The test protocols and procedures in this study, Figure 4.1, were developed as standard protocols under the U.S. DOE's "Deep-Dive" project on enabling high-voltage lithium-ion cells. Briefly, each cell underwent four initial formation cycles at C/10 charge and discharge rates. Cycle life tests were conducted using C/3 charge/discharge rates, with a three-hour voltage hold at the top of each charge, rate performance tests were conducted before initiating cycle-life testing and after every 20 cycles of the life tests. The rate tests included one charge/discharge cycle at C/10 followed by one charge at C/3 and subsequent discharge at 1C. The 1C rate was defined in terms of the practically achieved capacity during rate testing (not shown) and was determined to be ~180 mAh/g. The voltage limits for all tests were constant between 3.0-4.4 V. Differential voltage analysis was completed using the C/3 voltage curves at each 20-cycle interval.

HPPC testing [15] was used to investigate the resistance of full cells at different depths of discharge (DODs). HPPC tests were performed before life testing and after every 20 aging cycles. Cells were first charged at a C/3 rate until the voltage reached 4.4 V, discharged at C/3 discharge rates to adjust the 10% DOD, and rested at OCV for 1 hour before the start of each HPPC test. The HPPC tests at every 10% DOD were composed of sets of discharge pulses at 2C for 10 sec., a rest for 40 sec., a regeneration (charge) pulse at 1.5C for 10 sec., and a rest for 40 sec. The resistance was calculated by using current and voltage differences before and after the HPPC discharge pulses.

Electrochemical impedance spectroscopy (EIS) was performed on selected cells before and after life testing. A VSP potentiostat system and EC-Lab (Bio-Logic Science Instruments SAS, France) were used for EIS measurement and impedance data fitting, respectively. Constant phase elements (CPEs) were used for the data fitting instead of capacitor elements because the surfaces of electrodes were not perfectly smooth and the large sizes of electrodes could cause uneven current distributions resulting in imperfect capacitance behavior. The Warburg element at the lowest-frequency domains was not considered in the EIS data fittings for resistance analysis since it is related to solid-state diffusion rather than the resistance.[17] EIS measurements were performed from 4.2 V to 3.0 V with 0.3 V intervals for full pouch-cells or every 25% charge and discharge intervals for half-cells from 400 kHz to 10 mHz and 5 mV amplitudes.

Table 4.2. **Electrolyte volume factor group, F, having five individual factor samples, f, in each group**

Factor group	Electrolyte volume to pore volume factor (ratio) of each cell, ***f***	Average
F 1.3	1.25, 1.29, 1.29, 1.33, 1.32 (from cell #1 to #5)	1.30
F 1.9	1.89, 1.94, 1.89, 1.93, 1.90 (from cell #6 to #10)	1.91
F 2.5	2.54, 2.50, 2.42, 2.42, 2.62 (from cell #11 to #15)	2.50
F 3.0	2.85, 3.10, 3.14, 3.16, 2.94 (from cell #16 to #20)	3.04
F 3.5	3.51, 3.52, 3.55, 3.49, 3.56 (from cell #21 to #25)	3.53

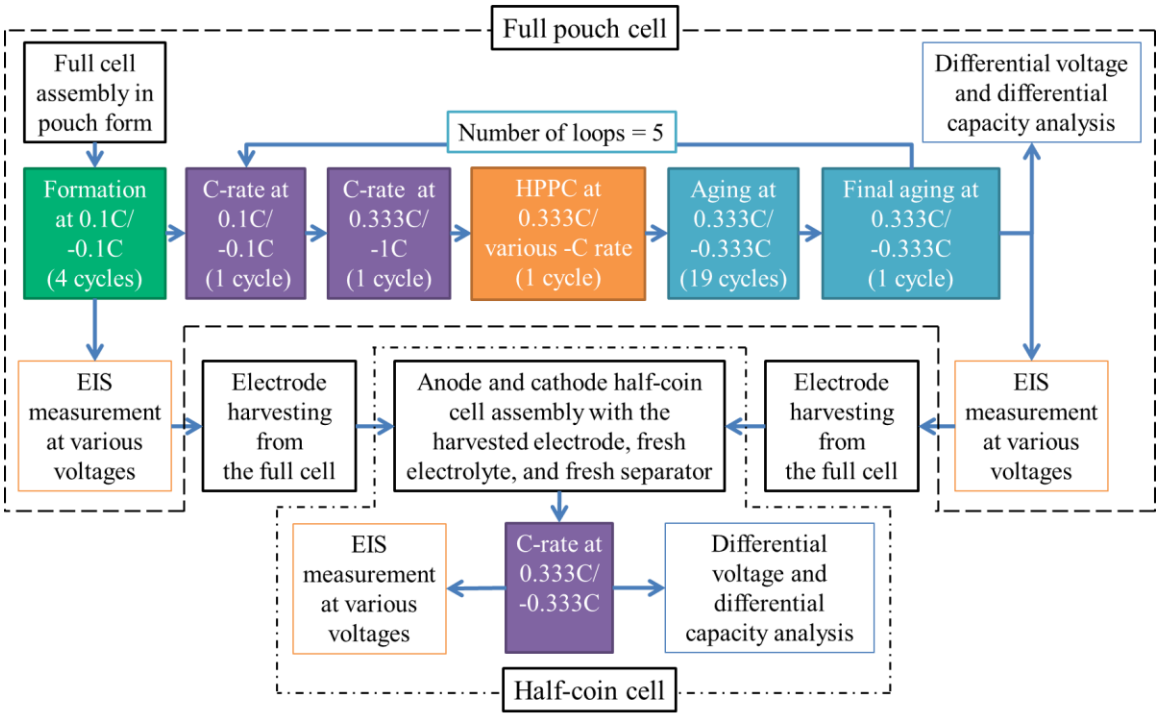


Figure 4.1. Test protocol and procedure.

In order to investigate the impedance of individual anodes and cathodes, half-cells were fabricated with electrodes harvested from the full pouch-cells that underwent aging cycles. The aged, full pouch-cells were disassembled and circular electrodes (half-inch diameter) were punched from the anodes and cathodes and assembled into Li/A12 graphite and Li/NMC-532 cathode half-cells, respectively, with fresh separators and GEN 2 electrolytes (***f*** ≈10). All cell disassembly and assembly processes were conducted in an Ar-atmosphere glove box to prevent the electrodes and SEI passivation layers from any reaction with impurities like water, CO_2, or O_2 in the atmosphere. All data processing and calculations were done using Matlab R2015 (MathWorks, inc).

Results and discussion

Correlation of electrolyte volume and capacity fade

Figure 4.2a shows the average capacities over the time on test from different electrolyte volume factor groups, ***F***, including error bars. All error bars reported this study correspond to 95% confidence intervals. Figure 4.2b plots similar information for selected individual cells within each group as a function of both electrolyte volume factor, ***f***, and the number of life-cycle testing, or aging, "loops" completed where each loop corresponds to 20 C/3 charge and discharge cycles. The individual cell with ***f***=1.25 (included in the lowest volume factor group) showed significant capacity fade, as seen in Figure 4.2b, relative to other cells in the same group and was excluded from the average capacity calculation of factor group ***F*** 1.3 shown in Figure 4.2a. Capacity retentions were determined by the initial and final C/3 capacities obtained during aging cycles. The C/3 average capacities for each cell group were also used in the calculation of capacity-fade rates. Breaks in the data, Figure 4.2a, occur at HPPC testing intervals.

The average C/3 capacity of factor group ***F*** 1.3 was 186 mAh g^{-1} on the 1st aging cycle when normalized to the NMC-532 mass, which is slightly higher than the average capacities of the other groups. However, the capacity fade of factor group ***F*** 1.3 decreased by 1.03 mAh g^{-1} per cycle during the first 20 cycles while the cell groups with higher electrolyte volume factors remained fairly constant. Over the 100 cycles on test, the average capacity factor group ***F*** 1.3 decreased by 35%. Slight increases in capacity can be seen after HPPC cycles for the ***F*** 1.3 group, the magnitude of which further increases with cycling. This is a reflection of the changing current rates used and an indication of increasing impedance with time on test. For example, before each HPPC cycle the cathode is more fully lithiated through a slow C/10 cycle, which minimized impedance effects.

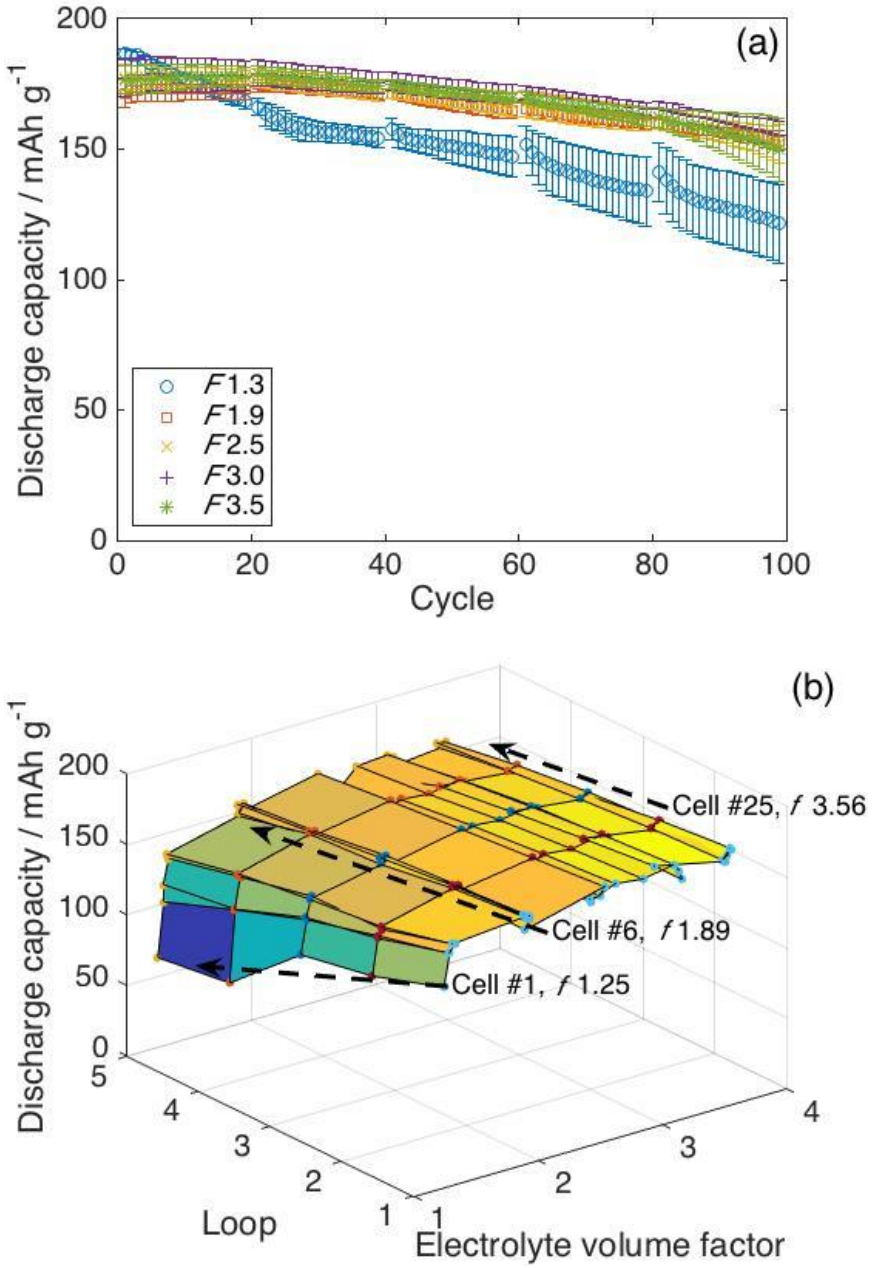


Figure 4.2. Correlation of electrolyte volume and cell cyclability (a) Discharge capacity fade at 0.33C/-0.33C for different electrolyte volume factor groups, F; (b) individual cell electrolyte volume factors, f, after each "loop", where each loop corresponds to 20 0.33C/-0.33C aging cycles. Cells with electrolyte volume factors greater than 1.9 demonstrate comparable cyclability.

Upon continued, C/3 aging, the capacity quickly fades to pre-HPPC levels. For the factor groups ***F*** 1.9 and higher, the average capacities were 176 mAh g^{-1} after the first aging cycle and decreased by only 11%-14% after 100 cycles. Although ***F*** 1.9 and above showed similar performance, the factor group ***F*** 3.5 had higher cell to cell variations after 85 cycles and slightly higher capacity fade than ***F*** 1.9 at the end of cycles. In a coin cell study from Long et al.,[14] the best capacity performance was shown at ***F*** 2.7 followed by ***F*** 4.7, ***F*** 8.7 and ***F*** 1.7. The electrolyte effect on coin cell performance is similar to that on pouch cells except that the optimal volume factor in pouch cells is lower (***F*** 1.9 vs. ***F*** 2.7) which is most likely due to cell configuration.

Figure 4.3 shows C/3 voltage vs. capacity plots of four representative samples, ***f***, from different cell groups, ***F***, on the first cycle of every 20-cycle aging loop. An example from the ***F*** 3.0 group is not shown because the performance was almost identical to that of the ***F*** 3.5 group shown in Figure 4.3d. The capacity fade rate and impedance effects of the ***F*** 1.3 sample was by far the highest out of the five sample groups as can be seen in Figure 4.3a.

Figure 4.4 shows the results of the C/10 and 1C rate performance tests before aging cycles and after every 20 aging cycles. Capacities among the groups at the slow C-rate of C/10 were fairly similar, while those at the high C-rate of 1C showed more significant differences, especially for the ***F*** 1.3 group. The differences at the higher rate are a reflection of the higher impedances of the ***F*** 1.3 group, possibly due to the inability to access all active material by the electrolyte at these low levels and/or more significant electrolyte depletion effects at high C-rate with less electrolyte. Regardless, this C-rate dependence is a clear indication of higher overall cell resistance in the low-electrolyte, ***F*** 1.3 group.

Hybrid pulse power characterization (HPPC) analysis

Figure 4.5 shows the average resistances of different factor groups derived from the HPPC testing cycles. The calculated resistances correspond well to the capacity fade results shown in Figure 4.2. The resistances of the factor group ***F*** 1.3 (in Figure 4.5a and 4.5f) dramatically increased right from the onset of cycling. After just 20 aging cycles (1^{st} loop), the resistances of ***F*** 1.3 cells exceeded those of higher factor groups that underwent 80 aging cycles (4^{th} loop), as shown in Figure 4.5e. After further cycling, the rate of resistance increases of ***F*** 1.3 group slowed and was similar to that of other higher factor groups. Unlike the other factor groups, data from the ***F*** 1.3 group indicates that multiple degradation processes significantly contributed during the first 20 cycles. Specifically, large changes in electrolyte concentration (following a first-order reaction in a closed system) as well as a passivation layer growth (which is

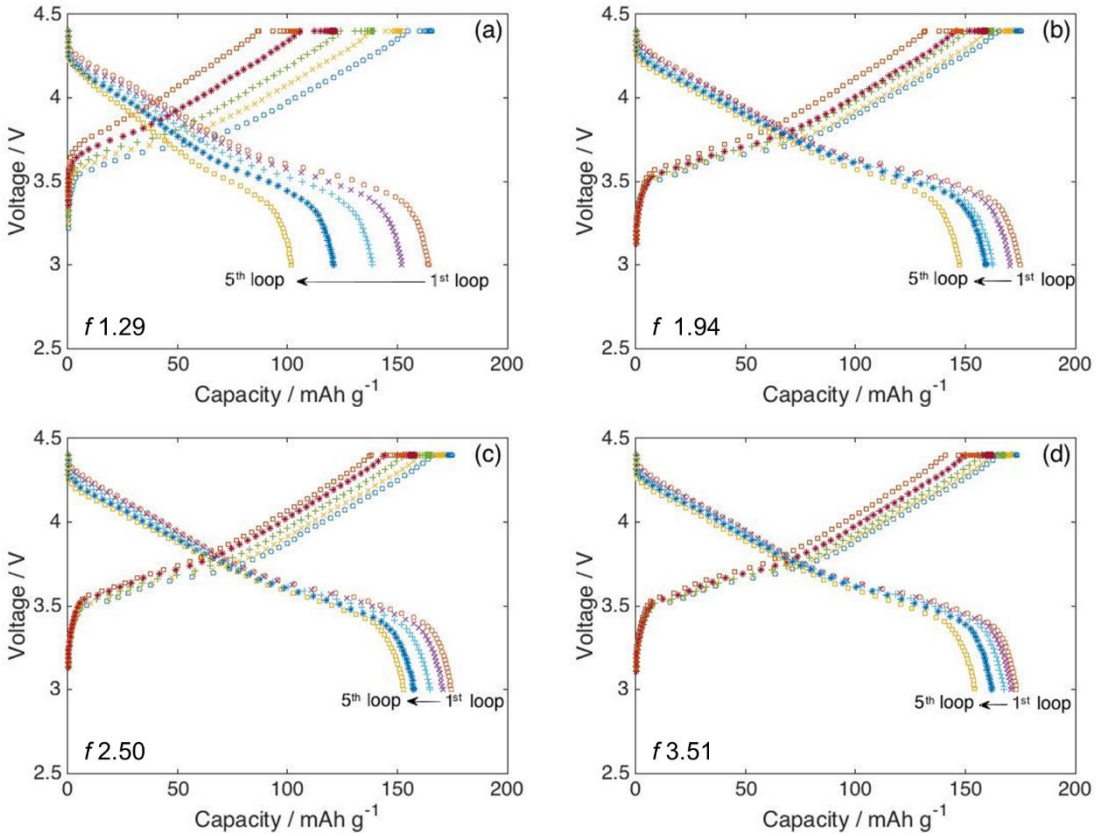


Figure 4.3. Voltage profiles of (a) f 1.29, (b) f 1.94, (c) f 2.50, and (d) f 3.51 on the first cycle of every C/3, aging-cycle test loop, where each loop includes 20 aging cycles.

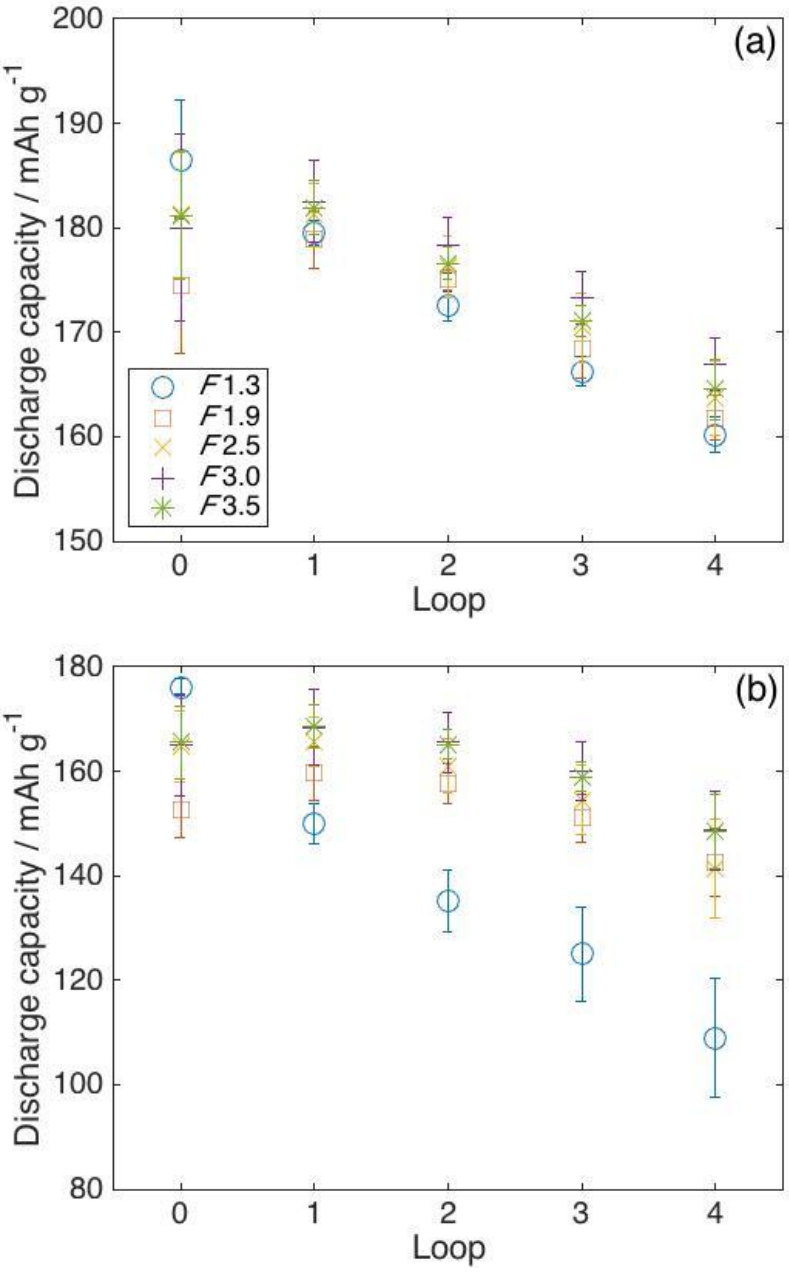


Figure 4.4. Discharge capacities of different electrolyte volume factor groups, F, at (a) C/10 and (b) 1C at the end of each life-cycle test loop, where each loop includes 20 aging cycles.

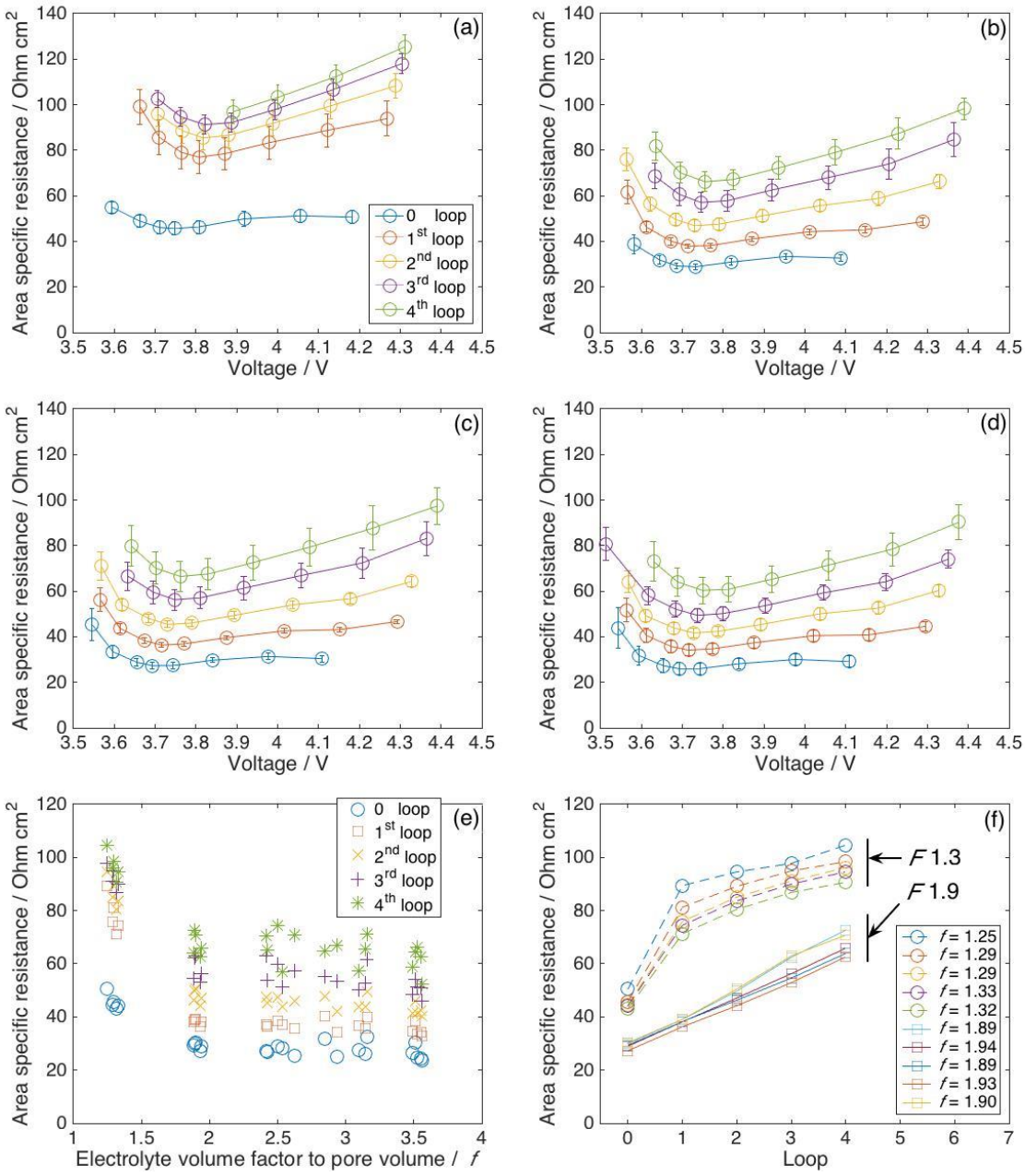


Figure 4.5. Resistances from HPPC tests at different voltages during discharge after every 20 aging cycles for electrolyte volume factor group F 1.3 (a), F 1.9 (b), F 2.5 (c), and F 3.5 (d); resistances of individual electrolyte volume factors, f, at 50% discharge (e) with "0 loop" representing resistance before cycling and each subsequent loop representing 20 additional aging cycles; resistances of individual cells at 50% discharge for electrolyte volume factor groups F 1.3 and F 1.9 (f).

proportional to the square root of time at constant temperature for diffusion-limited layer growth) may both contribute to impedance effects.[18]

It is likely that factor groups higher than ***F*** 1.9 would not show this significant concentration effect since the volume of the electrolyte was much larger. The average resistance value of the ***F*** 1.9 group (Figure 4.5b) was slightly higher than those of the ***F*** 2.5 (Figure 4.5c) and ***F*** 3.5 groups (Figure 4.5d) but all three were equal within the error. The resistances at 50% DOD (Figure 4.5e) clearly show low electrolyte volume, ***F*** *1.3*, caused an increase in resistance. More analysis on resistance contributions is discussed in the following AC impedance analysis section.

Impedance analysis - EIS

Since the above tests showed no significant difference among the factor groups ***F*** 1.9 and higher, and part of the goal is an optimization/minimization of electrolyte volumes, EIS studies were carried out on selected cells within the factor groups ***F*** 1.3 and ***F*** 1.9 only. Figure 4.6 shows Nyquist plots for electrolyte volume factors ***f*** 1.25, ***f*** 1.29, ***f*** 1.89, and ***f*** 1.94 from harvested NMC-532 cathodes, re-assembled in lithium half-cells, before and after 100 aging cycles. Based on the equivalent circuit model shown in the inset of Figure 4.6b, the charge transfer resistance (R_{ct}) and the resistance of the passivation layer (R_{pl}), before and after aging, were calculated at 3.6 V during the discharge.

The calculated values are compared in Figure 4.7a for the ***f*** 1.25 and ***f*** 1.89 cells. Since the Ohmic resistance (R_{Ω}) can be affected by many factors, including cell format, comparison of R_{Ω} from the aged, full pouch-cells with that of the half-cells (coin cells) is not particularly useful. Hence, the R_{Ω} from the coin-cells were not included in the comparisons of Figure 4.7; R_{Ω} values are, however, reported in Figure 4.7b for the aged pouch-cells. Based on Figure 4.7a, the R_{pl} and R_{ct} values of the NMC-532 increased by factors of ~1.5-2.0 after 100 aging cycles.

Analysis of full cells (Figure 4.7b, right) shows Ohmic resistances of the ***f*** 1.25, ***f*** 1.29, ***f*** 1.89, and ***f*** 1.94 were 91, 33, 14, and 13 Ohm cm^2, respectively. Ohmic resistances at 3.6 V (vs. LiC_x) of the ***f*** 1.94 and ***f*** 1.25 cells accounted for 15% and 46% of the overall resistance, respectively, where Ohmic resistance includes bulk electrolyte resistance and electrical resistances of all components and connections. Assuming the electrical resistances of all components and connections are similar in all cells, the bulk electrolyte resistance is the only difference in the Ohmic component among the different electrolyte volume factors. Hence, it can be concluded from Figure 4.7b that the resistance of the electrolyte of the full cells was a major component of the overall resistance for ***f*** 1.25 in the factor group ***F*** 1.3.

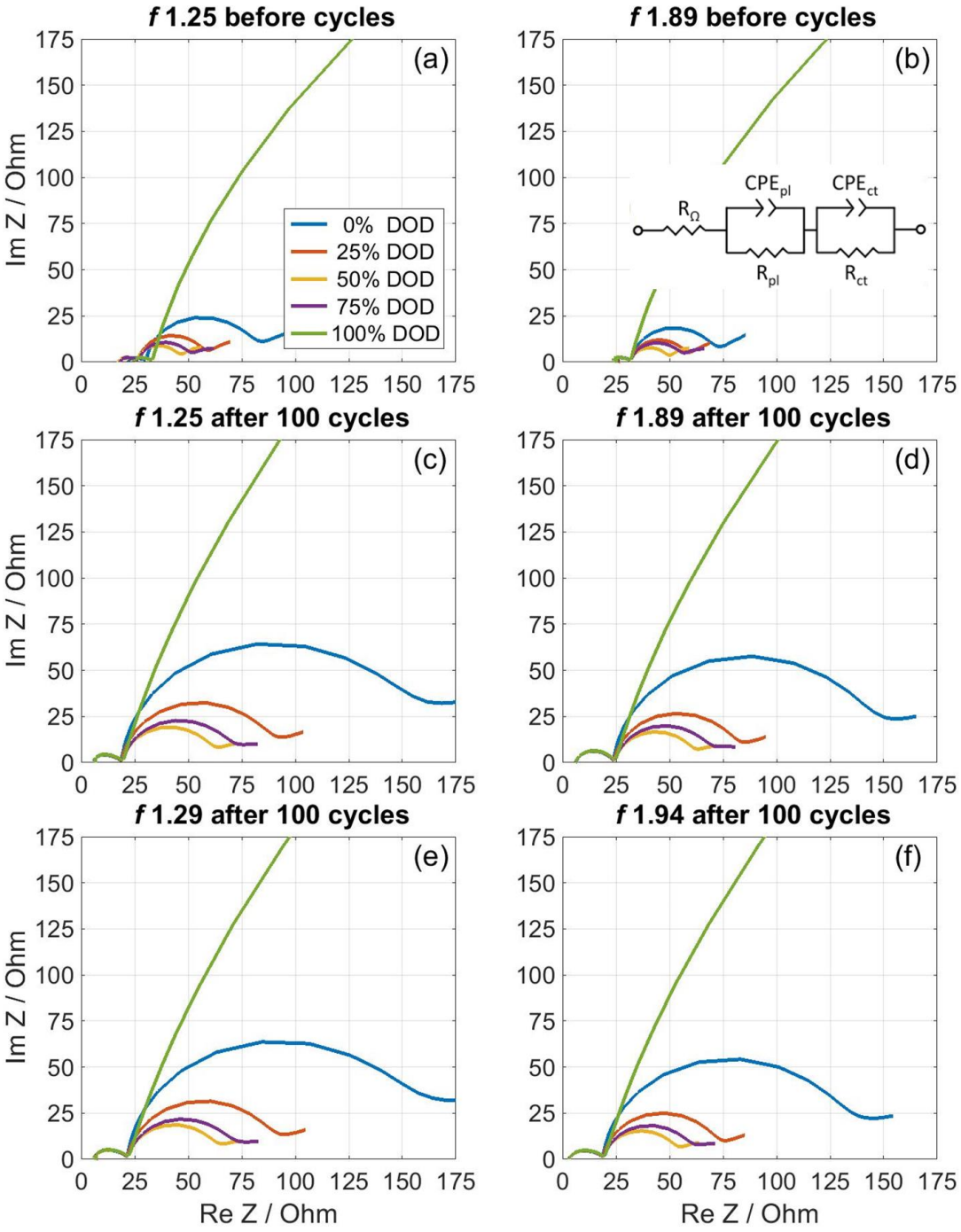


Figure 4.6. EIS data of NMC cathode half-cells from harvested pouch-cells before cycling (a-b) with electrolyte volume factors of f 1.25 (a) and f1.89 (b) and after 100 cycles (c-f) with different electrolyte volume factors of f 1.25 (c), f 1.89 (d), f 1.29 (e), and f 1.94 (f).

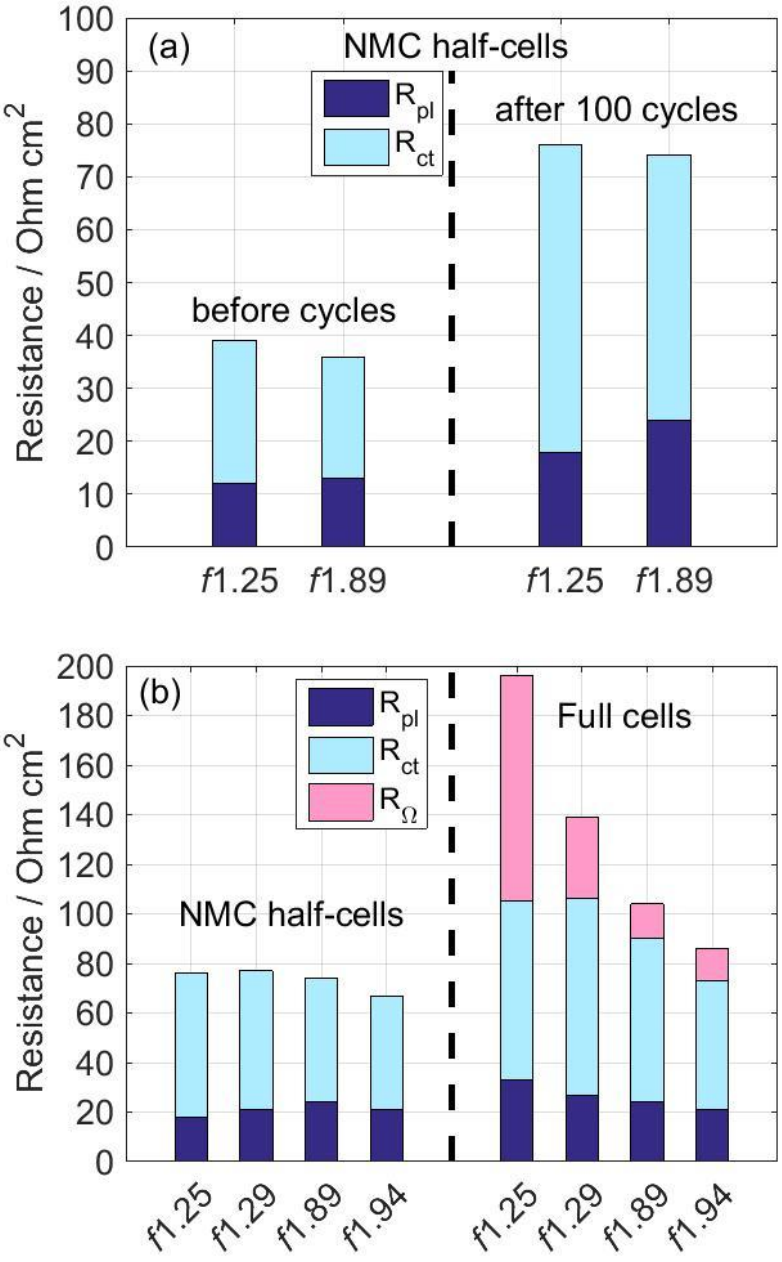


Figure 4.7. Resistances of NMC cathode half-coin cells at 3.6V vs. Li/Li+ (a) calculated using Figure 4.6 data and the equivalent circuit model in Figure 4.6b inset, resistance of half-coin cells at 3.6 V vs. Li/Li+ and full pouch-cells at 3.6 V (vs. LiCx) during discharge after 100 cycles (b).

As shown in Figure 4.7b (left), the harvested NMC-532 half-cells had slightly lower resistances (R_{pl} and R_{ct}) than those of the full pouch-cells (Fig. 4.7b, right) because the resistances of a graphite anode are not present in the half-cells. However, resistance increases are known to be minimal for aged graphite electrodes[19] and the values from the aged NMC-532 half-cells agrees fairly well with those from the full pouch-cells, implying that most of R_{pl} and R_{ct} increases of full pouch-cells can be attributed to the cathode electrode as previously reported.[19]

Effect of electrolyte volume

Figure 4.8 shows differential voltage plots of half-cells with electrodes harvested from full pouch-cells after 100 cycles for the ***f*** 1.94 (Figures 4.8a and 4.8c) cell of the ***F*** 1.9 factor group and the ***f*** 1.29 (Figures 4.8b and 4.8d) cell of the ***F*** 1.3 factor group. Since there was no significant difference in differential voltage curves for the anode before and after aging, only one anode curve is shown for each factor. All half-cells were filled with the same amount of fresh electrolyte to eliminate electrolyte volume effects on half-cell differential voltage analysis.

Unlike the differential voltage curves for the ***f*** 1.94 cell in Figure 4.8a, those of the ***f*** 1.29 cell in Figure 4.8b did not exhibit an “N-shape” in the high anode DOD region (dashed boxes, Figures 4.8a and b); the latter curve being relatively featureless. In Figure 4.8c, it can be seen that the N-shape and its DOD position for the ***f*** 1.94 cell did not change significantly over the ~100 aging cycles. But the size of the N-shape changed. Therefore, based on the size of the peak at the N-shape location, the anode DOD can be estimated in a full cell without a reference electrode. However, this is not the case for the ***f*** 1.29 cell where no clear “N-shape” marker is observed.

NMC-532 cathode half-cell curves, before and after aging, are shown under the A12 graphite anode half-cell curves in Figures 4.8a and 4.8b, labeled as (1) and (2) respectively. The NMC-532 cathode positions in a full cell vary depending on the anode DOD, which cannot be measured without a full cell reference electrode. Hence, the positions of the NMC-532 cathode curves were estimated to illustrate the correlations with the anode DOD. Overall capacity in a full cell is purposely cathode-limited in order to prevent lithium dendrite formation.[20] Comparing half-cells in Figure 4.8a with a full cell in Figure 4.8c, the NMC-532 curve (2) is observed to shift towards lower DOD during cycling, away from N-shaped peak position of the anode.

This shift indicates that anode voltage at lower cut-off cell voltage is shifting downwards because of lithium losses in anode as cell is aged. At the same time,

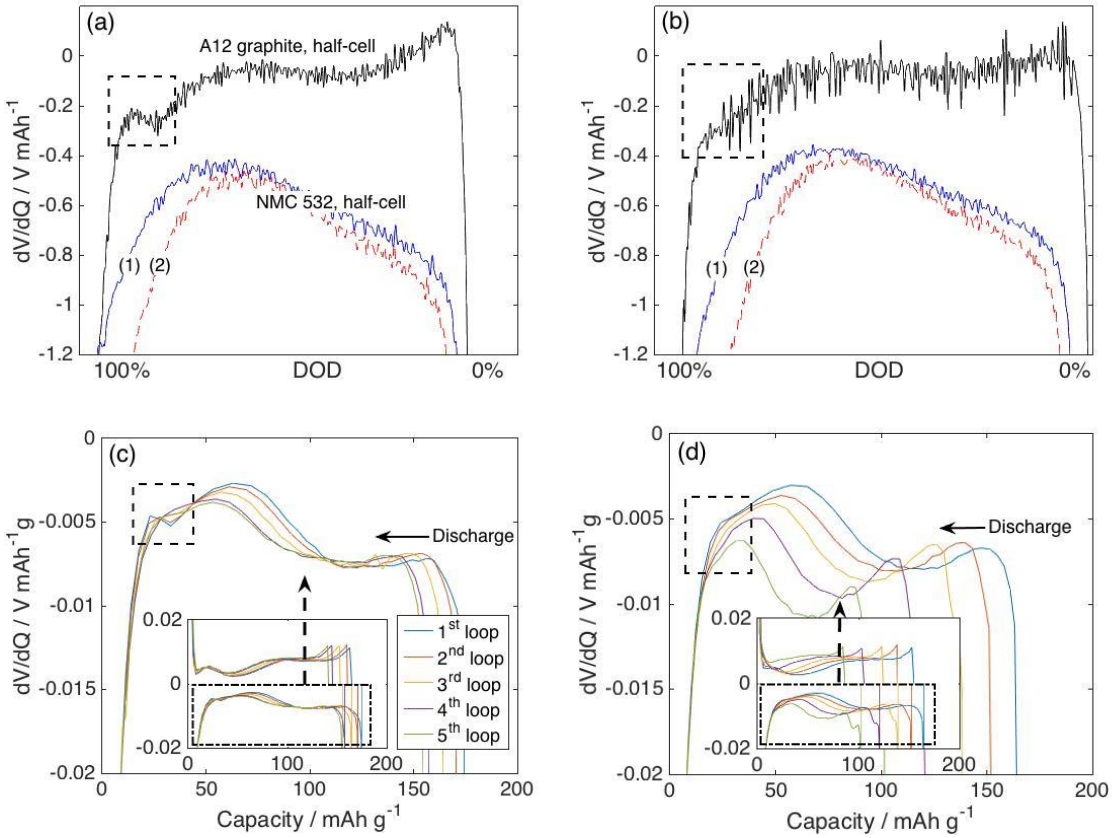


Figure 4.8. Differential voltage curves of harvested half-cells from full pouch cells with f 1.94 (a) and f 1.29 (b) and differential voltage curves of full pouch cells with f 1.94 (c) and f 1.29 (d). (1) and (2) are cathode curves before and after aging cycles, respectively.

the anode voltage at higher cut-off cell voltage is shifting upwards because of cathode capacity losses. Based on the analysis of Figure 4.8, the anode is neither fully charged due to lithium losses in anode nor fully discharged due to cathode capacity loss when the cathode is aged. It was also demonstrated that cathode resistance was relatively higher than that of the anode since the absolute values of differential voltage, |dV/dQ| in Figure 4.8a and 4.8b, are proportional to resistance. The absolute values of the differential voltage curves in Figure 4.8c and 4.8d corresponded to increases in overall full cell resistance as they were cycled.

Conclusions

Correlations of electrolyte volume with performance in 70 mAh lithium ion batteries having graphite/ $LiNi_{0.5}Mn_{0.3}Co_{0.2}O_2$ (NMC-532) was investigated. It is demonstrated that the electrolyte volume to total pore volume of electrodes and separators needs to be at least 1.9 in this study to achieve desired performance while a factor of 2.7 was identified as a better volume to pore ratio in coin cell studies.[14] The lower optimal electrolyte volume in pouch cells is ascribed to the smaller dead volume portion and confirms that cell configurations affect the optimal electrolyte volume. Less electrolyte resulted in higher capacity fade. In addition, there was no significant improvement in cyclability and impedance reduction on further increasing the electrolyte volume factor above 1.9. Thus, the optimum electrolyte volume factor was determined to 1.9 from this work.

References

1. An, S. J.; Li, J.; Daniel, C.; Mohanty, D.; Nagpure, S.; Wood, D. L., The State of Understanding of the Lithium-ion-Battery Graphite Solid Electrolyte Interphase (SEI) and its Relationship to Formation Cycling. *Carbon* **2016,** *105*, 52-76.
2. Goodenough, J. B.; Kim, Y., Challenges for Rechargeable Li Batteries. *Chemistry of Materials* **2010,** *22*, 587–603.
3. Waldmann, T.; Wilka, M.; Kasper, M.; Fleischhammer, M.; Wohlfahrt-Mehrens, M., Temperature dependent ageing mechanisms in Lithium-ion batteries – A Post-Mortem study. *Journal of Power Sources* **2014,** *262*, 129-135.
4. Xu, M.; Tsiouvaras, N.; Garsuch, A.; Gasteiger, H. A.; Lucht, B. L., Generation of Cathode Passivation Films via Oxidation of Lithium Bis(oxalato) Borate on High Voltage Spinel (LiNi0.5Mn1.5O4). *The Journal of Physical Chemistry C* **2014,** *118*, 7363-7368.
5. Zheng, H.; Sun, Q.; Liu, G.; Song, X.; Battaglia, V. S., Correlation between dissolution behavior and electrochemical cycling performance for LiNi1/3Co1/3Mn1/3O2-based cells. *Journal of Power Sources* **2012,** *207*, 134-140.
6. Mohanty, D.; Huq, A.; Payzant, E. A.; Sefat, A. S.; Li, J.; Abraham, D. P.; Wood, D. L.; Daniel, C., Neutron Diffraction and Magnetic Susceptibility Studies on a High-Voltage Li1.2Mn0.55Ni0.15Co0.10O2Lithium Ion Battery Cathode: Insight into the Crystal Structure. *Chemistry of Materials* **2013,** *25*, 4064-4070.
7. Mohanty, D.; Sefat, A. S.; Li, J.; Meisner, R. A.; Rondinone, A. J.; Payzant, E. A.; Abraham, D. P.; Wood, D. L. r.; Daniel, C., Correlating cation ordering and voltage fade in a lithium-manganese-rich lithium-ion battery cathode oxide: a joint magnetic susceptibility and TEM study. *Physical chemistry chemical physics : PCCP* **2013,** *15*, 19496-509.
8. Yang, L.; Ravdel, B.; Lucht, B. L., Electrolyte Reactions with the Surface of High Voltage LiNi[sub 0.5]Mn[sub 1.5]O[sub 4] Cathodes for Lithium-Ion Batteries. *Electrochemical and Solid-State Letters* **2010,** *13*, A95.
9. Abraham, D. P.; Spila, T.; Furczon, M. M.; Sammann, E., Evidence of Transition-Metal Accumulation on Aged Graphite Anodes by SIMS. *Electrochem. Solid-State Lett.* **2008,** *11*, A226.
10. Vetter, J.; Novák, P.; Wagner, M. R.; Veit, C.; Möller, K. C.; Besenhard, J. O.; Winter, M.; Wohlfahrt-Mehrens, M.; Vogler, C.; Hammouche, A., Ageing mechanisms in lithium-ion batteries. *J. Power Sources* **2005,** *147*, 269-281.
11. Wood, D. L.; Li, J.; Daniel, C., Prospects for reducing the processing cost of lithium ion batteries. *Journal of Power Sources* **2015,** *275*, 234-242.
12. Wood, D. L.; Li, J.; Mohanty, D.; Daniel, C.; Armstrong, B.; Dinwiddie, R.; Safa-Sefat, A.; Wang, H.; Trejo, R.; Gallego, N.; Contescu, C.; Howe, J.; Meisner, R.; Kiggans, J.; Brown, B., Advanced Materials Processing and Novel Characterization Methods for Low-Cost, High Energy-Density Lithium-Ion Batteries. *Advanced Automotive Battery Conference* **2013**.

13. Li, J.; Daniel, C.; Wood, D. L., Materials processing for lithium-ion batteries. *Journal of Power Sources* **2011,** *196*, 2452–2460.
14. Long, B. R.; Rinaldo, S. G.; Gallagher, K. G.; Dees, D. W.; Trask, S. E.; Polzin, B. J.; Jansen, A. N.; Abraham, D. P.; Bloom, I.; Bare˜no, J.; Croy, J. R., Enabling High-Energy, High-Voltage Lithium-Ion Cells: Standardization of Coin-Cell Assembly, Electrochemical Testing, and Evaluation of Full Cells. *J. Electrochem. Soc.* **2016,** *163*, A2999-A3009.
15. Idaho National Laboratory, Battery Test Manual For Plug-In Hybrid Electric Vehicles. *Prepared for the U.S. Department of Energy Assistant Secretary for Energy Efficiency and Renewable Energy* **2010,** *INL/EXT-07-12536, Revision 1*, 1-56.
16. Li, J.; Daniel, C.; An, S. J.; Wood, D., Evaluation Residual Moisture in Lithium-Ion Battery Electrodes and Its Effect on Electrode Performance. *MRS Advances* **2016,** *1*, 1029-1035.
17. Aurbach, D., Review of selected electrode–solution interactions which determine the performance of Li and Li ion batteries. *J. Power Sources* **2000,** *89*, 206-218.
18. Lipowsky, R.; Huse, D. A., Diffusion-limited growth of wetting layers. *Phys Rev Lett* **1986,** *57*, 353-356.
19. Li, Y.; Bettge, M.; Polzin, B.; Zhu, Y.; Balasubramanian, M.; Abraham, D. P., Understanding Long-Term Cycling Performance of Li1.2Ni0.15Mn0.55Co0.1O2-Graphite Lithium-Ion Cells. *Journal of the Electrochemical Society* **2013,** *160*, A3006-A3019.
20. Kim, C.-S.; Jeong, K. M.; Kim, K.; Yi, C.-W., Effects of Capacity Ratios between Anode and Cathode on Electrochemical Properties for Lithium Polymer Batteries. *ELECTROCHIMICA ACTA* **2014,** *155*, 431-436.

CHAPTER V
ELECTROLYTE VOLUME EFFECTS ON ELECTROCHEMICAL PERFORMANCE AND SOLID ELECTROLYTE INTERPHASE IN SI-GRAPHITE/NMC LITHIUM-ION POUCH CELLS

A version of this chapter was originally published by Seong Jin An, Jianlin Li, Claus Daniel, Harry M. Meyer III, Stephen E. Trask, Bryant J. Polzin, and David L. Wood III:

Seong Jin An, Jianlin Li, Claus Daniel, Harry M. Meyer III, Stephen E. Trask, Bryant J. Polzin, and David L. Wood III "Electrolyte Volume Effects on Electrochemical Performance and Solid Electrolyte Interphase in Si-Graphite/ NMC Lithium-Ion Pouch Cells" *ACS Applied Materials & Interfaces*, 9 (2017): 18799–18808.

All experiments, data analysis, and initial draft for this article were done by Seong Jin An. The draft was improved and finalized by Seong Jin An, Jianlin Li, and David L. Wood III. The electrodes used in this study were provided by Bryant J. Polzin and Stephen E. Trask. All other co-authors provided comments on contents.

Abstract

This study aims to explore the correlations between electrolyte volume, electrochemical performance, and properties of the solid electrolyte interphase in pouch cells with Si-graphite composite anodes. The electrolyte is 1.2 M $LiPF_6$ in ethylene carbonate:ethylmethyl carbonate with 10 wt.% fluoroethylene carbonate. Single layer pouch cells (100 mAh) were constructed with 15 wt.% Si-graphite / $LiNi_{0.5}Mn_{0.3}CO_{0.2}O_2$ electrodes. It is found that a minimum electrolyte volume factor of 3.1 times the total pore volume of cell components (cathode, anode, and separator) is needed for better cycling stability. Less electrolyte causes increases in ohmic and charge transfer resistances. Lithium dendrites are observed when the electrolyte volume factor is low. The resistances from the anodes become significant as the cells are discharged. Solid electrolyte interphase thickness grows as the electrolyte volume factor increases and is non-uniform after cycling.

Introduction

The attention for anode materials has recently shifted from graphite to silicon and its composites because of its high theoretical capacity (3,579 mAh g^{-1} for $Li_{13}Si_4$ and 4,199 mAh g^{-1} for $Li_{22}Si_5$).[1-3] However, silicon suffers from a volume change of up to 311% with lithiation. The unit cell volume is 160.2 $Å^3$ for cubic Si, 308.9 $Å^3$ for rhombohedral $Li_{14}Si_6$ ($Li_{2.33}Si$), 538.4 $Å^3$ for orthorhombic $Li_{13}Si_4$ ($Li_{3.25}Si$), and 659.2 $Å^3$ for cubic $Li_{22}Si_5$ ($Li_{4.4}Si$).[4] These excessive volume changes result in unstable SEI and mechanical breakdown of the electrode. Furthermore, the unstable SEI leaves fresh Si surface exposed to electrolyte. This causes

continuous SEI formation via electrolyte decomposition and leads to low Coulombic efficiency.[5]

Due to the large volume changes of silicon, use of pure silicon as an electrode is challenging. Hence, many scientists have studied Si-based composites or mixed materials such as Si alloys, Si-C composites, Si with carbon nanomaterials, or Si with graphene.[6-7] Replacing micron-sized silicon particles with nanoscale morphologies also helps to mitigate large stresses associated with the volume changes.[8] A mixture of graphite and nanoscale Si was selected for the anode active materials in this study. While many types of Si have been investigated, electrolytes and additives have also been studied to improve capacity retention. Electrolytes are the origins of SEI components and a key factor controlling SEI integrity and reversible capacity.[9]

Despite the importance of the electrolyte, the impact of electrolyte volume on the stability of cells with Si-based anodes has not been reported. Many of the results reported in the literature are derived from experiments with coin cells, where the electrolyte volume is in large excess (essentially flooded). While the electrolyte volume in practical lithium-ion cells is barely reported in literature, our previous study with graphite/$LiNi_{0.5}Mn_{0.3}CO_{0.2}O_2$ (NMC) pouch cells demonstrated that 1.9 times of electrolyte volume to pore volume of electrode and separator was optimum among tested volume ratios (1.3, 1.9, 2.5, 3.0, and 3.5) for long-term cycling stability with low impedance.

Low electrolyte volume results in an increase of the ohmic resistances.[10] The previous electrolyte volume experiments were performed in order to compare results from pouch cells and coin cells.[11] In this study, efforts have been made to optimize the volume of electrolyte used in 15 wt.% Si-graphite/NMC full cell systems in pouch format. The effect of electrolyte volume on cell performance was characterized in terms of capacity fade, impedance change, and hybrid pulse power characterization (HPPC). Surface elements were characterized using X-ray photoelectron spectroscopy (XPS) with sputter depth profiles. The thickness and composition of the SEI was determined.

Experimental

The electrolyte was 90 wt.% “Gen 2” and 10 wt.% fluoroethylene carbonate (FEC). Gen 2 is the electrolyte formulation adopted by Argonne National Laboratory (ANL) and Oak Ridge National Laboratory (ORNL) and is 1.2 M $LiPF_6$ in ethylene carbonate:ethylmethyl carbonate (EC:EMC) (3:7 by weight). FEC was included as an additive in Gen 2 because of improvement in cycle life of Si anode with it.[12-13] Electrolyte volume factor, ***F***, was defined as the supplied electrolyte volume divided by the total cell pore volume (the sum of pore volumes in anode,

cathode, and separator). It is noted that the contribution of electrode separation and edge effects to the total void volume depends on the cell geometry and configuration. Thus, the optimum factor, ***F***, would be expected to be different for other cell designs. The electrolyte volume would also vary with the surface roughness of the electrodes. Five volume factors from 1.6 to 3.5 were investigated at 25ºC with four cells in each volume factor group. Each cell had 100 mAh capacity at C/20 with a single-side coated anode and cathode. Tables 5.1 and 5.2 show cell component chemistries and the five electrolyte volume factor groups, ***F***, respectively. Details of the processes and conditions for the cell assembly, test equipment, and test set-up are elaborated elsewhere.[10] All cell assembly was completed in the DOE Battery Manufacturing R&D Facility (BMF) dry room (dew point ≤ -55°C) at ORNL. The electrodes were fabricated at, and provided by, the Cell Analysis, Modeling, and Prototyping (CAMP) Facility at ANL. The anode contained 73 wt.% graphite, 15 wt.% 50-70 nm silicon, 10 wt.% lithium polyacrylate (LiPAA), and 2 wt.% carbon.[14] The LiPAA binder was prepared by titration of polyacrylic acid with LiOH to neutral pH.

The test protocols (shown in bold boxes in Figure 5.1) were developed as standard protocols under the U.S. DOE's "Deep-Dive" project on enabling high-energy/high-voltage lithium-ion cells. Testing included 3 formation cycles at C/20 charge and discharge rates, an initial DC resistance test (1 cycle), 92 aging cycles, a final DC resistance test (1 cycle), and 3 final cycles.[14] Cells were cycled with cut-off voltages of 4.1 V and 3.0 V for all tests. The voltages were held at 4.1 V during charging until the current dropped to C/20. AC electrochemical impedance spectroscopy (EIS) tests were included after the final cycles to analyze resistances in detail. The flow diagram for the test protocols and procedures is shown in Figure 5.1. The hybrid pulse power characterization (HPPC) test was used to investigate the DC resistance of full cells at different depths of discharge (DOD). Discharge C-rate for the HPPC pulses was 3C (1C rate is based on 130 mAh g^{-1} of NMC). Other details of test procedures including the set-up for HPPC and AC impedance measurement are described elsewhere.[10] Bio-Logic potentiostats / galvanostats (VSP) and EC-Lab® software version 11 were used to obtain and fit EIS data and extract the ohmic resistance (R_{ohmic}), surface film resistance ($R_{sf,}$ or SEI resistance), anode charge transfer resistance (R_{ct1}), and cathode charge transfer resistance (R_{ct2}). All data processing and calculations except the EIS data fitting were done using Matlab R2016 (MathWorks, Inc.).

XPS (K-Alpha, Thermo Scientific) was adopted to analyze the surface elements from harvested anodes. XPS depth profiles were also used to estimate the SEI layer thicknesses. All cells were discharged to 3 V at C/20 before disassembly, and the anodes were harvested in an argon atmosphere glove box. The harvested electrodes were lightly rinsed with EMC solvent, dried in the glove box, and loaded in a vacuum transfer module to avoid air and moisture contact.

Table 5.1. Pouch cell information

	Composition	Loading	Size	Porosity
Anode	73 wt.% Hitach MAGE, 15 wt.% NanoAmor Silicon (50-70 nm), 2 wt.% C-45 carbon (Timcal), 10 wt.% LiPAA (LiOH titrate)	3.28 mg/cm^2	86.4 mm × 58 mm × 30 μm	46.4%
Cathode	90 wt.% $LiNi_{0.5}Mn_{0.3}Co_{0.2}$ (TODA), C-45 carbon (Timcal), 5 wt.% PVDF (Solvay® 5130)	11.32 mg/cm^2	84.4 mm × 56 mm × 42 μm	33.6%
Separator	Polypropylene–polyethylene–polypropylene (Celgard® 2325)	-	89 mm × 61 mm × 25 μm	39%
Electrolyte	90 wt.% “Gen2” (1.2 M $LiPF_6$ in EC:EMC 3:7 by weight), 10 wt.% FEC	-		

Table 5.2. Electrolyte volume factor group, *F*, having five individual factor samples in each group

Factor group	Ratio of electrolyte volume to pore volume (*F*) for each cell	Average
F1.6	1.69, 1.69, 1.53, 1.53 (from cell #1 to #4)	1.61
F2.1	2.08, 2.07, 2.07, 2.08 (from cell #5 to #8)	2.08
F2.6	2.58, 2.57, 2.55, 2.53 (from cell #9 to #12)	2.55
F3.1	3.05, 3.07, 3.07, 3.08 (from cell #13 to #16)	3.07
F3.5	3.55, 3.56, 3.48, 3.49 (from cell #17 to #20)	3.52

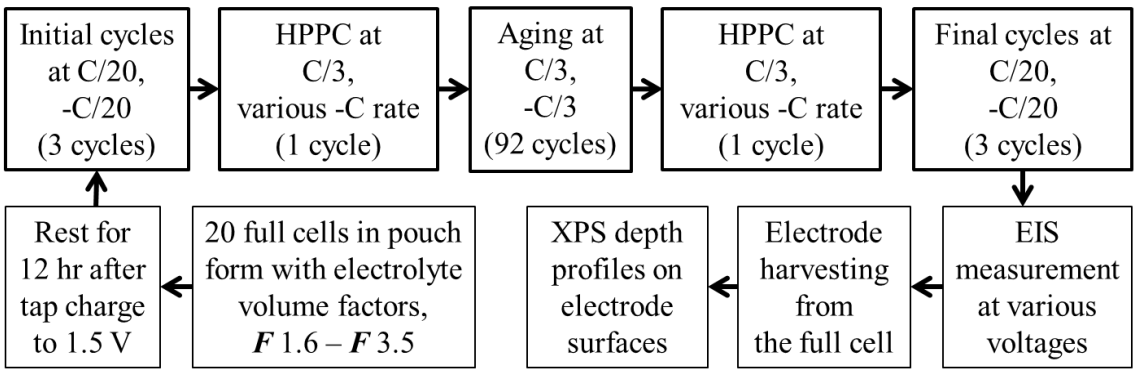


Figure 5.1. Test protocol and procedure.

The transfer module was directly inserted into the XPS chamber with a base pressure 10^{-9} Torr. Hence, the electrode samples analyzed by XPS were never exposed to ambient air and moisture. The X-ray source was monochromated Al Kα with a spot size of 400 μm and 1486.6 eV photon energy. The system used an electron flood gun for charge compensation. The analysis depth is expected to be 5−10 nm.[15] Additional information about the XPS system and data analysis are available in our previous work.[16] Scanning electron microscopy (SEM, Merlin VP, Zeiss) combined with energy dispersive spectroscopy (EDS) was used to collect anode surface images and elemental information.

Results and discussion

Correlation of electrolyte volume and capacity fade

During the first three cycles, cell-to-cell variations in discharge capacity were large for all factor groups. Figure 5.2 shows average discharge capacities and irreversible capacity losses (ICLs) during first three (1^{st} – 3^{rd} cycle) at C/20, aging cycles (4^{th} – 97^{th} cycle) at C/3, and last three cycles (98^{th} – 100^{th} cycle) at C/20 charge and discharge rates with 95% confidence intervals as error bars. Among them during the first three cycles (Figure 5.2a – 5.2b), *F1.6* showed the lowest average discharge capacities (87 - 97 mAh g^{-1}) with the largest error bars (44 - 43 mAh g^{-1}, one-side) while *F2.1* showed the smallest error bars (9 - 3 mAh g^{-1}, one-side) and the highest average discharge capacities (134 mAh g^{-1}). ICLs at *F1.6* were also the highest (30.4 mAh g^{-1}, 3.6%) while those at *F2.6* were the lowest (21.3 mAh g^{-1}, 1.5%). After 100 cycles (Figure 5.2e – 5.2f), *F3.5* group showed the highest discharge capacity (65 mAh g^{-1}) which was slightly higher than *F3.1* group (63 mAh g^{-1}) but the difference was insignificant considering the error range. Their ICLs were also the lowest (2.7%). Capacities of *F1.6* at C/20 during the final cycles seem closer to those of *F3.1* and higher than those of *F2.1* and *F2.6*. However, the capacities of *F1.6* remained far below the other groups during the aging cycles at higher rate (C/3) (Figure 5.2c). While the error bars for the *F1.6* group were large, clear trends in the capacity and ICL were observed for the other groups after the aging cycles (Figures 5.2e and 5.2f).

During the aging cycles, both *F3.1* and *F3.5* showed the highest capacity retentions (about 52% from the maximum capacity to the final capacity) and the lowest ICLs (Figure 5.2c and 5.2d). In general, capacity and capacity retention increased with increasing volume factor up to *F3.1*. The ICLs of all groups continuously increased as cells were cycled, which is opposite to what was observed for graphite anodes without Si.[10] Since it is believed that ICL is strongly related to electrolyte decomposition, the increase in the ICL indicates that the SEI on Si particles was not stable.

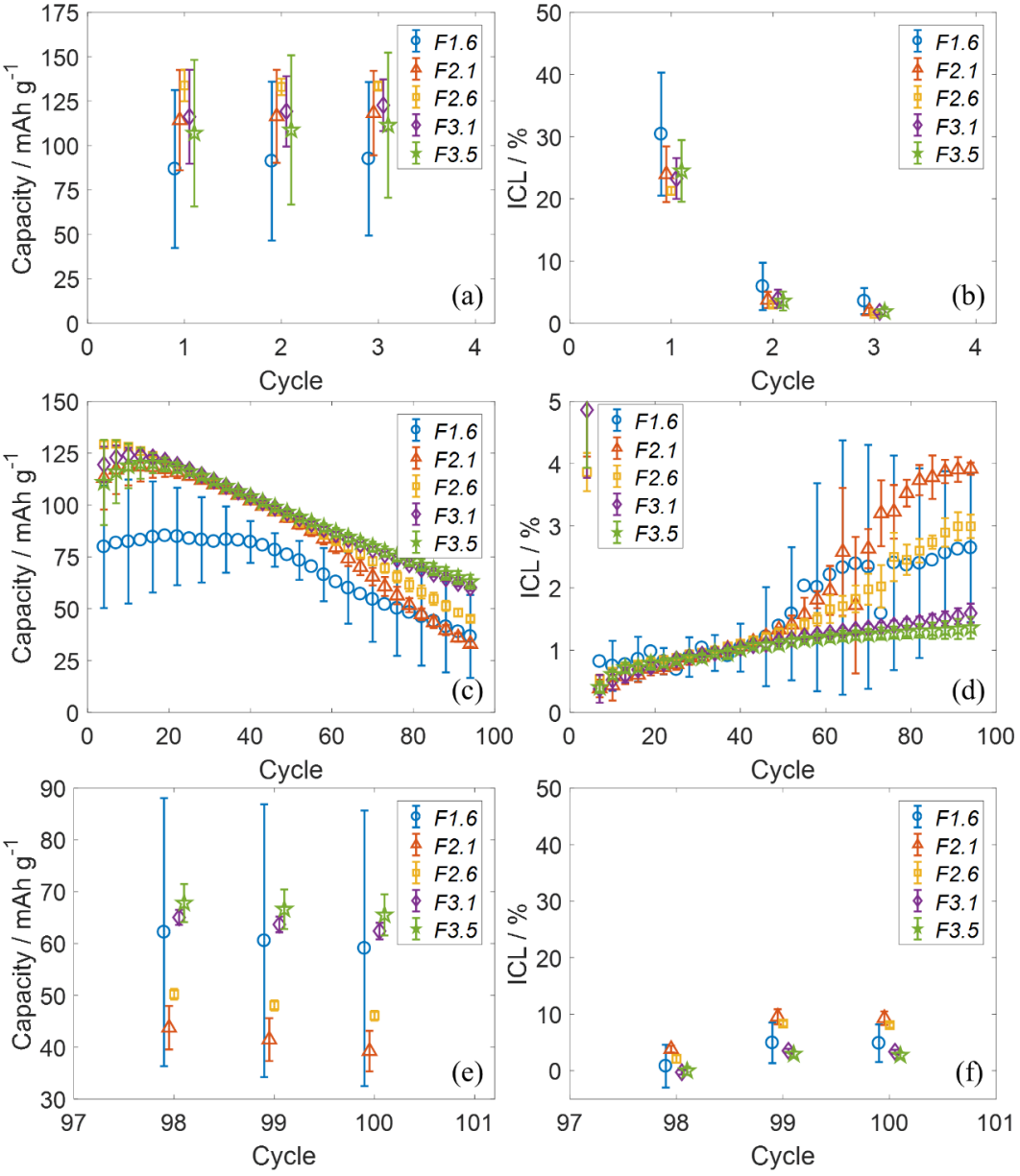


Figure 5.2. Correlation of electrolyte volume and cell cyclability. Discharge capacities during (a) first three cycles at 0.05C/-0.05C, (c) aging cycles at 0.333C/-0.333C, and (e) last three cycles at 0.05C/-0.05C for different electrolyte volume factor groups, *F*; corresponding irreversible capacity losses (ICLs) during (b) the first three cycles, (d) aging cycles and (f) the last three cycles. Cut-off voltages were 3 and 4.1 V. Voltage for the aging cycle was held at 4.1 V until current reached 0.05C. Error bars correspond to 95% confidence intervals.

This instability is probably due to pulverization induced by large stress from volume changes during charging and discharging.[17] Jansen et al. reported thickness of silicon based anodes increased by 50 to 60 % after charge.[18] The volume expansion also depends on the compression during testing which we are working on and will be reported in the future.

The Si particles experienced changes not only in volume but also in shape, which further destabilized the SEI layer. Figure 5.3 shows top-down SEM images of (a) the pristine Si-graphite anode and (b) *F1.6* and (c) *F3.5* anodes cycled for 100 times and discharged. Unlike the pristine anode, which showed spherical Si and conductive carbon particles (not distinguishable in the image), the shape of particles covered by SEI became irregular after cycling. The change in particle shape agreed well with an earlier TEM study.[19] SEI covering the particles was bulkier for *F3.5* compared to *F1.6*, which implies that electrolyte decomposed more on Si particles at *F3.5* due to the more abundant electrolyte (reactant). SEI thickness analysis also showed thicker SEI at *F3.5* than at *F1.6* and is elaborated in section 3.3.

The SEM images also show the presence of some relatively bare graphite particles that were not covered with silicon and carbon. EDS results from *F1.6* and *F3.5* (Figure 5.4 and Table 5.3) showed that the silicon-carbon rich zone (Zone 2) had more oxygen and fluorine elements than the graphite-rich zone (Zone 1). This indicates that SEI was formed preferentially on the silicon-carbon zone, since oxygen and fluorine are key elements of SEI components such as lithium carbonate and LiF. EDS analysis showed 3.5-4.8 atomic percentage of Si at the graphite rich zone because effective analysis depth is large at 20 kV (e.g. 1-2 μm in Si). Because of the same reason, silicon atomic percentage was not significantly high at the silicon-carbon rich zone.

Low electrolyte volume, *F1.6*, caused lithium dendrite formation on an anode (Figure 5.5). After 100 cycles, the separator for *F1.6* was also dry. Visual inspection of the *F1.6* anode revealed that some regions of the electrode did not contribute to charge-discharge processes properly due to lack of electrolyte. These areas were relatively bright and light green in color, similar to the pristine anode. Darker areas indicated where the electrode did cycle. The color change is due to the conversion of crystalline Si to amorphous Si during lithiation. The dendrites formed on dark areas surrounded or near by the relatively-bright areas due to the locally low negative-to-positive capacity ratio. Unlike *F1.6*, there was plenty of electrolyte on the separator for *F2.6* and *F3.5* groups and no lithium dendrites were observed.

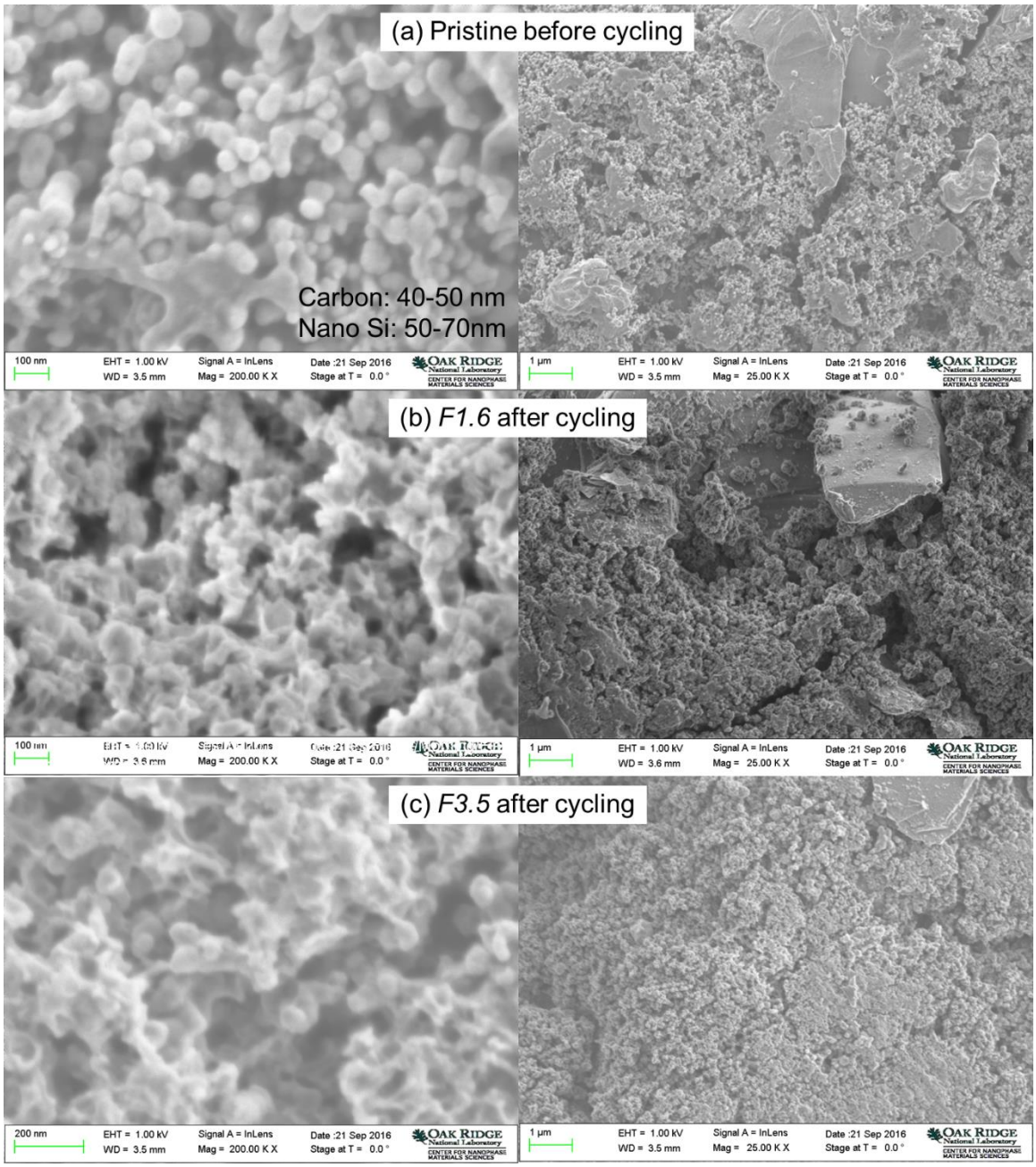


Figure 5.3. SEM images of (a) pristine 15 wt.% Si-graphite anode and (b) *F1.5* and (c) *F3.5* anode cycled 100 times. Magnification of the images on left and right are 200,000 X and 25,000 X, respectively.

Table 5.3. Atomic percentages of elements from EDS analysis on cycled anodes of *F1.6* and *F3.5*. The locations of Zone 1 (graphite rich) and Zone 2 (silicon-carbon rich) are indicated at Figure 5.5

	Atomic percentage / %			
	Zone 1, graphite rich		Zone 2, silicon-carbon rich	
	F1.6	*F3.5*	*F1.6*	*F3.5*
Carbon	61	63	51	48
Oxygen	27	25	33	33
Fluorine	9	6	10	12
Silicon	3	5	5	6
Phosphorus	< 1	< 1	< 1	< 1

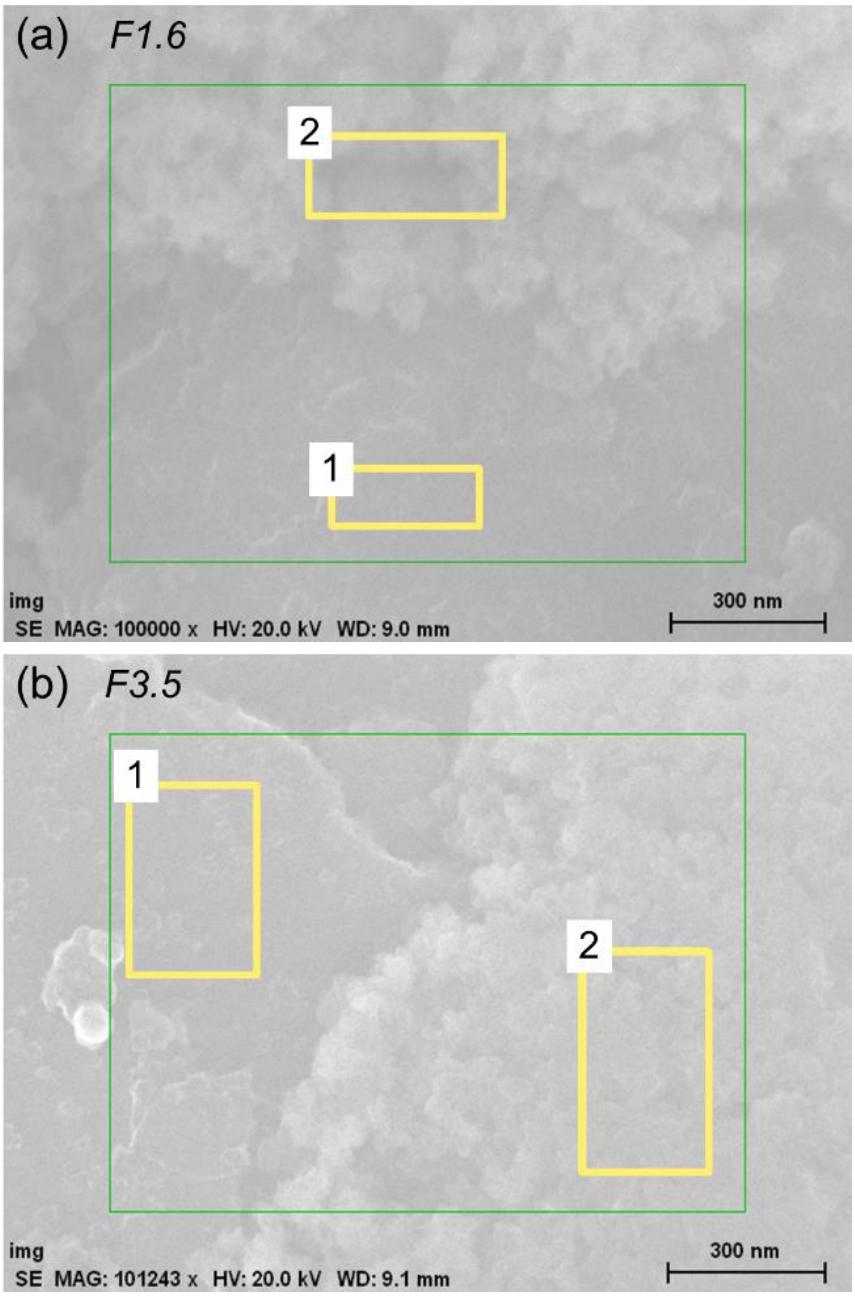


Figure 5.4. Different EDS analysis areas from cycled anodes of (a) *F1.6* and (b) *F3.5*. Rectangular zone 1 and 2 focus on graphite and Si mixed with carbon, respectively. EDS data are shown in Table 5.3.

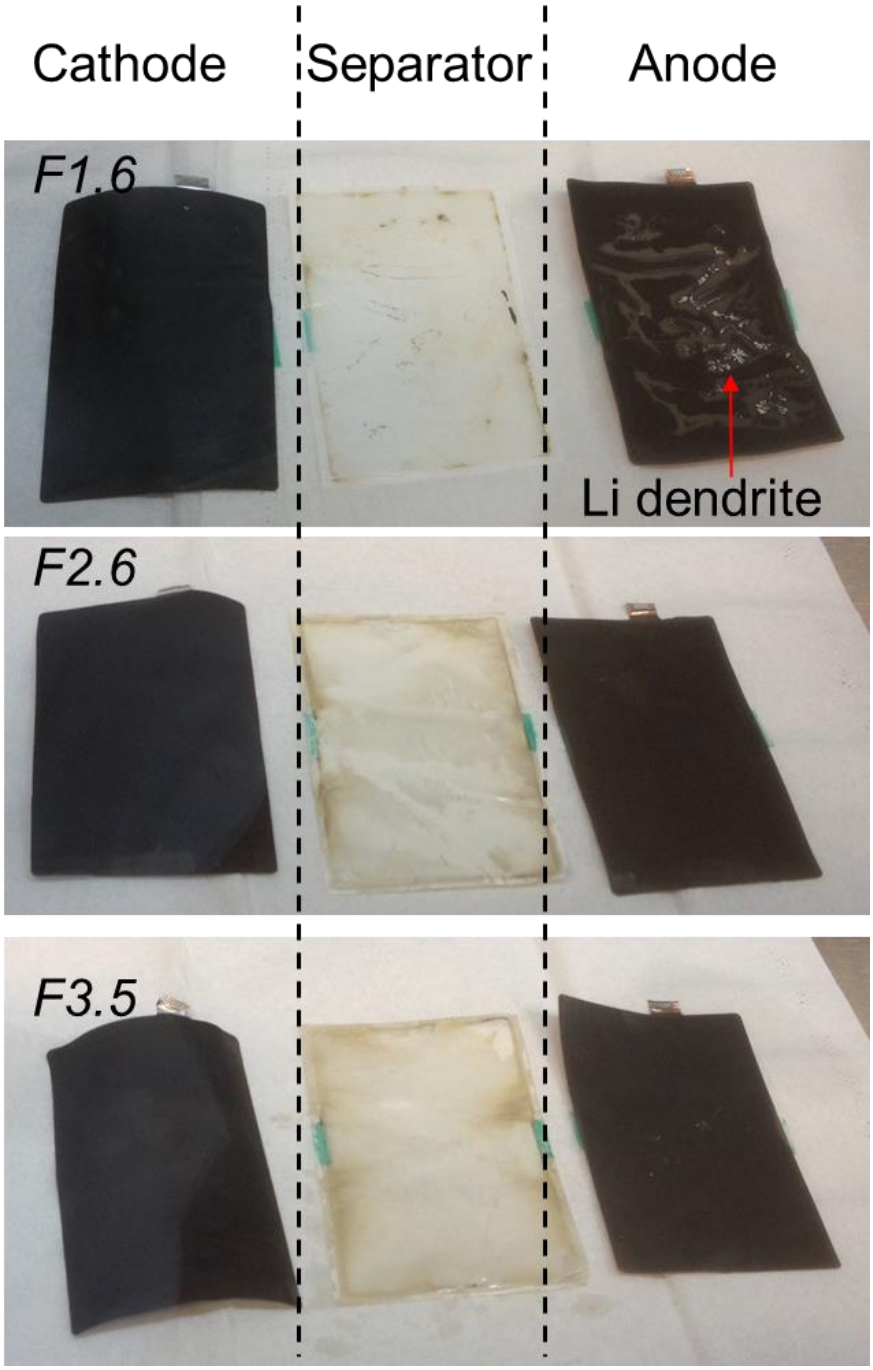


Figure 5.5. Images of cathodes, anodes and separators from *F1.6*, *F2.6*, and *F3.5* after 100 cycles.

Resistance analysis

Resistances were characterized before and after aging cycles using HPPC. Figure 5.6 shows the individual cell resistances during discharge for different factor groups. The HPPC test was programmed to end when the lower cut-off voltage of 3.0 V was reached. This resulted in different numbers of resistance data points for different samples and cycle numbers. The initial capacities from two of *F1.6* cells were lower than the other two, and the cells reached the lower cut-off voltage instantly, resulting in a complete bypass of the HPPC test. Hence, the *F1.6* data at Figure 5.6a were from only two samples having lower resistance than the other two cells in the group. *F1.6* showed the highest resistance on average with large cell-to-cell variations. In general, the resistances of all cells increased as voltage decreased. The initial resistances (4^{th} cycle) of *F2.1* and above were almost identical (32 – 35 Ohm-cm^2 near 3.6 V) while those of *F1.6* were much higher (57 – 66 Ohm-cm^2 near 3.6 V). After the 97^{th} cycle, cells in the *F3.1* and *F3.5* groups demonstrated the lowest resistance (about 50 Ohm-cm^2 near 3.6 V), followed by *F2.6* (average 73 Ohm-cm^2), *F2.1* (over 90 Ohm-cm^2), and *F1.6* (average 127 Ohm-cm^2). Hence, *F3.1* represented the minimum electrolyte amount to minimize resistance increase during cycling. This was also consistent with the long-term cycling data (Figure 5.3), which showed the least capacity fade for the *F3.1* and *F3.5* groups.

The resistances were also measured using EIS at different voltages after 100 cycles. Figure 5.7 shows selected impedance data of different factor groups between 3.7 V and 3.8 V and areal resistances at different voltages. The EIS results were in agreement with the HPPC results with the lowest resistance at *F3.1* and *F3.5* groups (26 – 30 Ohm-cm^2 near 3.6 V), which was just a few Ohm-cm^2 lower than the HPPC results. Similar to the HPPC results, there was no significant difference in resistances from *F3.1* and above.

Figure 5.8a shows the equivalent circuit model used to fit the EIS data along with definitions of the circuit elements and their frequency domains. As examples, Figure 5.8b and 8c illustrate EIS data ranges and the corresponding frequency domains of *F3.5* for the fits at 4.1 V and 3 V. The resistance elements obtained in this study were ohmic resistance (R_{ohmic}), surface film resistance (R_{sf}, or SEI resistance), charge transfer resistance I (R_{ct1}, or anode charge transfer resistance), and charge transfer resistance II (R_{ct2}, or cathode charge transfer resistance). For full cells with graphite anodes, the frequency domain III that belongs to anode charge transfer resistance, R_{ct1}, does not generally appear as a distinct semi-circle.[10, 16] However, the R_{ct1} was a significant component for full cells with Si-containing anodes, especially at low voltages.

Each resistance derived from the EIS after 100 cycles is shown in Figure 5.9. The electrolyte resistances indicated as R_{ohmic} were affected by low electrolyte

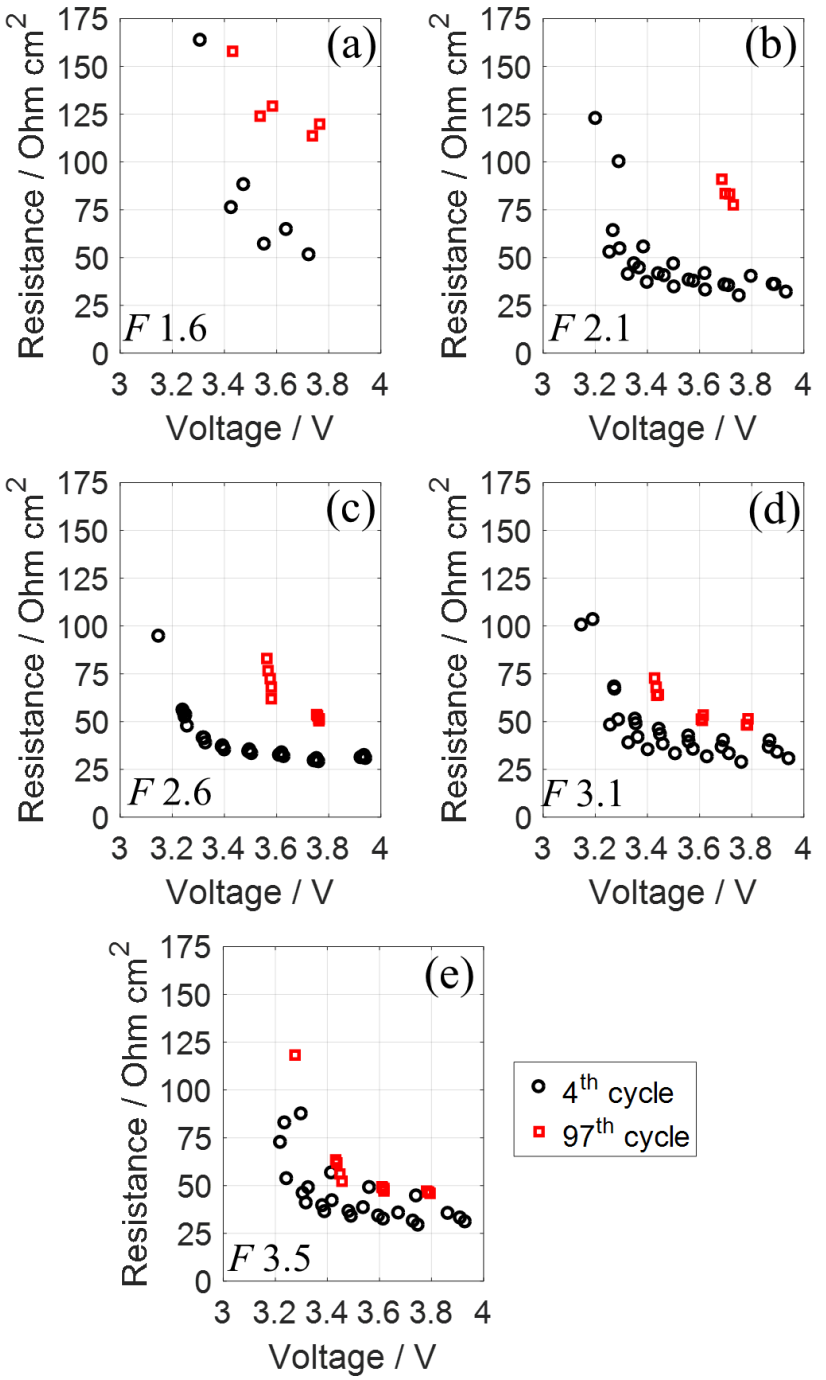


Figure 5.6. Resistances of 15 wt.% Si-graphite/NMC532 cells from HPPC tests at different voltages during discharge at 4th and 97th cycles for electrolyte volume factor group *F1.6* (a), *F2.1* (b), *F2.6* (c), *F3.1* (d), and *F3.5* (e).

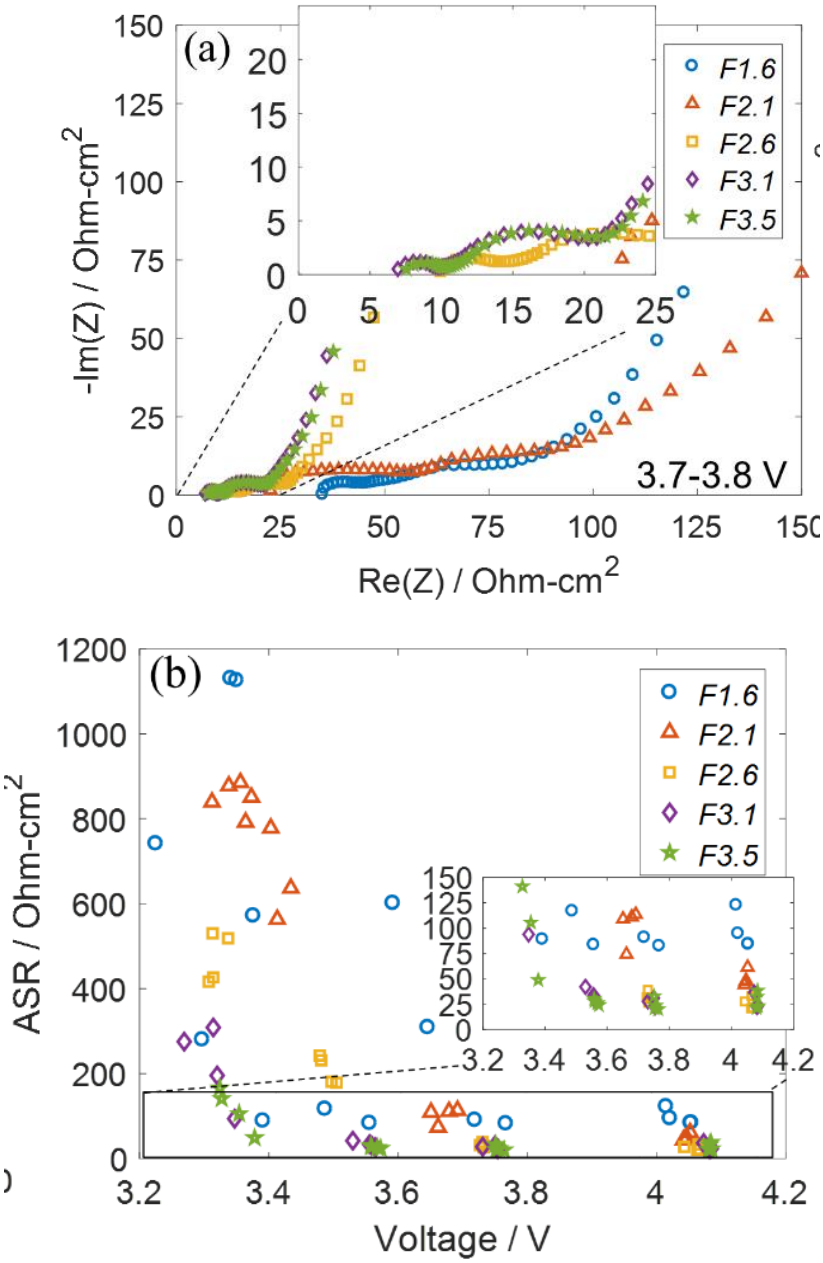


Figure 5.7. (a) Impedance spectra of 15 wt.% Si-graphite/NMC532 cells near 3.75 V after 100 cycles with different electrolyte volume factor groups. (b) Total resistances from EIS at different voltages. Equivalent circuit model for the EIS data fitting is shown in Figure 5.8.

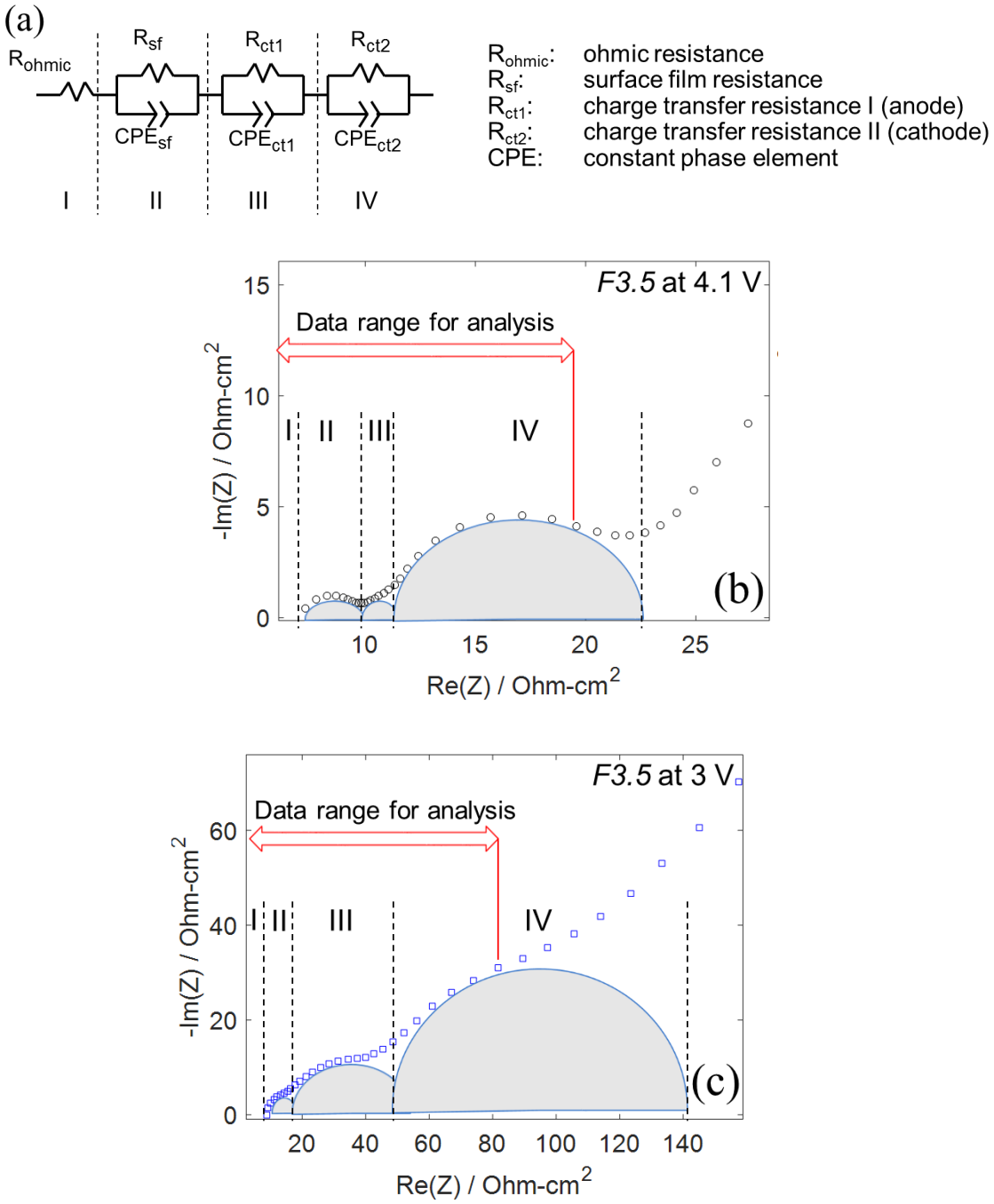


Figure 5.8. (a) Equivalent circuit model for EIS data fitting and definitions and four frequency domains of elements. As examples, EIS data of *F3.5* at (b) 4.1 V and (c) 3 V after 100 cycles and their data ranges for the fittings.

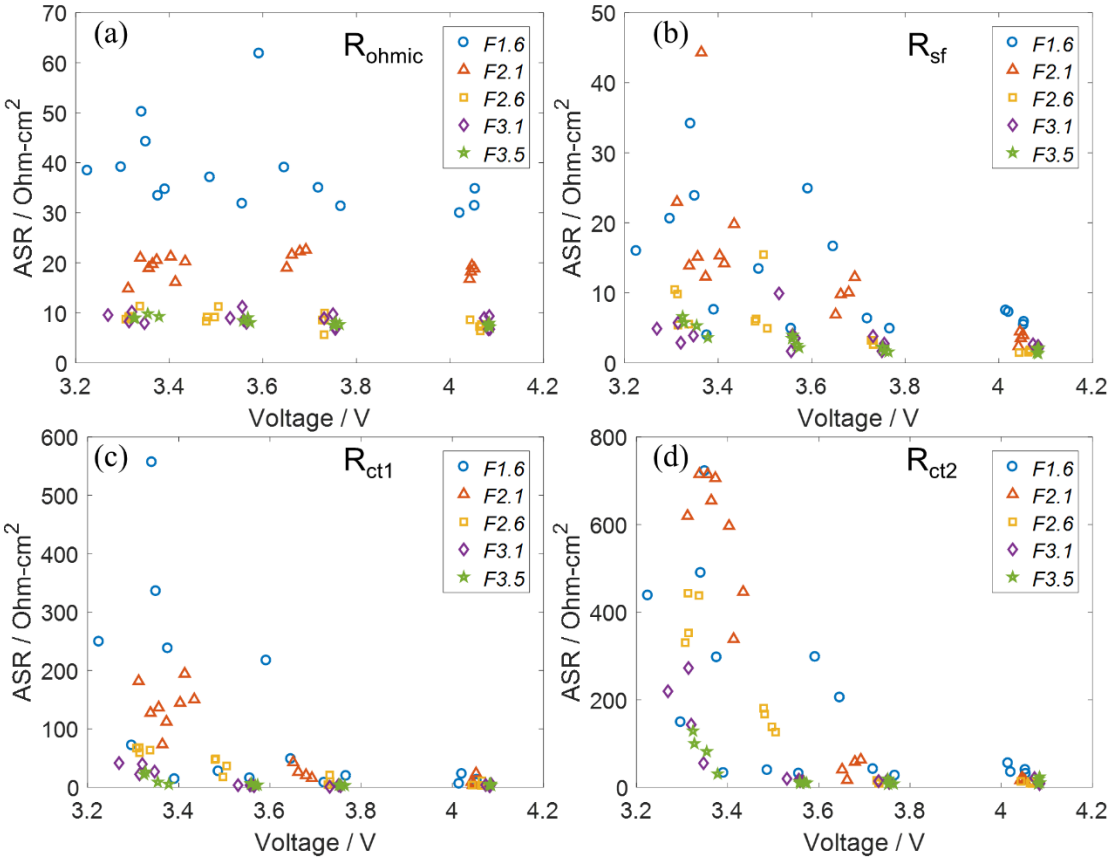


Figure 5.9. Areal specific resistances (ASR) from EIS at different voltages in different electrolyte volume factor groups, (a) ohmic resistance (R_{ohmic}), (b) surface film resistance (R_{sf}), (c) anode charge transfer resistance (R_{ct1}), and (d) cathode charge transfer resistance (R_{ct2}).

volumes. The highest R_{ohmic} was measured for *F1.6* (about 35 Ohm-cm^2) followed by *F2.1* (about 20 Ohm-cm^2). *F2.6* and above showed similar electrolyte resistance (about 10 Ohm-cm^2). R_{ohmic} was independent of voltage, as expected. In contrast, all other resistances increased at lower voltages. Surface film resistance, R_{sf}, is related to the SEI layer and was the lowest at *F3.1* and *F3.5* (2 - 3 Ohm-cm^2 near 3.6 V). While the SEI layer for the higher factor group (*F3.5*) was thicker than the lower factor group (*F1.6* and *F2.6*), this SEI layer was likely porous. Anode surface analysis section explains SEI thicknesses and porosities in detail. *F3.1* and *F3.5* also showed the lowest anode (R_{ct1}, 2 - 3 Ohm-cm^2 near 3.6 V) and cathode charge transfer resistance (R_{ct2},12 - 13 Ohm-cm^2 near 3.6 V). The charge transfer resistances for volume factors of *F2.6* and below were higher than those of *F3.1* and *F3.5* especially at voltages below 3.6 V. The charge-transfer resistance also became more voltage-dependent as the electrolyte volume decreased. This is reasonable because energy requirement resulting in voltage loss becomes higher as the electrolyte volume decreases: fewer opportunities for transferring electrons.

Anode surface analysis

Three factor groups (*F1.6*, *F2.6*, and *F3.5*) were selected for anode surface analysis since the electrochemical performance of *F3.1* is similar to *F3.5*. The thicknesses of the surface film (SEI) were estimated using XPS depth profiles. Figure 5.10 shows surface film element profiles of the three groups along the depth direction from the surfaces. All specimens were taken from the same location at each anode to avoid a geometric effect. The depth was calculated based on the assumption that the film has the same etching rate as SiO_2. The counts per second (CPS) data from element peaks were smoothed using the LOESS model (locally weighted polynomial regression). The thicknesses were estimated based on the CPS of elements corresponding to SEI or silicon active components along the thickness direction.[16] Four elements were chosen for the estimation: Li from LiF (55.6 eV), Si from bulk Si^0 (99.6 eV) and Li_xSiO_y (102.8eV), C from carbonates (292.6 eV), and O from carbonates (532 eV for C = O and 533.5 eV for C - O). LiF and carbonates form SEI components from electrolyte decomposition. Li_xSiO_y forms from the conversion of surface silicon oxides and is one of dominant species on cycled silicon surfaces.[15, 20-21] In Figure 5.10, each CPS of elements was normalized by its own maximum because the CPS varied with different elements. The following assumptions were made to define the SEI thickness:

1) CPS of the Li peak from LiF increases as the depth approaches the Si active particles because LiF is more abundant in the inner surfaces of the SEI.
2) CPS of the Si peak from Si-Si increases until the depth reaches to the center of the Si particles.

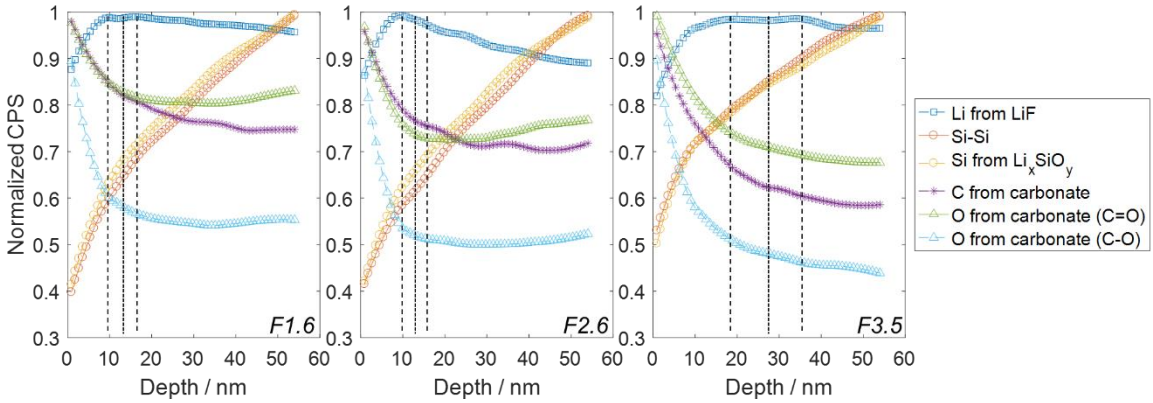


Figure 5.10. Depth profiles of SEI (LiF and carbonates) and active material (Si-Si and Li_xSiO_y) elements. Black dashed and dotted lines are possible ranges of SEI/Si interface and averages of the ranges, respectively. The depth on x-axis was based on the assumption that the film has the same etching rate as SiO_2. CPS of each element was normalized by its own maximum value.

3) CPS of the C and O peaks from bulk carbonates decreases as the depth approaches the Si active particles because they are mostly abundant in the outer surfaces of SEI.

Based on the assumptions, the ranges of estimated SEI thicknesses were 9-16 nm for both *F1.6* and *F2.6*, and 17-34 nm for *F3.5*. The estimated thickness of SEI at *F3.5* is near the radius of the original Si particle (50-70 nm). The thick SEI layer is ascribed to Si because the SEI layers on pure graphite anodes without Si are only about 10 nm thick or less.[16] Since the electrochemical reactions for *F1.6* were not uniform (*F1.6* anode in Figure 5.5), the results from the *F1.6* specimen only represent the dark (cycled) areas at which the local current density might have been higher. The SEI thickness increased significantly from *F1.6* and *F2.6* to *F3.5*. This increase can happen when an SEI layer on an electrode is not electronically insulating or insufficiently dense to prevent electrolyte diffusion towards the electrode surface. In either case the electrolyte continuously decomposes. This result agreed well with SEM images showing larger SEI precipitations at *F3.5* than *F1.6*. On the other hand, the surface film (SEI) resistance of *F1.6* from the EIS analysis was higher than that of *F3.5*, which seems inconsistent with SEM and XPS results. This apparent contradiction can be explained if the SEI is porous. A porous SEI would appear in EIS as a part of the ohmic resistance rather than the surface film resistance.

Considering all of the results from EIS, SEM, and XPS, larger electrolyte volume formed thicker SEI layers with some porosity or channels/cracks. The thickness of the SiO_2 layer on Si was not estimated since Li_xSiO_y continuously increased like Si-Si during the depth analysis, which implies that the SiO_2/Si interface was not sharply delineated. Instead, it is possible that Li_xSiO_y was present throughout the Si particles because its CPS even increased continuously at the depth of original diameter of the silicon particle (50 - 70 nm). The spherical shape of silicon particle probably changed to rough shapes, larger surface area, after large volume changes during cycling. The irregularly expended silicon surfaces after lithiation might partially cover Li_xSiO_y and leave or trap it in the inner surfaces during contraction. If this repeats, Li_xSiO_y can be found in side of the silicon although the silicon may not cover it entirely.

The non-uniform SEI was verified from the Si2p peaks in Figure 5.11a (0 nm depth) and Si atomic percentages in Figure 5.11b. Si^0 (99.6 eV for Si 2p) was clearly detected from the top surfaces of the anode, especially at *F3.5*, implying SEI did not cover the Si particle surfaces uniformly. It should be noted that the electron escape depth is only 5−10 nm beneath the anode surface. Hence, Si^0 was present not only under the SEI but also on top of the SEI or near the top surface. In Figure 5.11a, Li 1s, O 1s and P 2p peaks indicated the amount of dense lithium compounds (e.g., LiF, Li_2O, Li_2CO_3) increased as the analysis depth approached the SEI/Si interface. C 1s, O 1s, and P 2p peaks showed

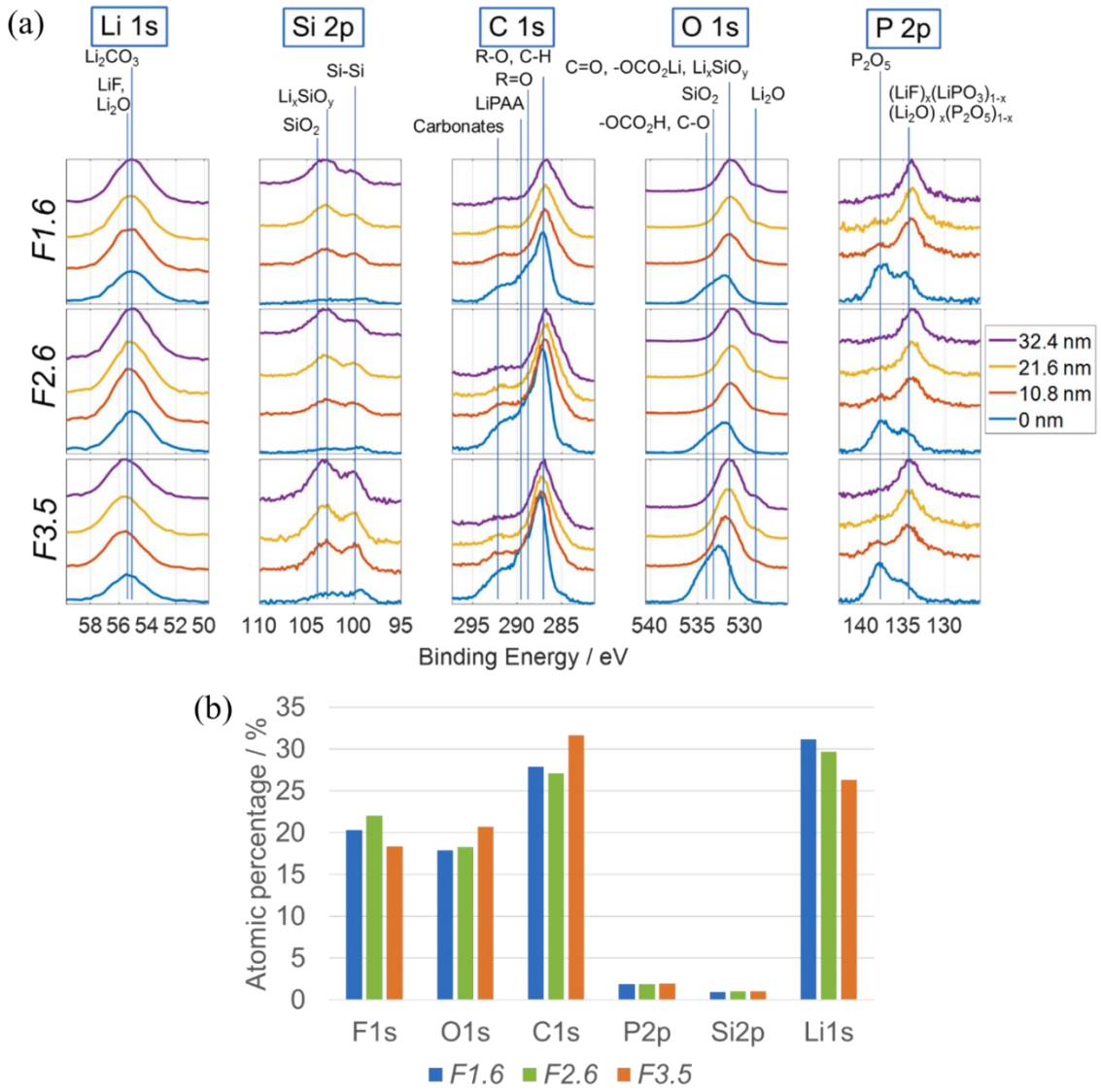


Figure 5.11. (a) XPS peaks from depth profiles of *F1.6*, *F2.6*, and *F3.5* and (b) atomic percentages from the top surface (before sputtering) from XPS survey scans. Depth was calculated based on the sputter rate for SiO_2.

polymeric carbonates and phosphorus compounds mostly distributed in the outer surface of the SEI. The graphite peak intensity (284.5 eV) was not clear after 100 cycles, which also happened in another study.[14] According to the results of XPS survey scans from the top surface (before sputtering) (Figure 5.11b), *F3.5* showed a higher ratio of carbonate compounds (C 1s and O 1s) and lower ratio of Li compounds (Li 1s) than *F1.6* and *F2.6*. Hence, *F3.5* might have a higher ratio of polymeric compounds than the lower electrolyte volume factor groups.

Conclusions

Electrolyte volume effects were investigated with lithium ion batteries in pouch format with 15 wt.% Si-graphite as the anode and $LiNi_{0.5}Mn_{0.3}Co_{0.2}O_2$ (NMC532) as the cathode. The electrolyte was 90 wt.% 1.2 M $LiPF_6$ in EC:EMC with 10 wt.% FEC. This work determined a baseline condition for electrolyte volume when integrating Si into graphite anode, which provided insights on practical cell and pack design. The electrolyte volume to total pore volume needs to be at least 3.1 to achieve the best performance. However, the optimized capacity retention in this study was still lower than that of cells with pure graphite anodes without silicon. Less electrolyte resulted in higher ohmic resistance, larger cell-to-cell capacity variation, and greater capacity fade. HPPC tests demonstrated the lowest resistance for the volume factor 3.1 and 3.5 groups, followed by 2.6, 2.1, and 1.6. For the volume factor 1.6, lithium dendrites were found on the anode surface after cycling. Unlike typical full cells having graphite anodes, significant anode charge transfer resistances were detected in EIS measurements and became more pronounced as the cell voltage decreased. Irreversible capacity loss also continuously increased in all factor groups as cells were cycled. SEM and EDS analysis showed that SEI covering the active particles was bulkier for the volume factor 3.5 compared to 1.6. SEI formed thicker layers on Si-rich areas compared to graphite-rich areas. XPS results also showed SEI thicknesses around 10 to 35 nm after 100 cycles, and the SEI thickness increased as the electrolyte volume factor increased. The XPS elemental analysis along the depth of anode indicated that Li_xSiO_y formed throughout the Si particles rather than just as a surface layer. Considering all of the results from EIS, SEM, and XPS, it was found that the SEI on Si has large pores or channels that are permeable to electrolyte.

References

1. Obrovac, M. N.; Chevrier, V. L., Alloy Negative Electrodes for Li-ion Batteries. *Chem. Rev.* **2014,** *114*, 11444-11502.
2. Liang, B.; Liu, Y.; Xu, Y., Silicon-Based Materials as High Capacity Anodes for Next Generation Lithium Ion Batteries. *J. Power Sources* **2014,** *267*, 469-490.
3. Goriparti, S.; Miele, E.; De Angelis, F.; Di Fabrizio, E.; Proietti Zaccaria, R.; Capiglia, C., Review on Recent Progress of Nanostructured Anode Materials for Li-ion Batteries. *J. Power Sources* **2014,** *257*, 421-443.
4. Boukamp, B. A.; Lesh, G. C.; Huggin, R. A., All-Solid Lithium Electrodes with Mixed-Conductor Matrix. *J. Electrochem. Soc.* **1981,** *128*, 725-729.
5. Etacheri, V.; Marom, R.; Elazari, R.; Salitra, G.; Aurbach, D., Challenges in the Development of Advanced Li-ion Batteries: A Review. *Energy Environ. Sci.* **2011,** *4*, 3243-3262.
6. An, S. J.; Li, J.; Daniel, C.; Mohanty, D.; Nagpure, S.; Wood, D. L., The State of Understanding of the Lithium-ion-Battery Graphite Solid Electrolyte Interphase (SEI) and its Relationship to Formation Cycling. *Carbon* **2016,** *105*, 52-76.
7. Su, X.; Wu, Q.; Li, J.; Xiao, X.; Lott, A.; Lu, W.; Sheldon, B. W.; Wu, J., Silicon-Based Nanomaterials for Lithium-Ion Batteries: A Review. *Adv. Energy Mater.* **2014,** *4*, 1300882(1)-1300882(23).
8. Szczech, J. R.; Jin, S., Nanostructured Silicon for High Capacity Lithium Battery Anodes. *Energy Environ. Sci.* **2011,** *4*, 56-72.
9. Xu, K., Electrolytes and Interphases in Li-ion Batteries and Beyond. *Chem. Rev.* **2014,** *114*, 11503-11618.
10. An, S. J.; Li, J.; Mohanty, D.; Daniel, C.; Polzin, B. J.; Croy, J. R.; Trask, S.; Wood, D. L., Correlation of Electrolyte Volume and Electrochemical Performance in Lithium-ion Pouch Cells with Graphite Anodes and NMC532 Cathodes. *J. Electrochem. Soc.* **2017,** *164*, A1195-A1202.
11. Long, B. R.; Rinaldo, S. G.; Gallagher, K. G.; Dees, D. W.; Trask, S. E.; Polzin, B. J.; Jansen, A. N.; Abraham, D. P.; Bloom, I.; Bare˜no, J.; Croy, J. R., Enabling High-Energy, High-Voltage Lithium-Ion Cells: Standardization of Coin-Cell Assembly, Electrochemical Testing, and Evaluation of Full Cells. *J. Electrochem. Soc.* **2016,** *163*, A2999-A3009.
12. Choi, N.-S.; Yew, K. H.; Lee, K. Y.; Sung, M.; Kim, H.; Kim, S.-S., Effect of fluoroethylene carbonate additive on interfacial properties of silicon thin-film electrode. *J. Power Sources* **2006,** *161*, 1254-1259.
13. Etacheri, V.; Haik, O.; Goffer, Y.; Roberts, G. A.; Stefan, I. C.; Fasching, R.; Aurbach, D., Effect of fluoroethylene carbonate (FEC) on the performance and surface chemistry of Si-nanowire Li-ion battery anodes. *Langmuir* **2012,** *28*, 965-976.

14. Bareño, J.; Shkrob, I. A.; Gilbert, J. A.; Klett, M.; Abraham, D. P., Causes and Mitigation of Capacity Fade in NCM523/Si-Gr Lithium-ion Cells. *J. Electrochem. Soc.* **2017**, Under review.
15. Philippe, B.; Dedryvère, R.; Allouche, J.; Lindgren, F.; Gorgoi, M.; Rensmo, H.; Gonbeau, D.; Edström, K., Nanosilicon Electrodes for Lithium-Ion Batteries: Interfacial Mechanisms Studied by Hard and Soft X-ray Photoelectron Spectroscopy. *Chem. Mater.* **2012,** *24*, 1107-1115.
16. An, S. J.; Li, J.; Sheng, Y.; Daniel, C.; Wood III, D. L., Long-Term Lithium-Ion Battery Performance Improvement via Ultraviolet Light Treatment of the Graphite Anode. *J. Electrochem. Soc.* **2016,** *163*, A2866-A2875
17. Sethuraman, V. A.; Chon, M. J.; Shimshak, M.; Srinivasan, V.; Guduru, P. R., In Situ Measurements of Stress Evolution in Silicon Thin Films During Electrochemical Lithiation and Delithiation. *J. Power Sources* **2010,** *195*, 5062-5066.
18. Jansen, A. N.; Trask, S. E.; Polzin, B. J., Impact of Silicon Expansion upon Lithiation on Electrode and Cell Thickness. *ECS Meeting* **2015,** *227th*, 303-303.
19. Nie, M.; Abraham, D. P.; Chen, Y.; Bose, A.; Lucht, B. L., Silicon Solid Electrolyte Interphase (SEI) of Lithium Ion Battery Characterized by Microscopy and Spectroscopy. *J. Phys. Chem. C* **2013,** *117*, 13403-13412.
20. Young, B. T.; Heskett, D. R.; Nguyen, C. C.; Nie, M.; Woicik, J. C.; Lucht, B. L., Hard X-ray Photoelectron Spectroscopy (HAXPES) Investigation of the Silicon Solid Electrolyte Interphase (SEI) in Lithium-Ion Batteries. *ACS Appl Mater Interfaces* **2015,** *7*, 20004-20011.
21. Philippe, B.; Dedryvère, R.; Gorgoi, M.; Rensmo, H.; Gonbeau, D.; Edström, K., Role of the LiPF6Salt for the Long-Term Stability of Silicon Electrodes in Li-Ion Batteries – A Photoelectron Spectroscopy Study. *Chem. Mater.* **2013,** *25*, 394-404.

CHAPTER VI
DESIGN AND DEMONSTRATION OF THREE-ELECTRODE POUCH CELLS FOR LITHIUM-ION BATTERIES

A version of this chapter was originally published by Seong Jin An, Jianlin Li, Claus Daniel, Sergiy Kalnaus, and David L. Wood III:

Seong Jin An, Jianlin Li, Claus Daniel, Sergiy Kalnaus, and David L. Wood III "Design and Demonstration of Three-Electrode Pouch Cells for Lithium-Ion Batteries" *Journal of The Electrochemical Society*, 164 (7) (2017): A1755-A1764.

All experiments, simulation, data analysis, and initial draft for this article were done by Seong Jin An. The draft was improved and finalized by Seong Jin An, Jianlin Li, and David L. Wood III. All other co-authors provided comments on contents.

Abstract

Simple three-electrode pouch cells which can be used in distinguishing the voltage and resistance in individual electrodes of lithium ion batteries have been designed. Baseline (1 mm-staggered alignment, cathode away from a reference electrode) and aligned electrodes to a reference electrode located outside of the anode and cathode were studied to see alignment effects on resistance analysis. Cells composed of A12 graphite anodes, $LiNi_{0.5}Mn_{0.3}Co_{0.2}O_2$ (NMC 532 or NCM 523) cathodes, lithium foil references, microporous tri-layer membranes, and electrolytes, were cycled with cathode cutoff voltages between 3.0 V and 4.3 V for formation cycles or 4.6 V for C-rate performance testing. By applying a hybrid pulse power characterization (HPPC) technique to the cells, resistances of the baseline cells contributed by the anode and cathode were found to be different from those of the aligned cells, although overall resistances were close to ones from aligned cells. Resistances obtained via electrochemical impedance spectroscopy (EIS) and 2D simulation were also compared with those obtained from HPPC.

Introduction

Increasing battery size poses some problems, such as nonuniform cell degradation due to uneven distributions of current, voltage, and/or temperature in the cells.[1-2] Likewise, the geometry and conformation of cells also affect battery performance.[3-4] Hence, testing battery cells of similar size and geometry in final products is useful to determine precise electrochemical performance and understand mechanisms of degradation.

It is also beneficial to diagnose and distinguish the individual electrode performance for battery design. This could be done by three-electrode cells capable of monitoring charge and discharge potentials at the anode and cathode in batteries.[5-7] However, most three-electrode cells typically consist of millimeter-

size electrodes, like the ones used in micro coin cells; expensive and delicate Pt or Pt-coated reference electrodes; bulk hardware such as fittings to hold cell components; and compressible sealants to prevent electrolyte leakage.[8] Furthermore, these coin cells with small electrodes generally have more cell-to-cell variations than pouch cells with large electrodes. In this study, three-electrode pouch cells were assembled to understand their behavior and reliability using reference electrodes outside of anode and cathode which is facile in cell assembly.

Three-electrode pouch cells were designed and built with a common lithium foil as a reference electrode. Compared with a typical pouch cell, the only new part in the three-electrode pouch cells was a lithium foil. Hence, no additional fittings or devices for the assembly were needed. Assembling the three-electrode pouch cell was simple and convenient. The lithium foil used as a reference electrode was embedded in a pouch cell with graphite as the anode and $LiNi_{0.5}Mn_{0.3}Co_{0.2}O_2$ (NMC 532, also called NCM 523) as the cathode. To accelerate performance degradation, the three-electrode pouch cells were cycled with a higher cut-off voltage, 4.6 V_{WE-RE} after formation.

Experimental

Pouch cells were fabricated using single-sided A12 graphite (ConocoPhillips) anodes, $LiNi_{0.5}Mn_{0.3}Co_{0.2}O_2$ (NMC 532) (Toda America) cathodes, lithium foil reference electrodes, 1.2 M $LiPF_6$ in ethylene carbonate (EC) : diethyl carbonate (DEC) (3:7 by weight) electrolyte (BASF), and tri-layer separators (Celgard 2325). Table 6.1 shows the cell components.[9] Commercially relevant anode and cathode electrodes were coated and dried on copper foils and aluminum foils, respectively, using a slot-die coater (Frontier Industrial Technology). The electrodes were not calendered to simplify the cell assembly and avoid any possible resulting variables such as porosity variation and uneven stress. Reliable reproducibility of the uncalendered electrodes in pouch format at Oak Ridge National Laboratory (ORNL) can be found elsewhere.[10-11] Electrolyte volume was controlled at 2 times to the total pore volume of the electrodes and separator since it plays such an important role in cell performance.[11-12] All assembly processes were done in a dry room, RH 0.2% at 21 °C, to avoid water-vapor-related decomposition effects on the electrolyte.[13]

Lithium foils and the electrolyte were stored in an argon-filled glove box prior to use. Pouch cells were sealed under vacuum. Single-side-coated electrodes were used in this study, but the design is also applicable to multiple double-side-coated electrodes for higher capacity cells.

Table 6.1. Cell information

	Composition	Size (loading) [porosity]
Anode	Electrode: 92wt% A12 graphite (ConocoPhillips), 2wt% C-65 carbon black (Timcal), 6wt% PVDF (Kureha 9300) Current collector: Cu foil Tab: nickel	Electrode only 86.4 mm×58 mm×65 μm (6.5 mg/cm^2) [55%]
Cathode	Electrode: 90wt% $LiNi_{0.5}Mn_{0.3}Co_{0.2}O_2$ (TODA America Inc.), 5wt% powder grade carbon black (Denka), 5wt% PVDF (Solvay Solef® 5130) Current collector: Al foil Tab: aluminum	Electrode only 84.4 mm×56 mm×64 μm (11.9 mg/cm^2) [55%]
Reference	99.9% lithium foil (Alfa Aesar)	3 mm × 80 mm × 0.75 mm
Separator	Polypropylene–polyethylene–polypropylene (Celgard® 2325)	89 mm × 61 mm × 25 μm [39%]
Electrolyte	1.2 M $LiPF_6$ in EC:DEC (3:7 by weight, BASF)	-

A common 0.75 mm thick lithium foil was cut into 3 mm by 80 mm and used as the reference electrode. The lithium foil was physically attached to a nickel tab on the upper part of the foil (Figure 6.1b and h) and was wrapped using the right portion of a separator sheet, as shown in Figure 6.1a and 1b. Then, single-side-coated anode and cathode were placed on the remaining portion of the separator immediately adjacent to the wrapped lithium foil. All parts were fixed for electrode alignment to the reference electrode using battery-grade adhesive tapes. The sandwiched assembly and electrolyte were inserted in a pouch and sealed under vacuum. In Figure 6.1b, WE, CE, and RE denote working electrode, counter electrode, and reference electrode, respectively. Abbreviations used in this study are defined in Table 6.2.

Two types of pouch cells were assembled with 3 cells for each type. One type of pouch cells had 1-mm staggered alignment to the reference cell (Figure 6.1b, case 1, baseline cell) and the other type had no staggered alignment (Figure 6.1b, case 2, aligned cell). In this work, the anodes were 2 mm larger than the cathodes in both width and length (1mm larger on each side), which is conventional in electrode design to minimize lithium plating. Hence, when a reference was placed next to the anode and cathode (Figure 6.1b), a baseline cell had 1-mm staggered alignment to the reference electrode (Case 1: baseline) while an intentionally-aligned cell had no staggered alignment to the reference electrode side and 2 mm-staggered alignment on the other side (Case 2: aligned).

All pouch cells were tested using a VSP potentiostat (EC-Lab, Bio-Logic Science Instruments SAS) connected to an environmental chamber (ESPEC Corp.) at 30 °C. Five leads were used to connect a cell with the potentiostat (Figure 6.1c): two current control/measurement leads for anode and cathode and three control/measurement leads for the electrode potentials at anode, cathode, and reference. The pouch cells went through two sequential formation cycles, hybrid pulse power characterization (HPPC) and electrochemical impedance spectroscopy (EIS) for initial resistance. Then, C-rate performance tests were conducted for 15 cycles, followed by HPPC and EIS for resistance increase after the C-rate tests. The formation cycles were performed at C/10 charge and discharge rates between 3 V_{WE-RE} and 4.3 V_{WE-RE} to provide stable solid electrolyte interphase where 1C was based on 160 mA/g.[14] During the C-rate tests, the cells were charged at constant current (C/5) until the voltage reached 4.6 V_{WE-RE} and discharged until the voltage reached 3 V_{WE-RE} at various C-rates (e.g., C/5, C/3, 1C, 3C).

The HPPC test[15] was adopted to investigate the resistance of cells at every 10% depth-of-discharge (DOD). Before the HPPC test, a cell was charged at a C/3 rate until the voltage reached 4.6 V_{WE-RE}. C/3 discharge rates were used to adjust

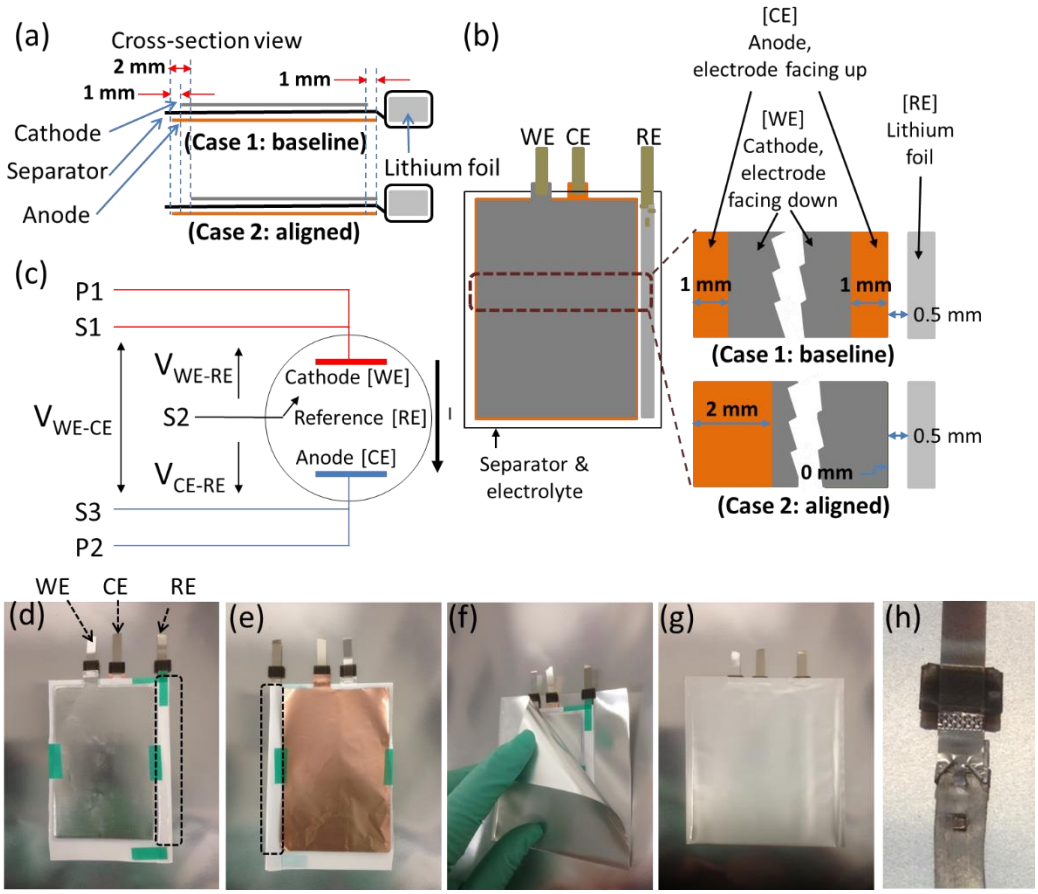


Figure 6.1. Cross-sectional (a) and planar (b) view of a schematic three-electrode assembly showing baseline (case 1) and aligned (case 2) electrodes, a schematic view of five leads connections between a cell and measurement instrument (c), images of three-electrode assemblies facing a cathode current collector side up (d), an anode current collector side up (e), an image of a three-electrode pouch cell before (f) and after (g) electrolyte filling and vacuum-sealing, and a lithium foil with a tab (h); WE, CE, and RE denote working electrode, counter electrode, and reference electrode, respectively; P1 and P2 denote power for the control and measurement of current flowing through the electrode; S1, S2, and S3 denote sense for the control and measurement of the electrode potential. The green films are battery-grade acrylic adhesive tapes.

Table 6.2. Abbreviations and definitions

Abbreviation	Definition
X [WE-CE]	Measured or calculated X value between working (WE) and counter electrodes (CE)
X [WE-RE]	Measured or calculated X value between working (WE) and reference electrodes (RE)
X [CE-RE]	Measured or calculated X value between counter (CE) and reference electrodes (RE)
X = R	Resistance
X = V	Voltage
+	State of charge
-	State of discharge
Baseline	A cell having cathode 1.5 mm away and anode 0.5 mm away from a reference electrode, 1 mm-staggered alignment.
Aligned	A cell having both cathode and anode 0.5 mm away from a reference electrode, no staggered alignment to the reference side and 2 mm-staggered alignment on the other side.

the 10% DOD. Then, the cell rested at OCV for 1 hour before the start of each HPPC test. The HPPC test was composed of sets of a discharge pulse at 2C for 10 sec, a rest for 40 sec, a regeneration (charge) pulse at 1.5C for 10 sec, and a rest for 40 sec. The resistance was calculated by using current and voltage differences before and at the end of the HPPC discharge pulses. After each HPPC test, the cells were charged and discharged at C/3 rates with the cut-off voltages at 3 V and 4.6 V_{WE-RE} to check charge/discharge performance.

After each HPPC test, the cells were stabilized for 1 hour before performing EIS measurements. The EIS measurements were performed in potentiostatic mode at 0 V vs. OCV at a frequency range from 400 kHz to 10 mHz with 5 mV oscillation amplitudes. Six points per decade were recorded during the measurement. Nyquist impedance data were fitted using EC-Lab software to analyze Ohmic resistance (R_{Ohmic}), surface film resistance ($R_{sf,}$ or SEI resistance), and charge transfer resistance (R_{ct}). An equivalent circuit model used for the impedance analysis is shown in Figure 6.7. [16-20] Warburg elements at low-frequency domains were not included in the EIS data fitting to obtain resistances because they are related to solid-state diffusion, [21] and were handled separately. A constant-phase element was applied instead of a capacitor element because of imperfect capacitor behavior in a large and porous electrode.[22-25] Lithium solid-state diffusion coefficients were calculated using Warburg slopes and imaginary impedances at the lowest frequency domain, 10 mHz.[26-27]

Differential capacity was analyzed after smoothing voltage values mathematically to produce clear peaks. The Gaussian average method was used to smooth voltages along with test time. All data processing and 2D simulations were done using Matlab R2016 (MathWorks, Inc).

Results and discussion

Charge and discharge

Capacities of the baseline and aligned cells were measured during formation cycles with C/10 charge and C/10 discharge rates and during C-rate performance tests with a C/5 charge rate and various discharge rates. Figure 6.2 shows charge and discharge capacities for each formation cycle, discharge capacities at different C-rates, and first and second formation polarization curves, including error bars. All error bars reported in this study correspond to 90% confidence intervals.

Both types of cells demonstrated similar capacity during formation cycling. For instance, the average discharge capacities during the 2nd formation cycle

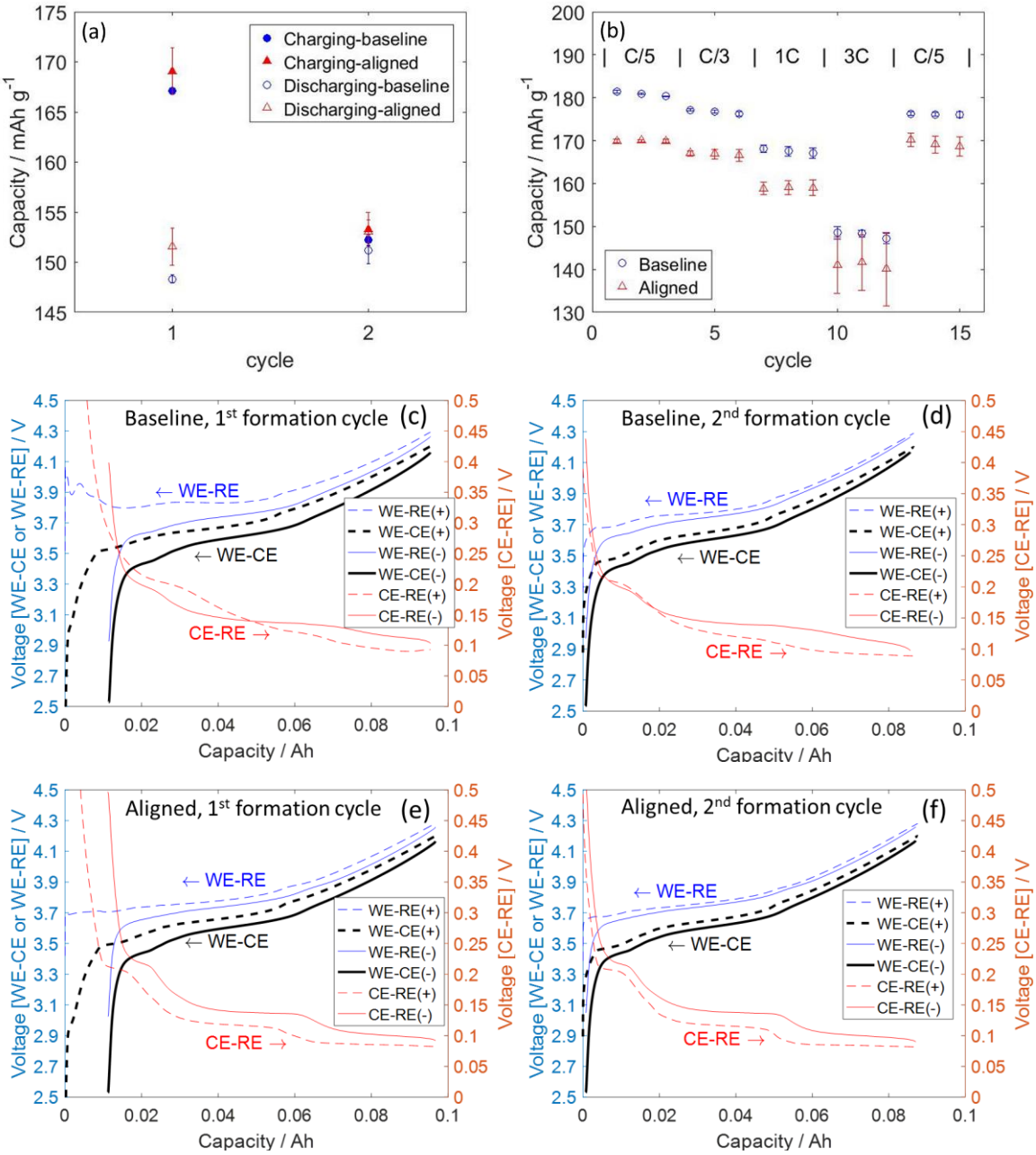


Figure 6.2. Capacities during formation cycles at C/10 and -C/10 with cut-off voltages of 4.3 V_{WE-RE} to 3 V_{WE-RE} (a) and discharge capacities at C/5, C/3, 1C, and 3C with cut-off voltages of 4.6 V_{WE-RE} to 3 V_{WE-RE} (b); voltage profiles of baseline (c, d) and aligned electrodes (e, f) with C/10 and –C/10 at first formation cycle (c, e), at second formation cycle (d, f). (+) and (-) denote charge and discharge, respectively.

between 4.3 V_{WE-RE} and 3 V_{WE-RE} were 151 mAh g^{-1} and 153 mAh g^{-1} for the baseline cells and the aligned cells, respectively, when normalized to the mass of NMC 532. Irreversible capacity losses for both types of cells were about 11% and 1% during the first and second formation cycles, respectively. During C-rate performance tests, the baseline cells showed higher capacities than aligned cells, which explains why conventional cells are assembled in the configuration of the baseline cells. The lower capacity in the aligned cells is ascribed to fewer available sites in the graphite anodes on the aligned side to intercalate and deintercalate lithium ions which results in lower rate performance and potential lithium deposition. Average discharge capacities when charged and discharged at C/5 between 4.6 V_{WE-RE} and 3 V_{WE-RE} were 181 mAh g^{-1} for the baseline cells and 170 mAh g^{-1} for the aligned cells initially but decreased to 176 mAh g^{-1} and 168 mAh g^{-1}, respectively, after 15 cycles of the C-rate tests.

The cathode voltages (WE-RE) of both the baseline and aligned cells were initially near 3.4 V_{WE-RE} before the first formation cycles, but they instantly increased to 3.7-3.8 V_{WE-RE} or more when the first formation charge cycle started and did not further increase until almost 40-50% state of charge (SOC), while anode voltage (CE-RE) dropped rapidly from 3.2 V_{CE-RE} to 0.25 V_{CE-RE}. Hence, a continuous increase in the cell voltage (WE-CE) during early charge was attributed to the anode voltage drop. The stagnant (even slightly decreasing) cathode voltage at the early charge stage, much significant at the baseline (Figure 6.2c), was not observed in the second formation cycle. The stagnant behavior at the first cycle was observed in all baseline cells. Further investigation in understanding such a phenomenon is currently ongoing and results will be discussed in a future publication.

As shown in Figure 6.3, two points of slope change were observed near 3.8 V_{WE-RE} (or 3.7 V_{WE-CE}) and 4.35 V_{WE-RE} (or 4.25 V_{WE-CE}). During discharge, similar trends were shown with slight voltage shifts. These slope changes might be related to different lithium insertion (or extraction) sites of the NMC. Lattice parameters of NMC can explain the different sites for lithium insertion. The a-lattice parameter increases during reduction of Ni^{4+} and Co^{4+} to Ni^{2+} and Co^{3+} (or decreases during oxidation of Ni^{2+} and Co^{3+}) while the c-lattice parameter deceases due to decrease in the electrostatic repulsion between oxygen layers as the lithium layer is filled with lithium ions.[28-29] But, according to Mohanty *et al.* and Lu *et al.*, increases in the c-lattice parameter were observed during lithium insertion into cathodes at high voltage region above 4.4 V.[28, 30] During lithium insertion into NMC, both c-lattice and a-lattice parameters of NMC crystal increase rapidly at the high voltage region above 4.35 V_{WE-RE}. In the middle voltage region, c-lattice decreases while a-lattice continue to increases. At the low voltage region below 3.8 V_{WE-RE}, both the increase rate of a-lattice and the decrease rate of c-lattice parameter slow down.

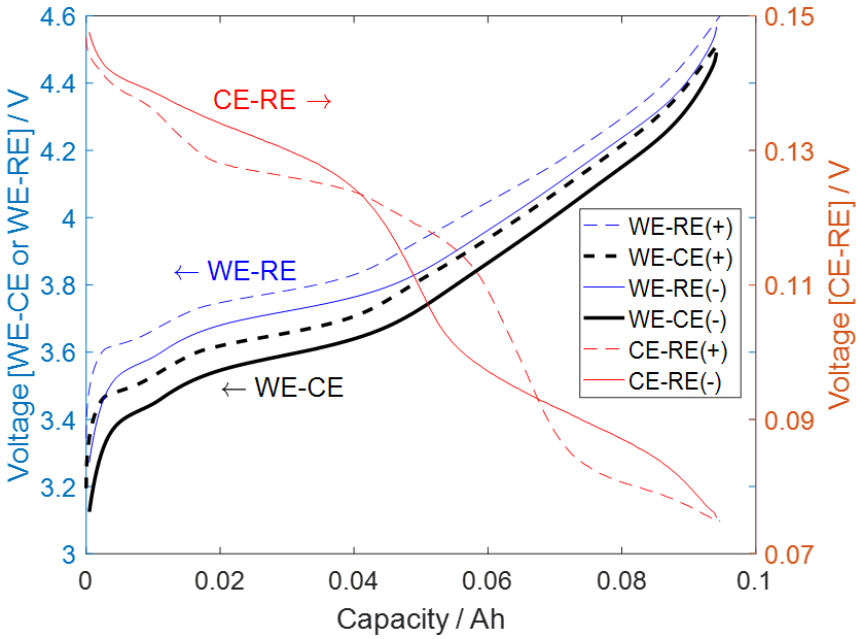


Figure 6.3. Voltage profiles on x-axis of capacity at C/5 and –C/5 with cut-off voltages of 3 V_{WE-RE} and 4.6 V_{WE-RE}. (+) and (-) denote charge and discharge, respectively.

Likewise, the anode showed the highest slope between 0.11 V_{CE-RE} and 0.09 V_{CE-RE} during charge and between 0.12 V_{CE-RE} and 0.1 V_{CE-RE} during discharge. Typically, in the high cell voltage region (WE-CE), Li_xC_6 where $x < 0.5$, most intercalation processes take place into the layered structure. The intercalation into amorphous structure participates in the low cell voltage region (WE-CE), $x > 0.5$. This x range varies depending on types of graphite (or carbon) and degree of graphitization. The processes usually include the coexistence of insertion/extraction into difference active particles.[31] Compared with open-circuit voltages (OCV) of Li_xC_6 in graphite,[32-34] the anode cycled at C/5 in this study had lithium range of x = 0.15-0.7, indicating the graphite anodes were neither fully charged nor fully discharged.

Differential capacities were analyzed with cathode (WE-RE), anode (CE-RE), and net voltage (WE-CE) at different C-rates. There were no significant differences between the differential capacities of baseline and aligned cells. C/5 charge and different C-rate discharge from baseline cells are shown in Figure 6.4. The cathode (WE-RE) peak of the C/5 differential capacity at 3.72 V_{WE-RE} (or 3.59 V_{WE-CE}) shifted to 3.65 V_{WE-RE} (or 3.52 V_{WE-CE}) at 1C. The anode (CE-RE) peak of C/5 at 0.091 V_{CE-RE} also shifted to 0.102 V_{CE-RE} at 1C. The voltage shifts in both cathode and anode peaks are attributed to the higher polarization at 1C.

Resistance

The HPPC test was carried out before and after the C-rate performance tests having the cut-off voltages of 3.0 V_{WE_RE} and 4.6 V_{WE_RE}. The test did not involve charge and discharge pulses at the fully charged state and the fully discharged state because the voltage could exceed the operating cut-off voltages due to the high current pulses, 2C discharge and 1.5C charge rates. Anode and cathode resistances were calculated at given discharge current pulses (ΔI) using Ohm's law (Eq.1) with voltage changes after 10 seconds (ΔV) measured between an electrode and reference (*i* = between CE and RE or between WE and RE).[15]

$$R_i = \frac{\Delta V_i}{\Delta \mathrm{I}} \qquad (1)$$

Overall resistances were from the voltage changes between WE and CE. The cathode resistance (WE-RE) and the anode resistance (CE-RE) from HPPC are marked on the corresponding net voltage (WE-CE) in Figure 6.5. Nyquist plots of EIS and resistances from the EIS fits from WE-CE and CE-RE are also shown in Figure 6.6 and 6.7 for comparisons of resistances from HPPC near 3.8 V. Unlike the results from differential capacity testing, voltage responses during the EIS and HPPC tests were dissimilar for the baseline cells and aligned cells. It was found that voltage changes under unsteady-state current perturbations (i.e., step-

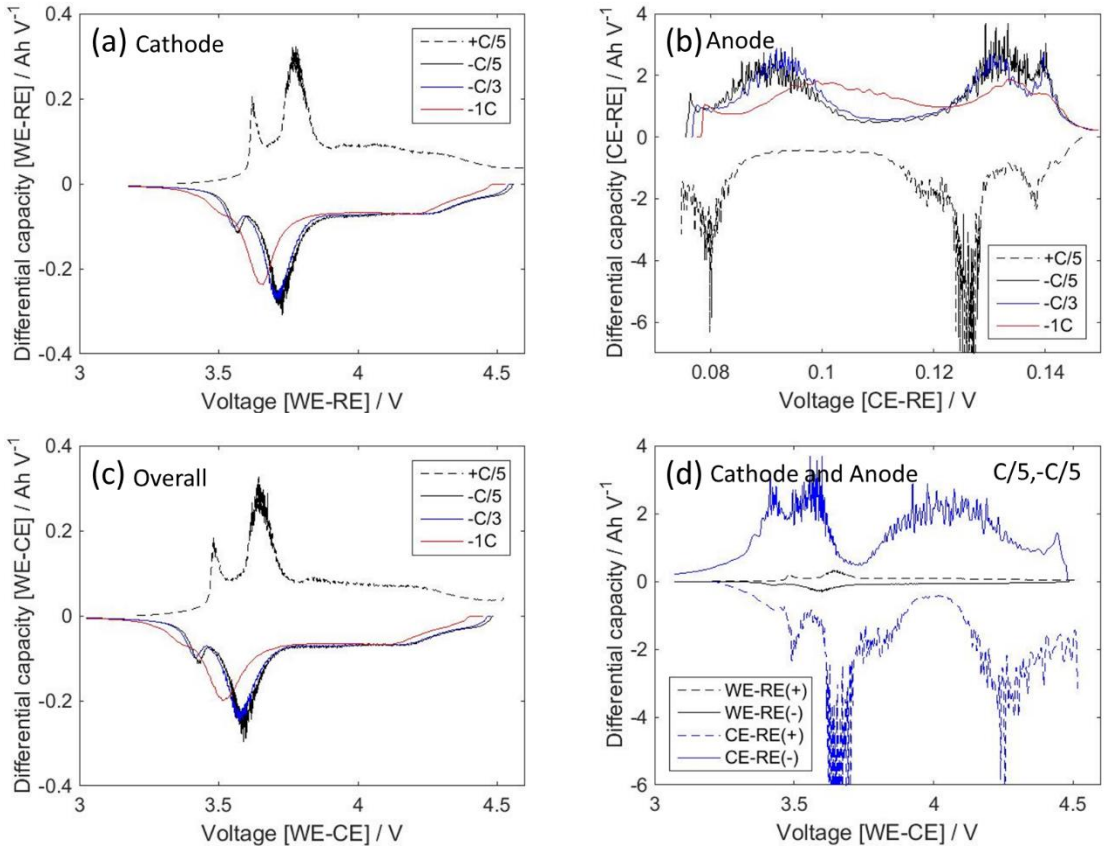


Figure 6.4. Differential capacities at different C-rates (a-c) between WE and RE (a), between CE and RE (b), and between WE and CE (c); differential capacities of anode (CE-RE) and cathode (WE-RE) at C/5 (d); (+) and (-) denote charge and discharge, respectively.

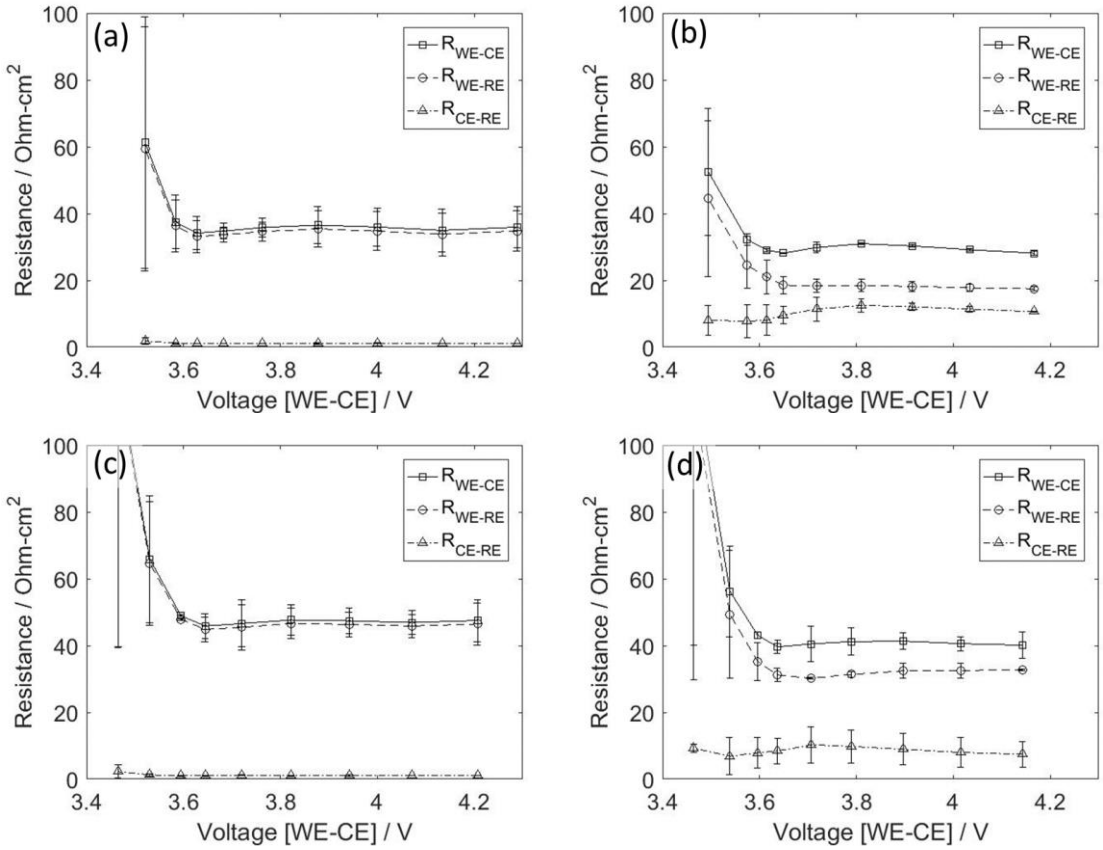


Figure 6.5. Resistances from HPPC at baseline (a, c) and aligned cells (b, d) before (a, b) and after 15 cycles of C-rate tests (c, d). R_{WE-CE}, R_{WE-RE}, and R_{CE-RE} denote resistances of a cell, cathode (working electrode), and anode (count electrode), respectively.

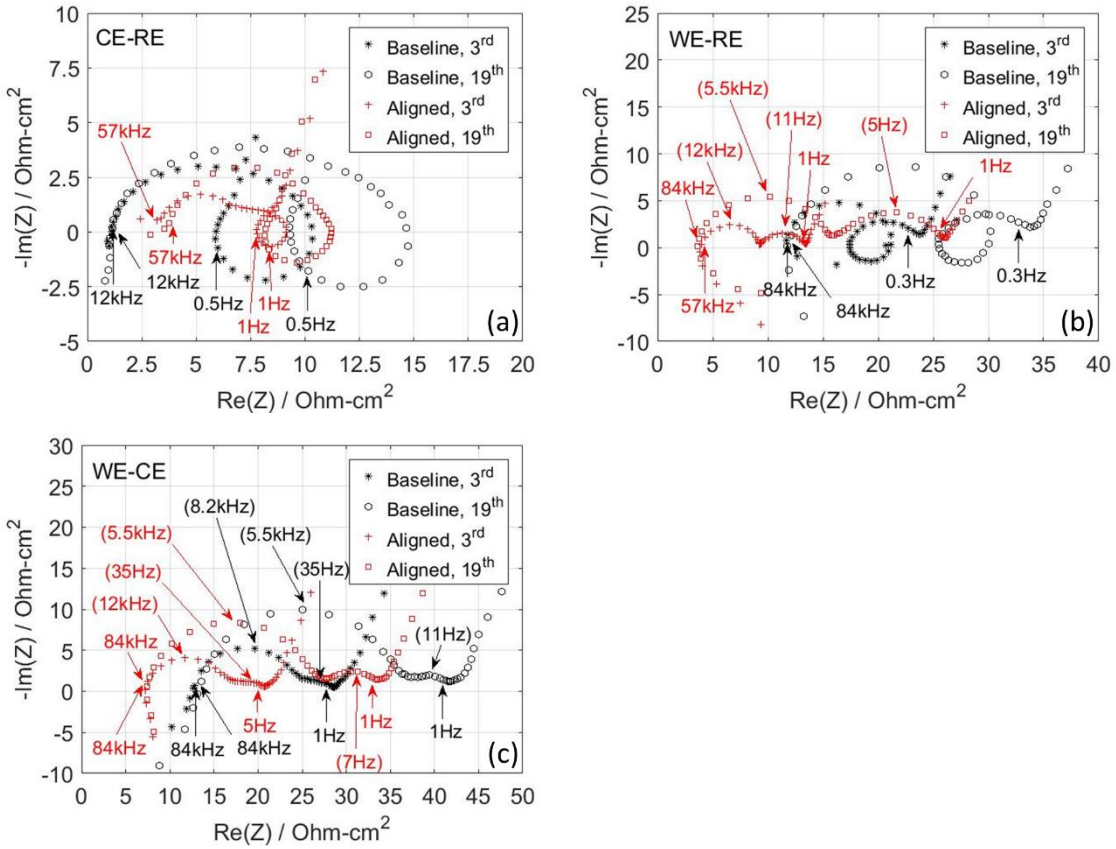


Figure 6.6. Nyquist plots of baseline and aligned-cell EIS from anodes (a), cathodes (b), and cells (c) at 50% DOD before, data at the 3rd cycle, and after 15 cycles of the C-rate tests, data at the 19th cycle. Frequency values with brackets indicate centers of semicircles and ones without brackets are high and low frequency ranges used for EIS data fits in Figure 6.7.

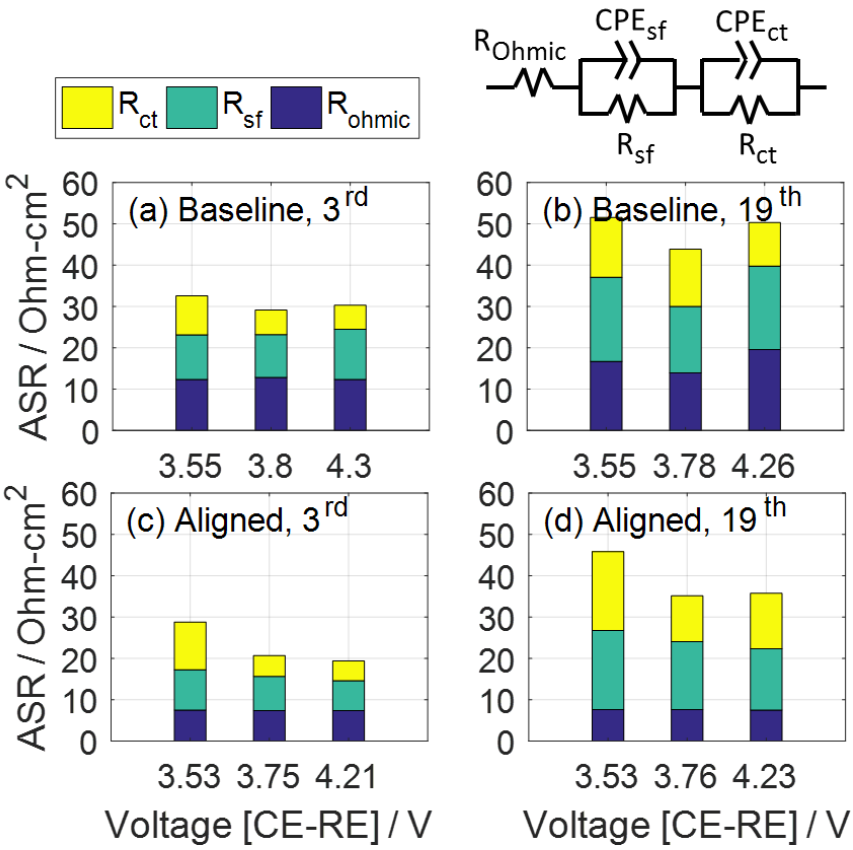


Figure 6.7. Resistances from baseline (a-b) and aligned cell EIS (c-d) for cells (WE-CE) at different voltages before, data at the 3rd cycle, and after 15 cycles of the C-rate tests, data at the 19th cycle. R_{ct}, R_{sf}, and R_{ohmic} denote charge transfer, surface film (SEI), and ohmic resistances, respectively. Equivalent circuit model to fit Nyquist plots is shown on top right.

or wave-like current changes at HPPC and EIS tests) were affected by the two different cell alignments.

Average resistances of the baseline cells from HPPC before 15 cycles of the C-rate tests were about 34.6 Ohm-cm^2 at the cathode, 1.2 Ohm-cm^2 at the anode, and 35.8 Ohm-cm^2 at the cell near 3.76 V_{WE-CE}. On the other hand, average resistances of the aligned cells before the C-rate tests were about 18.4 Ohm-cm^2 at the cathode, 12.5 Ohm-cm^2 at the anode and 30.9 Ohm-cm^2 at the cell near 3.81 V_{WE-CE}. Hence, average resistances of the baseline cells at the cathode were approximately 29 times higher than those at the anode while those of aligned cells at cathode were only 1.5 times higher. Total cell resistances at the baseline cells were about 4.9 Ohm-cm^2 (16%) higher than ones at the aligned cells. After 15 cycles of the C-rate performance tests with a higher cut-off voltage at 4.6 V_{WE-RE}, the average cathode resistances of the baseline cells near 3.6 V_{WE-CE} and above increased by about 12 Ohm-cm^2 at the cathode while those at anode decreased by about 0.1-0.2 Ohm-cm^2. Likewise, the resistances of the aligned cells also increased by about 13 Ohm-cm^2 at the cathode while those at anode decreased by about 2-3 Ohm-cm^2. Total cell resistances at the baseline cells were about 6.3 Ohm-cm^2 (15%) higher than ones at the aligned cells after the C-rate tests, which is close to the difference (16%) before the C-rate tests. From these results, it was found that anode resistances slightly decreased after the high voltage operation while the cathode resistances increased significantly and that total resistances (WE-CE) at the baseline cells were 15 - 16% higher than those at the aligned cells. To understand the difference of 15-16% in the resistances, EIS measurements were conducted and showed that the main differences were found at electrolyte resistance between two different cell alignments.

Figure 6.6 shows Nyquist plots of EIS from anodes (CE-RE), cathodes (WE-RE), and cells (WE-CE) near 3.8 V_{WE-CE}. Frequency values without round-brackets in Figure 6.6 are upper and lower frequency data ranges that are used for EIS data fits using the circuit models in Figure 6.7. The frequency values at centers of the semicircles are shown in round-brackets and are not shown where the domains are affected by inductive loops. The anode and cathode EIS showed inductive loops (the semicircle shown where -Im(Z) < 0) while the EIS from the cell (WE-CE) did not. These inductive loops are attributed to the lithium reference electrode outside of the electrode area.[35] Resistance values closest to -Im(Z) = 0 in the Nyquist plots are listed in Table 6.3 and were based on the assumptions that the first and second semicircles were due to surface film and charge transfer resistances at electrodes, respectively.

Unlike a cell (WE-CE), R_{sf} and R_{ct} of anode (CE-RE) and cathode (WE-RE) are not shown separately due to induction curves in the Nyquist plots but shown as a summation, $R_{sf} + R_{ct}$ in the table. Electrolyte resistance is found where the first

Table 6.3. Approximate resistances from the Nyquist plots in Figure 6.6

Cell type	Cell condition	Configuration	Resistance / Ohm-cm^2				
			R_{ohmic}	R_{sf}	R_{ct}	$R_{sf} + R_{ct}$	R_{total}
Baseline	Before cycling	CE-RE	1.2			4.8	5.9
		WE-RE	11.7			11.8	23.5
		WE-CE	12.8	11.7	4.5		29
	After cycling	CE-RE	1.2			8.2	9.3
		WE-RE	11. 8			22.2	34
		WE-CE	13	24	6		43
Aligned	Before cycling	CE-RE	3.4			4.3	7.7
		WE-RE	4			9.4	13.4
		WE-CE	7.4	9.4	4		20.8
	After cycling	CE-RE	3.5			4.7	8.2
		WE-RE	3.7			22.3	26
		WE-CE	7.3	20.2	6.3		33.8

semicircle crosses zero of -Im(Z) at high frequency domain (> 10 kHz) and is also known as ohmic resistance (R_{ohmic}). R_{ohmic} of the baseline anode (1.2 Ohm-cm^2) was much smaller than the one at baseline cathode (11.7 Ohm-cm^2). These values would be closer to each other if the reference were placed inside of anode and cathode and at the center point of the distance between the electrodes. On the other hand, R_{ohmic} of the aligned anode (3.4 Ohm-cm^2) was close to that at aligned cathode (3.5 Ohm-cm^2) but not the same. More analysis on resistance contributions is discussed in the simulation section. Overall ohmic resistances at the baseline cells (12.8-13 Ohm-cm^2) were also higher than at the aligned cells (7.3-7.4 Ohm-cm^2). Electrode resistances (sum of surface film (R_{sf}) and charge transfer (R_{ct})) are the distances between the first semicircle at high frequency domain (> 10 kHz) and last semicircle at low frequency domain (< 1 Hz) close to zero of -Im(Z). After C-rate tests with high voltage cut-off, like the HPPC results, anode resistance was slightly changed while cathode resistance significantly increased. Thus, the application of high voltages produced more significant effect on cathode resistance, which is consistent with other works.[36-37]

Figure 6.7 shows fitted resistance data at difference voltages for cells (WE-CE) and the equivalent circuit model for the fitting. Sums of square of residuals for the data fits were in the range of 10^{-3}. Fitted resistance data for anode (CE-RE) and cathode (WE-RE) EIS were not included because equivalent circuit models with an induction element resulted in considerable uncertainty of the obtained resistances. The resistances of both baseline and aligned cells from the EIS (WE-CE) were about 10% lower than those from the HPPC (Figure 6.5), which is expected due to differences in the techniques. At the aligned cell, ohmic (electrolyte) resistance did not increase during 15 cycles of C-rate tests. But surface film (SEI) resistance and charge transfer resistance increased significantly.

Solid-state lithium diffusion

Lithium diffusion coefficients in NMC particles were investigated to find differences in two different cell alignments and calculated using Warburg slopes and imaginary impedances Z'' at the low-frequency domain of the EIS (WE-RE), 10 mHz in this study. The solid-state lithium diffusion coefficient, D, can be calculated using the equation below:[26, 38]

$$D = \frac{l_c^2}{\tau} \qquad (2)$$

where l_c and τ denote the characteristic length of diffusion (40 nm) in a 250 nm diameter solid sphere (NMC primary particle) and the diffusion time constant, respectively. l_c was defined as the volume/area ratio, radius/3 for the sphere.

The diffusion time constant τ can be derived from the finite-space diffusion model and defined by the equation below:[39]

$$\tau = 2(C_{int}A_w)^2 \qquad (3)$$

C_{int} is the potential dependence of the differential intercalation capacity and inversely proportional to imaginary impedance value Z'' at the very low-frequency domain of the EIS.[21]

$$C_{int} = -(Z''\omega)^{-1} \ at \quad \omega \to 0 \qquad (4)$$

A_w is the Warburg slope in the medium frequency domain of the EIS where the differences of impedance in the real part $\Delta\mathrm{Re}$ are the same with those in the imaginary part $\Delta\mathrm{Im}$ at corresponding differences of angular frequencies $\Delta\omega$.[40]

$$A_w = \frac{\Delta\mathrm{Re}}{\Delta\omega^{-1/2}} = \frac{\Delta\mathrm{Im}}{\Delta\omega^{-1/2}} \qquad (5)$$

Figure 6.8 shows the calculated diffusion coefficients at cathode from the baseline and aligned cells before and after C-rate tests at various potentials. The calculated diffusion coefficients of NMC above 3.8 $V_{WE\text{-}RE}$ were above 10^{-10} cm^2/s at the aligned cells and below 10^{-10} cm^2/s at the baseline cells, where the result of Dees et al was around 10^{-10} cm^2/s.[41] Hence, two different cell alignments also affected the results of diffusion coefficient calculation.

2D simulation

The resistance difference between the baseline and the aligned cells was large, although they should ideally be similar. To understand the systems, cell geometries in electrolyte zones (Figure 6.9) were simulated using an unsteady-state diffusion equation (Eq. 6) and current and potential equation (Eq. 7) in the electrolyte.[42-44] The unsteady-state diffusion equation for the electrolyte is

$$\varepsilon\frac{\partial C}{\partial t} = \nabla \cdot D_{eff}\nabla \mathrm{C} \qquad (6)$$

where C is the concentration of the electrolyte. ε (separator porosity in electrolyte region, separator) and D_{eff} (effective diffusion coefficient) are assumed to be constant. Eq. 6 was applied to the electrolyte zone in Figure 6.9 while bulk areas of the anode and cathode were not included for simplicity. Concentration changes in the electrolyte zone (Eq. 6) were calculated using constant electrolyte concentrations on the cathode and anode edges (BC1 and BC2).

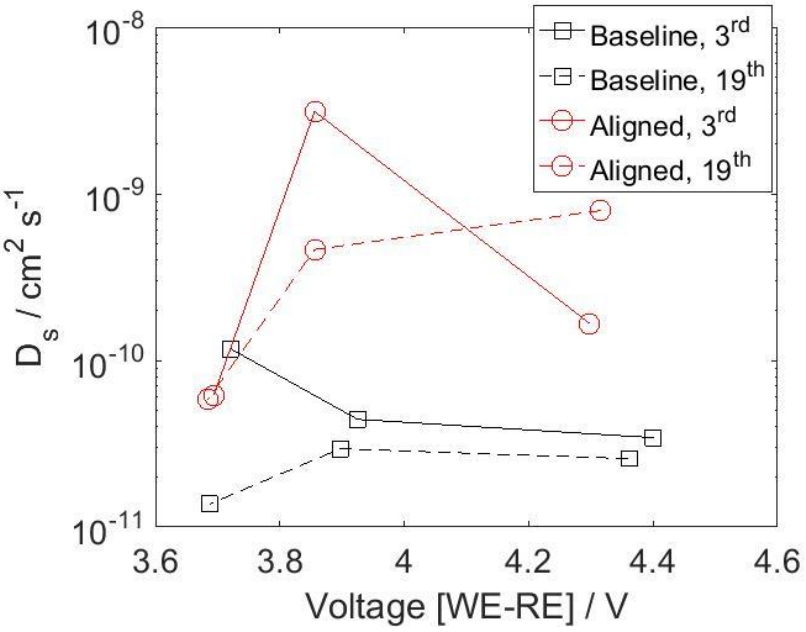


Figure 6.8. Lithium solid-state diffusion coefficients of cathodes from baseline and aligned cells before, data at the 3rd cycle, and after C-rate test, data at the 19th cycle.

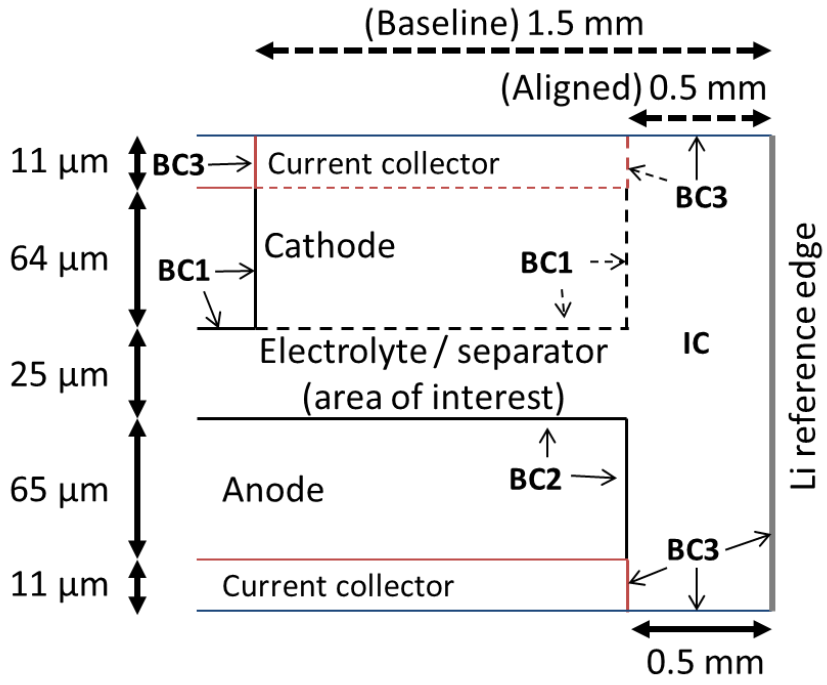


Figure 6.9. Cross-section geometries of baseline and aligned cells for 2D-simulations considering only electrolyte sections. All bulk areas of anode, cathode and current collectors were not included in the simulations while their edges facing the electrolyte were used for boundary conditions. Initial condition (IC) and each boundary condition (BC) are shown in Table 6.4. Scales of X- and Y-axes are different.

Figure 6.9 shows cross-section geometries of a baseline and aligned cell with boundary labels.

Table 6.4 shows the input parameters and the boundary conditions (BC) corresponding to BC1 through BC3 and initial condition (IC) in the Figure 6.9. To solve the equation, finite-difference method was used with the relative tolerance 10^{-4} and 53760 and 43264 triangles in the baseline and aligned meshes, respectively. Computations and mesh generations were performed using Matlab R2016 (Mathworks, Inc). A Matlab code was developed to solve Eq. 6 through Eq. 11 in the specified domain. The contour plots of the concentrations at the baseline and aligned geometry are shown in Figure 6.10a - 6.10b and Figure 6.10c - 6.10d, respectively, at time = 0.1 and 10 seconds. The simulations ran up to 10 seconds because the resistance from the HPPC experiment was obtained after 10 seconds of discharge.

To get potential changes ($\nabla\Phi$), the concentration results were applied to the current (i) and potential (Φ) equation (Eq. 7):

$$i = -k_{eff}\nabla\Phi + \frac{k_{eff}RT}{F}\left(1 + \frac{\partial \ln f_{\pm}}{\partial \ln C}\right)(1 - t_{+})\nabla C \qquad (7)$$

where R, T, and F are universal gas constant, temperature, and Faraday's constant, respectively. It was assumed that the solution is ideal for activity coefficient ($f_{\pm}$). The effective conductivity of the electrolyte with 2:1 v/v mixture of EC/DMC (k_{eff})[42] was used since the one with EC/DEC (3:7 wt) is unavailable. The k_{eff} and Li^{+} transference number in the electrolyte (t_{+})[45] are a function of concentration (Eq. 8 and 9).

$$k_{eff} = 4.1253 \times 10^{-4} + 5.007 \times 10^{-4}\, C - 4.7212 \times 10^{-4}\, C^2 + 1.5094 \times 10^{-4}\, C^3 - 1.6018 \times 10^{-4}\, C^4 \qquad (8)$$

$$t_{+} = 0.0107907 + 1.48837 \times 10^{-4}\, C \qquad (9)$$

The obtained potential changes between the reference electrode and anode or cathode were then applied to Eq. 10 and 11 to get anode and cathode resistance ratio to total resistance:

$$Ratio\ of\ R_{WE-RE} = \frac{R_{WE-RE}}{R_{WE-RE} + R_{CE-RE}} = \frac{\frac{\Delta\Phi_{WE-RE}}{\Delta I}}{\frac{\Delta\Phi_{WE-RE}}{\Delta I} + \frac{\Delta\Phi_{CE-RE}}{\Delta I}} = \frac{\Delta\Phi_{WE-RE}}{\Delta\Phi_{WE-RE} + \Delta\Phi_{CE-RE}} \qquad (10)$$

$$Ratio\ of\ R_{CE-RE} = 1 - Ratio\ of\ R_{WE-RE} \qquad (11)$$

Figure 6.11 shows the resistance ratios from the simulations for up to 10 seconds. Experimental results near 3.8V before cycling (Figure 6.5a and 6.5b) are included in the figure for comparisons.

Table 6.4. Parameters and their definitions in Figure 6.9 and for Eq.6 and Eq.7

Parameters	Condition or value	definition
IC	C = 1200 mole m^{-3}	Initial condition for electrolyte concentration
BC1	C = 1050 mole m^{-3} $\frac{dC}{dt} = 0$	Constant boundary condition for electrolyte concentration
BC2	C = 1350 mole/m^3 $\frac{dC}{dt} = 0$	Constant boundary condition for electrolyte concentration
BC3	∇C = 0	No diffusion through boundary
ε	0.41 [46]	Separator porosity in electrolyte region
D_{eff}	2.5×10^{-10} m^2 s^{-1} [47]	Electrolyte diffusion coefficient
i	42.07 A m^{-2}	Current density of electrolyte phase
Φ	Variable, V	Potential (measured with a lithium reference electrode in electrolyte)
k_{eff}	Variable, S m^{-1} [42]	Effective ionic conductivity of the electrolyte in region
R	8.314 J mol^{-1} K^{-1}	Universal gas constant
T	305.3 ºK	Temperature
C	Variable, mol m^{-3}	Electrolyte concentration
F	96487 C mol^{-1}	Faraday's constant
t+	Variable [45]	Li^+ transference number in electrolyte

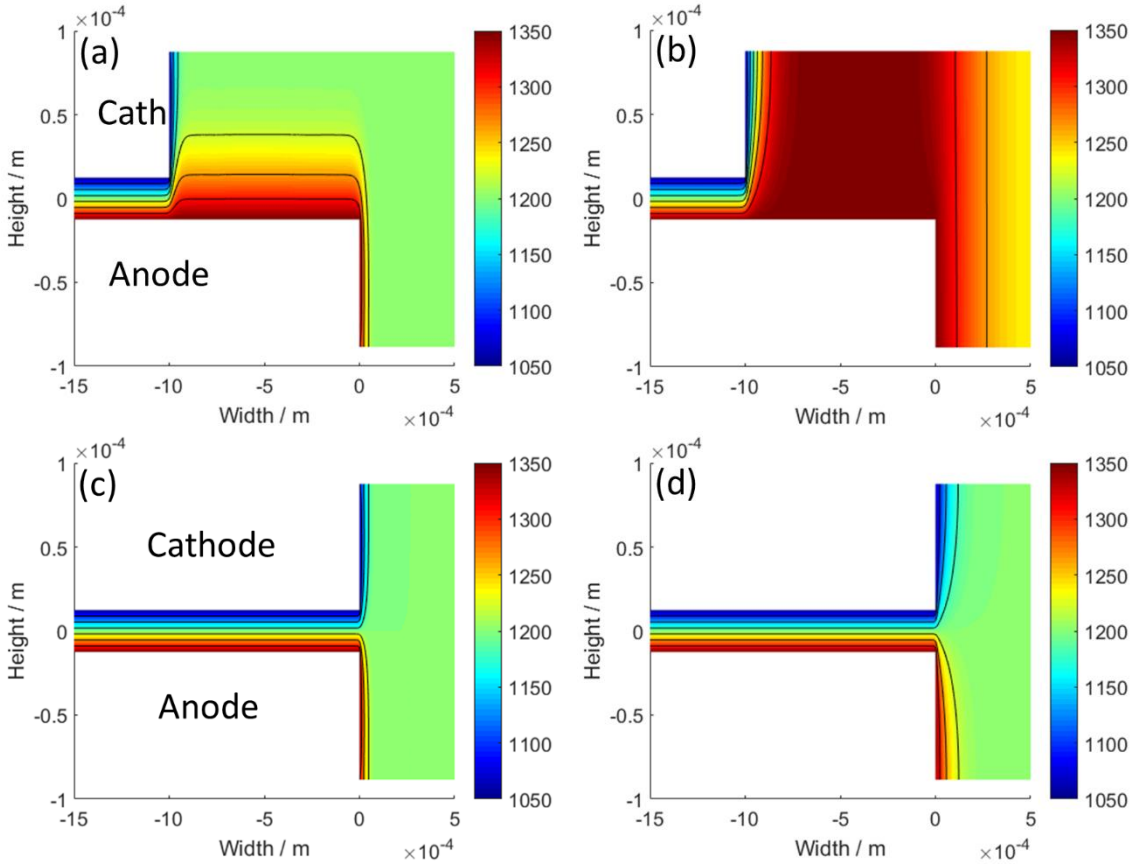


Figure 6.10. Contour plots of electrolyte concentrations at 2D cross-section geometries of the baseline cell at 0.1 sec. (a) and 10 sec. (b) and aligned cell at 0.1 sec. (c) and 10 sec. (c).

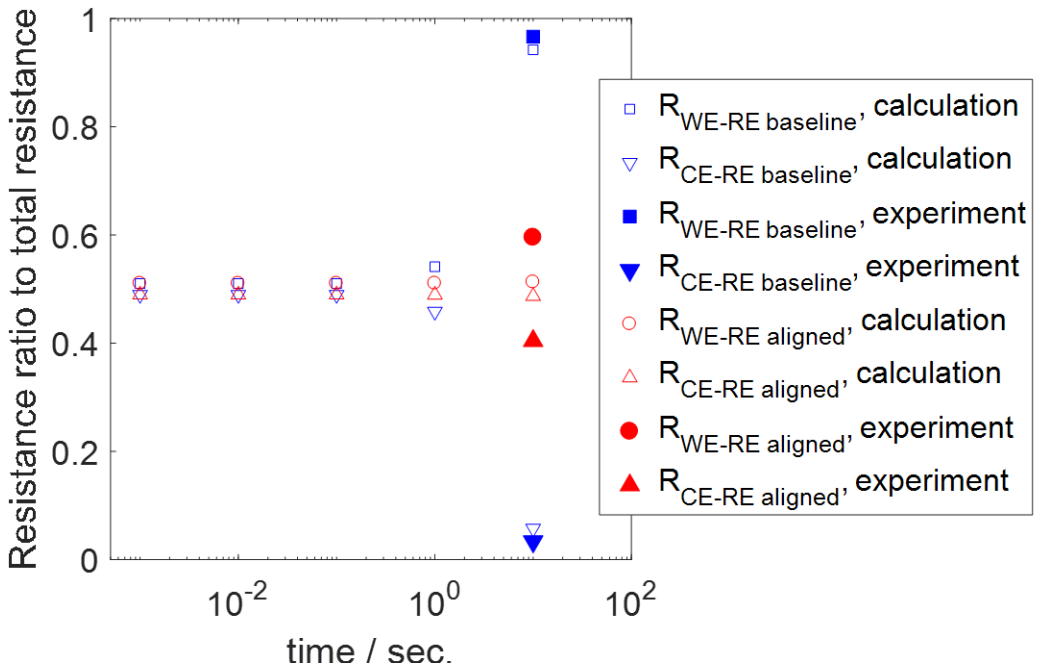


Figure 6.11. Resistance ratio of anode and cathode to total resistance from unsteady-state simulations and experiments near 3.8 V (Figure 6a and 6b).

The simulation results slightly differed from the experimental results because the electrolyte concentrations on electrode edges were unknown and set constant as Table 6.4 shows. Although different results at 10 seconds were obtained between the simulation and experiment, both sets of results showed good agreement in that the anode resistances ($R_{CE\text{-}RE}$) from the baseline cell were much smaller than ones from the aligned cell. This result supports the hypothesis that the distance between reference and anode or cathode in electrolyte affects resistance measurements. The aligned experimental data slightly shifted towards baseline data, causing the higher difference than baseline between simulation and experiment at 10 seconds. This higher difference in the aligned cells can occur when the aligned electrodes for the experiments were not exactly aligned like the geometry given for the simulation. The experiment results would have been close to the simulation ones if the experimental cells were perfectly aligned like the simulation.

Conclusions

A simple three-electrode pouch cell was designed and demonstrated in this study to distinguish the voltage profiles and resistances of the anode and cathode in full pouch cells during charge/discharge processes. Baseline (1-mm staggered alignment) cells and aligned cells were tested. Although, from the HPPC and EIS tests, overall cell resistances from the baseline were greater than ones from aligned cells, both cell types showed the initial resistances at the NMC 532 cathodes were greater than those at the graphite anodes after formation cycles. After 15 cycles of C-rate performance tests with the fast degradation induced by the higher cut-off voltage of 4.6 $V_{WE\text{-}RE}$, the cathode resistances significantly increased while the anode resistance slightly changed.

The baseline anode resistances were *less* than the resistances with the aligned cells, while the baseline cathode resistances were *greater* than the resistances for the aligned cells. The cell alignments affected voltage changes during unsteady-state voltage (current) perturbations like EIS and HPPC tests. According to EIS analysis, reference outside of electrodes was influenced by induction. The induction effect at anode (CE-RE) and cathode (WE-RE) was larger at the baseline than aligned cell while cells (WE-CE) did not show clear induction. HPPC and EIS tests showed total resistance and cathode resistance ratio increased as cathode moved away from the reference. Calculation results for solid-state diffusion rates using cathode EIS data were also influenced by the alignments, above 10^{-10} cm^2/s at the aligned cells and below 10^{-10} cm^2/s at the baseline cells.

EIS and 2D simulation showed that electrolyte resistance is the main contributor to the difference in cell resistances between the two cell configurations. The 2D

simulation showed electrolyte concentration distributions in the baseline differed from that in the aligned cell and resulted in higher cathode and lower anode resistances. This result was consistent with EIS analysis, higher cathode and lower anode ohmic resistance at the baseline than the aligned cell. Hence, it was determined that the location of a reference electrode should be carefully controlled to measure resistances at each electrode and solid-state diffusion rates.

References

1. Fleckenstein, M.; Bohlen, O.; Roscher, M. A.; Bäker, B., Current density and state of charge inhomogeneities in Li-ion battery cells with LiFePO4 as cathode material due to temperature gradients. *Journal of Power Sources* **2011,** *196*, 4769-4778.
2. Osswald, P. J.; Erhard, S. V.; Noel, A.; Keil, P.; Kindermann, F. M.; Hoster, H.; Jossen, A., Current density distribution in cylindrical Li-Ion cells during impedance measurements. *Journal of Power Sources* **2016,** *314*, 93-101.
3. Yi, J.; Kim, U. S.; Shin, C. B.; Han, T.; Park, S., Three-Dimensional Thermal Modeling of a Lithium-Ion Battery Considering the Combined Effects of the Electrical and Thermal Contact Resistances between Current Collecting Tab and Lead Wire. *Journal of the Electrochemical Society* **2013,** *160*, A437-A443.
4. Jeon, D. H.; Baek, S. M., Thermal modeling of cylindrical lithium ion battery during discharge cycle. *Energy Conversion and Management* **2011,** *52*, 2973-2981.
5. Nagasubramanian, G.; Doughty, D. H., 18650 Li-ion cells with reference electrode and in situ characterization of electrodes. *Journal of Power Sources* **2005,** *150*, 182-186.
6. McTurk, E.; Birkl, C. R.; Roberts, M. R.; Howey, D. A.; Bruce, P. G., Minimally Invasive Insertion of Reference Electrodes into Commercial Lithium-Ion Pouch Cells. *ECS Electrochemistry Letters* **2015,** *4*, A145-A147.
7. Waldmann, T.; Hogg, B.-I.; Kasper, M.; Grolleau, S.; Couceiro, C. G.; Trad, K.; Matadi, B. P.; Wohlfahrt-Mehrens, M., Interplay of Operational Parameters on Lithium Deposition in Lithium-Ion Cells: Systematic Measurements with Reconstructed 3-Electrode Pouch Full Cells. *Journal of The Electrochemical Society* **2016,** *163*, A1232-A1238.
8. Klink, S.; Madej, E.; Ventosa, E.; Lindner, A.; Schuhmann, W.; La Mantia, F., The importance of cell geometry for electrochemical impedance spectroscopy in three-electrode lithium ion battery test cells. *Electrochemistry Communications* **2012,** *22*, 120-123.
9. An, S. J.; Li, J.; Du, Z.; Daniel, C.; Wood, D. L., Fast formation cycling for lithium ion batteries. *J. Power Sources* **2017,** *342*, 846-852.
10. An, S. J.; Li, J.; Sheng, Y.; Daniel, C.; Wood III, D. L., Long-Term Lithium-Ion Battery Performance Improvement via Ultraviolet Light Treatment of the Graphite Anode. *J. Electrochem. Soc.* **2016,** *163*, A2866-A2875
11. An, S. J.; Li, J.; Mohanty, D.; Daniel, C.; Polzin, B. J.; Croy, J. R.; Trask, S.; Wood, D. L., Correlation of Electrolyte Volume and Electrochemical Performance in Lithium-ion Pouch Cells with Graphite Anodes and NMC532 Cathodes. *J. Electrochem. Soc.* **2017,** *164*, A1195-A1202.
12. An, S. J.; Li, J.; Daniel, C.; Meyer, H. M., 3rd; Trask, S. E.; Polzin, B. J.; Wood, D. L., 3rd, Electrolyte Volume Effects on Electrochemical Performance and Solid Electrolyte Interphase in Si-Graphite/NMC Lithium-Ion Pouch Cells. *ACS Appl Mater Interfaces* **2017,** *In Press*.

13. Li, J.; Daniel, C.; An, S. J.; Wood, D., Evaluation Residual Moisture in Lithium-Ion Battery Electrodes and Its Effect on Electrode Performance. *MRS Advances* **2016,** *1*, 1029-1035.
14. An, S. J.; Li, J.; Daniel, C.; Mohanty, D.; Nagpure, S.; Wood, D. L., The State of Understanding of the Lithium-ion-Battery Graphite Solid Electrolyte Interphase (SEI) and its Relationship to Formation Cycling. *Carbon* **2016,** *105*, 52-76.
15. FreedomCAR Battery Test Manual for Power-Assist Hybrid Electric Vehicles. *Idaho National Laboratory* **2003**, DOE/ID-11069, Oct.
16. Aurbach, D., Review of selected electrode–solution interactions which determine the performance of Li and Li ion batteries. *J. Power Sources* **2000,** *89* 206-218.
17. Levi, M. D.; Aurbach, D., Simultaneous Measurements and Modeling of the Electrochemical Impedance and the Cyclic Voltammetric Characteristics of Graphite Electrodes Doped with Lithium. *J. Phys. Chem. B* **1997,** *101*, 4630-4640.
18. Yamada, Y.; Iriyama, Y.; Abe, T.; Ogumi, Z., Kinetics of lithium ion transfer at the interface between graphite and liquid electrolytes: effects of solvent and surface film. *Langmuir : the ACS journal of surfaces and colloids* **2009,** *25*, 12766-70.
19. Aurbach, D.; Markovsky, B.; Weissman, I.; Levi, E.; Ein-Eli, Y., On the correlation between surface chemistry and performance of graphite negative electrodes for Li ion batteries. *Electrochim. Acta* **1999,** *45*, 67–86.
20. Ender, M.; Weber, A.; Ivers-Tiffee, E., Analysis of Three-Electrode Setups for AC-Impedance Measurements on Lithium-Ion Cells by FEM simulations. *J. Electrochem. Soc.* **2012,** *159*, A128-A136.
21. Levi, M. D.; Lu, Z.; Aurbach, D., Li-insertion into thin monolithic V2O5 films electrodes characterized by a variety of electroanalytical techniques. *Journal of Power Sources* **2001,** *97-98*, 482-485.
22. Rodrigues, S.; Munichandraiah, N.; Shukla, A. K., AC impedance and state-of-charge analysis of a sealed lithium-ion rechargeable battery. *J Solid State Electrochem* **1999,** *3*, 397-405.
23. Li, J.; Murphy, E.; Winnick, J.; Kohl, P. A., Studies on the cycle life of commercial lithium ion batteries during rapid charge–discharge cycling. *Journal of Power Sources* **2001,** *102*, 294–301.
24. Ecker, M.; Gerschler, J. B.; Vogel, J.; Käbitz, S.; Hust, F.; Dechent, P.; Sauer, D. U., Development of a lifetime prediction model for lithium-ion batteries based on extended accelerated aging test data. *Journal of Power Sources* **2012,** *215*, 248-257.
25. Umeda, M.; Dokko, K.; Fujita, Y.; Mohamedi, M.; Uchida, I.; Selman, J. R., Electrochemical impedance study of Li-ion insertion into mesocarbon microbead single particle electrode. *Electrochimica Acta* **2001,** *47*, 885-890.
26. Levi, M. D.; Aurbach, D., Diffusion Coefficients of Lithium Ions during Intercalation into Graphite Derived from the Simultaneous Measurements and

Modeling of Electrochemical Impedance and Potentiostatic Intermittent Titration Characteristics of Thin Graphite Electrodes. *J. Phys. Chem. B* **1997,** *101*, 4641-4647.
27. Levi, M. D.; Markevich, E.; Aurbach, D., The Effect of Slow Interfacial Kinetics on the Chronoamperometric Response of Composite Lithiated Graphite Electrodes and on the Calculation of the Chemical Diffusion Coefficient of Li Ions in Graphite. *J. Phys. Chem. B* **2005,** *109*, 7420-7427.
28. Mohanty, D.; Kalnaus, S.; Meisner, R. A.; Rhodes, K. J.; Li, J.; Payzant, E. A.; Wood, D. L.; Daniel, C., Structural transformation of a lithium-rich Li1.2Co0.1Mn0.55Ni0.15O2 cathode during high voltage cycling resolved by in situ X-ray diffraction. *Journal of Power Sources* **2013,** *229*, 239-248.
29. Aurbach, D.; Srur-Lavi, O.; Ghanty, C.; Dixit, M.; Haik, O.; Talianker, M.; Grinblat, Y.; Leifer, N.; Lavi, R.; Major, D. T.; Goobes, G.; Zinigrad, E.; Erickson, E. M.; Kosa, M.; Markovsky, B.; Lampert, J.; Volkov, A.; Shin, J. Y.; Garsuch, A., Studies of Aluminum-Doped LiNi0.5Co0.2Mn0.3O2: Electrochemical Behavior, Aging, Structural Transformations, and Thermal Characteristics. *Journal of the Electrochemical Society* **2015,** *162*, A1014-A1027.
30. Lu, Z.; Dahn, J. R., Understanding the Anomalous Capacity of Li/Li[Ni[sub x]Li[sub (1/3−2x/3)]Mn[sub (2/3−x/3)]]O[sub 2] Cells Using In Situ X-Ray Diffraction and Electrochemical Studies. *Journal of The Electrochemical Society* **2002,** *149*, A815.
31. Takami, N., Structural and Kinetic Characterization of Lithium Intercalation into Carbon Anodes for Secondary Lithium Batteries. *Journal of The Electrochemical Society* **1995,** *142*, 371.
32. Dahn, J. R.; Fong, R.; Spoon, M. J., Suppression of staging in lithium-intercalated carbon by disorder in the host. *Physical Review B* **1990,** *42*, 6424-6432.
33. Dahn, J. R., Phase diagram ofLixC6. *Physical Review B* **1991,** *44*, 9170-9177.
34. Wang, C. S.; Appleby, A. J.; Little, F. E., Charge–discharge stability of graphite anodes for lithium-ion batteries. *J. Electroanal. Chem.* **2001,** *497*, 33-46.
35. Hoshi, Y.; Narita, Y.; Honda, K.; Ohtaki, T.; Shitanda, I.; Itagaki, M., Optimization of reference electrode position in a three-electrode cell for impedance measurements in lithium-ion rechargeable battery by finite element method. *J. Power Sources* **2015,** *288*, 168-175.
36. Li, Y.; Bettge, M.; Polzin, B.; Zhu, Y.; Balasubramanian, M.; Abraham, D. P., Understanding Long-Term Cycling Performance of Li1.2Ni0.15Mn0.55Co0.1O2-Graphite Lithium-Ion Cells. *Journal of the Electrochemical Society* **2013,** *160*, A3006-A3019.
37. Klett, M.; Gilbert, J. A.; Trask, S. E.; Polzin, B. J.; Jansen, A. N.; Dees, D. W.; Abraham, D. P., Electrode Behavior RE-Visited: Monitoring Potential Windows, Capacity Loss, and Impedance Changes in Li1.03(Ni0.5Co0.2Mn0.3)0.97O2/Silicon-Graphite Full Cells. *Journal of The Electrochemical Society* **2016,** *163*, A875-A887.

38. Levi, M. D.; Salitra, G.; Markovsky, B.; Teller, H.; Aurbach, D.; Heider, U.; Heider, L., Solid-State Electrochemical Kinetics of Li-Ion Intercalation into Li1-xCoO2: Simultaneous Application of Electroanalytical Techniques SSCV, PITT, and EIS. *J. Electrochem. Soc.* **1999,** *146*, 1279-1289.
39. Levi, M. D.; Aurbach, D., Frumkin intercalation isotherm - a tool for the description of lithium insertion into host materials: a review. *Electrochim. Acta* **1999,** *45*, 167-185.
40. Prosini, P. P.; Lisi, M.; Zane, D.; Pasquali, M., Determination of the Diffusion Coefficient of LiFePO4. *Solid State Ionics* **2002,** *148*, 45-51.
41. Dees, D. W.; Abraham, D. P.; Lu, W.; Gallagher, K. G.; Bettge, M.; Jansen, A. N., Electrochemical Modeling and Performance of a Lithium- and Manganese-Rich Layered Transition-Metal Oxide Positive Electrode. *Journal of the Electrochemical Society* **2015,** *162*, A559-A572.
42. Doyle, M.; Newman, J., Comparison of Modeling Predictions with Experimental Data from Plastic Lithium Ion Cells. *J. Electrochem. Soc.* **1996,** *143*, 1890-1903.
43. Fuller, T. F.; Doyle, M.; Newman, J., Simulation and Optimization of the Dual Lithium Ion Insertion Cell. *J. Electrochem. Soc.* **1994,** *141*, 1-10.
44. Dees, D.; Gunen, E.; Abraham, D.; Jansen, A.; Prakash, J., Alternating Current Impedance Electrochemical Modeling of Lithium-Ion Positive Electrodes. *Journal ofThe Electrochemical Society* **2005,** *152*, A1409-A1417.
45. Doyle, M.; Fuller, T. F.; John, N., Modeling of Galvanostatic Charge and Discharge of the Lithium/Polymer/Insertion Cell. *J. Electrochem. Soc.* **1993,** *140*, 1526-1533.
46. Zhang, S. S., A review on the separators of liquid electrolyte Li-ion batteries. *J. Power Sources* **2007,** *164*, 351-364.
47. Lundgren, H.; Behm, M.; Lindbergh, G., Electrochemical Characterization and Temperature Dependency of Mass-Transport Properties of LiPF6 in EC:DEC. *Journal ofThe Electrochemical Society* **2015,** *162*, A413-A420.

CONCLUSION AND FUTURE WORK

A lithium-ion battery SEI literature review was given in CHAPTER I for the purpose of gaining fundamental understanding of the known SEI layer properties and improving long-term anode performance. Based on this review, three factors (surface property, electrochemical condition, and electrolyte concentration) affecting SEI formation and cycle life were considered in CHAPTER II to V. Experimentation and analysis of the SEI on harvested anodes proved difficult because of moisture sensitivity, changing compositions, and thicknesses of only a few nanometers. To understand the complicated and delicate SEI, various analysis techniques were applied. For example, XPS was an excellent tool for analysis of surface elements and compositions at the nanometer-scale and was used extensively with an environmental transfer module to preserve the SEI after cell disassembly. For non-destructive and real-time measurement methods, EIS was adopted to obtain SEI resistances from total resistances. The total resistances were also compared with the results from HPPC.

To improve surface properties of anodes, dried graphite anodes were treated with UV light for different periods of time (0, 20, 40, and 60 minutes). The anodes were more hydrophilic after UV treatment and were most hydrophilic when treated for 40 minutes. The UV-tread anodes were assembled in pouch cells with NMC 532 cathodes and tested for 300 cycles of life tests with 1C charging and discharging rates between 2.5 V and 4.2 V. When treated by UV for 40 minutes, the electrodes demonstrated the lowest increases in charge transfer resistance and the highest capacity retentions during the life tests while the electrodes without UV treatment showed the highest increases in the resistance and the fastest capacity fade. XPS analysis showed that the SEI was composed of more solvent decomposition products and fewer salt products on UV-treated anodes than on the untreated one. The average thicknesses of the SEI layers at the anode were the smallest at UV 20 min and UV 40 min, followed by UV 0 min and UV 60 min. The average thickness of the SEI layers was thinner at the anode than at the cathode. The XPS results of the A12 powder and PVDF film showed that UV light with humid air increased oxygen levels, particularly in hydroxyl form, on graphite surfaces while reducing fluorine levels in the PVDF binders. This increase in oxygen levels is believed to improve SEI formation and cycle life.

After observing the positive UV effects, other approaches may be considered to shorten treatment time. Possible approaches are use of oxygen or ozone instead of air, increase in humidity (moisture level), and use of high power UV. Oxygen radicals might be effective as well if they can be held in a UV chamber. H_2O_2 can be considered as it produces OH radicals under UV. Furthermore, different UV ranges would be a factor in controlling the oxygen level. In this study, the UV treatment was conducted on coated and dried anodes to add oxygen groups on the anode surface because this process is effective and can be easily applied to

other existing processes. However, if raw graphite powder were treated with UV light first and then coated on current collectors, oxygen groups would be more uniformly distributed on the graphite surfaces throughout the coated electrode. In this pretreatment, changes (or removals) of the oxygen groups should be confirmed after mixing processes in solvents and coating processes.

To understand differences between SEI formation in baseline and UV-treated electrodes, TEM instrument with EELS would be useful. Figure 7.1 shows TEM sample preparations for SEI directly formed on graphite on a TEM grid. This preparation prevents TEM samples from being exposed to air or moisture. Figure 7.2 depicts SEM images and EDS results of graphite obtained after the proposed sample preparations.

A new formation protocol was developed to shorten formation time and was applied to pouch cells to study the effects on cycle life. The new protocol consisted of shallow charge-discharge cycles between 3.9 V and 4.2 V and full depth of discharge cycles after the shallow cycles, which reduced the formation time by at least 6 times. The results of cycle life tests showed the new protocol even improved capacity retention. EIS analysis showed lower SEI resistance for the cells that underwent the new protocol than those that underwent the baseline protocol, implying that the new protocol provided a more robust and chemically stable electrolyte interphase layer. Based on the findings from this study, it is believed that formation time can be further reduced using high C-rates (e.g., C/3, 1C, 3C) below 3.9 V.

A modified fast formation protocol was also proposed and reduced SEI formation time by a factor of 8 or more without compromising cell performance. In the protocol, 1C and C/3 below 3.9 V were used in an attempt to reduce the formation time, while the same C/5 was applied between 3.9 and 4.2 V (shallow cycling region). Discharge capacities during the aging cycles and resistances after the aging cycles were the same with and without the modified protocol within the error range.

To reduce SEI formation time further, the following parameters should be controlled;

- different higher and lower cut-off voltages for the shallow cycling region,
- C-rate higher than C/5 in the shallow cycling region,
- number of cycles smaller than 5 for the shallow cycling,
- temperature higher than 30 °C.

To understand SEI structures and compositions after different formation protocols, X-ray photoelectron spectroscopy (XPS) and transmission electron microscopy (TEM) with electron energy loss spectroscopy (EELS) would be

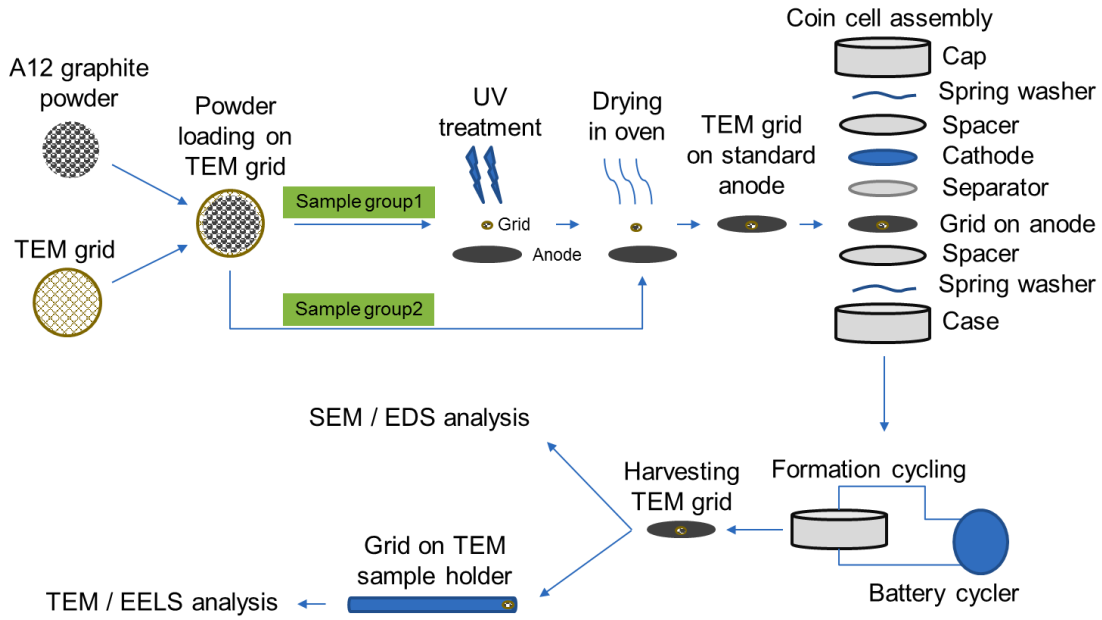
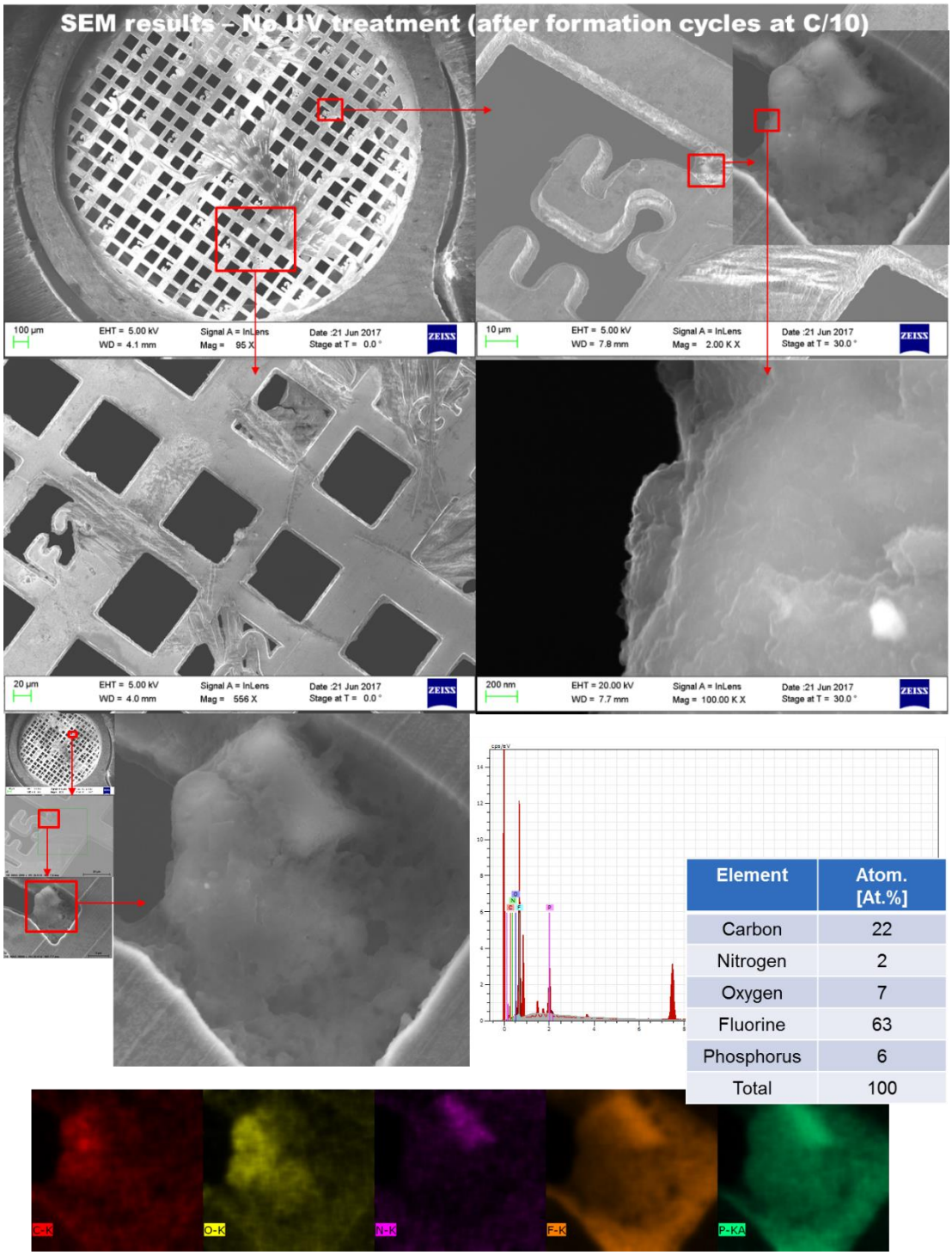


Figure 7.1. TEM sample preparation for SEI analysis.



Element	Atom. [At.%]
Carbon	22
Nitrogen	2
Oxygen	7
Fluorine	63
Phosphorus	6
Total	100

Figure 7.2. SEM images of TEM grids with graphite particles having SEI on them and EDS analysis results from a graphite particle.

helpful tools. The same technique shown in Figure 2.19 (TEM grid in a cell) with different formation protocols would be also useful for the SEI analysis.

To study electrolyte concentration effects on cycle life and anode SEI properties, electrolyte volume was controlled in pouch cells having graphite/ $LiNi_{0.5}Mn_{0.3}Co_{0.2}O_2$ (graphite cells) or 15wt%Si-graphite/$LiNi_{0.5}Mn_{0.3}Co_{0.2}O_2$ (Si cells). It was demonstrated that the electrolyte volume to total pore volume of electrodes and separators needed to be at least 1.9 for the graphite cells and 3.1 for the Si cells to achieve desired performance. Less electrolyte resulted in higher capacity fade in both graphite and Si cells. The graphite cells did not show significant improvement in cyclability and impedance reduction by further increasing the electrolyte volume factor above 1.9. The optimized capacity retention from the Si cells was lower than that from the graphite cells. Less electrolyte in the Si cells resulted in higher ohmic resistance, larger cell-to-cell capacity variation, and greater capacity fade. Unlike the graphite cells, significant Si anode charge transfer resistances were detected in EIS measurements and became more pronounced as the cell voltage decreased. Irreversible capacity loss also continuously increased as the Si cells were cycled. XPS results showed SEI thicknesses of the Si cells around 10 to 35 nm after 100 cycles, and the SEI thickness increased as the electrolyte volume factor increased. The XPS elemental analysis along the depth of the anode indicated that Li_xSiO_y formed throughout the Si particles rather than just as a surface layer. According to the results from EIS, SEM, and XPS, the SEI on Si seemed to have large pores or channels that are permeable to electrolyte.

Controlling surface properties using UV treatment, modified electrochemical potentials of the new formation protocol, and electrolyte volume control enhanced anode SEI properties and cell cycle life. SEI properties were investigated such as thicknesses, element compositions, and resistances under different conditions. However, more efforts are needed in the future to better understand SEI layer structure, morphology, formation mechanisms, etc. This study has covered some of the more important anode SEI properties and relationships to cycle life. However, as the lithium-ion battery field shifts toward high voltage cells (i.e., above 4.2 V), the cathode SEI may influence cell cycle life more than that of the anode. Hence, understating the cathode SEI properties will become increasingly important.

VITA

Seong Jin An was born in South Korea. He obtained a Bachelor of Science degree from Seoul National University of Science and Technology, Seoul, in Chemical Engineering in Feb. 1999 and a Master of Science degree from Yonsei University, Seoul, in Chemical Engineering in Feb. 2001. After graduation, he had worked at GS FuelCell for 2.5 years and Samsung SDI for 8.5 years as a researcher and senior researcher, respectively. Then, he entered USA in Dec. 2011 to pursue a higher degree and obtained a Master of Science degree from Carnegie Mellon University, PA, in Mechanical Engineering in May 2014. After that, he conducted research at Oak Ridge National Laboratory and graduated from the University of Tennessee Knoxville, TN, with a Doctor of Philosophy degree in Energy Science & Engineering in Aug. 2017.